AWARD NUMBER: W81XWH-10-1-1036

TITLE: *Simulation of Blast Loading on an Ultrastructurally-based Computational Model of the Ocular Lens*

PRINCIPAL INVESTIGATOR: Richard A. Regueiro, Ph.D.

CONTRACTING ORGANIZATION: University of Colorado, Boulder
Boulder, CO 80309-0001

REPORT DATE: December 2016

TYPE OF REPORT: Final

PREPARED FOR:
U.S. Army Medical Research and Materiel Command
Fort Detrick, Maryland 21702-5012

REPORT DOCUMENTATION PAGE

Form Approved
OMB No. 0704-0188

1. REPORT DATE *(DD-MM-YYYY)*	2. REPORT TYPE	3. DATES COVERED *(From - To)*
December 2016	Final	30Sep2010 – 29Sep2016

4. TITLE AND SUBTITLE
Simulation of Blast Loading on an Ultrastructurally-based Computational Model of the Ocular Lens

5a. CONTRACT NUMBER
W81XWH-10-1-1036

5b. GRANT NUMBER

5c. PROGRAM ELEMENT NUMBER

6. AUTHOR(S)

Richard Regueiro

Email: richard.regueiro@colorado.edu

5d. PROJECT NUMBER

5e. TASK NUMBER

5f. WORK UNIT NUMBER

7. PERFORMING ORGANIZATION NAME(S) AND ADDRESS(ES)

University of Colorado
   Boulder, CO 80309-0001

8. PERFORMING ORGANIZATION REPORT NUMBER

9. SPONSORING / MONITORING AGENCY NAME(S) AND ADDRESS(ES)
U.S. Army Medical Research and Materiel Command
Fort Detrick, Maryland 21702-5012

10. SPONSOR/MONITOR'S ACRONYM(S)

11. SPONSOR/MONITOR'S REPORT NUMBER(S)

12. DISTRIBUTION / AVAILABILITY STATEMENT
Approved for public release; distribution unlimited

13. SUPPLEMENTARY NOTES

14. ABSTRACT
This is the final report for a project funded to develop a multiscale computational model of ocular lens mechanics when subjected to dynamic loading.

15. SUBJECT TERMS
ocular lens rate-dependent mechanical properties, ocular lens ultrastructure, multiscale computational modeling of ocular lens mechanics

16. SECURITY CLASSIFICATION OF:			17. LIMITATION OF ABSTRACT	18. NUMBER OF PAGES	19a. NAME OF RESPONSIBLE PERSON USAMRMC
a. REPORT	b. ABSTRACT	c. THIS PAGE		286	19b. TELEPHONE NUMBER *(include area code)*
U	U	U	UU		

Standard Form 298 (Rev. 8-98)
Prescribed by ANSI Std. Z39.18

1 Introduction

In the life of a combat soldier, traumatic cataract in ocular lenses may result from blast loading, whereby (i) the lens capsule (Fig.1) is perforated by intraocular foreign bodies (IOFBs [Walter, 1962, Mader et al., 1993, Parver et al., 1993, Wong et al., 1997, Mader et al., 2006, Weichel and Colyer, 2008]) which in turn damage the lens fiber cells, (ii) the lens is loaded fluid dynamically by the surrounding aqueous and vitreous humors [Banitt et al., 2009] (see Fig.1), and/or (iii) the lens internal substance (crystallins lens fiber cells) is stressed by the passing shock wave. Traumatic cataract can result in a partially or fully clouded lens, complete dislocation of the lens (floating between aqueous and vitreous humors, see Fig.1), or zonule rupture such that partial or full vision loss may occur. The mechanisms of traumatic cataract formation that may require cataract surgery (implantation of an intraocular lens (IOL)) are not well understood in comparison to the mature and ever-improving surgical technology and procedures.

The **hypothesis of the research** is that an ultrastructurally-based computational finite element model of the ocular lens subjected to blast loading can assist in better understanding how traumatic cataract is formed in the combat soldier, and in turn improve our understanding of traumatic cataract in civilians whose eyes are subjected to impact loading. The **scope of the research** is to develop a multiscale, ultrastructurally-based, computational model of the ocular lens subjected to blast loading, in conjunction with imaging methods to identify lens capsule and internal substance structure and mechanical experiments for calibrating material model parameters.
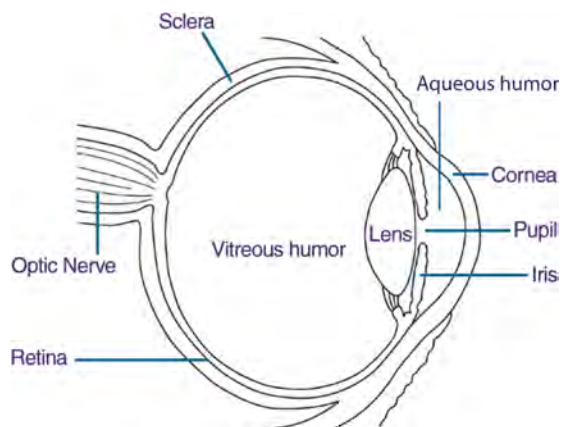

Figure 1. Eye cross-section. `www.nei.nih.gov`.

Figure 2 illustrates the overall multiscale computational modeling approach for the project. The multiscale modeling effort was separated into two parts: (i) the internal lens substance (fiber cells), and (ii) the lens capsule (type IV collagen ultrastructure).

2 Body

The Body of the Final Report will summarize the research Tasks accomplished, with details left to the Appendices. They are presented in order of accomplishment, rather than task number.

Task 4. unconfined compression testing of whole porcine lenses (0.001 - 1/s strain rate) to estimate whole lens mechanical response and generation of traumatic cataracts at higher strain rates (months 1-12):

Unconfined compression tests with flat platens were conducted on whole porcine lenses harvested from 2+yr-old and 6-9month old pigs within 36 hours of slaughter. This is necessary to obtain mechanical properties before the lens fiber cells degrade further. Lenses were submerged in balanced salt solution (BSS) at pig body temperature (39.2 °C), and then compressed to 10% and 20% axial strain at 0.1mm/s and 0.3mm/s displacement rates, and then held for ≈ 360 sec-
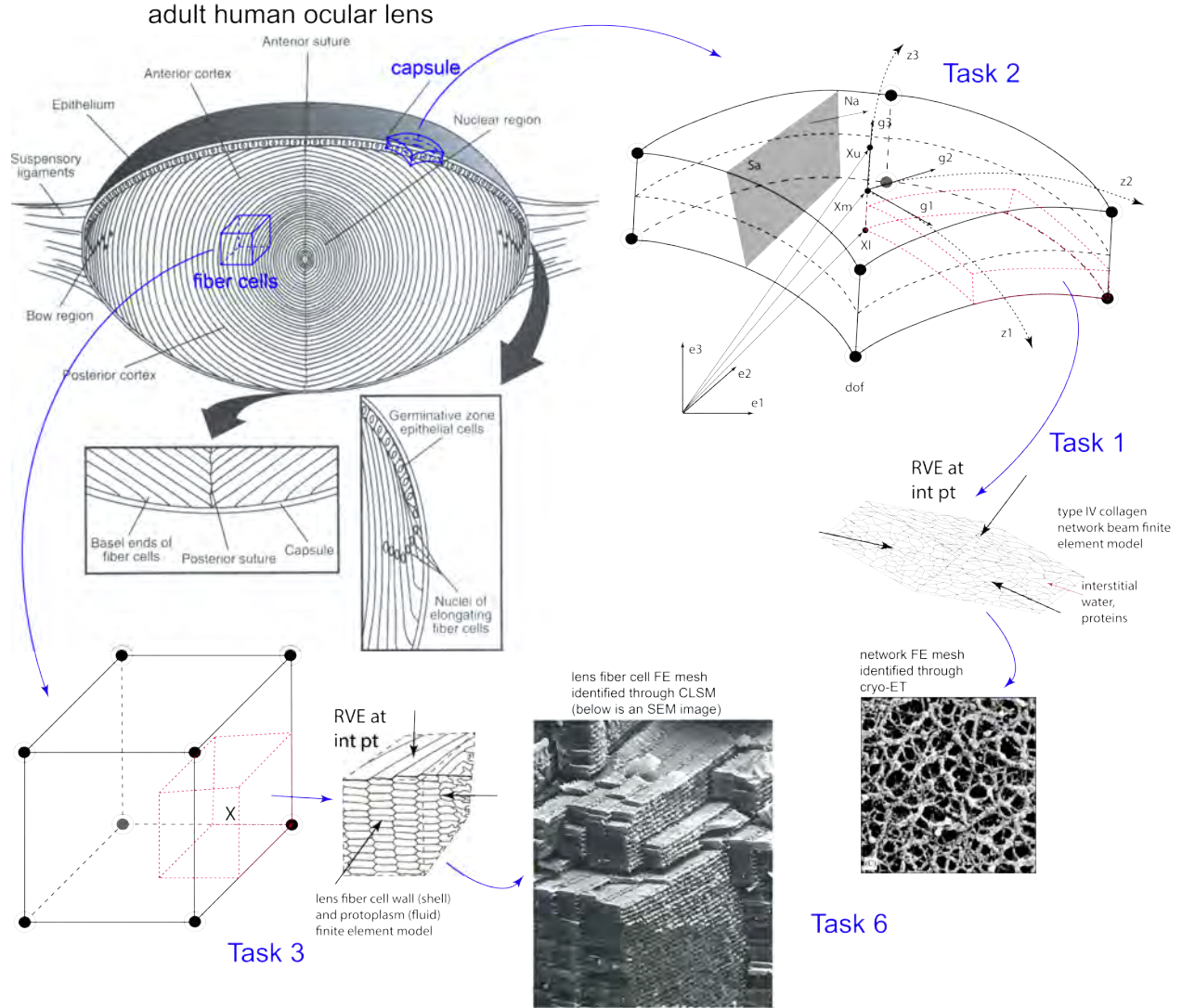
Figure 2. Schematic of the multiscale modeling approach for whole adult human lens [Kaufman and Alm, 2003] ultrastructurally-based model. The multiscale finite element models for the lens capsule (Tasks 1 and 2), and lens fiber cells (Task 3) are shown.

onds to measure the force versus time (i.e., a stress relaxation test). Pre-conditioning cycles were applied to attempt to minimize effects of mechanically testing tissue *in-vitro*. Examples for two lenses from 2+year old pigs compressed to 10% strain at multiple 0.1mm/s rates and holds are shown in Fig.3. The last load and hold curves from Fig.3 are used to fit parameters to a finite strain isotropic viscoelasticity model implemented in a finite element program that can simulate three-dimensional and axisymmetric loading, as shown in Figs.4,5. The lens capsule and lens internal substance are meshed separately, and the geometry of the lens mesh is taken from digital photos, such as in Fig.6. For this age pig, and at these loading conditions, these two eye data happen to bound the high and low force versus time (stress relaxation) test, with fits for a finite strain isotropic viscoelasticity model shown in Fig.4. The model parameters [Reese and Govindjee, 1998] are determined to be as follows: Eye3 lens capsule ($\tau = 10$sec, $\mu_{\mathrm{EQ}} = 1.275$MPa,

$\mu_{\text{NEQ}} = 0.65\text{MPa}$, $\kappa_{\text{EQ}} = 127.5\text{MPa}$, $\kappa_{\text{NEQ}} = 65\text{MPa}$), Eye3 lens internal substance ($\tau = 10\text{sec}$, $\mu_{\text{EQ}} = 1.275\text{e-4MPa}$, $\mu_{\text{NEQ}} = 6.5\text{e-5MPa}$, $\kappa_{\text{EQ}} = 0.1275\text{MPa}$, $\kappa_{\text{NEQ}} = 0.065\text{MPa}$), Eye2 lens capsule ($\tau = 9\text{sec}$, $\mu_{\text{EQ}} = 0.5175\text{MPa}$, $\mu_{\text{NEQ}} = 0.2\text{MPa}$, $\kappa_{\text{EQ}} = 51.75\text{MPa}$, $\kappa_{\text{NEQ}} = 20\text{MPa}$), Eye2 lens internal substance ($\tau = 9\text{sec}$, $\mu_{\text{EQ}} = 5.175\text{e-5MPa}$, $\mu_{\text{NEQ}} = 2\text{e-5MPa}$, $\kappa_{\text{EQ}} = 0.05175\text{MPa}$, $\kappa_{\text{NEQ}} = 0.02\text{MPa}$), where τ is the relaxation time, μ_{EQ} the equilibrium shear modulus, μ_{NEQ} the non-equilibrium shear modulus, κ_{EQ} the equilibrium bulk modulus, κ_{NEQ} the non-equilibrium bulk modulus. Example images of the lens before and after compression are shown in Fig.6. The remaining data for age range (6-9month and 2+year old pigs) and loading conditions (10% and 20% axial strain, and loading rates 0.1mm/s and 0.3mm/s) are being compiled and will be presented in a future journal article, along with remaining parameter fits.
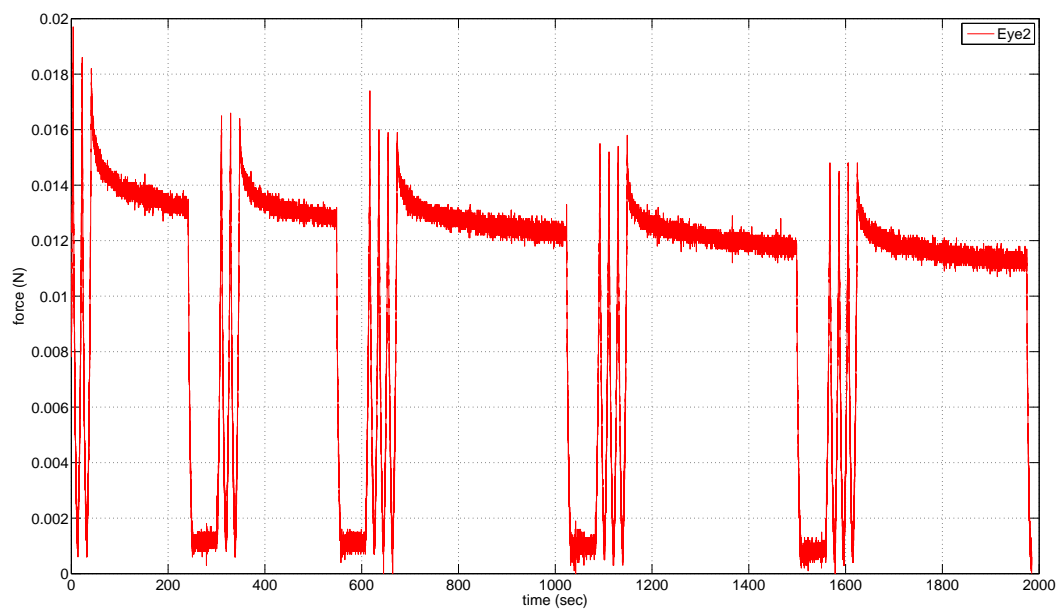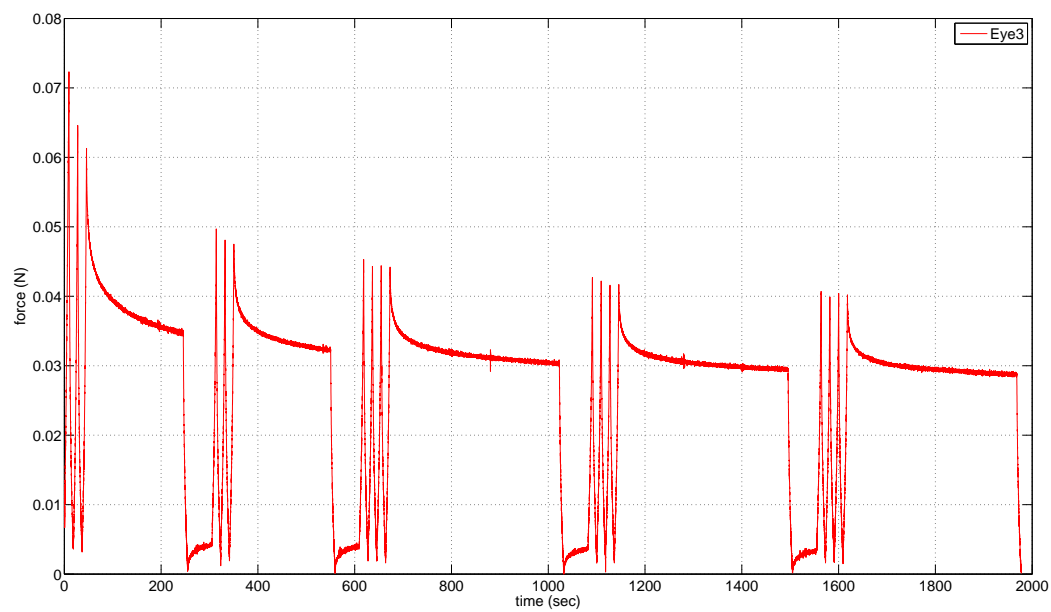
Figure 3. (top) Eye3. (bottom) Eye2.

4

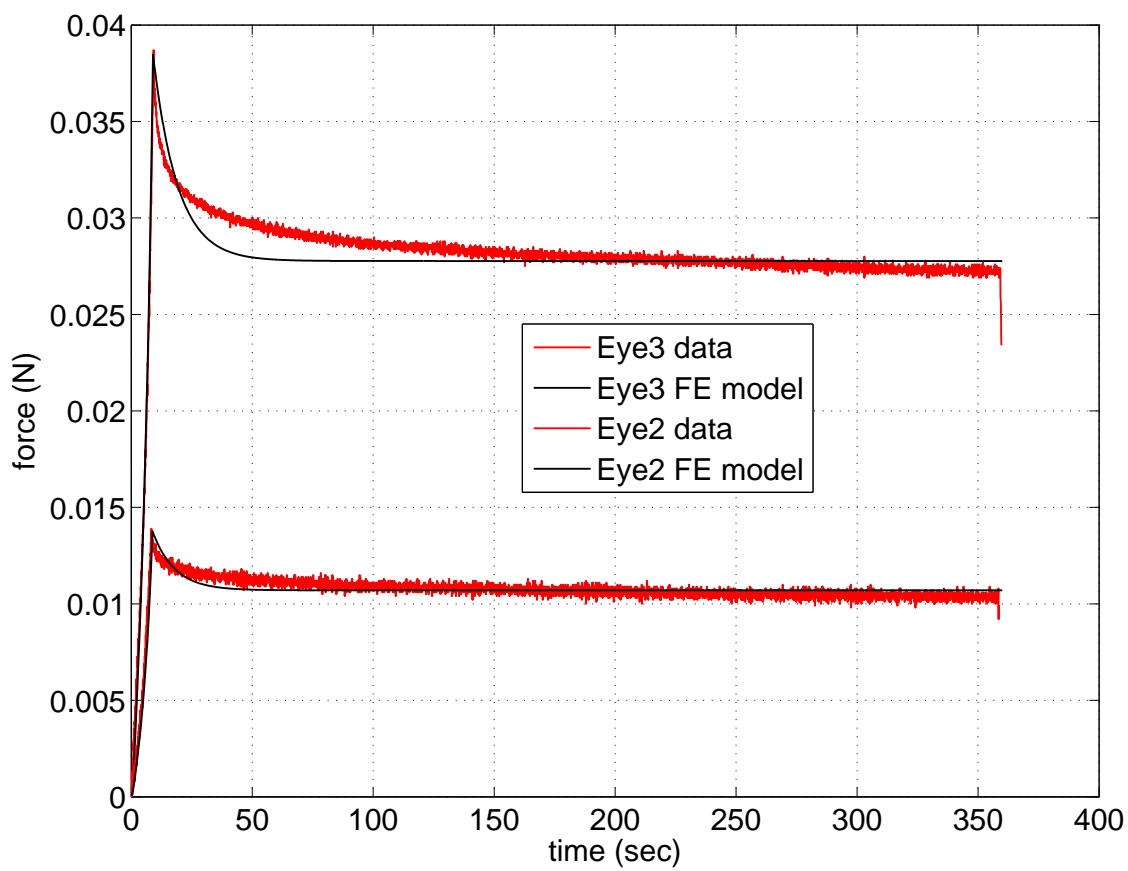Figure 4. Fit of finite strain isotropic viscoelastic constitutive model in an axisymmetric finite element program, against Eye3 and Eye2 data.
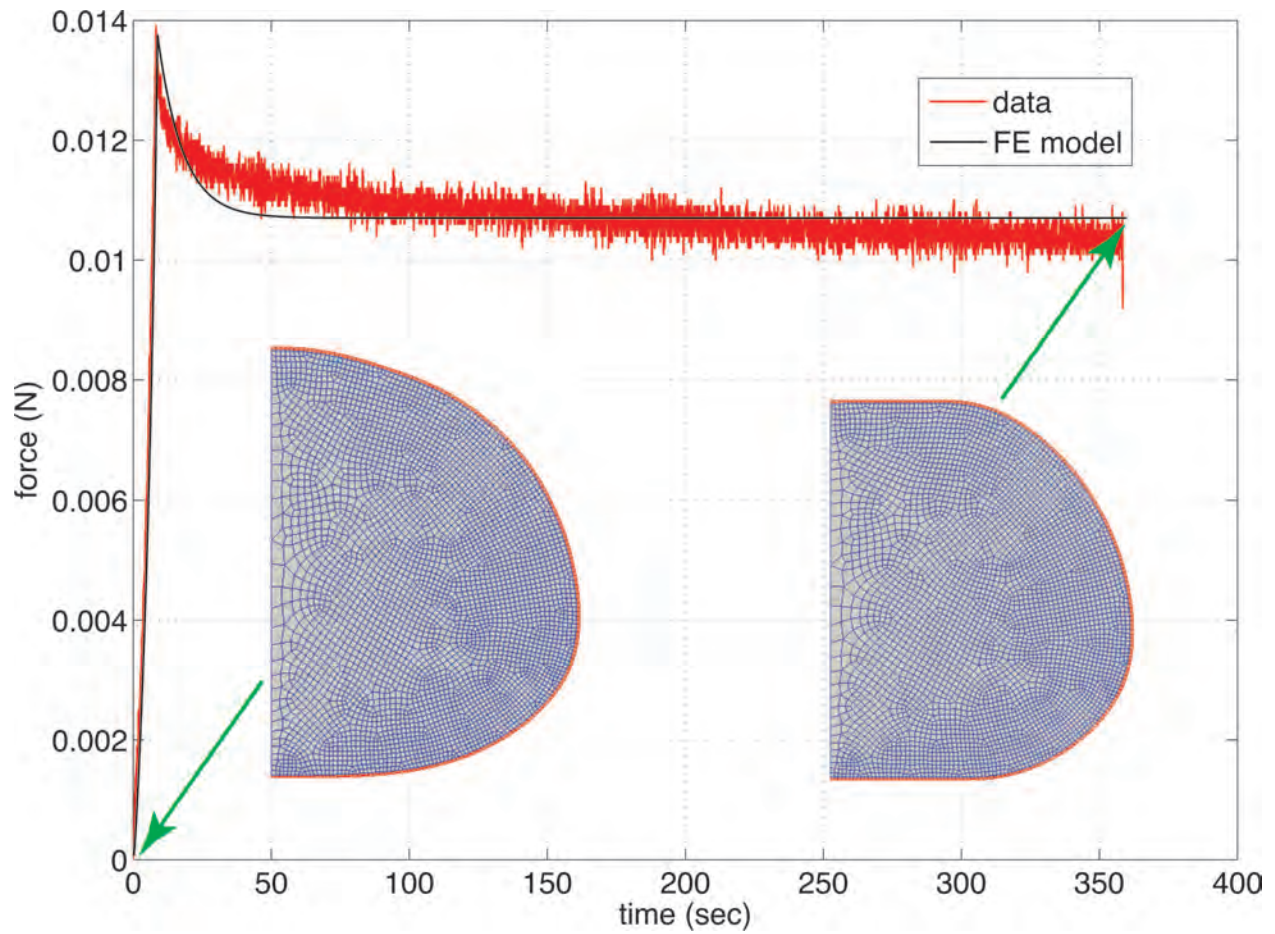
Figure 5. Fit of finite strain isotropic viscoelastic constitutive model in an axisymmetric finite element program, against Eye2 data, also showing undeformed and deformed meshes.
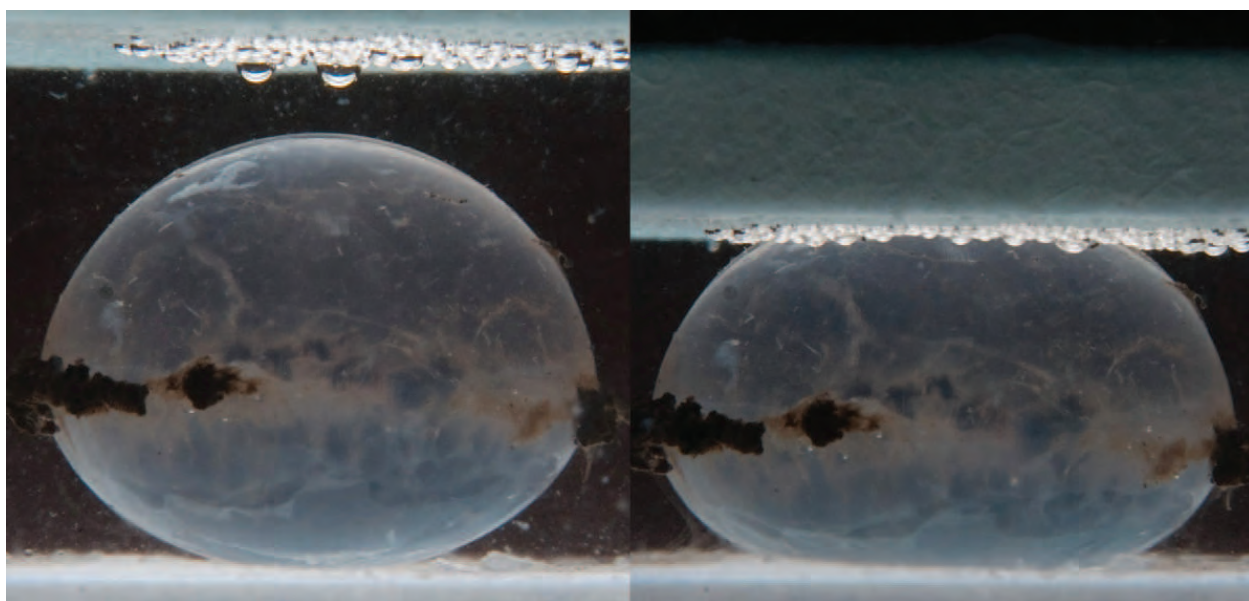
Figure 6. Example images of lens before and after compression to 10% strain during stress relaxation test.

Another form of unconfined compression is a puncture test, with image of test and results shown in Fig.7. We are in the process of simulating this experiment using a hybrid Lagrangian-Eulerian numerical analysis. Further puncture tests are being performed on the anterior and posterior sides of the lens.

Figure 7. Setup of lens puncture test for estimating penetration strength of lenses, and resulting force versus displacement data. The lenses are cupped with anterior side at the puncture tip. Tests are also conducted on the posterior side.

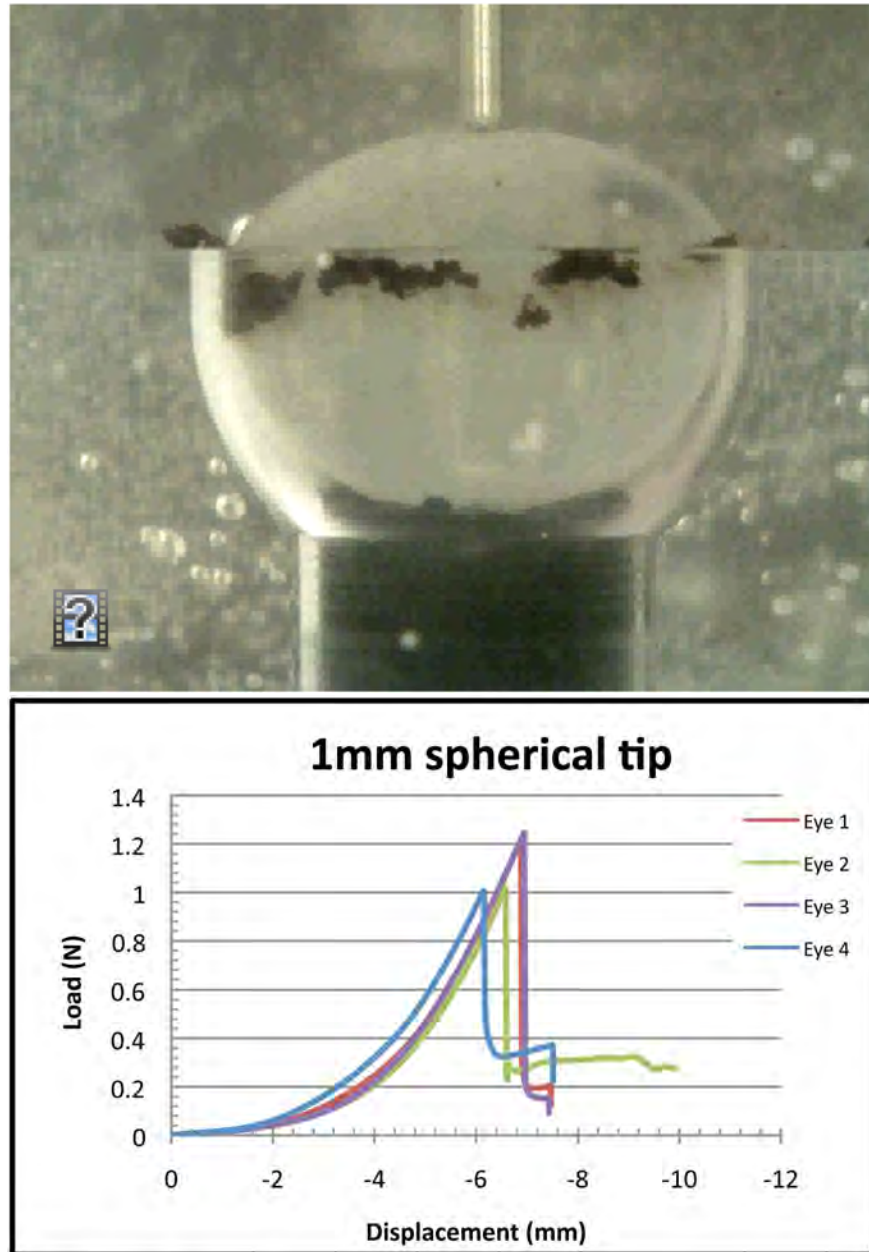**4a. Conduct unconfined compression tests at slower strain rates (0.001/s) to measure force versus time mechanical response, and image before and after testing the lens fiber cell geometry using CSLM in subtask 6a (months 1-6).**

The slower strain rate unconfined compression test results, and associated constitutive model parameter fitting, are discussed in Chapter 3 of Bay's MS thesis [Bay, 2012] (see Appendix A). It was observed that a finite strain, isotropic, viscoelastic constitutive model [Reese and Govindjee, 1998] used in the lens capsule and internal lens substance meshes separately (Fig. 3.15), with related but separate constitutive parameters, was able to model the stress relaxation response of whole porcine lenses for various hold strains and strain rates (Figs. 3.17, 3.19, 3.21, 3.23, 3.25, 3.27, 3.29, 3.31). An approximation that is not valid for human lenses is to ignore differences in mechanical properties between the nucleus and cortex [Burd et al., 2002]. This can be resolved as confocal laser scanning microscopy (CSLM) identifies the structure of human lens tissue.

CSLM was used to identify ultrastructure of the internal lens substance, the lens fiber cells in Chapter 7 [Bay, 2012]. It was observed that the fiber cell membranes could be discerned in green color, longitudinally and cross-sectionally. We are in the process of obtaining more images at various slices in the lens to see how an overall lens fiber ultrastructure can be reconstructed from these slice images.

CSLM was not conducted after unconfined compression because the methods are still being refined to identify the lens fiber cell structure.

Task 5. smooth and sharp nanoindentation testing on porcine lenses to approximate lens capsule multiscale elasticity and strength parameters, and mechanical parameters of internal lens substance material (months 12-24):

5a. Design and fabricate a fixture to clamp lens capsules for nanoindentation onto samples immersed in aqueous solution (months 12-15).

5b. Test use of new fixture in nanoindentation machine (month 16).

5c. Conduct smooth nanoindents on porcine lens capsules (months 16-18).

The procedure of nanoindentation, including substrate design and fabrication (Fig. 5.2), and preliminary results for creep testing with a 1 μm spherical tip (Figs. 5.4-5.27), is described in Chapter 5 [Bay, 2012]. We learned that the standard hold times (not surprising) for metals are too short to enable full creep of the lens capsules. Thus, we are in the process of testing in creep at longer hold times, approximately 5 minutes (300 seconds), compared to the 30-40 second hold times in the results in Figs. 5.4-5.27. It is clear a steady-state strain (displacement) has not been achieved. We plan to simulate with finite element analysis the same initial boundary value problem (IBVP) in order to calibrate gross viscoelastic properties of the capsule, and also the fibril viscoelastic properties for the three-dimensional finite strain beam model representing the type IV meshwork ultrastructure (**Task 6b**).

The next step is continuing smooth nanoindentation to longer creep times, and then conduct sharp nanoindentation (**Task 5d**) to measure the cutting force of lens capsules and possibly its time dependence. Nanoindentation on whole lenses most likely will not be conducted (**Tasks 5e and 5f**) because we are collecting data on large puncture tests of whole lenses (Chapter 4 [Bay, 2012]). These puncture data are more meaningful for understanding gross whole lens puncture resistance.

6b. On as-received porcine lens capsules, image type IV collagen ultrastructure in lens capsule using cyro-electron tomography (months 1-4).

Identification of type IV collagen meshwork ultrastructure in the lens capsule using cyro-electron microscopy/tomography is described in Chapter 6 [Bay, 2012]. Through standard freeze-substitution sample preparation methods, in conjunction with electron tomography (ET) to generate a stack of images, we see in Figs. 6.5-6.7 structure that begins to resemble type IV collagen meshwork ultrastructure identified in other works [Barnard et al., 1992, Inoue, 1994]. We plan to use this structure to then construct our 3D beam finite element mesh of the type IV collagen for our multiscale modeling in **Task 1**. Figure 6.8 demonstrates the initial procedure for obtaining a beam finite element mesh from such images.

One current focus of the research is to determine if the images in Figs. 6.5-6.7 are indeed structure, or if they are an artifact of the freezing process. There is currently a dispute among our collaborators in the Molecular, Cellular, and Development Biology (MCDB) Department at the University of Colorado Boulder, about this topic. More experiments are being conducted to determine whether what we are seeing is structure or artifact, and gelatin is being used as a control.

Higher Strain Rate Axial Compression Experiments on Whole Porcine Ocular Lenses

4b. Conduct unconfined compression tests at higher strain rates (up to 1/s) to measure force versus time mechanical response, and image before and after testing the lens fiber cell geometry using CSLM in subtask 6a to see if traumatic cataracts are generated (months 6-12).

First, we would like to acknowledge the support of Dr. Tusit Weerasooriya and his Member of Technical Staff, Dr. Brett Sanborn, in using their high strain rate experimental laboratory at ARL APG. They provided assistance to Mr. Bay during his one week visit to ARL in July 2012 to obtain the preliminary results presented here, in order to determine which high strain rate experiments on which to focus for future research.

For all compression tests, whether high strain rate compress and hold, or high strain rate impulse and release, or high strain rate puncture, the test apparatus shown in Figs.8-11 was used in Dr. Weerasooriya's lab at ARL APG. Just as at CU-Boulder, all lenses were compressed along their posterior-anterior poles, because this is how the lenses normally rest on a flat surface when placed in the BSS bath, except for puncture tests where we can also test the anterior side (Fig.4.5 of Bay [2012]).
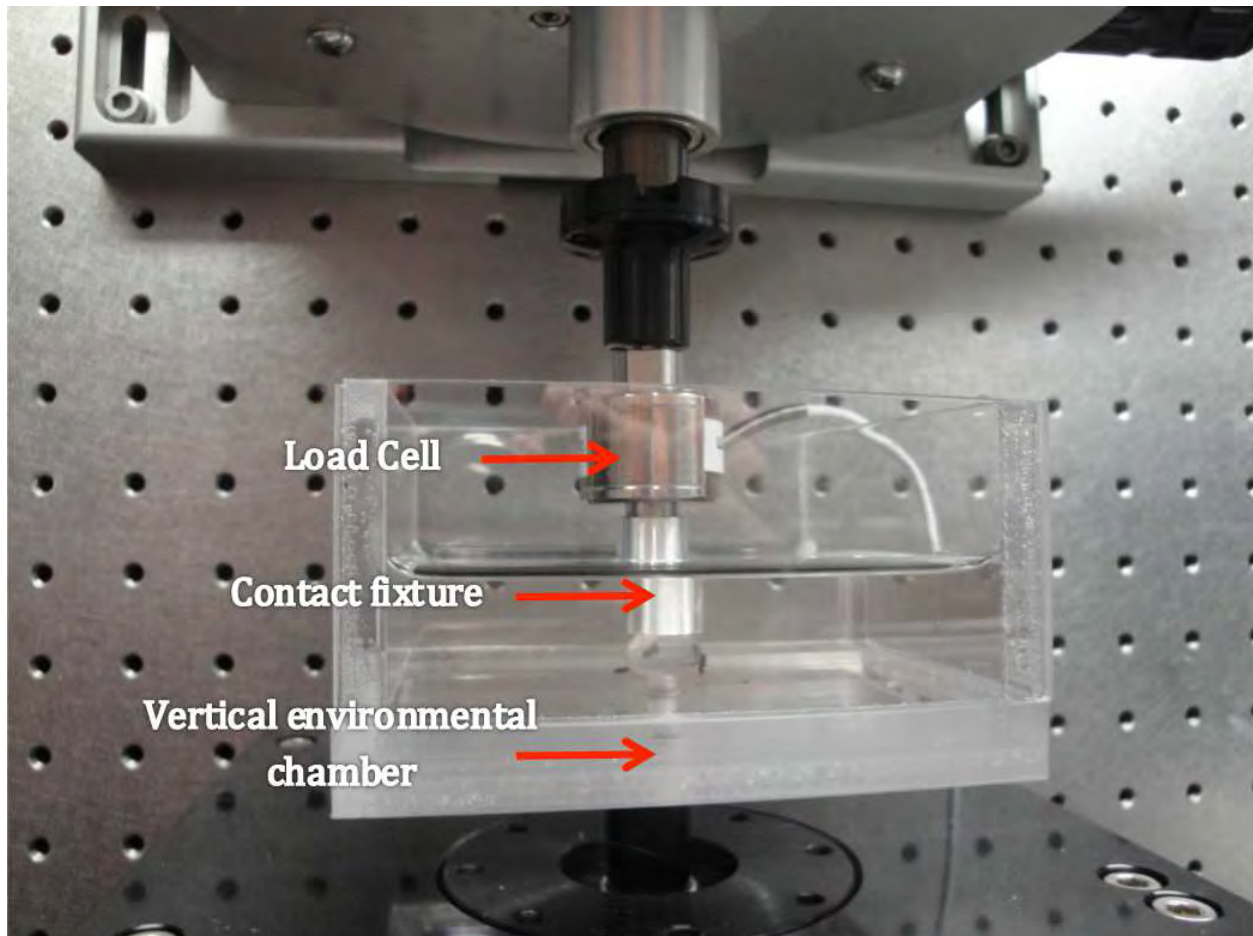

Figure 8.   Close-up of test setup with Bose Electroforce vertically compressing an ocular lens in Balance Salt Solution (BSS), with a porcine lens beneath the contact fixture. The load cell is rated at 250 g.
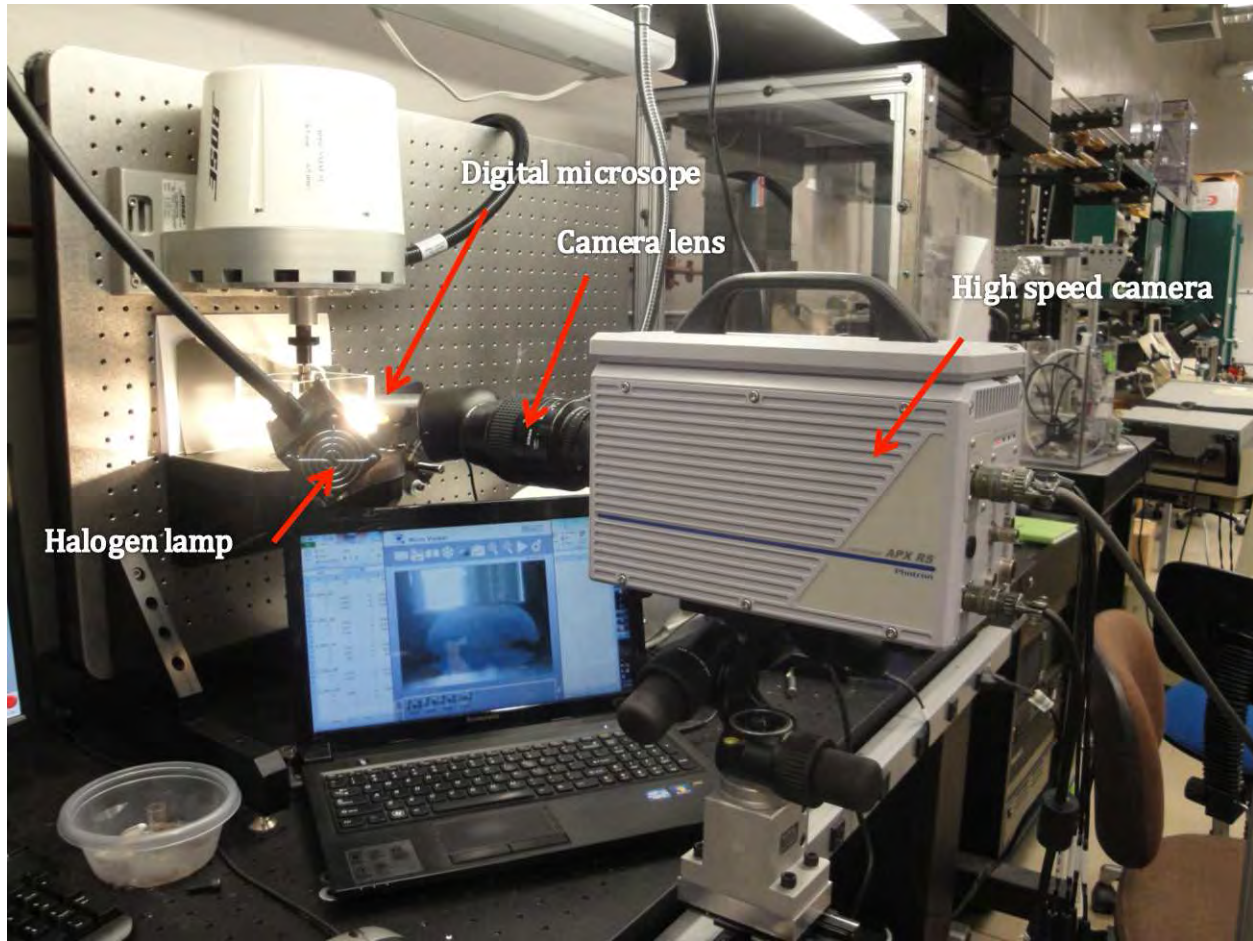
Figure 9. Overall test setup, showing the Bose Electroforce vertically mounted, the halogen lamp lighting the test bath with ocular lens, the high speed digital camera, and the image of the compressed lens on the laptop screen.

As an example of a high strain rate compression and hold experiment for stress relaxation, see the force versus time curve in Fig.12. This test involved a 1000 mm/s axial displacement rate to 10% axial strain and then held for ≈350 seconds. With a lens height of 8.67 mm, this leads to an axial strain rate nominally of 115/s. We can use these data, and for a range of strain rates, to calibrate the viscoelastic and poroelastic parameters of the material models. But further experiments are required to ensure repeatability of the data before material model parameter calibration.

As an example of a high strain rate impulse test on a lens, refer to the force versus time curve in Fig.13. This test involved a 500 mm/s axial displacement rate to 20% axial strain and then released. With a lens height of 8.96 mm, this leads to an axial strain rate nominally of 56/s. The results in Fig.13(top) are interesting, in that after the application of the impulse at ≈ 0.024sec, there is wave propagation axially through the lens as it contacts the contact fixture and the flat bottom surface of the environmental chamber. There is also dependence on the height of the contact fixture after impulse loading. For a 1000 mm/s axial displacement rate to 60% axial strain, with higher release of the contact fixture after impulse, we see larger motion of the lens dynamically after impulse loading. There clearly is a fluid dynamic effect of the BSS on the lens after impulse for
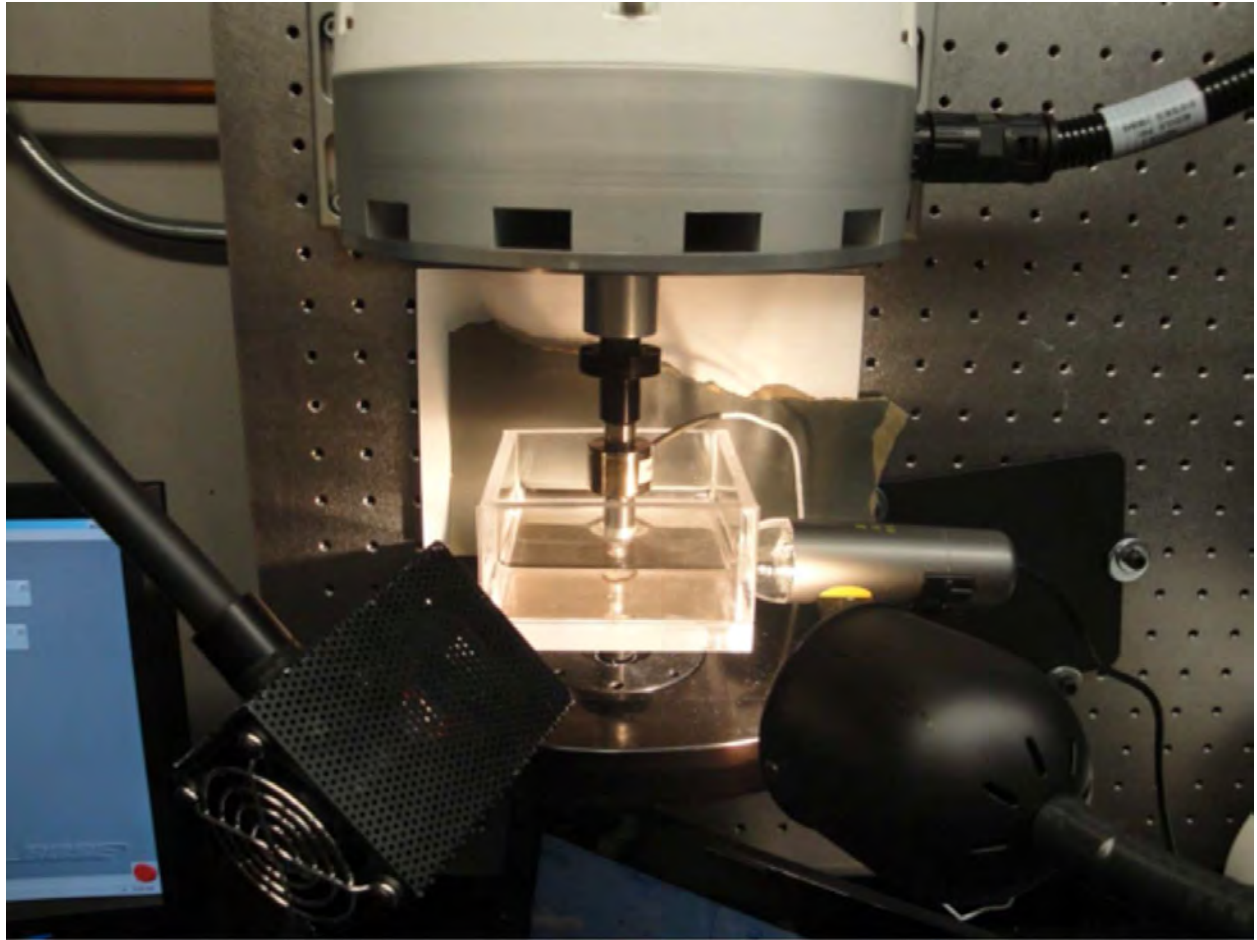
13

Figure 10. Closeup of setup with halogen lamps, and a lower resolution digital scope at the right for checking configuration of the contact on the lens during compression.
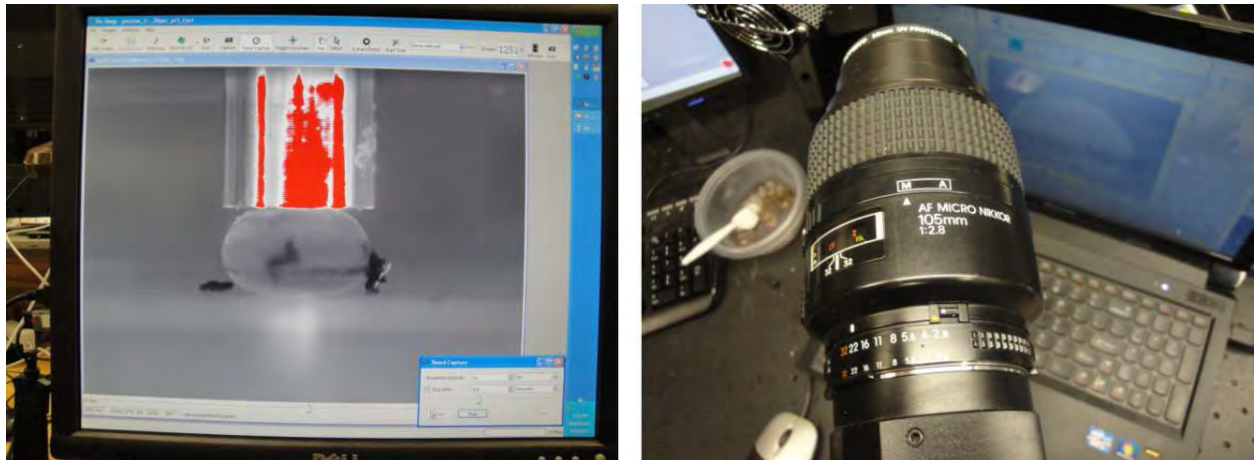

Figure 11. (left) Image from the high speed camera on the porcine ocular lens. (right) The high speed camera lens itself.

this experiment.

We can use these data, and for a range of strain rates, to calibrate the viscoelastic and poroelastic parameters of the material models. But further experiments are required to ensure repeatability of the data before material model parameter calibration.

As an example of a high strain rate puncture test on a lens, refer to the force versus time curve in Fig.14. This test involved a 1000 mm/s axial displacement rate through puncture, with 1mm diameter flat circular post. The results in Fig.14(top) show the quick ramp up of load over 0.25sec, and then decrease after the lens capsule puctured. Figure 14(bottom) attempts to show corresponding deformed lenses during the puncture process.

We can use these data, and for a range of strain rates, to calibrate the viscoelastic and poroelastic parameters of the material models. But further experiments are required to ensure repeatability of the data before material model parameter calibration.
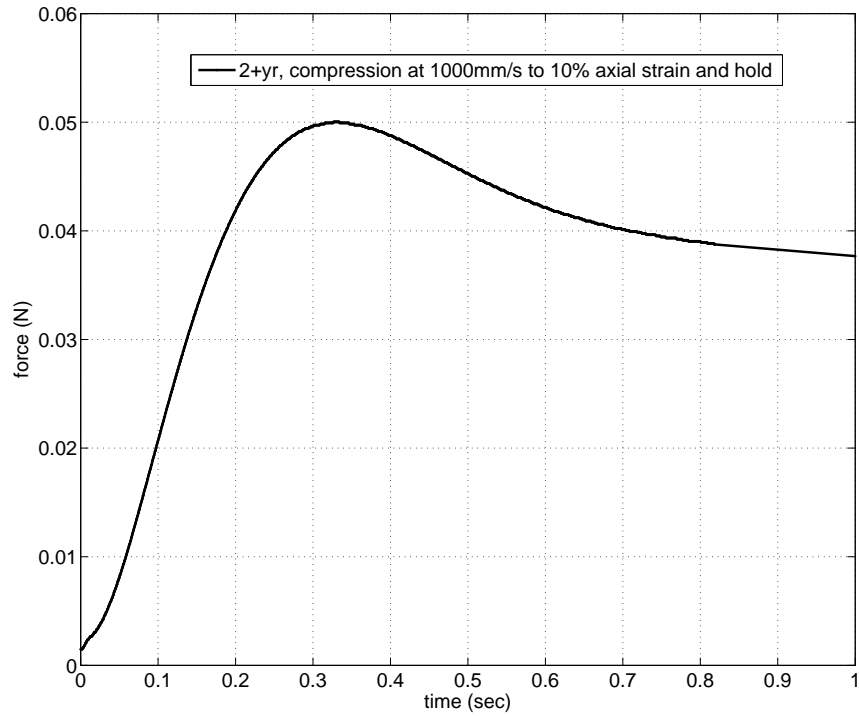
Figure 12. (top) Force versus time curve for a high strain rate stress relaxation test on a 2+year old porcine lens. (bottom) Zoom in plot of the same curve, showing smooth peak force and transition to relaxation.

Figure 13. (top) Force versus time curve for a high strain rate impulse test on a 2+year old porcine lens. (bottom) Zoom in plot of the same curve, showing the impulse load profile, and associated deformed lens images.
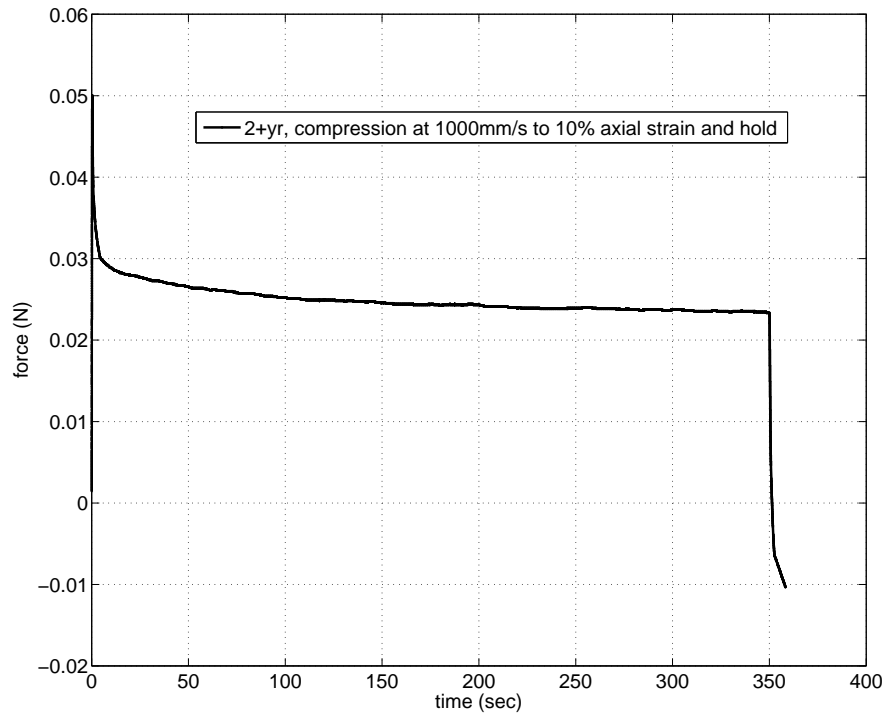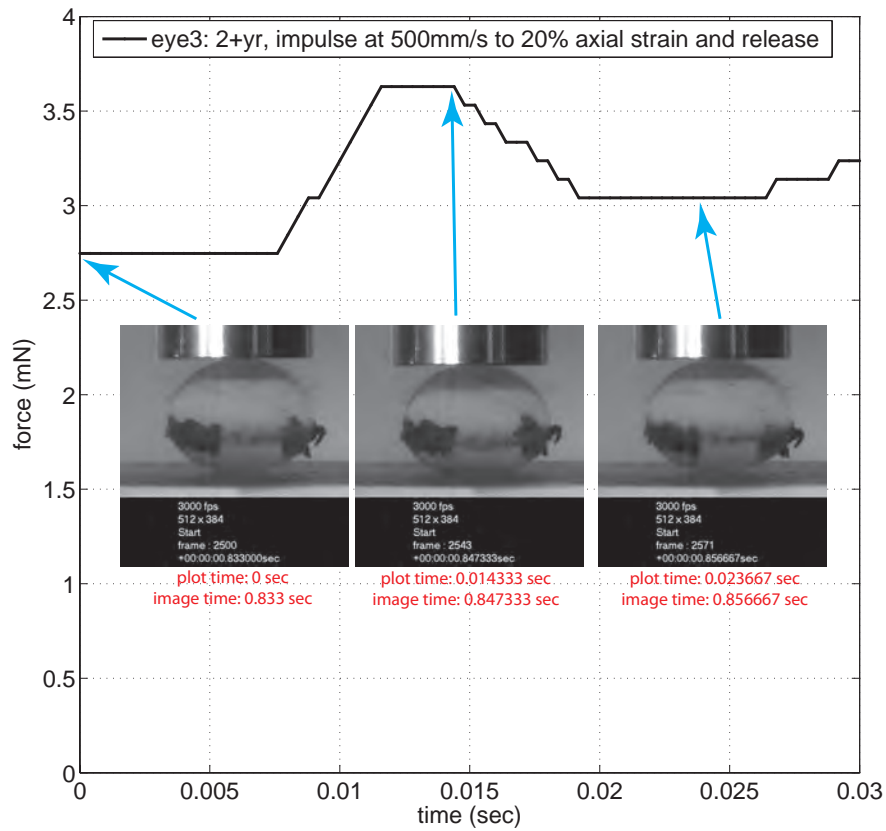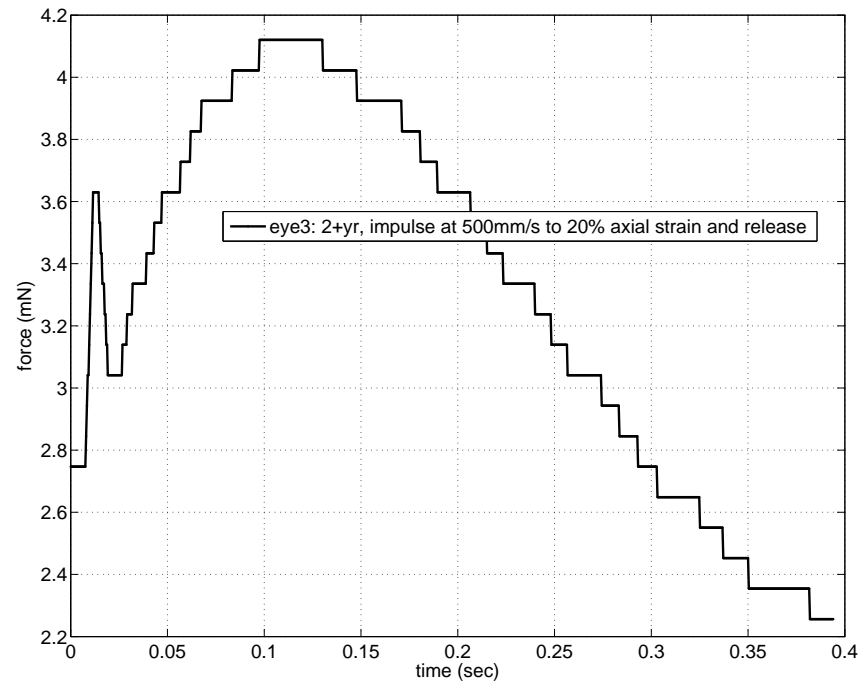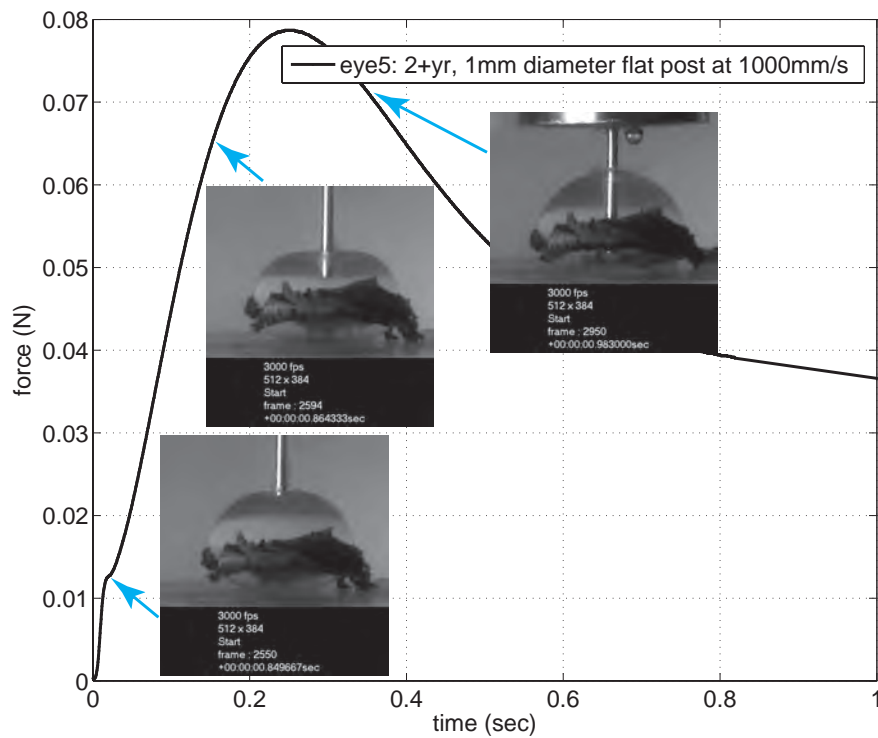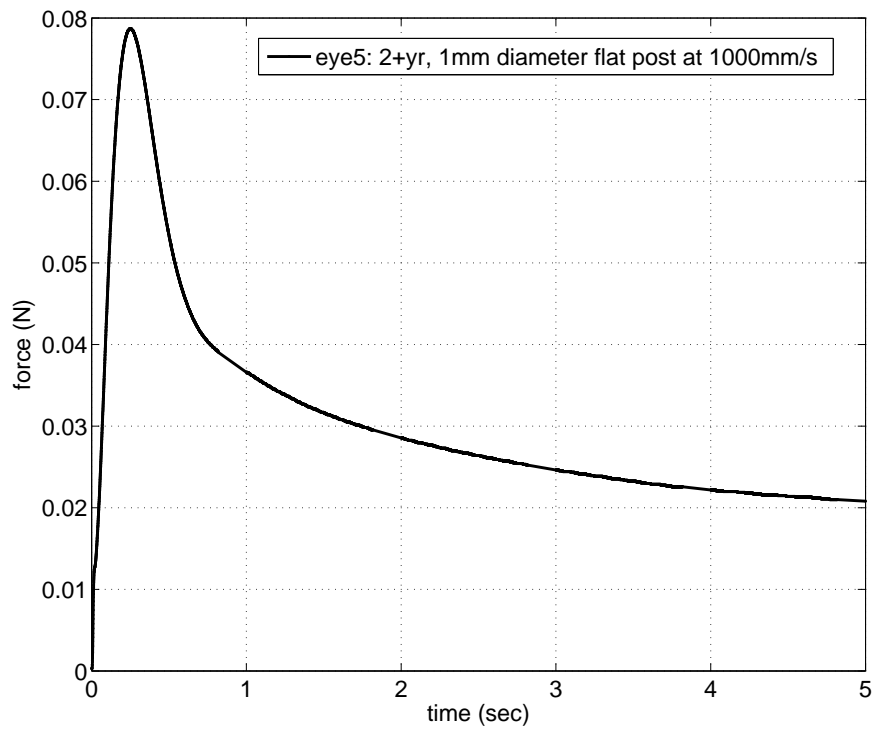
Figure 14. (top) Force versus time curve for a high strain rate puncture test on a 2+year old porcine lens. (bottom) Zoom in plot of the same curve, showing the peak load, and associated deformed lens images.

Future Testing at ARL APG

Future testing at ARL APG in Dr. Weerasooriya's lab would focus on expanding the data set that was initially generated. This would be done by repeating tests that were completed, and conducting new tests with the younger porcine tissue (6-9 month old). If there is enough confidence in the testing of the porcine lenses, testing on human lenses would be performed as well. The response of the lens would be recorded with a dynamic load cell in addition to the Bose Electroforce load cell to ensure that we are capturing the full response of the lens, especially with the higher strain rate tests. The tables below describe tests that would be completed.

Compression (Stress Relaxation) Testing			
Age of tissue	Strain (%)	Rate (mm/s)	# samples
2+ year	10, 20	0.1, 0.3, 10, 30, 100, 300, 600, 1000	5
6-9 month	10, 20	0.1, 0.3, 10, 30, 100, 300, 600, 1000	5
		Total tests	160

Impulse Testing			
Age of tissue	Strain (%)	Rate (mm/s)	# samples
2+ year	10, 20, 40, 60	10, 30, 100, 300, 600, 1000	5
6-9 month	10, 20, 40, 60	10, 30, 100, 300, 600, 1000	5
		Total tests	240

Puncture Testing			
Age of tissue	Surface	Rate (mm/s)	# samples
2+ year	Anterior, Posterior	5, 50, 250, 500, 1000	5
6-9 month	Anterior, Posterior	5, 50, 250, 500, 1000	5
		Total tests	240

6a. Before and after whole porcine lens unconfined compression, image lens fiber cell geometry using CLSM (low strain rate subtask 4a: months 1-4; higher strain rate subtask 4b: months 6-8).

In collaboration with Dr. Christopher English of the Molecular, Cellular, and Developmental Biology (MCDB) department, we attempted to refine the procedure of CLSM for identifying the ultrastructure, at various cross-sections through the whole lens, of the internal lens fiber cells. We focused our efforts on as-received porcine lenses and one human lens.

We have conducted preliminary analysis on confocal images of human interior lens substance, attempting to identify the ultrastructure of the lens fiber cells. The first image of the slice, and the location of the slice in the context of a drawing of the lens fiber cell ultrastructure (drawing from pg99 of [Kessel and Kardon, 1979]) is shown in Fig.15. The donor was a 66-year-old male, with lens obtained in Balanced Salt Solution (BSS) within 48hrs post mortem. When the lens was prepared for confocal laser scanning microscropy (refer to Section 7.1 of Christopher Bay's MS thesis [Bay, 2012]), the nucleus and cortex separated, and thus in the image only the cortex section is shown.
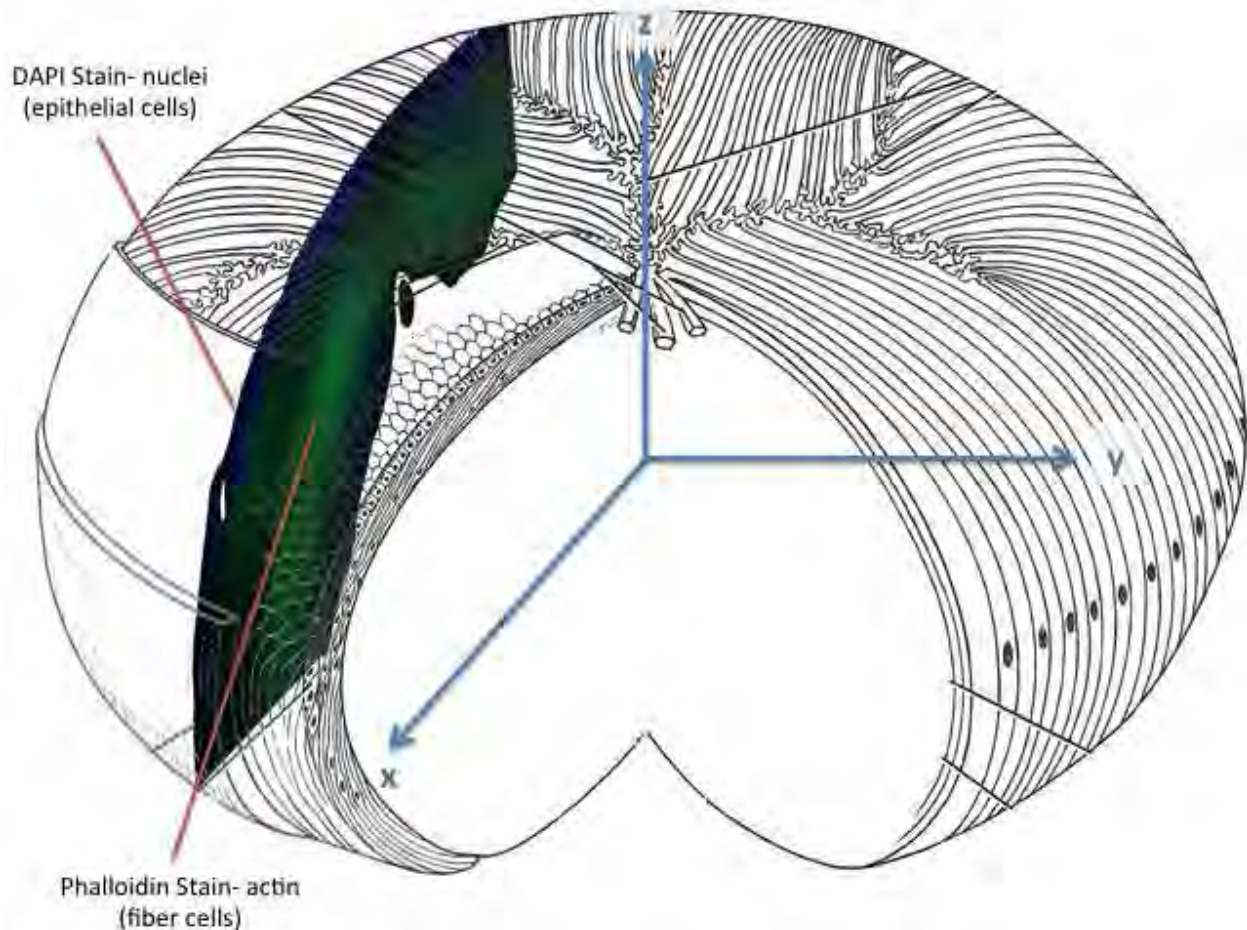

Figure 15. CLSM slice of human lens fiber cell structure aligned with approximate location within full lens (drawing from pg99 of [Kessel and Kardon, 1979]).

Figure 16 shows zoomed-in images of the lens fiber cell ultrastructure. When compared to images for the 2+yr old pig lens (see Chapter 7 of Bay [2012]), the 66-year-old male fiber cell ultrastructure is less identifiable. One hypothesis for this less-identifiable fiber cell ultrastructure in the older human lens is the wearing or degradation of the lens fiber cells over longer time. This hypothesis remains to be tested as more data are obtained for younger human lenses, and from other older human lenses.

Figure 1: 10X confocal image of human lens (image superimposed in lens model)

Figure 2: 20X (region of human lens outlined by red square)

Figure 3: 20X (region of human lens outlined by purple square)

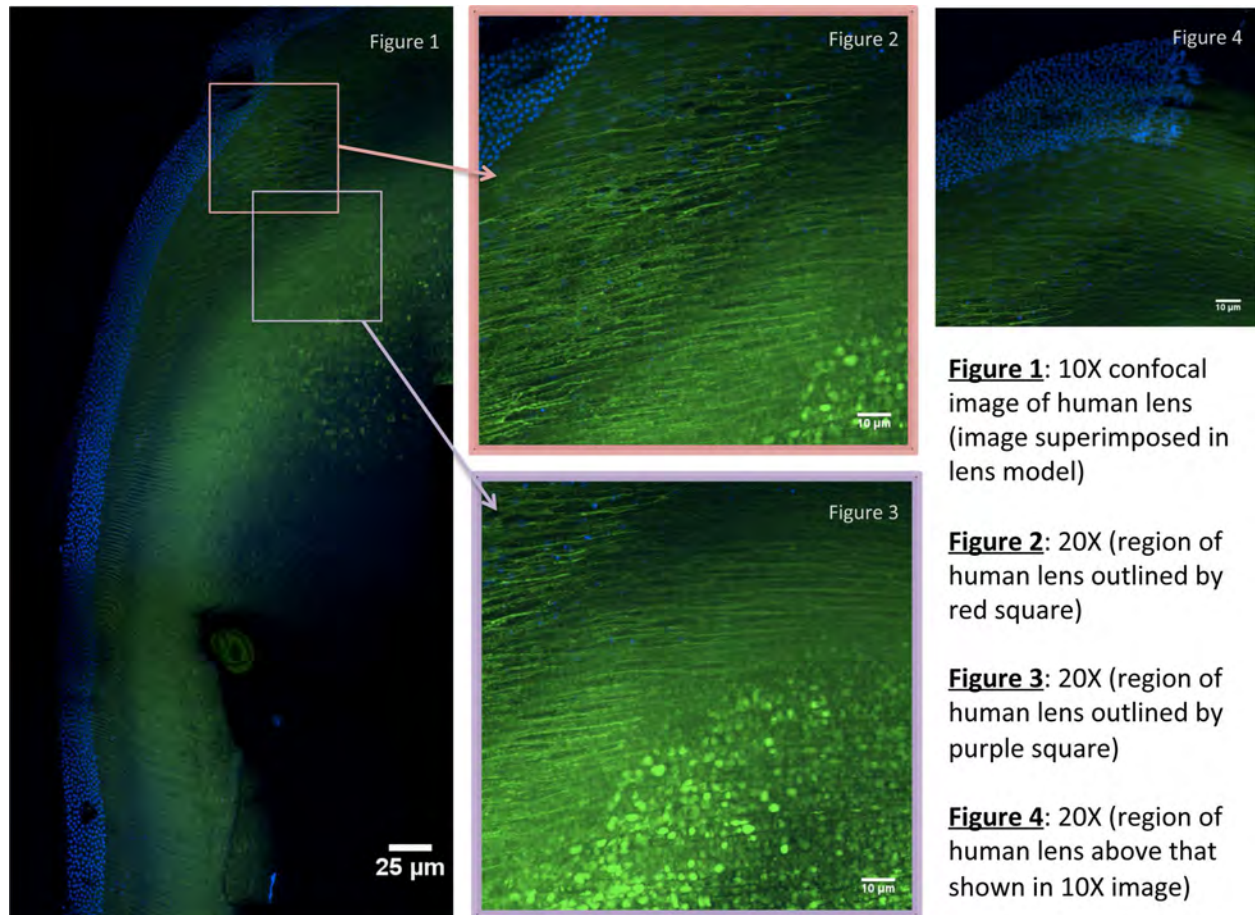**Figure 4**: 20X (region of human lens above that shown in 10X image)

Figure 16. Zoomed-in images of CLSM slice of human lens fiber cell structure.

6b. On as-received porcine lens capsules, image type IV collagen ultrastructure in lens capsule using cyro-electron tomography (months 1-4).

Identification of type IV collagen meshwork ultrastructure in the lens capsule using cyro-electron microscopy/tomography is described in Chapter 6 of Bay [2012], included as Appendix A. One focus of the research was to determine if the images we are obtaining, such as in Fig.26, are indeed structure, or if they are an artifact of the freezing process. We collaborated with Dr. Thomas Giddings and Dr. Andreas Hoenger of the Molecular, Cellular, and Development Biology (MCDB) Department at the University of Colorado Boulder, about this topic. More experiments are being conducted to determine whether what we are seeing is structure or artifact, such as increasing the percentage of cryo-protectant solution.
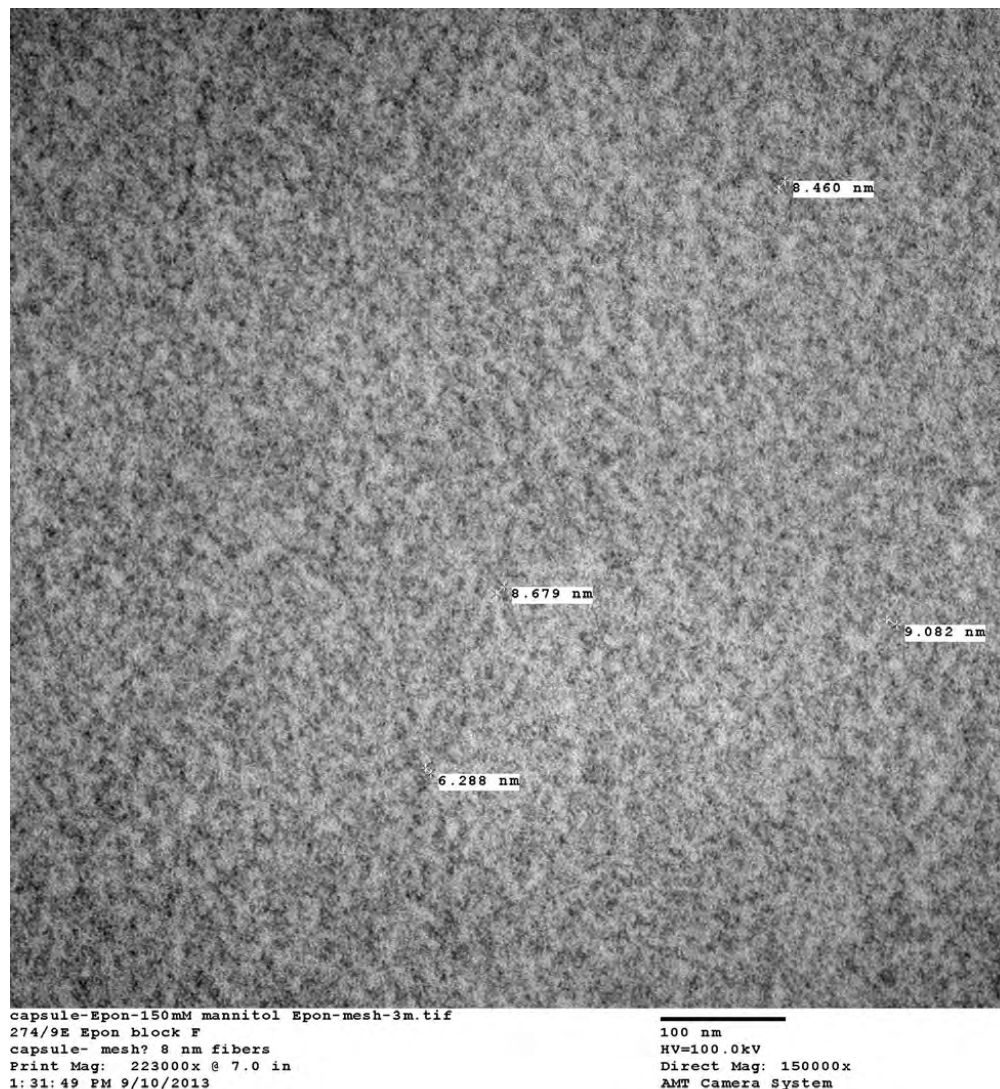

Figure 17. Cryo EM image of what is possibly type IV collagen structure.

2c: Formulation and finite element implementation of multiscale perforating finite strain biphasic mixture (solid and fluid) solid-shell continuum model of lens capsule in Tahoe, to model cutting/ perforation of lens capsule based on implementation in subtasks 1c and 2b (months 28-36). 3b: Using result of subtask 3a, formulate and implement multiscale hierarchical, anisotropic, lens fiber cell equivalent soft viscoelastic constitutive model of the internal lens substance (months 40- 48).

Large Deformation Lagrangian-Eulerian Computational Modeling of Lens Puncture and Also Solid-Fluid interaction between Lens and Surrounding Fluids:

For computational modeling, we are attempting a large deformation hybrid Lagrangian-Eulerian simulation of lens puncture tests in order to eventually model penetration by Intra-Ocular Foreign Bodies (IOFBs) (Secondary Blast), but also shock propagation and solid-fluid interaction between the lens and vitreous and aqueous humors (Primary Blast). This is in collaboration with Professor Franck Vernerey, and his PhD student Louis Foucard, both at CU-Boulder. The images below illustrate a preliminary simulation of spherical tip indentation into a 2+yr old pig lens.

The method takes an Eulerian approach to describe the large deformations of an elastic membrane and its interactions with the surrounding fluid. The membrane is modeled as a two-dimensional elastic surface, across which discontinuities of continuum fields such as pressure and fluid velocity in the tangential direction can naturally be enforced using the extended finite element method (X-FEM). The tracking and evolution of the membrane is handled with the Grid Based Particle method that is well suited to evaluate the membrane higher order geometrical information.

The results of the simulation of indentation of a pig lens by a spherical indenter are compared with experimental data. The experimental data are obtained for a 2+ year-old porcine lens undergoing indentation by a 2mm (in diameter) indenter with a spherical tip (Fig.18). The indenter is lowered at a speed of 0.5mm/s until failure/puncture of the capsule. The simulation was carried out using a newly developed Eulerian approach able to describe the large deformations of an elastic membrane and its interactions with the surrounding and enclosed fluid (Fig.18). The capsule membrane is assumed to be incompressible and isotropic, for the time being. The Mooney-Rivlin strain-energy function was chosen to model membrane elastic response, in Eq.(1)

$$W = \frac{\mu}{2(1+\alpha)} \left[(1-\alpha)(\lambda_1^2 + \lambda_2^2 + \lambda_1^{-2}\lambda_2^{-2} - 3) + \alpha(\lambda_1^2 + \lambda_2^2 + \lambda_1^2\lambda_2^2 - 3) \right] \tag{1}$$

where μ is the infinitesimal shear modulus of the elastic material, α is a parameter that controls the deviation from a linear Hookean response, and λ_1 and λ_2 are the principal stretches in direction 1 (radial) and 2 (axial) . In the simulation, the capsule is considered filled with a Newtonian viscous fluid of viscosity μ_f.

In this simulation, the indenter (black cylinder) in Fig.18 progressively approaches and deforms the elastic capsule filled with a viscous fluid and resting on a plane surface. The initial geometry of the eye lens was extracted from the experimental video of indentation at time $t = 0$, and the system was meshed accordingly using a 23x30 element grid. The (friction-less) interaction between the capsule and the indenter is handled via the penalty method. Figure 19 shows the dilatation (jacobian J) of the elastic membrane. Figure 19 shows the deformation gradient components in the axial (F_{22}) and radial (F_{11}) directions. One can observe the very large deformation (approaching 800%) and dilatation of the membrane at the tip of the indenter, which would prove very difficult
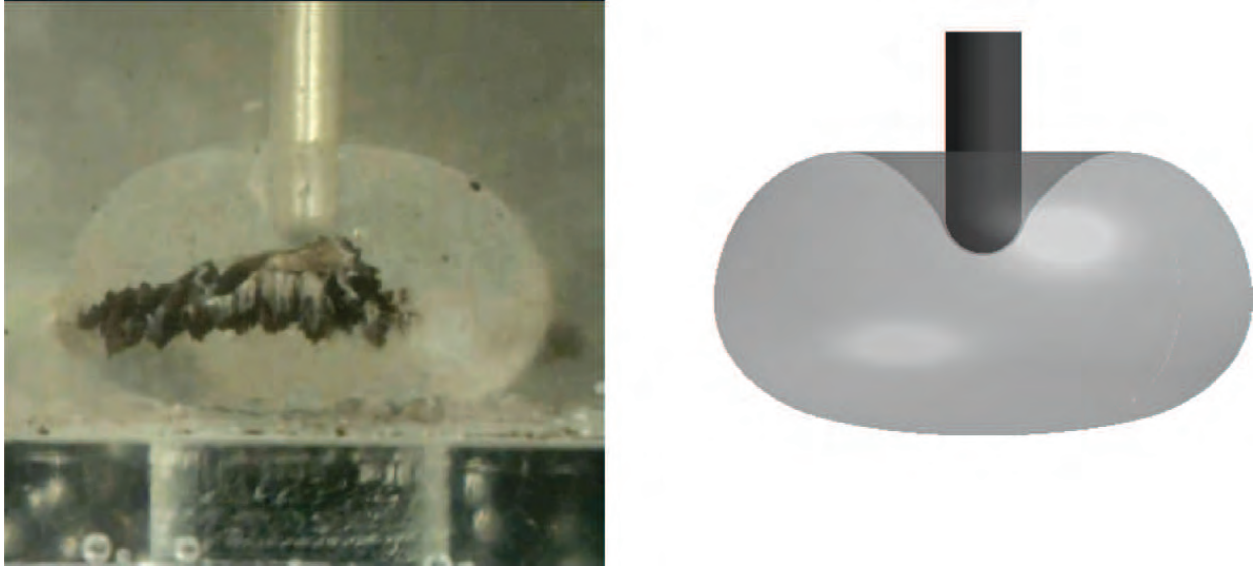
23

Figure 18. Indentation and large deformations of the porcine (2+years old) lens: (left) experiment, (right) simulation. The indenter has a 2mm diameter and a spherical tip and is lowered at 0.5mm/s until puncture of the capsule.

to simulate using a Lagrangian approach. This stress concentration at the tip of the indenter is also consistent with the fact that the rupture of the capsule membrane was observed to take place at the same location experimentally. Finally, Fig.19 shows the normalized force versus displacement curve for both the simulation and the experimental results. Up to the point of failure of the capsule (peak), the simulation results show good consistency with the experimental data.
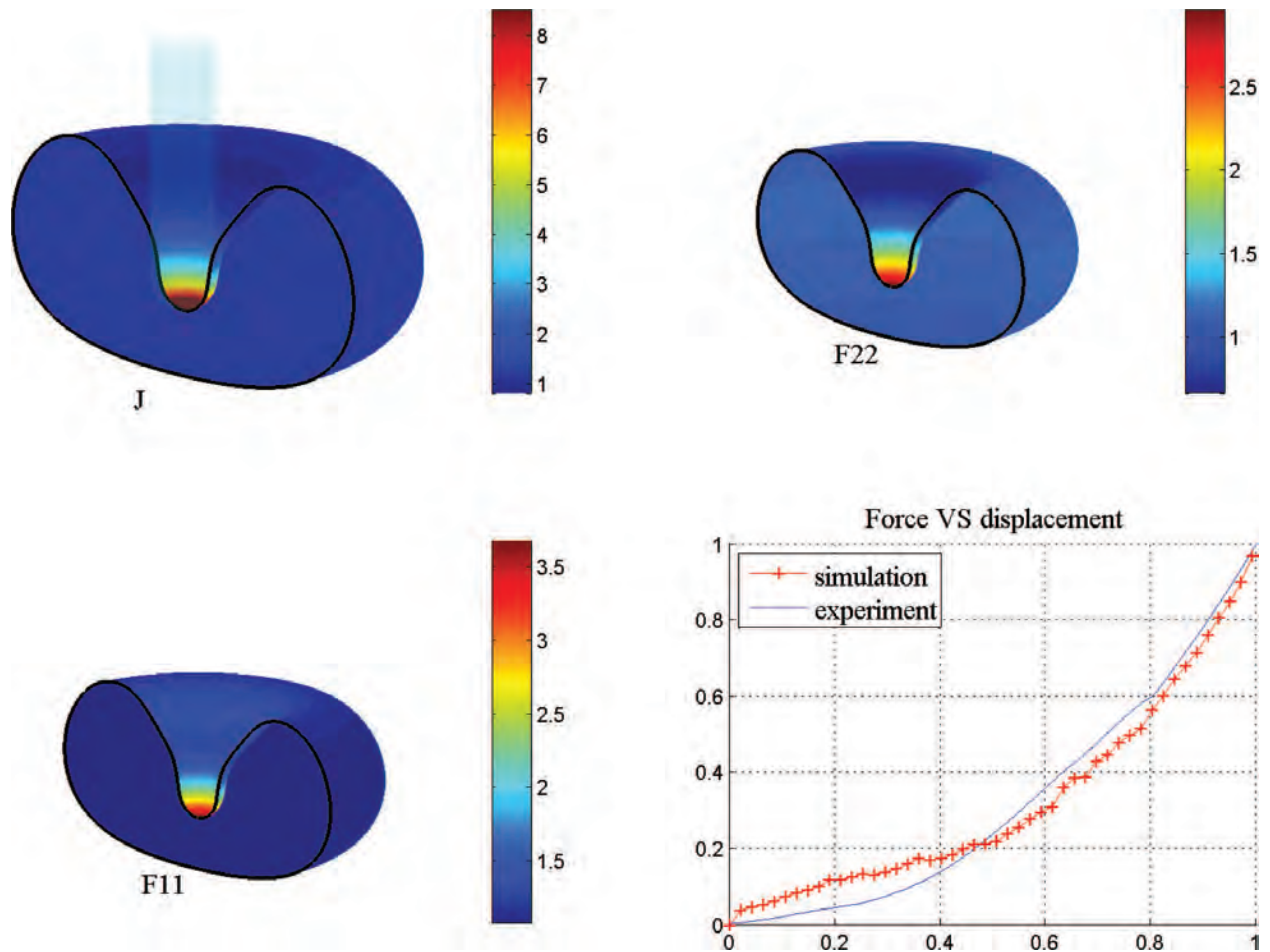
Figure 19. Indentation and large deformations of lens. (top left) dilatation of the surface (Jacobian), while (top right) and (bottom left) show deformation gradient in axial (F_{22}) and radial (F_{11}) directions. (bottom right) normalized force versus displacement curve for both the simulation results and the experimental data.

25

6a. Before and after whole porcine lens unconfined compression, image lens fiber cell geometry using CLSM (low strain rate subtask 4a: months 1-4; higher strain rate subtask 4b: months 6-8).

In collaboration with Dr. Christopher English of the Molecular, Cellular, and Developmental Biology (MCDB) department, we have obtained reasonable resolution images of cross sections of porcine lens fiber cell structure, such that numerical geometric models (a.k.a., "meshes") can be determined based on these images. More details are provided in the Senior Thesis (*Ultrastructural Identification of the Internal Fiber Cells of the Mammalian Ocular Lens*, Appendix B) by Ms. Srinidhi Radhakrishnan, who graduated in May 2014 from the Department of Chemical and Biological Engineering at UCB.

It was determined that fiber cells imaged with $10\times$ objective (see Figs.20,21) produced enough resolution to discern the lens fiber cell structure, whereas images obtained with $5\times$ objective (see Figs.22,23,24) did not provide enough resolution, essentially rendering all fiber cell walls to appear straight (Fig.24) instead of having waviness to them (Fig.21). As was demonstrated in Bay [2012] (and Fig.25), $40\times$ objective could discern the hexagonal cross-sectional pattern of the lens fiber cells in porcine lenses, but such resolution is too high to reconstruct a whole structural image/geometrical model of the lens fiber cells (see Fig.20 for one full through-thickness slice using $10\times$ objective, and Fig.21 for a zoomed region).
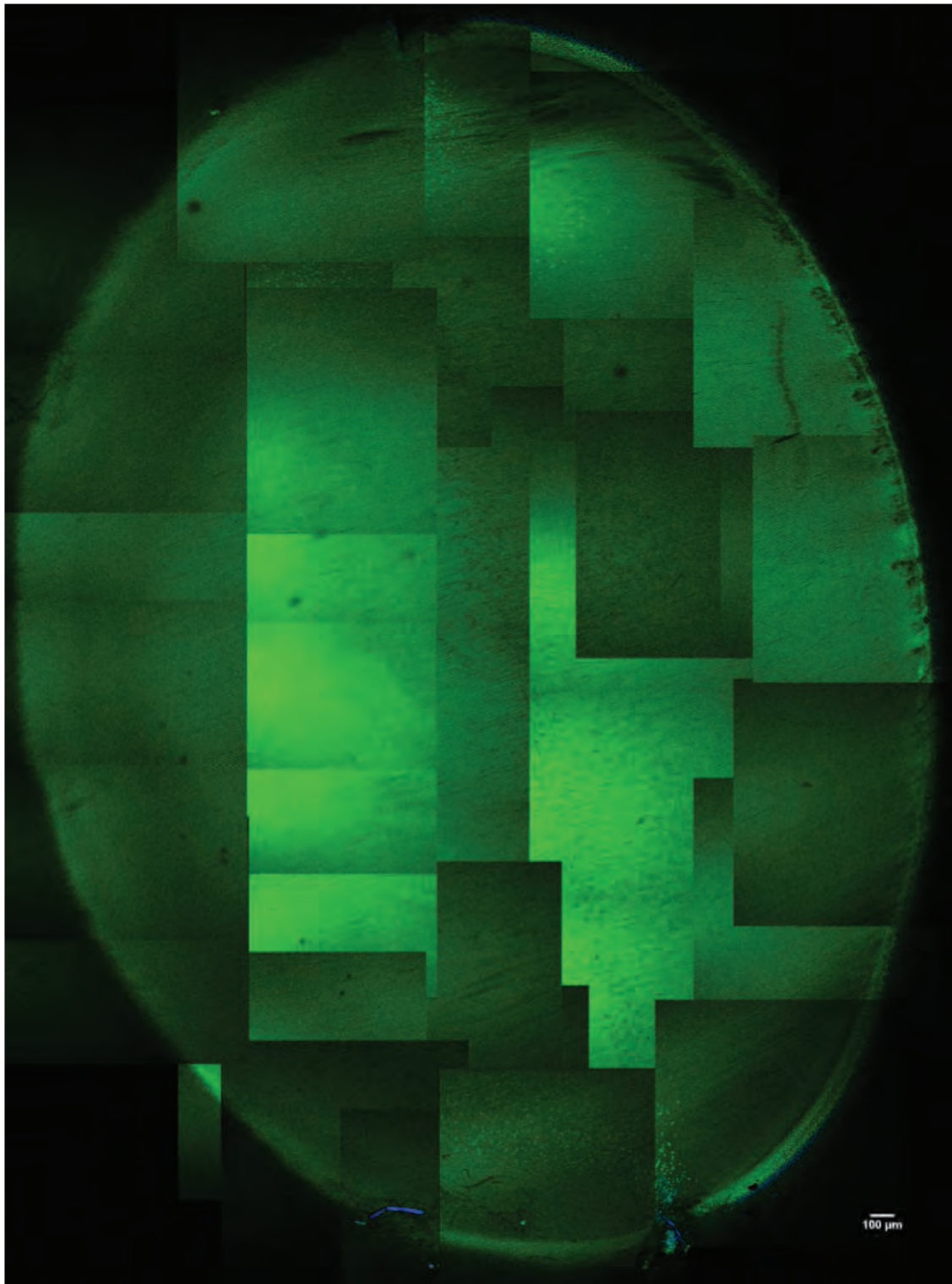
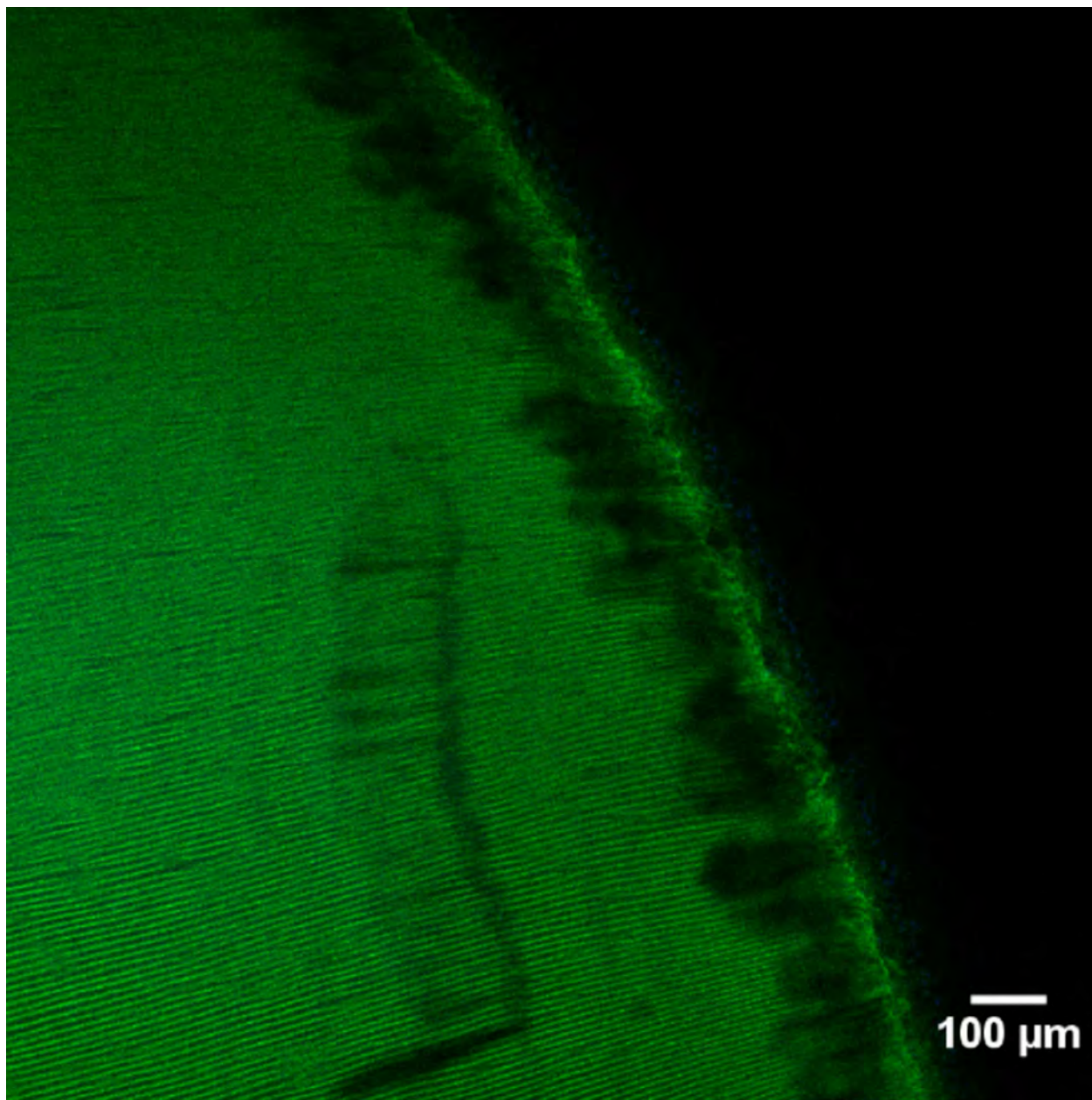Figure 20. Full through-thickness CLSM slice of porcine lens fiber cell structure at 10X objective.

Figure 21. Zoom-in on upper right region of CLSM slice (in Fig.20) of porcine lens fiber cell structure at 10X objective.
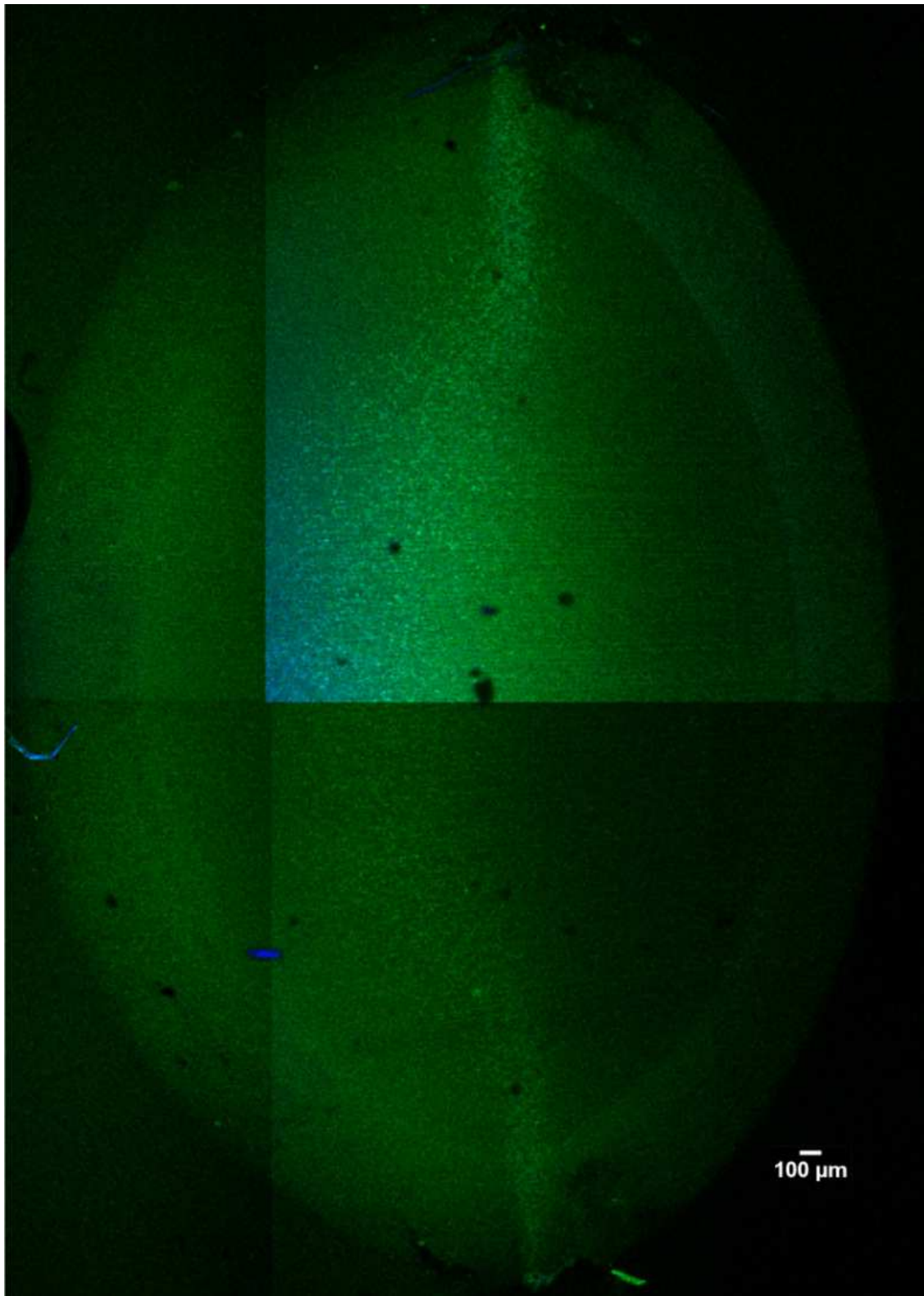
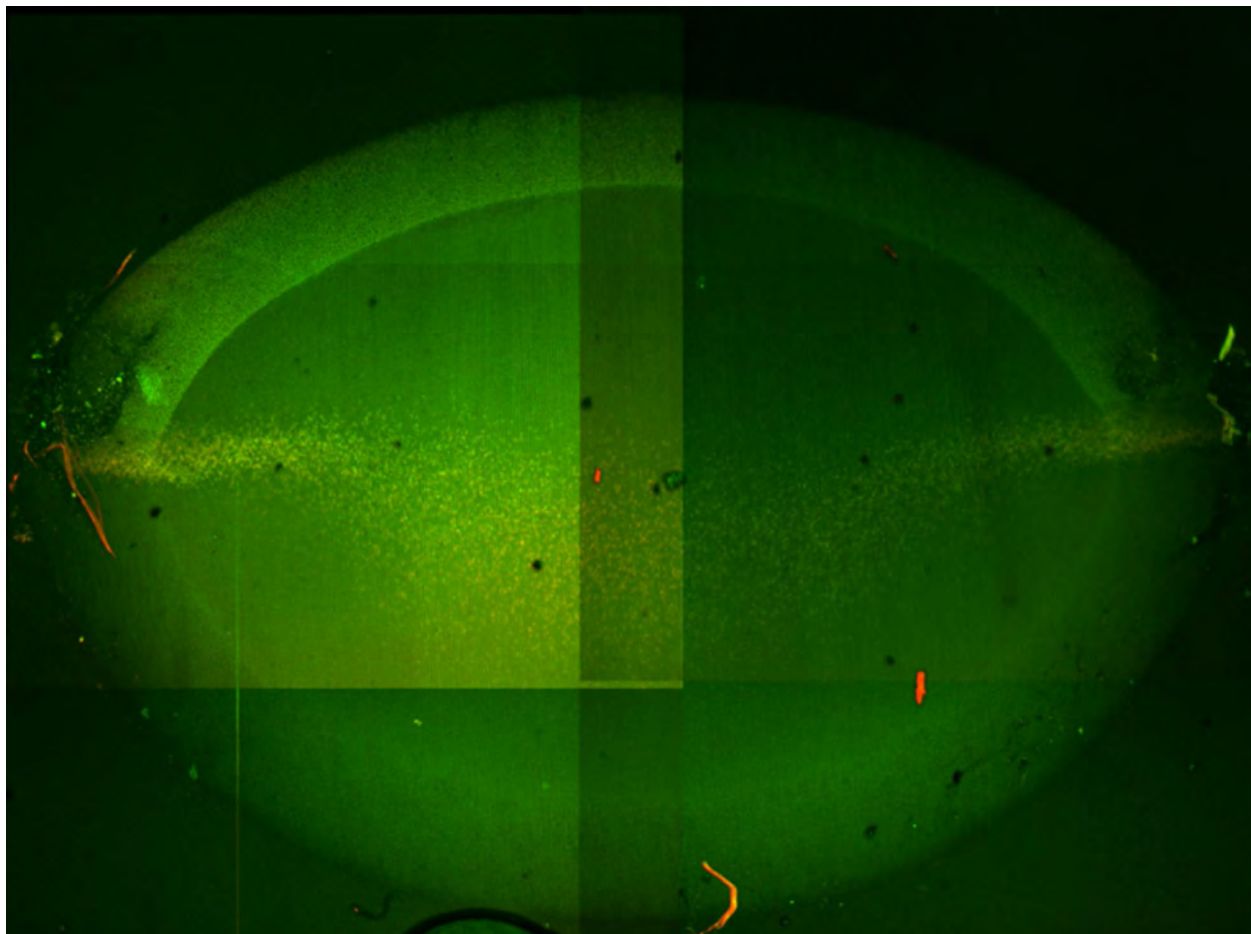Figure 22. Full through-thickness CLSM slice of porcine lens fiber cell structure at 5X objective.

Figure 23. Full through-thickness CLSM slice of porcine lens fiber cell structure at 5X objective.
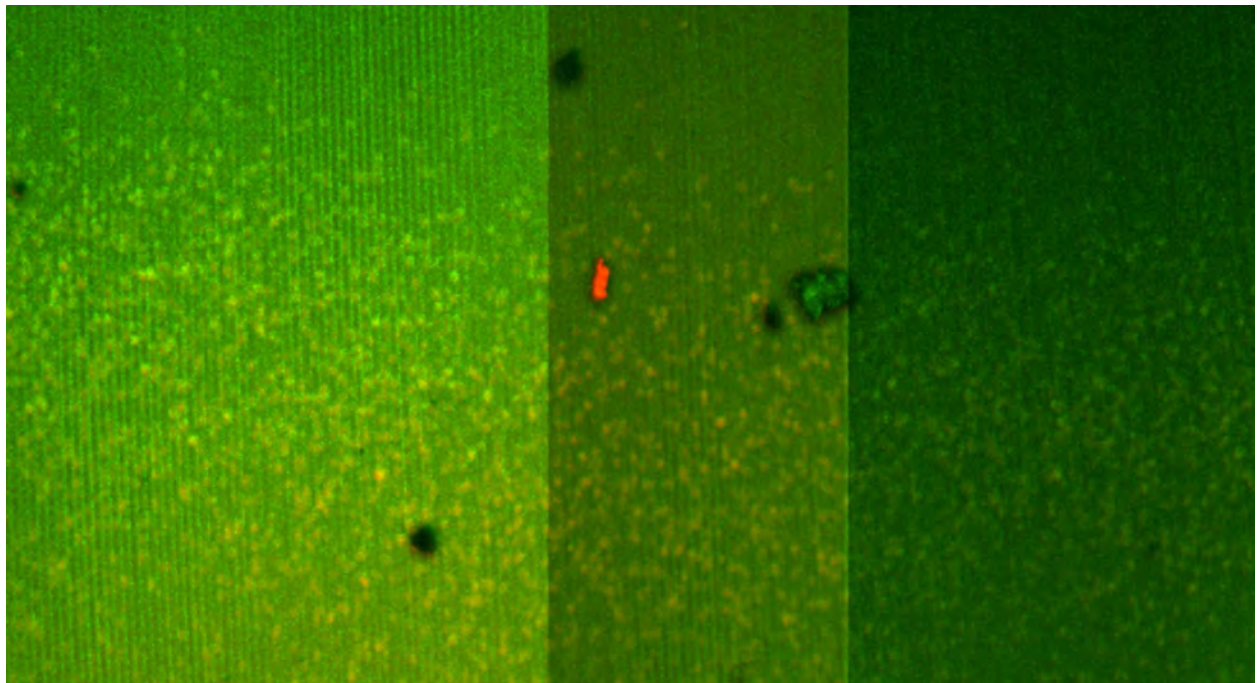
Figure 24. Zoom-in on CLSM slice of porcine lens fiber cell structure at 5X objective (refer to red dot in center of image in Fig.23).
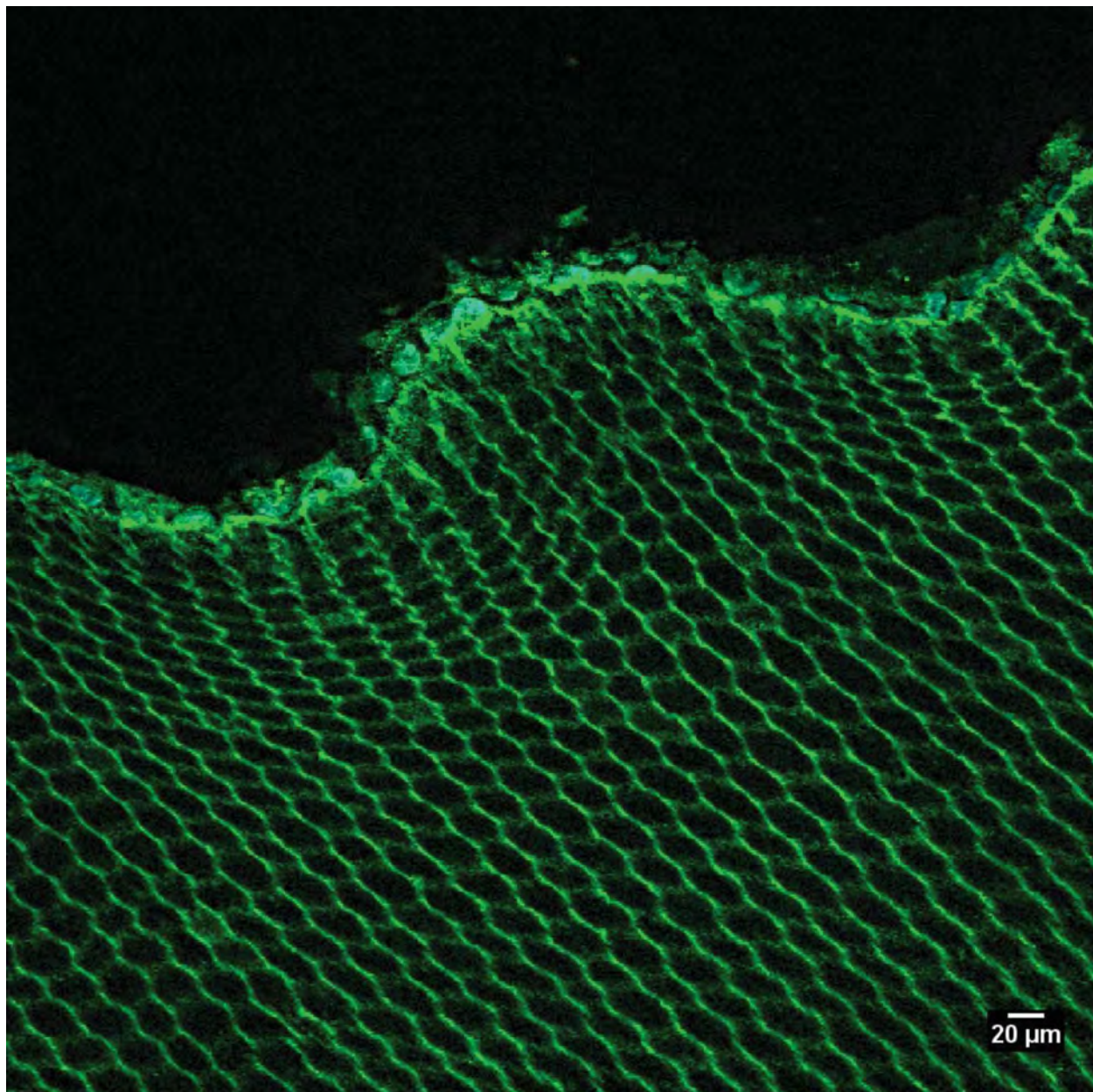
Figure 25. CLSM slice of porcine lens fiber cell structure at 40X objective.

6b. On as-received porcine lens capsules, image type IV collagen ultrastructure in lens capsule using cyro-electron tomography (CryoET) (months 1-4).

The debate was eventually settled within the Department of Molecular, Cellular, and Developmental Biology (MCDB) at the University of Colorado Boulder (UCB) as to whether the structural images we are obtaining of the type IV collagen meshwork of the lens capsule via CryoET are in fact an artifact of the pressurized freezing process, or actual ultrastructure of the tissue. It is believed that the observed "structure" in Fig.26, for instance, is an artifact of the freezing process. Procedures to etch the proteins away, except the type IV collagen, are being investigated anew. Initially, the CryoET was preferred because it would preserve the native structure as much as possible, but then the process also preserves the state of other proteins as well. The more invasive procedures that attempt to wash away all proteins except type IV collagen are being considered. Also, shadowing techniques like that used in Barnard et al. [1992] are being considered to see if such images can be replicated. Such a machine exists at UCB in the MCDB department, but it is currently not working. This research is continuing.
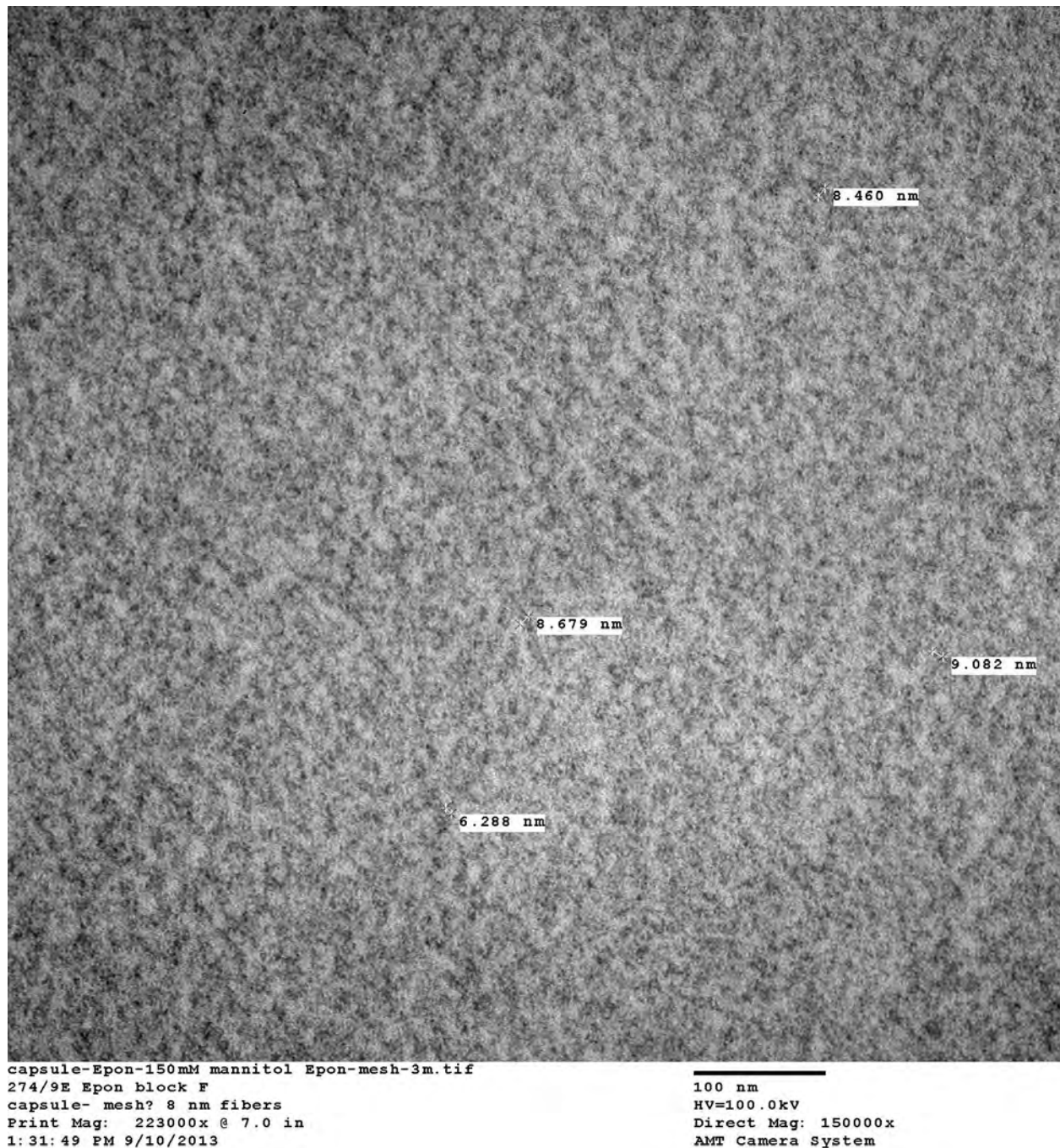
Figure 26. Cryo EM image of what is possibly type IV collagen structure. It has been determined by MCDB at UCB that what appears to be structure is in fact an artifact of the freeze-substitution process.

2c: Formulation and finite element implementation of multiscale perforating finite strain biphasic mixture (solid and fluid) solid-shell continuum model of lens capsule in Tahoe, to model cutting/ perforation of lens capsule based on implementation in subtasks 1c and 2b (months 28-36). 3b: Using result of subtask 3a, formulate and implement multiscale hierarchical, anisotropic, lens fiber cell equivalent soft viscoelastic constitutive model of the internal lens substance (months 40- 48).

For the computational modeling, we are continuing to work on a large deformation hybrid Lagrangian-Eulerian simulation of the lens puncture tests in order to eventually model penetration by Intra-Ocular Foreign Bodies (IOFBs), but also shock propagation and solid-fluid interaction between the lens and vitreous and aqueous humors. This is in collaboration with Assoc. Prof. Franck Vernerey, and his recently graduated PhD student Dr. Louis Foucard, at UCB.

The current status of the research is a preliminary attempt to relate the type IV collagen ultra-structure to the macroscale lens capsule mechanical response. Assumptions include (1) in-plane stretching of two-dimensional type IV collagen meshwork (rather than actual 3D structure and out-of-plane loading, not yet identified by CryoET; similar assumption made by Burd [2009]), (2) bending allowed at fibril junctions (better than assuming pinned junctions, such as in Burd [2009]), and (3) periodic boundary conditions (appropriate for large deformation under indentation, but not tearing/puncture). An illustration of the concept and preliminary results compared to the Krag and Andreassen [1996] data, and Burd's fit of the Krag data, and the fit provided by our model, are shown in Fig.27.

In addition, PI Regueiro spent his sabbatical in Autumn 2014 at the University of Oxford collaborating with Dr. Harvey Burd on multiscale finite element modeling of the lens capsule.

Macroscopic scale | Mesoscopic scale | Microscopic scale

(a) full lens indentation & compression test

(b) lens capsule modelled as a continuum thin membrane

Replica of the collagenous human lens capsule. Barnad *et al* (1992)

(c) membrane microstructure

(a)

Membrane traction (N/m) vs Stretch ratio

Legend:
— + — Krag data
— o — Burd truss model
Beam model

Legend:
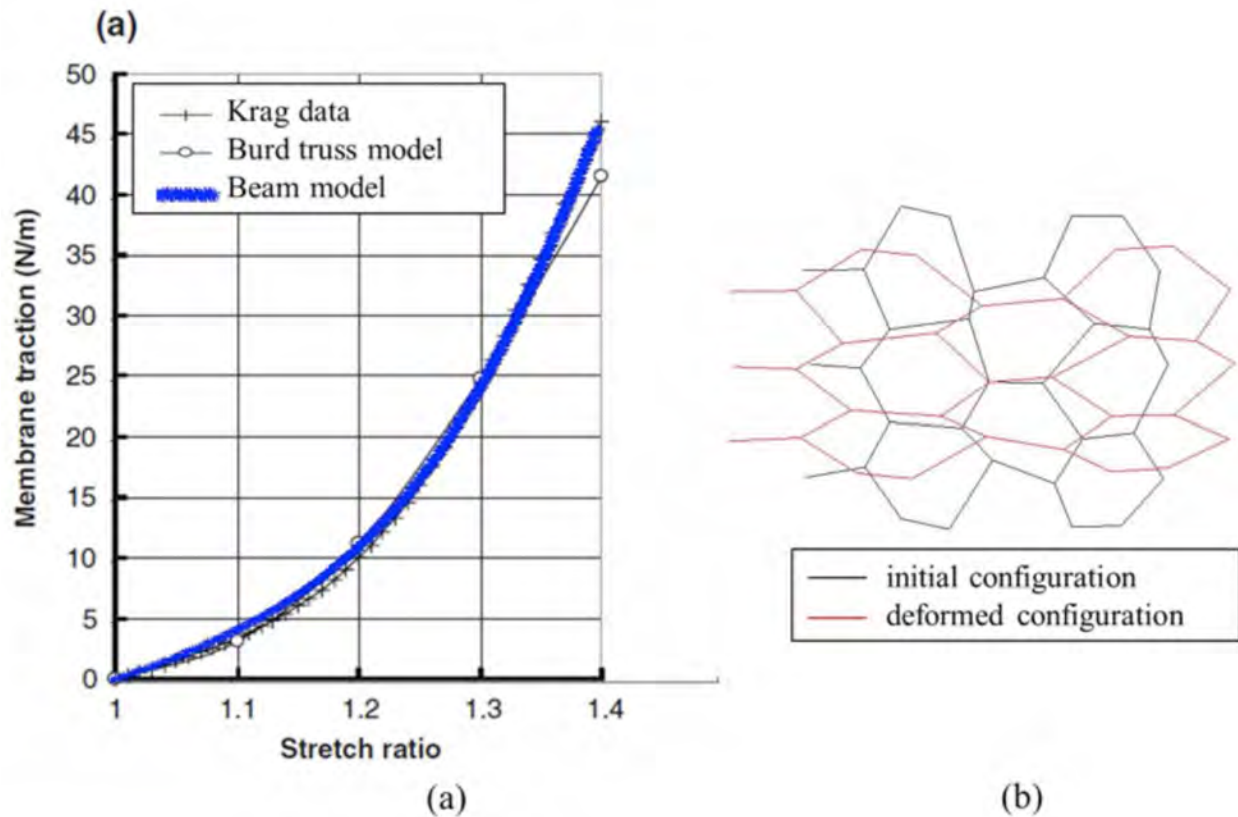— initial configuration
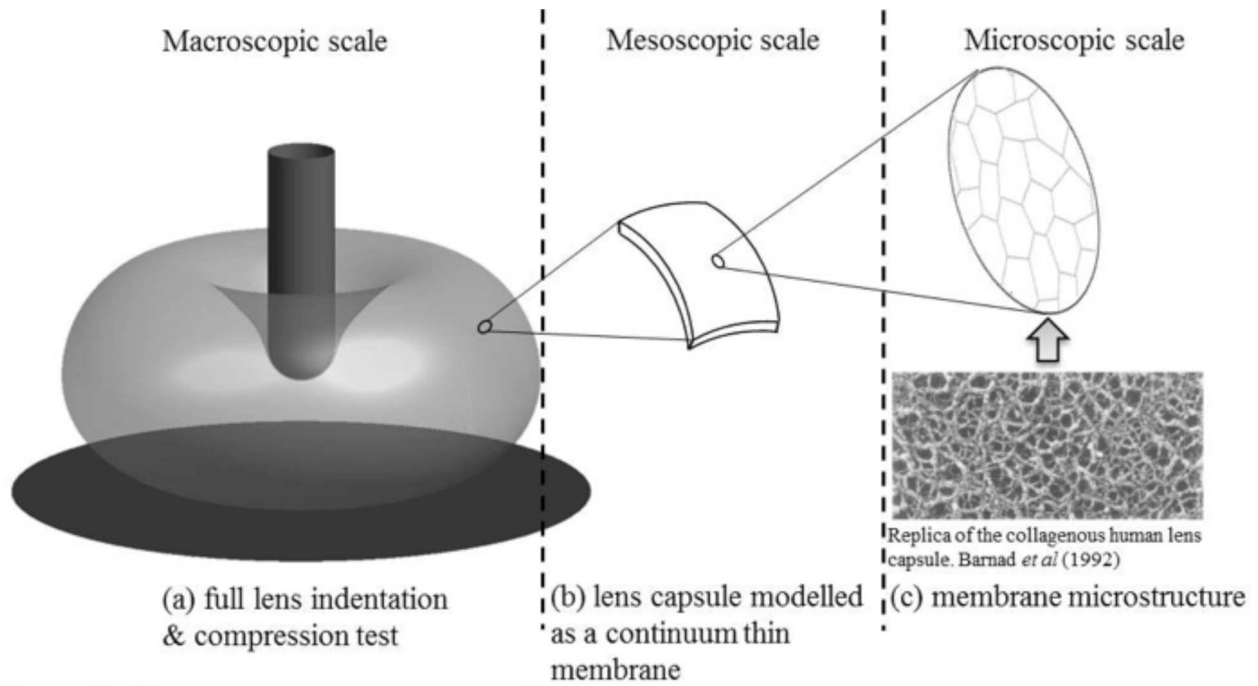— deformed configuration

(a)

(b)

Figure 27. (top) Concept of multiscale modeling of lens capsule, showing network approximation based on ultrastructural imaging [Barnard et al., 1992]. (bottom) Comparison of traction versus stretch ratio of lens capsule experimental data [Krag and Andreassen, 1996], other truss network model [Burd, 2009], and our beam model.

Axisymmetric, multiscale, hyperelastic, membrane finite element model of the lens capsule at finite strain, with extension to poromechanics

For my sabbatical in Autumn 2014, I spent it in the Engineering Science Department at Oxford University, hosted by Dr. Harvey Burd. Dr. Burd is an expert in researching the mechanics of the ocular lens, and developing finite element models that can be used to simulate experimental test conditions, as well as physiologically-accurate loading conditions during accommodation. During my stay at Oxford, I worked with Dr. Burd on revising an earlier axisymmetric, multiscale, hyperelastic, membrane finite element model of the lens capsule at finite strain that he developed, helping to clarify the formulation of the global consistent tangent accounting for the multiscale network model of type IV collagen. Having a properly-formulated consistent tangent will lead to improved numerical simulation performance, making computations faster and possibly obtaining converged solutions that would not otherwise have converged. Our collaborative efforts resulted in a published journal paper (Appendix D): Burd, H.J., Regueiro, R.A. (2015) "Finite element implementation of a multiscale model of the human lens capsule," Biomech. Model. Mechanobiology 14(6):1363-1378. Dr. Burd visited my research group in April 2015. We plan to continue our research collaboration, extending the model we worked on together to include poromechanics of the lens capsule. This research falls within the scope of the USAMRMC project. Also, our collaboration has lead to an interdisciplinary research proposal submitted to the NIH (see Reportable Outcomes), but that was not funded.

In April 2016, PI Regueiro visited Dr. Harvey Burd at Oxford University to continue collaboration on multiscale computational modeling of the human lens capsule. One objective is to formulate and implement a phenomenological continuum constitutive model of the lens capsule based on the multiscale micronet model (Burd & Regueiro BMMB 2015). This phenomenological model will capture the salient features of the multiscale micronet model, but will be much more efficient computationally. We worked on how the phenomenological model could be implemented into the commercial FEA software program Abaqus for 3D analysis and optimization of implantable, accommodating IOLs. Work is ongoing.

3 Key Research Accomplishments

- We have accumulated unconfined compression data for whole porcine lenses at two axial strains (10% and 20%) and displacement rates (0.1mm/s and 0.3mm/s) for estimating finite strain isotropic viscoelasticity parameters. Parameter fits are being completed for a future paper.

- We concluded that identifying structure of type IV collagen meshwork with cryo-electron microscopy is not sufficient, and thus we are working on using cryo-electron tomography instead.

- Quasi-static puncture testing data were presented on 2+ year old and 6-9 month old porcine eyes, which will be used to calibrate parameters for failure modeling of the lens capsule, and internal lens substance (lens fiber cells).

- Preliminary creep data for spherical tip nanoindentation testing were presented, which will be used to calibrate directly the multiscale, 3D beam network model of type IV collagen meshwork in the lens capsule.

- CLSM was applied to internal lens substance to provide preliminary images of the lens fiber cell ultrastructure. This will be used to identify the lens fiber cell structure for the multiscale modeling of the internal lens substance.

- Electron Tomography (ET) images are beginning to provide identification of type IV collagen meshwork ultrastructure, although our MCDB collaborators believe that what appears to be "structure" is in fact an artifact of the freezing process.

- Preliminary high strain rate compression (stress relaxation), impulse, and puncture tests were conducted in Dr. Weerasooriya's lab at ARL APG. The results are promising, and we hope to have the opportunity to conduct more tests.

- CLSM images of the internal lens fiber cell structure are showing promise, and we are confident we can obtain good structural identification of lens fiber cell structure pre and post-test. This will be used to identify the lens fiber cell structure for the multiscale modeling of the internal lens substance.

- Preliminary large deformation Lagrangian-Eulerian axisymmetric computational modeling of lens indentation, and also solid-fluid interaction between the lens and surrounding fluids, shows promise for providing a robust large deformation computational mechanics framework for simulating Primary and Secondary blast on the lens, as well as the whole eye globe, potentially.

- CLSM images of the internal lens fiber cell structure have successfully reconstructed one through-thickness slice at $10\times$ objective for a porcine lens, with discernable fiber cell membrane geometry.

- The MCDB department and Bio3D lab `bio3d.colorado.edu` at UCB have determined that the Cryo-EM/ET techniques used thus far have generated images which only show "artifact structures" of the freeze-substitution process, and not actual type IV collagen ultrastructure.

- A preliminary network model, and multiscale techniques for the lens capsule have demonstrated the ability to match experimental data and other models of lens capsule tissue stretching.

- A tightly-coupled, properly-linearized, multiscale axisymmetric hyperelastic membrane finite element model of the lens capsule was developed, with parameters calibrated against experimental data for human lens capsule tissue, and used to predict other human ocular lens mechanics data.

4 Reportable Outcomes

1. ARVO posters:

   (a) Experiments and Finite Element Modeling of Indentation and Puncture of the Lens. C. Bay (presenter), R. Regueiro. *ARVO 2012*. #1349. Ft. Lauderdale, FL.

   (b) Experiments and Finite Element Analysis of Stress Relaxation upon Compression of Whole Porcine Lenses. R. Regueiro (presenter), C. Bay. *ARVO 2012*. #1350. Ft. Lauderdale, FL.

   (c) Large deformation indentation of porcine ocular lenses: experiments and computational modeling. R. Regueiro (presenter), L. Foucard, C. Bay, F. Vernerey. *ARVO 2015*. #1081. Denver, CO.

2. Chris Bay's MS thesis: Bay, C.J. (2012) *Biomechanics and Ultrastructure of the Ocular Lens*, MS thesis, University of Colorado, Boulder.

3. August 2013, Experiments and Finite Element Analysis of Stress Relaxation upon Compression of Whole Porcine Lenses, *EMI 2013*, Northwestern University.

4. On June 24-25, Dr. Matthew Reilly from the University of Texas, San Antonio (UTSA), visited PI Regueiro to discuss each other's research and how we can work together.

5. Radhakrishnan, S., *Ultrastructural Identification of the Internal Fiber Cells of the Mammalian Ocular Lens*, Senior Thesis, Department of Chemical and Biological Engineering, University of Colorado Boulder, April 2014.

6. Regueiro, R.A., Zhang, B., Wozniak, S.L. (2014) Large deformation dynamic three-dimensional coupled finite element analysis of soft biological tissues treated as biphasic porous media, *Comp. Model. Eng. Sci.*, 98(1):1-39.

7. Burd, H.J., Regueiro, R.A. (2015) "Finite element implementation of a multiscale model of the human lens capsule," Biomech. Model. Mechanobiology 14(6):1363-1378.

8. Proposal submitted, not funded: NIH PAR-15-085, "Relating biochemistry to ultrastructure and multiscale mechanics in predictively simulating tissue mechanical behavior during aging: ocular lens accommodation as example," 9/1/16 - 8/31/21, $3,456,868 (PI Regueiro, Co-I Ferguson, Co-I Hoenger, CU-Boulder; Co-I Reilly, UTSA; Co-I Glickman, UTHSCSA; Co-I Burd, Co-I Wilson, University of Oxford, UK)

5 Conclusion

The experimental research progress to date has included unconfined compression with flat platen and puncture tips for estimating material constitutive parameters and puncture resistance, smooth indent creep testing for nanoindentation of lens capsules, structure identification of the lens capsule using cryo-electron microscopy and tomography, structure identification of the internal lens fiber cells using confocal laser scanning microscropy, and preliminary high strain rate compression, impulse, and puncture testing in Dr. Tusit Weerasooriya's laboratory at the Army Research Laboratory (ARL), Aberdeen Proving Ground (APG). We would like to conduct future tests at ARL APG, if possible, given the preliminary data are promising. All of these data and images of structure will provide the basis for the multiscale computational finite element models of the ultrastructural response of whole lenses under dynamic loading.

The collaboration with Dr. Vernerey of CU Boulder on large deformation Lagrangian-Eulerian computational modeling of the lens will be extended to three-dimensions (3D) and ultra-structurally-based modeling of capsule and fiber cells. Such modeling could be extended to the whole eye globe, given the ease of using Eulerian-based methods in large deformation computational mechanics and solid-fluid interaction. Tracking interfaces is the challenge, and such details are being investigated as part of the research.

The collaboration with Dr. Burd of the University of Oxford continues to provide meaningful steps toward developing a multiscale computational model of the ocular lens being able to simulate large deformations under traumatic loading.

References

M.R. Banitt, J.B. Malta, S.L. Mian, and H.K. Soong. Rupture of anterior lens capsule from blunt ocular injury. *Journal of Cataract and Refractive Surgery*, 35(5):943–945, 2009.

K. Barnard, S.A. Burgess, D.A. Carter, and D.M. Woolley. Three-dimensional structure of type IV collagen in the mammalian lens capsule. *J. Struct. Biol.*, 108(1):6–13, 1992.

C.J. Bay. Biomechanics and Ultrastructure of the Ocular Lens. Ms thesis, University of Colorado at Boulder, 2012.

H.J. Burd. A structural constitutive model for the human lens capsule. *Biomechanics and Modeling in Mechanobiology*, 8(3):217–231, 2009.

HJ Burd, SJ Judge, and JA Cross. Numerical modelling of the accommodating lens. *Vis. Res.*, 42 (18):2235–2251, AUG 2002. ISSN 0042-6989.

S Inoue. Basic structure of basement-membranes is a fine network of cords, irregular anastomosing strands. *MICROSCOPY RESEARCH AND TECHNIQUE*, 28(1):29–47, 1994.

P. L. Kaufman and A. Alm. *Adler's physiology of the eye*. Mosby, St. Louis, MO, tenth edition, 2003.

R.G. Kessel and R.H. Kardon. *Tissues and Organs: a text-atlas of scanning electron microscopy*. W.H. Freeman and Co., San Francisco, CA, first edition, 1979.

S. Krag and T.T. Andreassen. Biomechanical measurements of the porcine lens capsule. *Exp. Eye Res.*, 62(3):253–260, 1996. ISSN 0014-4835.

T.H. Mader, J.V. Aragones, A.C. Chanlder, J.A. Hazlehurst, J. Heier, J.D. Kingham, and E. Stein. Ocular and ocular adnexal injuries treated by United States military ophthalmologists during operations Desert Shield and Desert Storm. *Ophthalmology*, 100(10):1462–1467, OCT 1993.

T.H. Mader, R.D. Carroll, C.S. Slade, R.K. George, J.P. Ritchey, and S.P. Neville. Ocular war injuries of the Iraqi insurgency, January-September 2004. *Opthalmology*, 113(1):97–104, 2006.

L.M. Parver, A.L. Dannenberg, B. Blacklow, C.J. Fowler, R.J. Brechner, and J.M. Tielsch. Characteristics and causes of penetrating eye injuries reported to the National Eye Trauma System Registry, 1985-91. *Public Health Reports*, 108(5):625–632, SEP-OCT 1993.

S. Reese and S. Govindjee. A theory of finite viscoelasticity and numerical aspects. *Int. J. Solids Struct.*, 35:3455–3482, 1998.

W.L. Walter. Intralenticular foreign body - as a cause of traumatic cataract. *American Journal of Ophthalmology*, 54(5):856–&, 1962.

E.D. Weichel and M.H. Colyer. Combat ocular trauma and systemic injury. *Current Opinion in Ophthalmology*, 19(6):519–525, 2008.

T.Y. Wong, M.B. Seet, and C.L. Ang. Eye injuries in twentieth century warfare: A historical perspective. *Survey of Ophthalmology*, 41(6):433–459, MAY-JUN 1997.

A   Master of Science Thesis

The appendix includes the Master of Science Thesis of Mr. Christopher Bay, 2012, *Biomechanics and Ultrastructure of the Ocular Lens*, to which is referred in early sections of this Final Report.

Biomechanics and Ultrastructure of the Ocular Lens

by

Christopher Joseph Bay

B.S., Univeristy of Colorado Boulder, 2012

A thesis submitted to the

Faculty of the Graduate School of the

University of Colorado in partial fulfillment

of the requirements for the degree of

Masters of Science

Department of Mechanical Engineering

2012

This thesis entitled:
Biomechanics and Ultrastructure of the Ocular Lens
written by Christopher Joseph Bay
has been approved for the Department of Mechanical Engineering

Richard Regueiro

Virginia Ferguson

Mark Rentschler

Date

The final copy of this thesis has been examined by the signatories, and we find that both the
content and the form meet acceptable presentation standards of scholarly work in the above
mentioned discipline.

Bay, Christopher Joseph (M.S., Mechanical Engineering)

Biomechanics and Ultrastructure of the Ocular Lens

Thesis directed by Associate Professor Richard Regueiro

Study of the biomechanics of the ocular lens is imperative to increasing our understanding of the role of the ocular lens in accommodation, to improving current surgical methods (cataract and intraocular lens replacement), and to better qualify the nature and mechanics of injuries sustained to the ocular lens (lens dehiscence, lens perforation, and traumatic cataract). Previous work done to determine and model the mechanical properties of the ocular lens includes non-ideal experimental assumptions and lack of qualified data. The goal of this work is to produce and analyze data suitable for the creation of an ultrastructurally based computational model of the ocular lens and make progress toward the generation of such a model.

The creation of a model requires the determination of the material properties as well as identification of the ultrastructure of the tissue to be modeled. Unconfined compression testing of the whole porcine ocular lens, puncture testing of the whole porcine ocular lens, and nanoindentation of the anterior porcine and human lens capsule were performed to generate data from which to calculate material properties of the lens. Cryo-electron tomography and confocal scanning LASER microscopy were employed to determine the ultrastructure of the porcine lens capsule and porcine lens fiber cells, respectively.

Test data were produced from the mechanical tests and the fitting of parameters to calculate material properties were started. Potential identification of the type-IV collagen meshwork of the lens capsule and positive identification of the lens fiber cells were achieved. Preliminary modeling work was started with the data available using Abaqus (simulia.com) and Tahoe (tahoe.sourceforge.net).

Dedication

First and foremost, this thesis is dedicated to my mom, Sharon, and my two younger sisters, Crystal and Kayla. Thank you mom, for your constant support in the pursuit of my dreams, the occasional Chipotle gift card to curb my hunger, and for helping to keep me going when I thought different. Crystal, thank you for reminding me of my humility and showing me the importance of serving others through your studies and work. And Kayla, thank you for keeping me grounded in reality while encouraging me to shoot past the stars. I love you all and would not be who I am today without you.

Secondly, I would like to thank my uncle Wayne for being such a positive influence throughout my life. You have only begun showing me the secrets of, as well as how to so thoroughly enjoy the art of fishing, and I hope we can reel 'em in for years to come.

Next, I would like to thank my good friend Kyle Blackmer. You have been, and always will be a brother to me. Thank you for your guidance, your wisdom, and your unconditional friendship throughout my college career and beyond. I love you man.

Lastly, I would like to thank my girlfriend, Laura Willson. Your support and encouragement throughout this whole ordeal has been tremendous. From keeping me focused, to providing comedic interludes, I couldn't have completed this without your help. Thank you for all the baking sustenance, hours of laughs, and escapes from reality. You mean the world to me and I love you.

Acknowledgements

Contents

Tables

Table

Chapter 1

Introduction

The benefits of understanding the biomechanics of the ocular lens have far reaching implications for the research community, armed forces, and general populace. For example, currently accommodation (the process of the ocular lens focussing) as well as presbyopia (the loss of accommodation over time) are not fully understood. This is partly due to a lack of adequate material property determination and structure identification of the ocular lens. While research has been done to find the material properties [Bailey et al., 1993, Krag et al., 1997, Yang et al., 1998a, Krag and Andreassen, 2003b] and identify the ultrastructure of the ocular lens, specifically the lens capsule [Barnard et al., 1992], the majority of data suffers from many assumptions made in regards to the experimental techniques, such as 1-D/uniaxial measurements and alterations to the native structure of the tissue. Recently, work has been done to measure the multiaxial properties of the lens capsule [Heistand et al., 2005, Pedrigi et al., 2007, David et al., 2007] and material properties of the lens fibers [Erpelding et al., 2005, Reilly and Ravi, 2009], more work is needed. An increased understanding of the biomechanics and structure of the ocular lens are necessary to answer the question of how accommodation occurs and why presbyopia happens.

With a better understanding of the material properties and structure of the ocular lens, current surgical treatments for presbyopia (mainly intraocular lens replacement surgery) and cataract surgery can be improved. Design specifications of the IOLs such as elasticity and geometry could be optimized for the human lens [McLeod et al., 2003]. With the study of lens properties in regards to age, IOLs could be individually customized for the patient. The interactions of surgical devices

and prostheses can be computationally modeled and studied, allowing for the advancement of IOL and surgical device design. This could result in lower rates of complications after surgery as well as decreases in healthcare costs related to ocular treatments. In order for this to take place, more study is needed of the mechanical properties and ultrastructure of the ocular lens.

Trauma can occur to the ocular lens, either through blunt force contact, blast-wave loading (due to a percussive wave generated from an explosion), or through the introduction of an intraocular foreign body (IOFB, commonly small pieces of metal or glass). Partial or complete dislocation of the ocular lens can occur [Jain et al., 2004, Kim et al., 2009], as well as the formation of traumatic cataracts [Fineman et al., 2000, Nguyen et al., 2002] and perforation of the ocular lens [Mader et al., 1993, Mader et al., 2006]. Trauma to the lens is of particular interest to the armed forces and their personnel, especially in light of the increased use of improvised explosive devices (IEDs) in recent military actions [Muzaffar et al., 2000, Mader et al., 2006, Weichel and Colyer, 2008, Weichel et al., 2008, Colyer et al., 2008]. Ocular trauma can also occur in civilians in workplace accidents or during everyday life [Lee and Song, 2001]. Better material properties and structure identification are needed for the creation of an ultrastructurally based computational mechanical model. With such a model, the lens could be simulated under such trauma conditions. Information from simulations such as these could be used to better understand the mechanics of the injuries suffered to the ocular lens and lead to the design of adequate protective gear and improved treatments.

The goal of this work was to gather and analyze data towards the production of an ultrastructurally based computational mechanical model. The model is part of a larger area of research towards modeling the entire eye in a variety of conditions and producing simulations that lead to increased understanding of the ocular lens. This was done through mechanical testing of the ocular lens to determine material properties, specifically the whole porcine ocular lens and anterior porcine lens capsule tissue, and imaging of the ocular lens ultrastructure, specifically the anterior porcine lens capsule and the porcine lens fibers.

Chapter 2

Background

2.1   Characteristics of the Lens

The ocular lens is a relatively small, transparent body placed behind the cornea and aqueous humor in the eye (see Figure 2.1). It is suspended between the aqueous humor and the vitreous humor by ciliary zonules which attach near the equator of the lens. The ciliary zonules are anchored to the ciliary body, which encircles the opening that the lens is suspended in. Within the ciliary body is the ciliary muscle. Through a process called accommodation, the lens (coupled with the curvature of the cornea) allows for the focussing of near and far images by changing its shape. Currently, the most widely held theory of accommodation is the Helmholz Theory [Burd et al., 1999, Glasser and Campbell, 1999, Martin et al., 2005, Stachs et al., 2005], originally introduced in 1855 [Helmholz, 1855]. The theory states the lens is accommodated and in its lowest stressed state when the tension in the zonules are relaxed [Krag and Andreassen, 2003a]. This occurs when the ciliary muscle contracts. With the ciliary muscle relaxed, the zonules are put into tension thus flattening the lens and putting it in the un-accommodated state. Figure 2.2 shows the un-accommodated state on the left and the accommodated state on the right.

Presbyopia is the loss of accommodation of the lens as we age. It has been proposed that presbyopia occurs due to a change in the mechanical properties of the eye over time. Some have attributed this to a change in the mechanical properties of the lens internal substance and the lens capsule [Beers and van der Heijde, 1996, Glasser and Campbell, 1998, Glasser and Campbell, 1999, Heys et al., 2004a, Breitenfeld et al., 2005, Richdale et al., 2008, Ziebarth et al., 2008] some to a
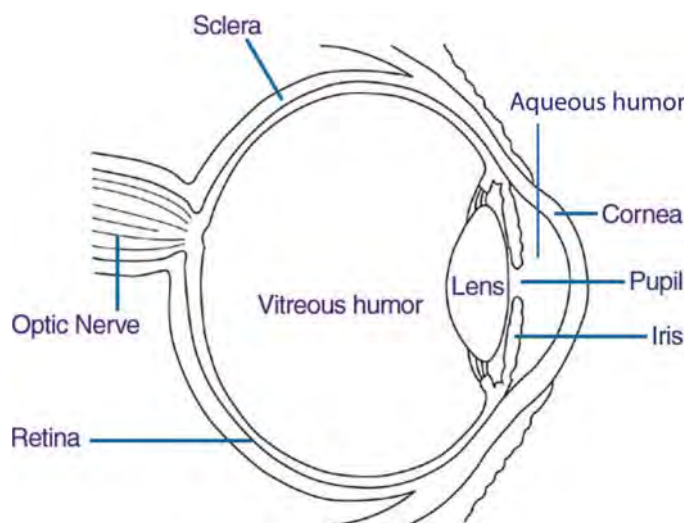
Figure 2.1: General Anatomy of the Eye (nei.nih.gov).
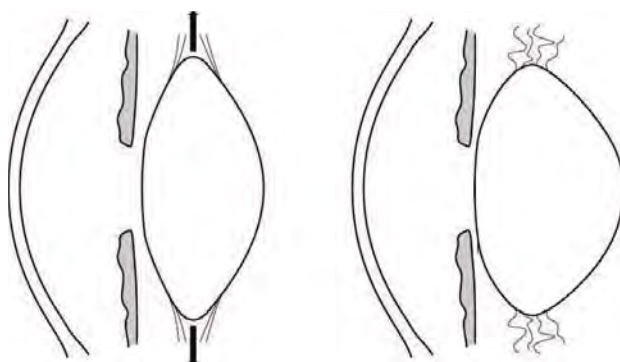
Figure 2.2: Theory of How Accommodation Occurs: On the left in the lens is shown in the unaccommodated state, where the zonules are in tension. On the right the lens is shown in the accommodated state, where the zonules are not in tension due to the contraction of the ciliary muscle [McLeod et al., 2003].

change in the zonules [Stachs et al., 2005], and others to a change in the ability of the ciliary muscle to contract [Abolmaali et al., 2007]. Previous work has shown that a change in the lens's mechanical properties results in a decrease of the accommodative power of the lens [Krag and Andreassen, 1996, Krag et al., 1997, Glasser and Campbell, 1998, Krag and Andreassen, 2003a, Strenk et al., 2004, Heys et al., 2004a, Weeber et al., 2005]. Although prior work has been done to characterize the mechanical properties of the lens [Krag et al., 1997, Glasser and Campbell, 1999, Weeber et al., 2005, Heistand et al., 2005], there has not been enough work for people to agree on one set of properties or range of properties. To fully comprehend the mechanisms of presbyopia, an understanding of the mechanical properties of the ocular lens is needed. The ocular lens is comprised of 2 main parts, shown in Figure 2.3. A more detailed description of each part is provided below.
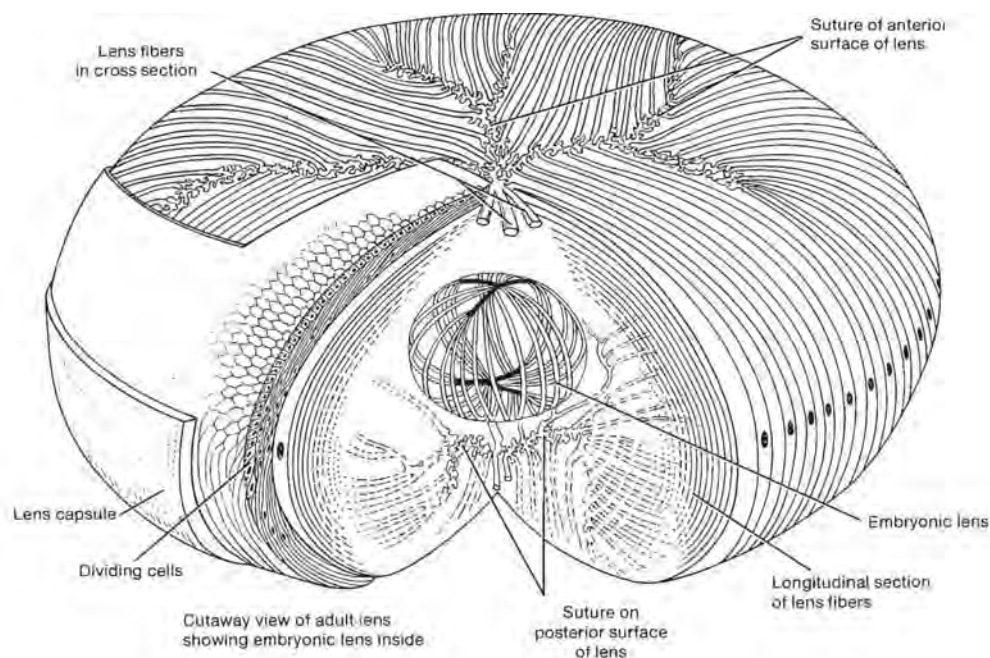
Figure 2.3: Detailed Anatomy of the Ocular Lens [Kessel and Kardon, 1979].

2.1.1 Capsule

The exterior portion of the ocular lens is the lens capsule. The capsule acts as a bag-like membrane for the lens, containing the lens fibers and helping to maintain the proper ionic

balance for the lens fibers. The ultrastructure of the lens capsule is a type-IV collagen 3-D mesh-work [Barnard et al., 1992]. This mesh-work provides for nearly 65% of the dry weight of the lens capsule, acting as a support structure [Barnard et al., 1992]. The human lens capsule thickness has been found to vary depending on radial location and anterior vs posterior surfaces. The anterior thickness varies from 11-33 μm while the posterior thickness varies from 4-9 μm [Krag et al., 1997, Krag and Andreassen, 2003b]. As mentioned earlier, ciliary zonules attach to the lens along its equator, interweaving with the lens capsule [Stachs et al., 2005]. Through this attachment, it is thought that the tension in the zonules is transmitted to the lens capsule, allowing it to deform the interior lens fibers when in the un-accommodated state [Beers and van der Heijde, 1996]. The lens capsule continues to grow throughout most of life [Krag and Andreassen, 2003a].

2.1.2   Lens Fiber Cells

The lens fibers make up the majority of the volume of the ocular lens. They are contained within the lens capsule. A gel-like substance, the lens fibers cells are elongated cells comprised mainly of proteins called crystallins [Kaufman and Alm, 2003]. These cells are arranged in layers [Kessel and Kardon, 1979], much like an onion, as can be seen in Figure 2.3. The interior lens fibers are separated into 2 main regions: the inner nucleus, and the outer cortex [Kaufman and Alm, 2003]. It has been found in studies that the interior nucleus is stiffer than the cortex [Heys et al., 2004a, Erpelding et al., 2005]. Cross-sectional area of the lens fiber cells has been found to range from 5 μm^2 to 148 μm^2, depending on the region [Taylor et al., 1996]. It has been shown that misalignment of the lens fiber cells by trauma or IOFBs can result in formation of cataracts [Rofagha et al., 2008]. New lens fibers are produced along the lens capsule throughout most of life [Kaufman and Alm, 2003].

2.2 Previous Research

2.2.1 Capsule

2.2.1.1 Property Determination

Various research has been completed to characterize the mechanical properties of the lens. One study done by Krag, et al. (1997) involved cutting the anterior lens capsule into circular segments using a laser and then stretching these circular segments uniaxially and measuring the force response. One issue with this test is that by sectioning the lens capsule into circular segments essentially destroys the native structure and in vivo stress confition of the lens capsule, resulting in a different force response than native tissue. Also, this test neglected preconditioning of the lens capsule, which is frequently necessary when testing biological tissue [Fung, 1993]. One study looked at puncturing whole lenses [Yang et al., 1998a]. The test was limited in its force measuring technique, based off of a spring with a weight attached, a machine to lower the spring, and a stopwatch. More recently, Heistand, et al. (2005) developed an experiment to measure the multiaxial mechanical behavior of the anterior lens capsule. The experiment involves two cameras measuring the displacement of microspherules on the anterior surface of the lens capsule as it is inflated with fluid [Heistand et al., 2005]. Other multiaxial strain research has been done [David et al., 2007, Pedrigi et al., 2007] as well as work involving a multiaxial lens stretcher [Reilly et al., 2008]; however, more data is needed to find conclusive results.

Additionally, several modeling studies involving the lens capsule assume it to be an elastic material [Burd et al., 2002, Burd et al., 1999, Liu et al., 2006, Pedrigi and Humphrey, 2011]. However, experiments have shown viscoelastic behavior of the lens capsule [Thim et al., 1993, Krag and Andreassen, 2003a].

2.2.1.2 Structure Identification

Little work has been done with regard to the identification of the ultrastructure of the lens capsule [Barnard et al., 1992]. Barnard utilized cryoelectron microscopy to image lens capsule

[Barnard et al., 1992]. The process involved with preparing the sample for the imaging, unfortunately, has the high probability of altering the native structure of the lens capsule. After being frozen in a high-pressure freezer, the samples were subjected to extraction in order to remove the material between the type-IV collagen fibers. This step can result in overall dimension and stress changes as the material between the mesh-work can act to support or even push apart the fibers. After extraction, samples underwent a platinum deposition, creating a replica of the type-IV collagen mesh-work. Due to the inconsistencies of the depositions layers inherent with the process, the true thickness and spacing of the fibers cannot be observed as they have been enlarged by unequal amounts. Additionally, the data presented was only 2-dimensional, when 3-dimensional structure identification is needed.

2.2.2   Lens Fiber Cells

2.2.2.1   Property Determination

Microindentation of the interior lens fibers was performed by Reilly, et al. (2009). Porcine lenses were immersed in preserving medium shortly after death and then fixed within a gel for sectioning [Reilly and Ravi, 2009]. Lenses were bisected along the optical axis or in the equatorial plane through the middle of the lens [Reilly and Ravi, 2009]. Lens fibers were then microindented and the force response was measured. The sectioning process involved can lead to the damaging of the lens fibers or the alteration of material properties. Another test involved using a fine conical probe to measure the resistance to penetration of different layers of the lens [Pau and Kranz, 1991]. Again, the damage done to the lens fiber cells is not ideal when measuring their material properties.

2.2.2.2   Structure Identification

Transmission electron microscopy and scanning electron microscopy have both been done on the lens fibers to image the ultrastructure and organization of the fiber cells [Taylor et al., 1996, Kessel and Kardon, 1979]. This has resulted in decent results, but the preparation and fixation processes used can result in alteration of the native structure of the lens fibers. Additionally, fluores-

cent confocal microscopy has been done [O'Connor et al., 2008, Shestopalov and Bassnett, 2000], but more data is needed, specifically analysis of the 3-D nature of the structure to include in an ultrastructurally based computational model.

2.3   What is Needed

While there has been an increased focus on researching the ocular lens, its properties, and behavior, an accurate model that is based off of the ultrastructure of the involved tissues has not been generated. We are aware of only one model that has included ultrastructure data in their model [Burd, 2009] for the lens capsule. Furthermore, majority of models do not model the lens as viscoelastic, neglecting this part of the tissues behavior nor the potential poroelasticity of the lens capsule (thickest basement membrane in the human body). What is needed is a ultrastructurally based computational finite element model which will allow for the simulation various conditions, leading to increased understanding of the ocular lens and its mechanics. In order for this to be possible, more testing is needed to generate data from which material properties can be calculated. Also, further imaging is needed of the ultrastructure of the lens capsule and lens fibers, focussing on the 3-D nature of the structure. The data gathered from the following work is a first step toward the creation of such a model.

Chapter 3

Parameter Fitting of Unconfined Compression Testing Data

In order to create a computational mechanical model of the ocular lens, the material properties of the lens must be known. While previous work has been completed on determining the material properties of the lens as mentioned earlier, varying methods and assumptions have not produced a defining set of material properties. Unconfined compression testing was completed in order to produce data that could be used to determine the material properties of the whole ocular lens, specifically τ (relaxation time constant), μ_{EQ} (equilibrium shear modulus), and μ_{NEQ} (nonequilibrium shear modulus). From these properties, bulk moduli and viscosities can also be calculated, as described in the Methods of Fitting Parameters section. The data were fitted using DAKOTA (Design Analysis Kit for Optimization and Terascale Applications) which is developed by Sandia National Laboratories (dakota.sandia.gov). Once approximate fits were found, meshes were generated using CUBIT, a geometry and mesh generation toolkit also developed by Sandia National Laboratories (cubit.sandia.gov). Images of lenses before being tested were taken for 2 test groups. From these images, geometric data were collected and used in the generation of the meshes. With the parameters determined from the data fits and the mesh generations, simulations were run for particular cases of each test group using Tahoe, a research-oriented platform geared towards the development of numerical methods and material models. Tahoe was initially developed by Sandia National Laboratories (tahoe.sourceforge.net) and is currently being developed by several academic and industry partners. Furthermore, preliminary modeling in Abaqus (www.simulia.com) is being completed, to compare with Tahoe results and investigate the material properties. The first round

of tests (completed by a previous student) included preconditioning (as described in the Previous Testing Done section). The idea being that the lens is in a preconditioned state within the eye as it constantly focuses and accommodates. Also, as mentioned earlier, it is known that biological tissue often requires preconditioning when collecting data [Fung, 1993]. A second round of tests has been completed without preconditioning and fits are currently being generated (the testing data are shown below in Section 3.6) for comparison with the preconditioned data and to show the lenses' initial response characteristics.

3.1   Previous Testing Done

A previous student, Laura Hatanaka, completed a series of unconfined compression testing on whole ocular porcine lenses. Whole ocular globes were collected and shipped by Animal Technologies, Inc. (Tyler, TX), overnight on wet ice. Upon receipt, the whole lenses were extracted by making an incision approximately midway in the sclera and cutting through the sclera until the lens could be accessed from the posterior direction (see Figure 3.1).

Figure 3.1: Dissection of Globe to Remove Ocular Lens.

Excess vitreous humor was removed with tweezers and scissors. The zonules were then cut around the lens, and the lens was fully extracted from the globe. Excess zonules were removed by rolling the lens along its equator on tissue paper (see Figure 3.2).

Lenses were then transported in Alcon Balanced Salt Solution (BSS) to the MTS Insight II electromechanical testing system for testing. A 2N load cell (sensitivity: 2.04 mv/V) was used to

Figure 3.2: Removing Excess Zonules from Ocular Lens with Tissue Paper.

record the force exerted by the lens in each test. The lens was placed in a pedestal containing Alcon BSS (see Figure 3.3a). The testing pedestal was surrounded by a heated water bath within an environmental chamber (see Figure 3.3b). The water bath was heated to 37 ℃ to help approximate in vivo conditions.

The lens was tested with the anterior surface facing downwards, due to the greater curvature of the posterior surface and the lens's natural tendency to rest on its anterior surface when free (see Figure 3.4). The lens was compressed by a flat platen (the platen can be seen at the top of Figure 3.4).

Tests were completed on tissue from two different tissue age groups: from pigs aged 6-9 months or pigs aged 2 or more years. Tissue from each age group was compressed to 2 strains (10% and 20%) at 2 loading rates (0.1 mm/s and 0.3 mm/s). For each test group, 10 samples were tested for a total of 80 lenses. A summary of the testing configurations and number of samples can be seen in Table 3.1. Lenses underwent preconditioning through 5 cycles of testing. The first 2 cycles would load and unload the lens to the desired strain 2 times and then load and hold the lens at the desired strain for 200 seconds. The last 3 cycles would load and unload the lens to the desired strain 3 times and then load and hold the lens at the desired strain for 350 seconds. See Figure 3.5 to view an example of preconditioning. For the parameter fitting, only the last load and hold curve was used.

13

(a) Testing Pedestal with BSS Solution in Testing Platform.
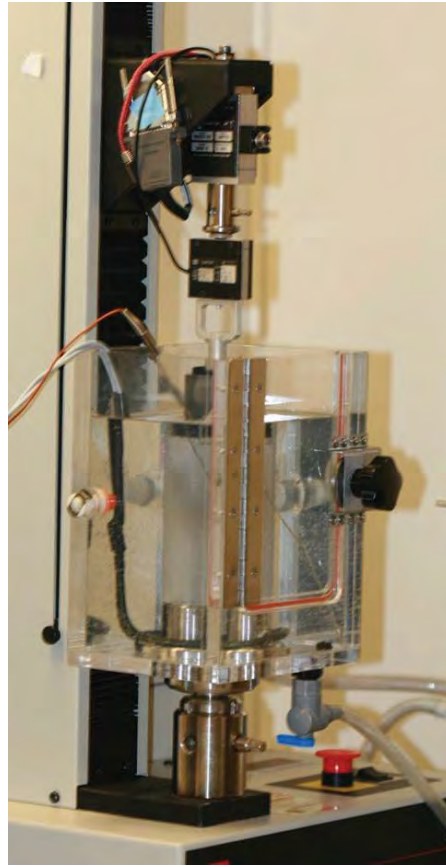
(b) Test Setup for Unconfined Compression Testing.

Figure 3.3: Test Setup for Unconfined Compression Testing.

Figure 3.4: Shape of Lens (Anterior Surface Facing Down) Testing in Testing Platform, Showing Upper Load Platen.

Table 3.1: Unconfined Compression Testing Conditions and Number of Whole Ocular Porcine Lenses Tested With Preconditioning.

| | Age of Tissue | | | |
| | Strain | | | |
Loading Rate	6-9 month 10%	6-9 month 20%	2+ year 10%	2+ year 20%
0.1 mm/s	10	10	10	8
0.3 mm/s	10	10	10	10
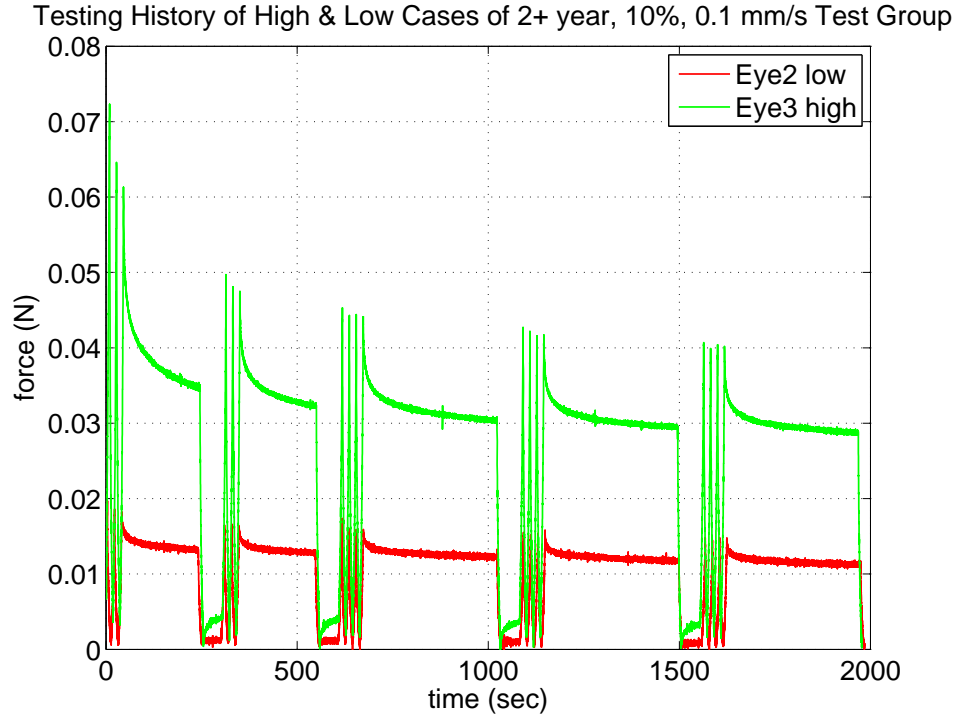
Figure 3.5: Example Showing Data with Preconditioning.

Below are graphs showing the previous data that were collected. As mentioned above, only the last load and hold curve of the test was used in the parameter fitting. Each graph shows the 10 eyes tested for that test group.
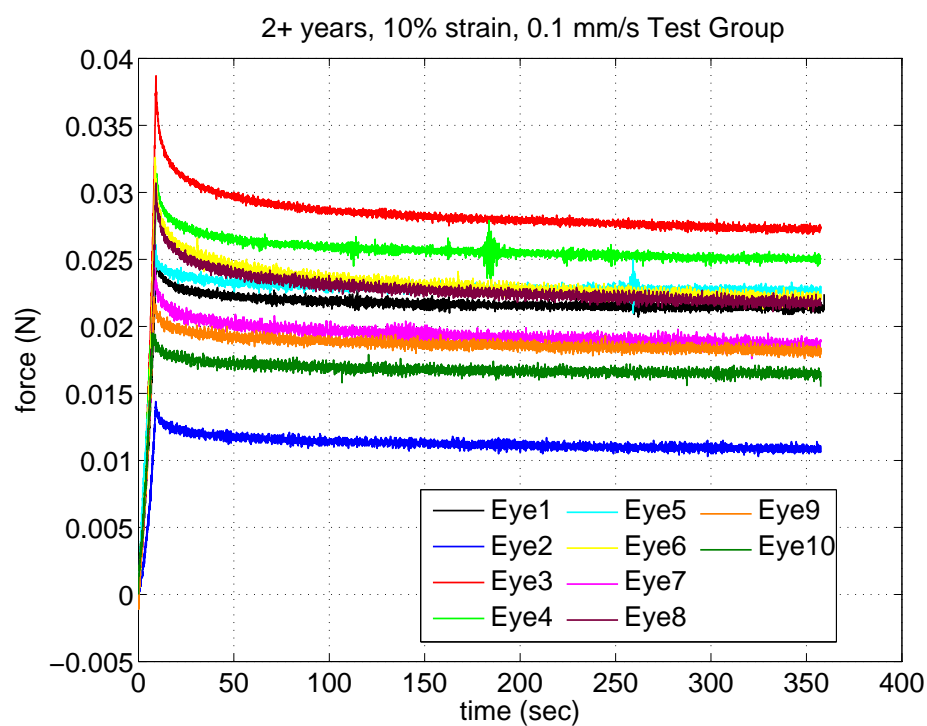
Figure 3.6: Graph of all eyes from the 2+ year 10% strain 0.1 mm/s Group.
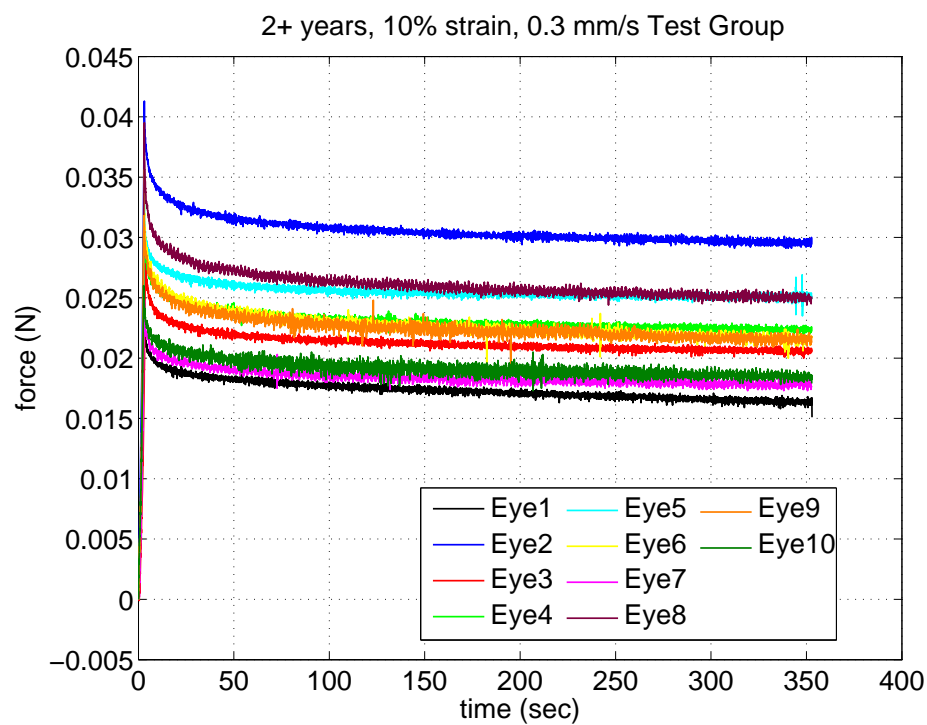
Figure 3.7: Graph of all eyes from the 2+ year 10% strain 0.3 mm/s Group.
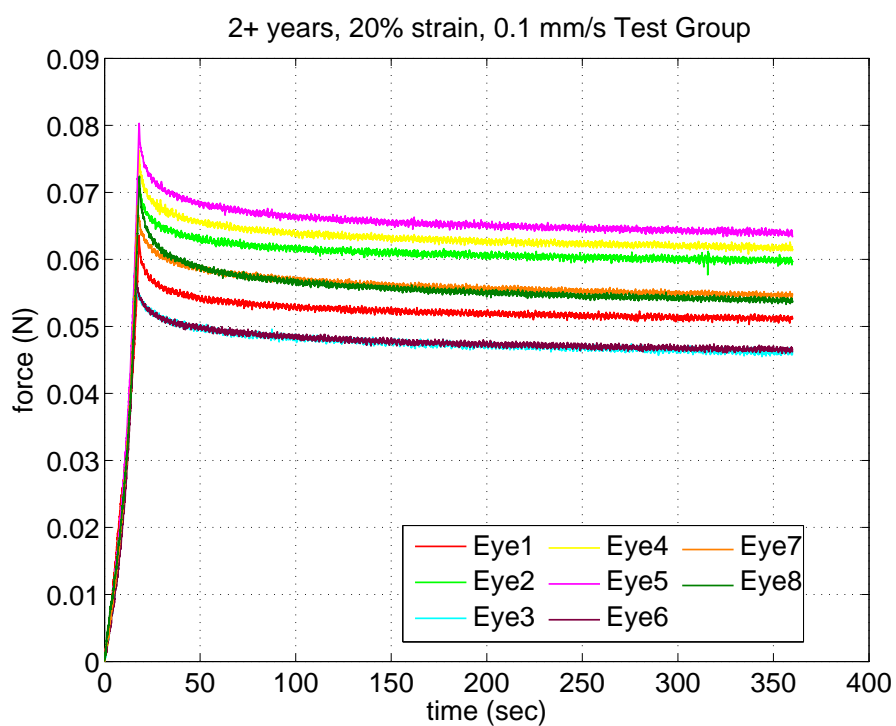
Figure 3.8: Graph of all eyes from the 2+ year 20% strain 0.1 mm/s Group.
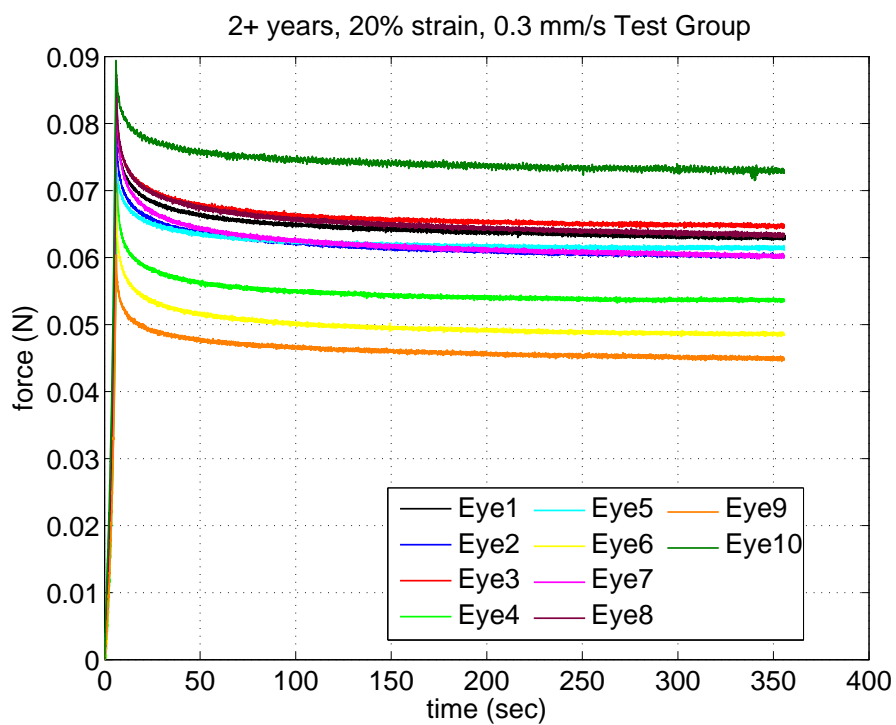
Figure 3.9: Graph of all eyes from the 2+ year 20% strain 0.3 mm/s Group.
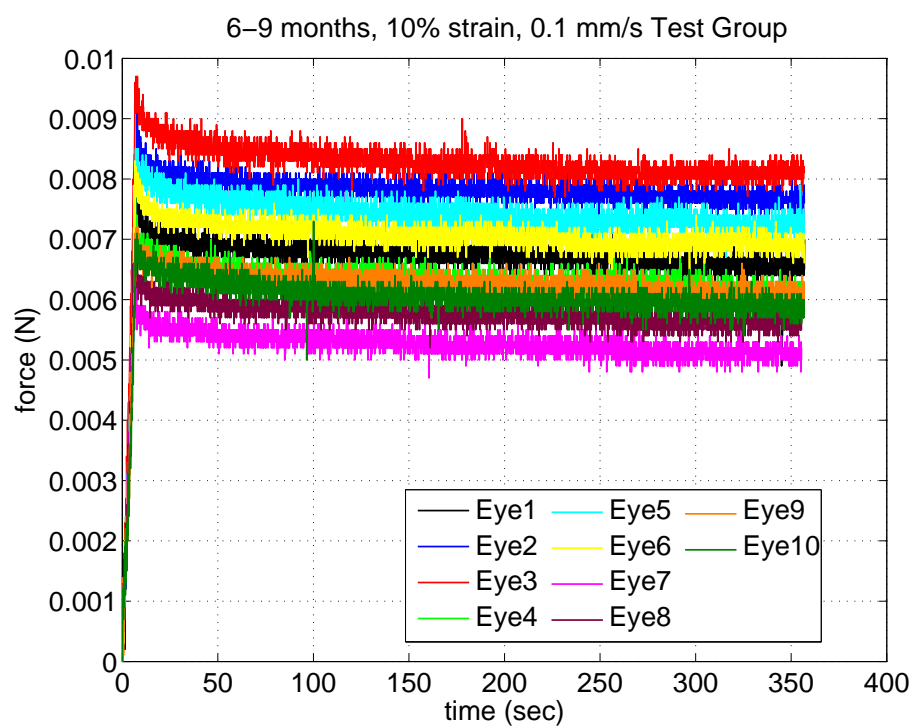
Figure 3.10: Graph of all eyes from the 6-9 month 10% strain 0.1 mm/s Group.
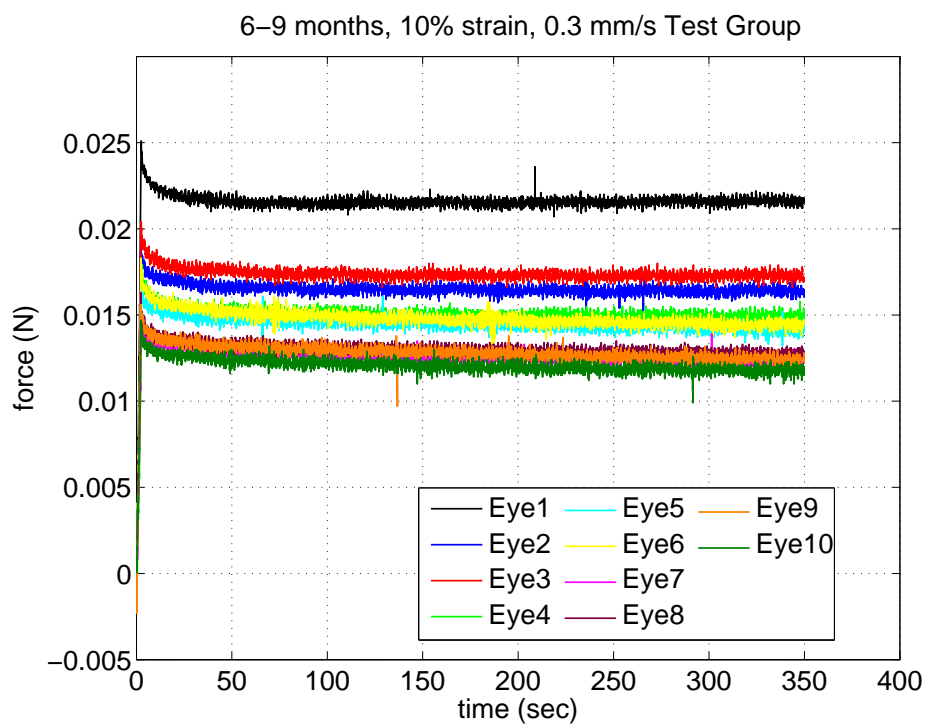
Figure 3.11: Graph of all eyes from the 6-9 month 10% strain 0.3 mm/s Group.
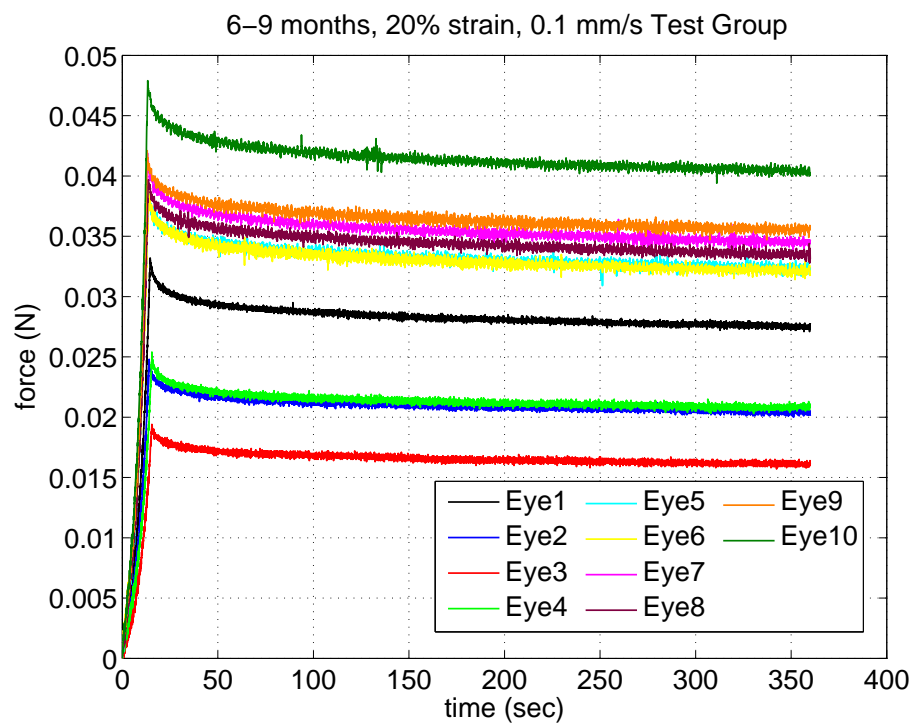
Figure 3.12: Graph of all eyes from the 6-9 month 20% strain 0.1 mm/s Group.
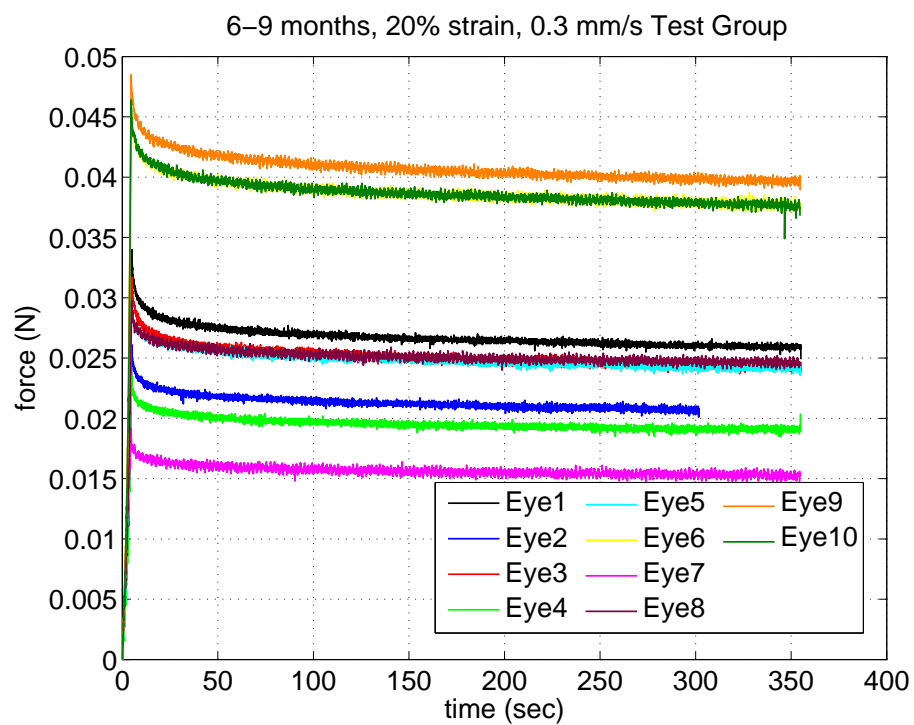
Figure 3.13: Graph of all eyes from the 6-9 month 20% strain 0.3 mm/s Group.

3.2   Methods of Fitting Parameters

DAKOTA (dakota.sandia.gov) was used for optimizing the parameters during the data fitting process. A constitutive framework based off of a finite deformation, isotropic, viscoelasticity model developed by Reese and Govindjee [Reese and Govindjee, 1998] was implemented within Tahoe (tahoe.sourceforge.net) by Prof. Thao (Vicky) Nguyen (Johns Hopkins University), and being used by Prof. Richard Regueiro (University of Colorado Boulder) and his research group. The input parameters for Tahoe are τ (relaxation time constant), μ_{EQ} (equilibrium shear modulus), and μ_{NEQ} (nonequilibrium shear modulus). From these parameters, the bulk moduli and viscosities can be calculated. Equations 3.1 through 3.5 show how to calculate the bulk moduli (κ_{EQ} and κ_{NEQ}) and the viscosities (η_{D} and η_{V}). Figure 3.14 shows an analogy of the model implemented in Tahoe to a standard linear solid. The upper spring provides for the long-term elastic effects of the lens tissue while the bottom dashpot and spring in series provides for the viscoelastic properties.

$$\kappa_{\mathrm{EQ}} = A\mu_{\mathrm{EQ}} \tag{3.1}$$

$$\kappa_{\mathrm{NEQ}} = A\mu_{\mathrm{NEQ}} \tag{3.2}$$

$$\eta_{\mathrm{D}} = \tau\mu_{\mathrm{NEQ}} \tag{3.3}$$

$$\eta_{\mathrm{V}} = \tau\kappa_{\mathrm{NEQ}} \tag{3.4}$$

$$A = 100(\text{capsule}), 1000(\text{substance}) \tag{3.5}$$

Additionally, meshes were generated based off of the geometric data gathered from the images of the lenses. Images of the lenses were overlaid with a coordinate grid and coordinates were taken along the right side of the lens starting from the midpoint on the bottom of the lens to the midpoint at the top of the lens. These coordinates were normalized from 0 to 1 and then multiplied by the height of the lens, previously measured during testing. For lenses that were not imaged, an average set of coordinates normalize from 0 to 1 were used, multiplied by the height of the non-imaged lens. Using these coordinates, 2-D axisymmetric meshes (see Figure 3.15) were generated with the

μ_{EQ} , κ_{EQ}

η_D , η_V μ_{NEQ} , κ_{NEQ}

F
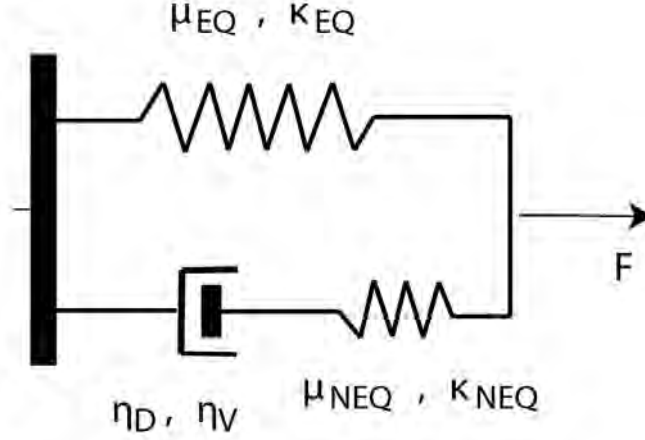
Figure 3.14: Analogy of Model Implemented in Tahoe to a Standard Linear Solid.

software CUBIT (cubit.sandia.gov). Meshes were setup such that they had 2 sections: the outer lens capsule and the interior lens fibers (see Figure 3.15). The thickness of the capsule is 60 μm, based off of the measurements of previous work [Krag and Andreassen, 1996].

An initial guess of the 3 material properties τ (relaxation time constant), μ_{EQ} (equilibrium shear modulus), and μ_{NEQ} (nonequilibrium shear modulus) was made with lower and upper bounds for each parameter. DAKOTA then utilized the model in Tahoe and the generated mesh for each lens as it completed 27 different variations of the initial parameter guesses. Once finished, plots of force vs. time from the simulations were analyzed and used to adjust the parameter guesses. This process was completed until a satisfactory approximate fit was achieved. Out of each test group, the highest and lowest force vs. time curves were fitted.

3.3   Sample Preparation

Sample preparation for the first round of testing is described above in Previous Testing Done. Sample preparation for the second round of testing differed slightly and is described below. As before, whole ocular globes were collected and shipped by Animal Technologies, Inc. (Tyler, TX), overnight on wet ice. Upon receipt, the whole lenses were extracted by first removing the cornea. This was done by making a small incision in the cornea with a diamond-head scalpel and cutting
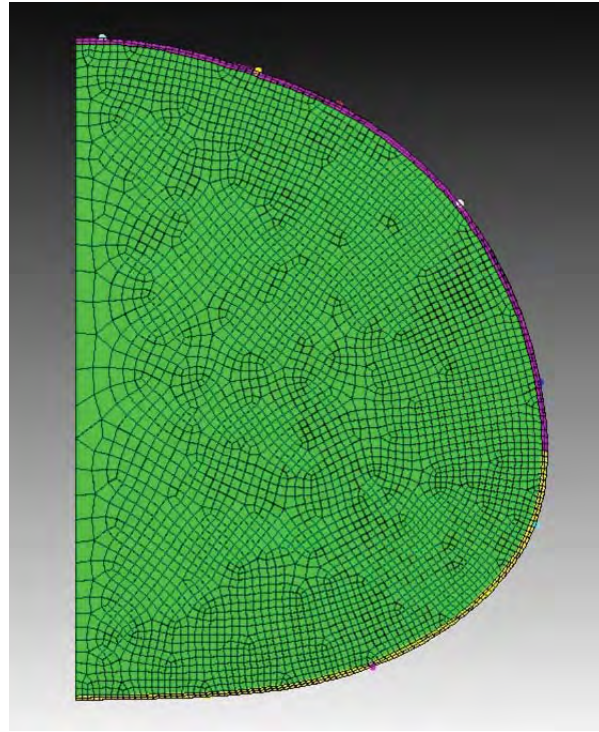
Figure 3.15: Example of Lens Mesh Generated by CUBIT - Notice the two sections: the exterior lens capsule (yellow and purple) and the interior lens fiber cells (green).

around the cornea with a pair of curved microsurgery scissors. Once the cornea was removed, the processed was repeated by making an incision through the zonules and cutting around the zonules until the whole lens was free. Excess zonules were removed as described earlier, and the whole lenses were transported in Alcon BSS to the MTS Insight II.

3.4   Experimental Setup

The same MTS Insight II testing system was used as describe earlier. Lenses were loaded in the same testing pedestal as used before (see Figure 3.3a) and used the same water bath heated to 37 ℃. The same flat loading platen was used (can be seen in the top of Figure 3.4).

3.5   Experimental Method

Whole porcine ocular lenses were tested with the same test groups as before, only this time there were 5 samples per test group. No preconditioning was used and the lenses were loaded to the defined strain at the defined loading rate and held there for 350 seconds. A summary of the test configurations and samples per test can be seen below in Table 3.2. Images of each lens tested were taken pre-test and the tests were video recorded to get gross deformation of the lenses as they were loaded.

Table 3.2: Unconfined Compression Testing Conditions and Number of Whole Ocular Porcine Lenses Tested With No Preconditioning

| | Age of Tissue | | | |
| | Strain | | | |
Loading Rate	6-9 month 10%	6-9 month 20%	2+ year 10%	2+ year 20%
0.1 mm/s	5	5	5	5
0.3 mm/s	5	5	5	5

3.6   Results

Below are the overall testing history and parameter fits generated for the high and low curves of each test group with pre-conditioning. Fits are approximate and the next iteration of parameter fits will be done after adjustments to the constitutive framework within Tahoe.
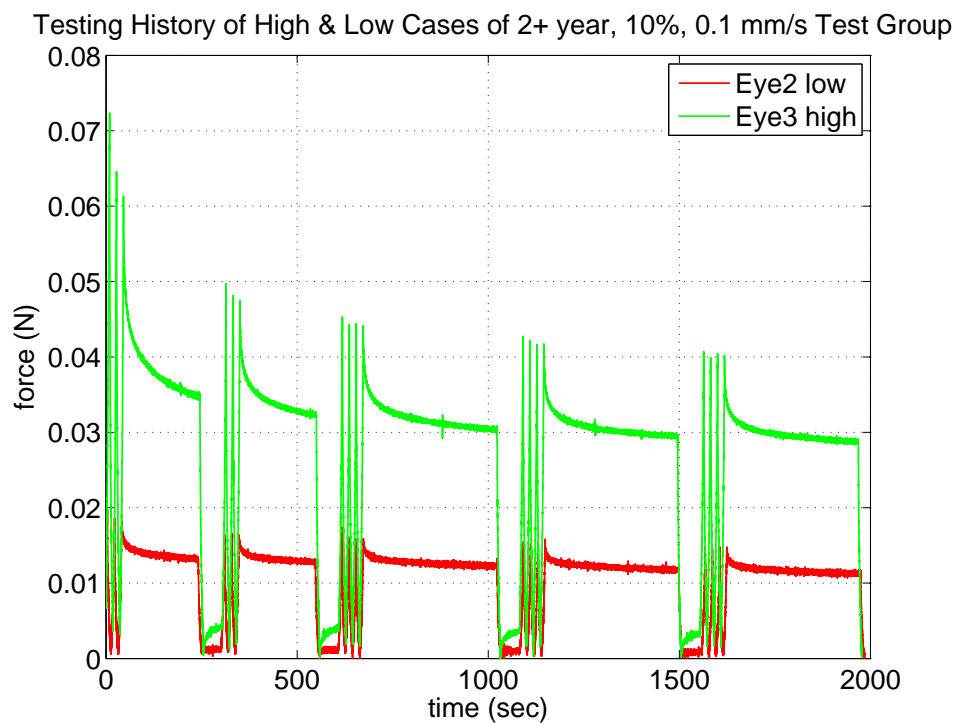
Figure 3.16: Graph of Eye2 and Eye3 from the 2+ year 10% strain 0.1 mm/s Group.
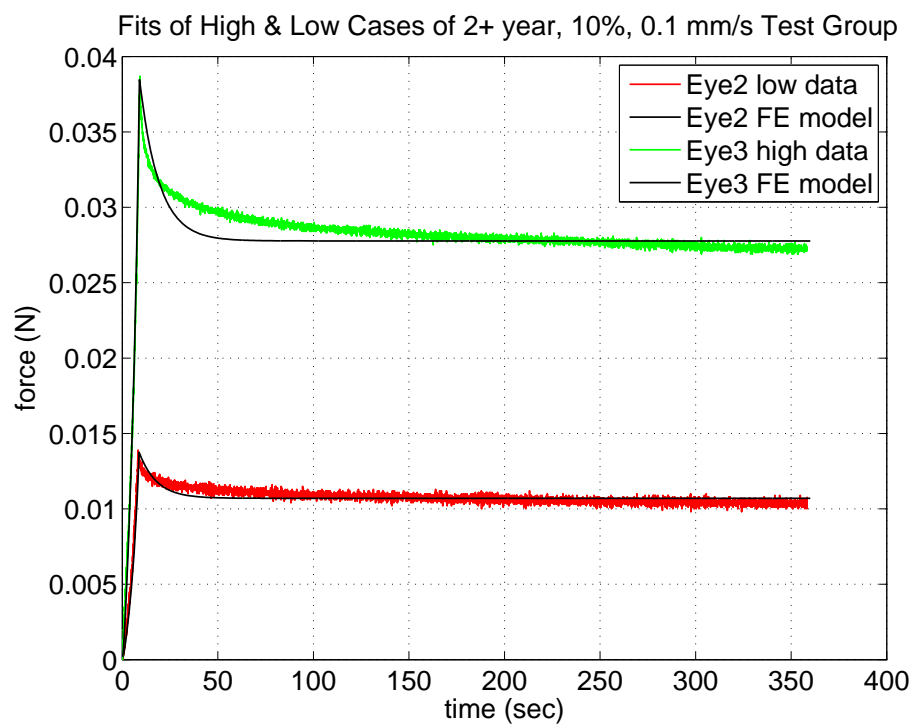
Figure 3.17: Graph of Eye2 and Eye3 vs Tahoe from the 2+ year 10% strain 0.1 mm/s Group.
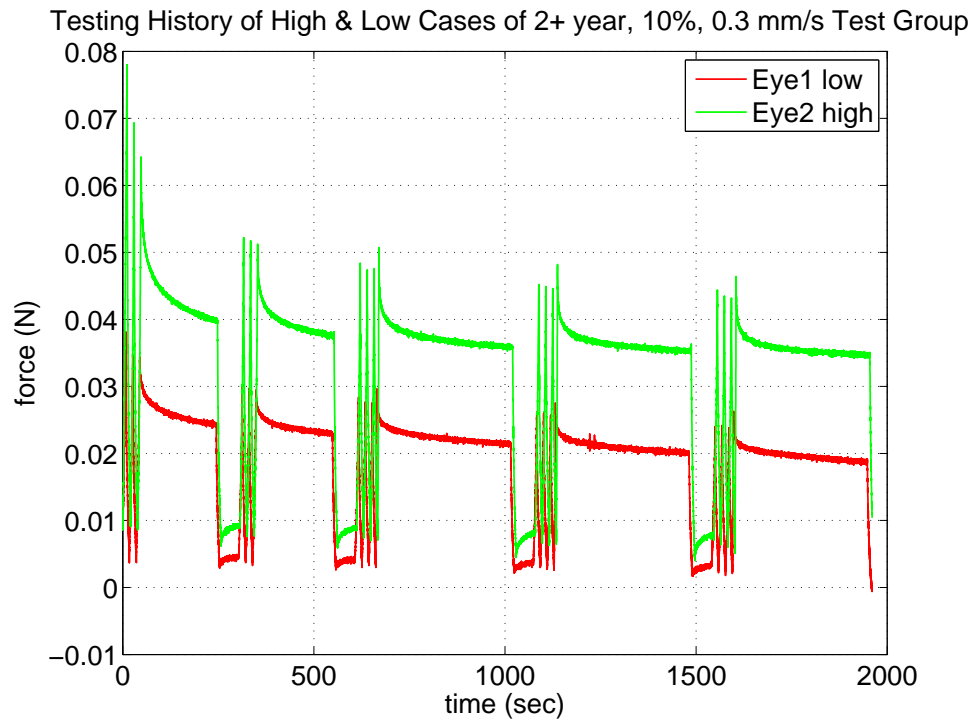
Figure 3.18: Graph of Eye1 and Eye2 from the 2+ year 10% strain 0.3 mm/s Group.
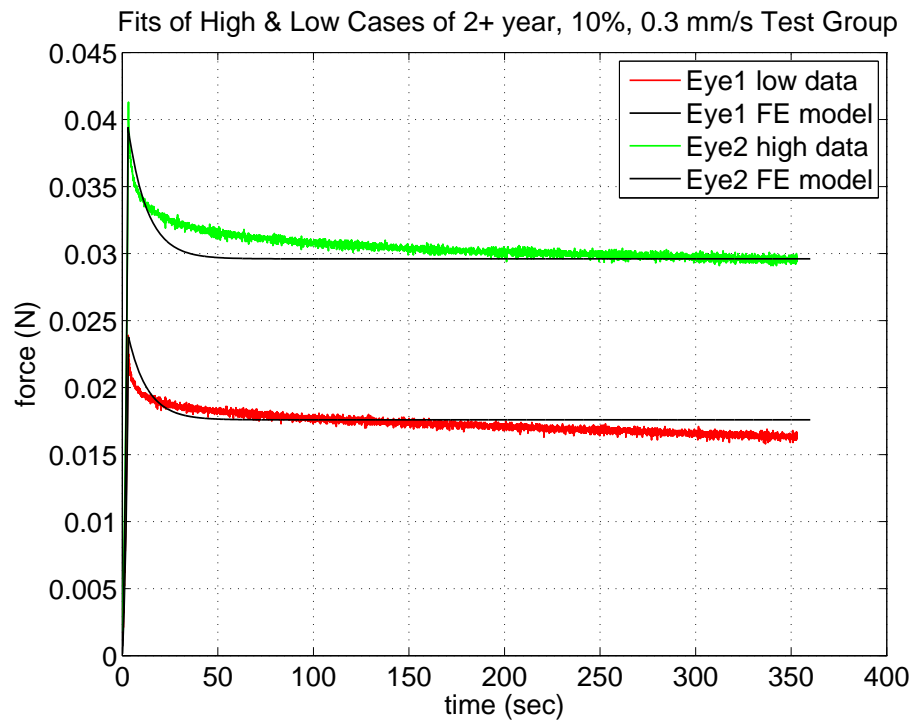
Figure 3.19: Graph of Eye1 and Eye2 vs Tahoe from the 2+ year 10% strain 0.3 mm/s Group.
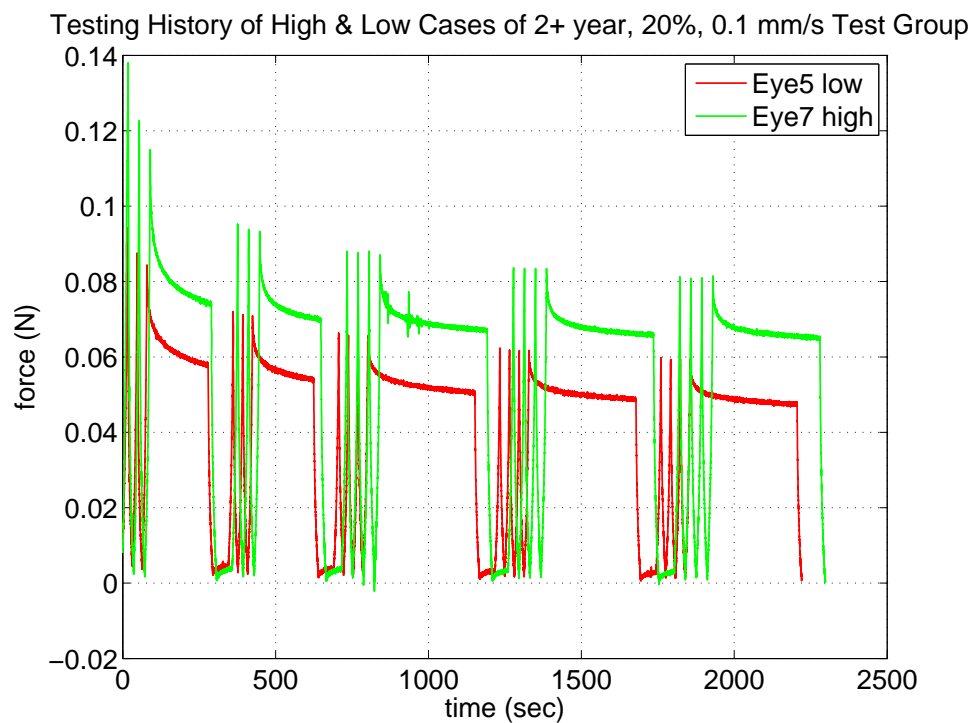
Figure 3.20: Graph of Eye5 and Eye7 from the 2+ year 20% strain 0.1 mm/s Group.
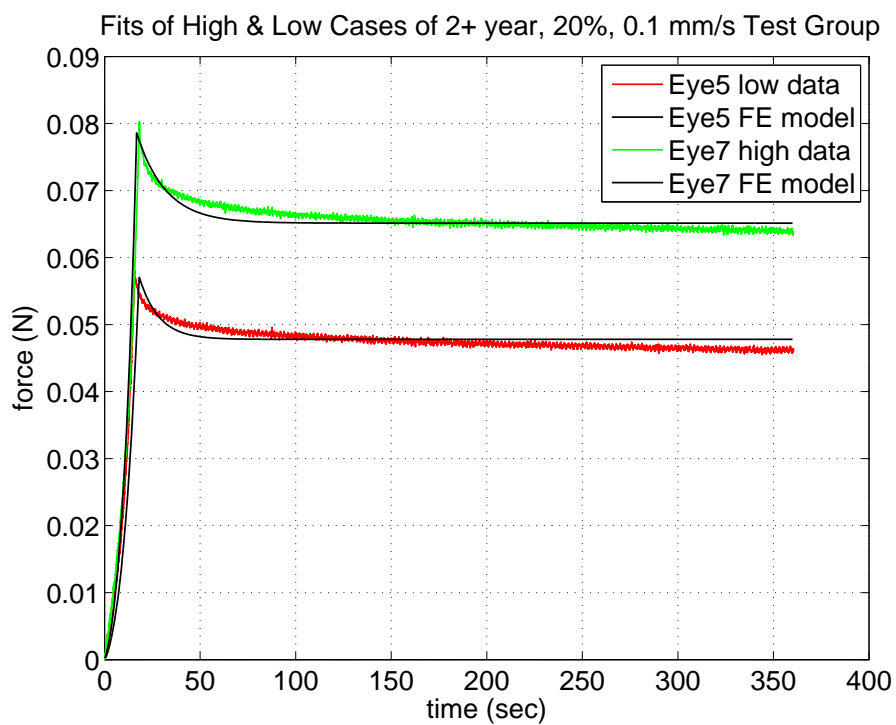
Figure 3.21: Graph of Eye5 and Eye7 vs Tahoe from the 2+ year 20% strain 0.1 mm/s Group.
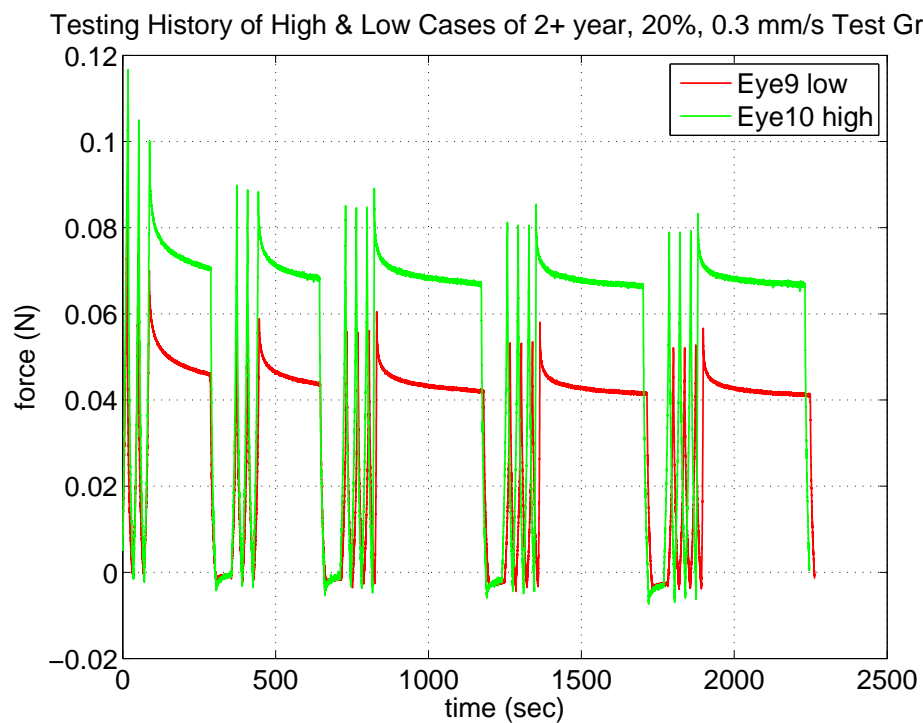
Figure 3.22: Graph of Eye9 and Eye10 from the 2+ year 20% strain 0.3 mm/s Group.
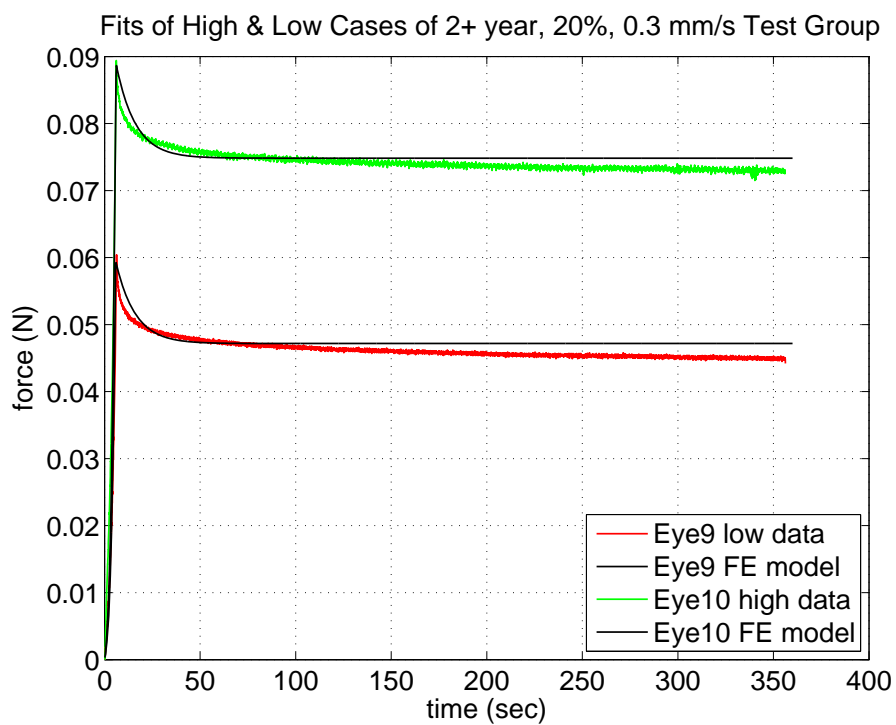
Figure 3.23: Graph of Eye9 and Eye10 vs Tahoe from the 2+ year 20% strain 0.3 mm/s Group.
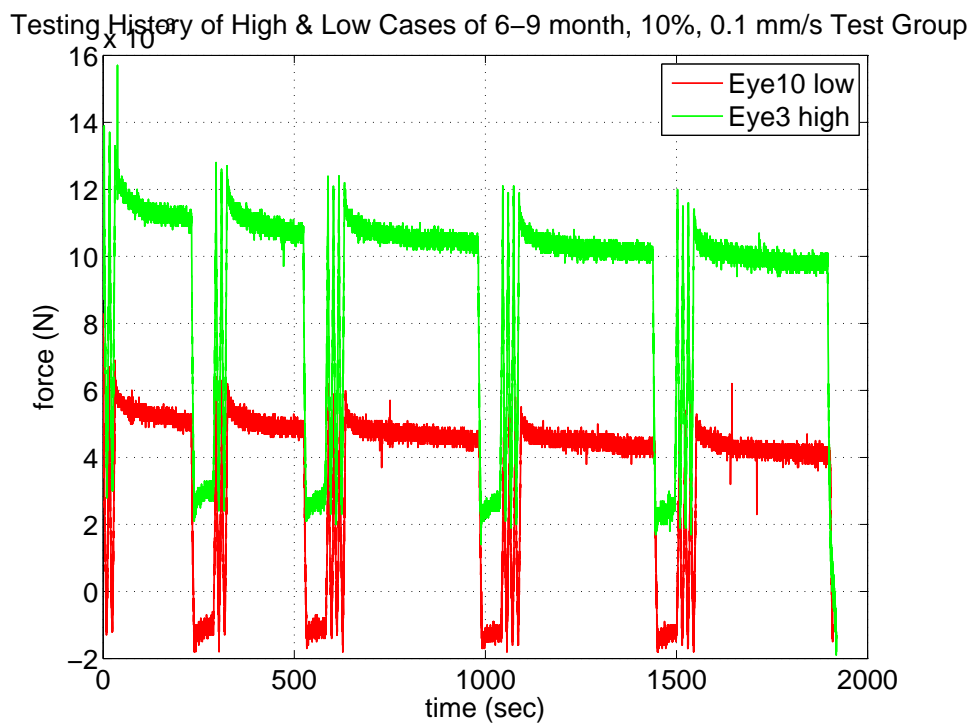
Figure 3.24: Graph of Eye10 and Eye3 from the6-9 month 10% strain 0.1 mm/s Group.
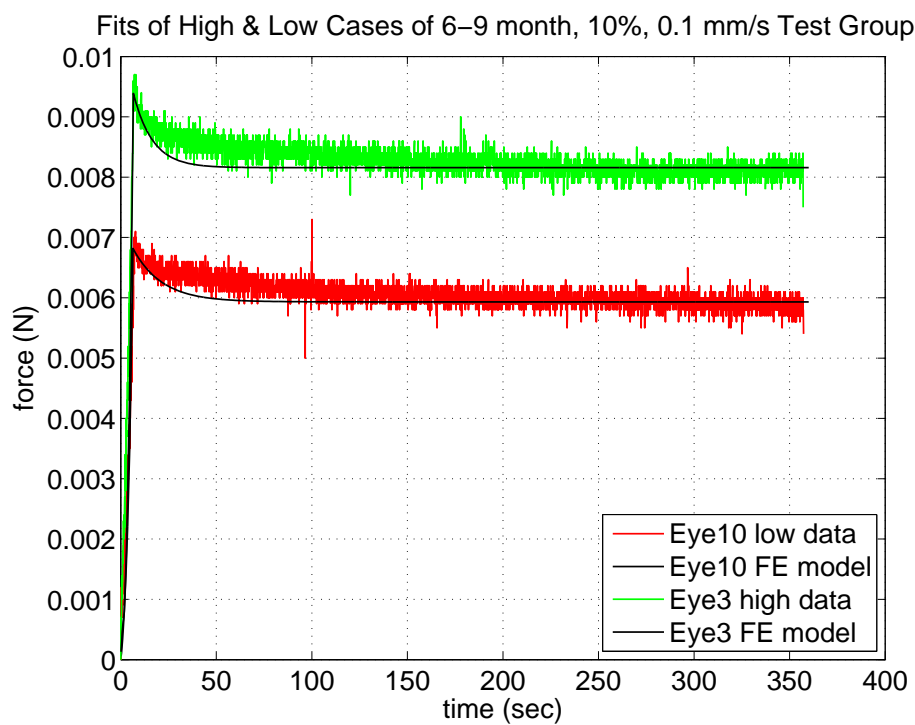
Figure 3.25: Graph of Eye10 and Eye3 vs Tahoe from the 6-9 month 10% strain 0.1 mm/s Group.
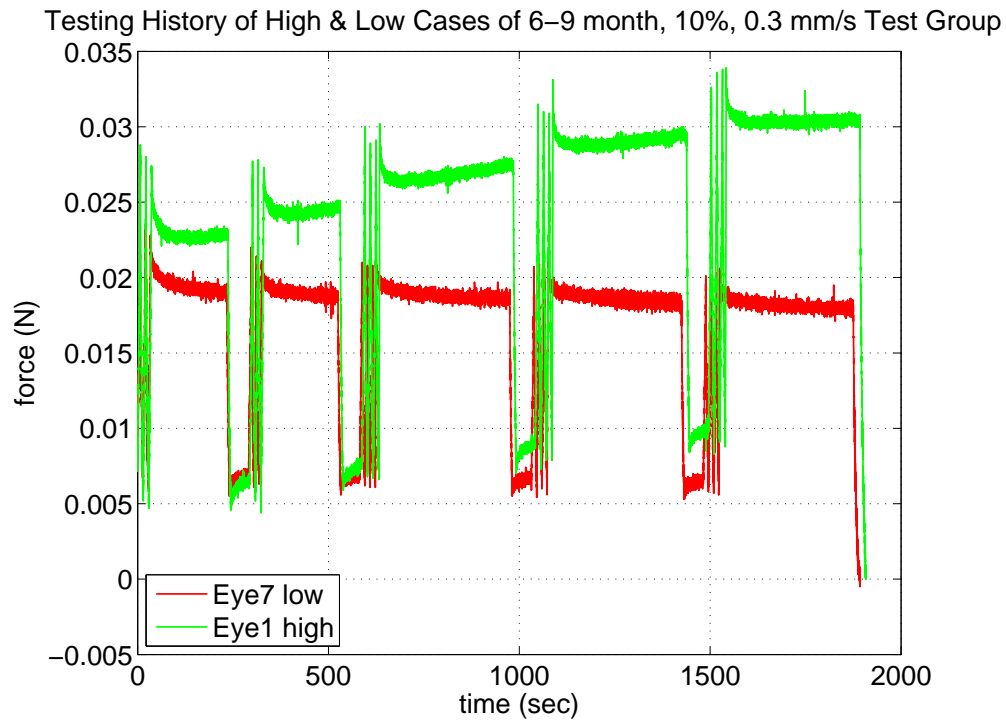
Figure 3.26: Graph of Eye7 and Eye1 from the6-9 month 10% strain 0.3 mm/s Group.
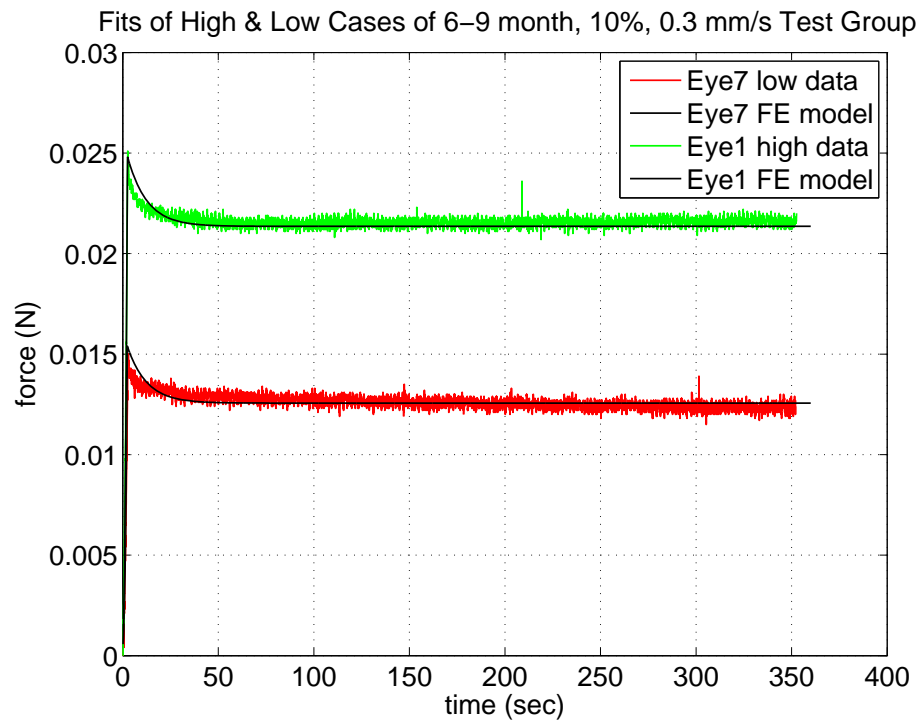
Figure 3.27: Graph of Eye7 and Eye1 vs Tahoe from the 6-9 month 10% strain 0.3 mm/s Group.
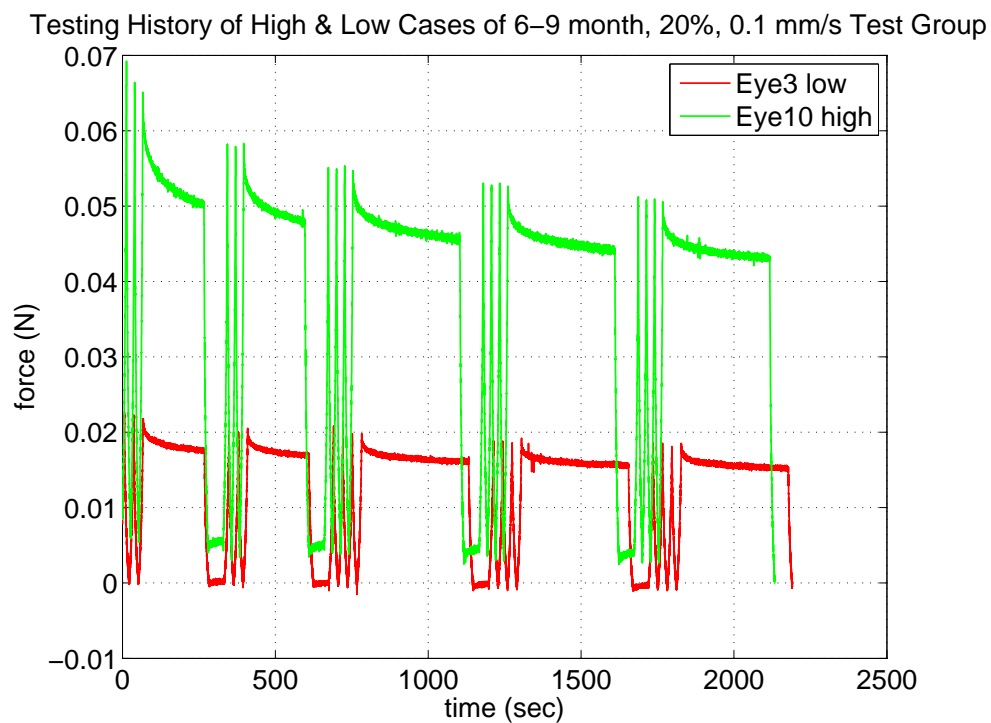
Figure 3.28: Graph of Eye3 and Eye10 from the6-9 month 20% strain 0.1 mm/s Group.
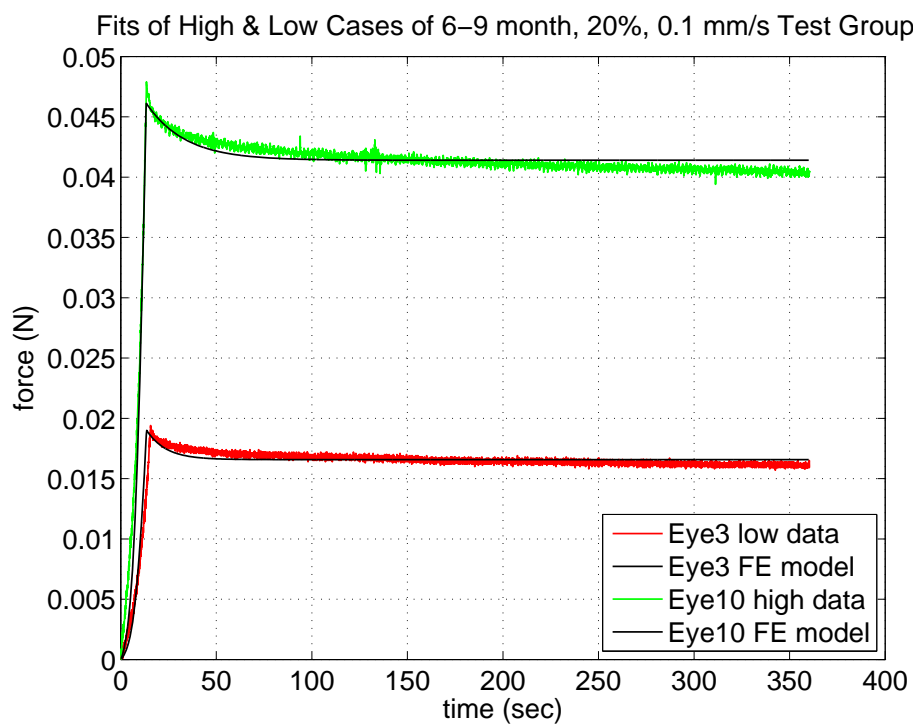
Figure 3.29: Graph of Eye3 and Eye10 vs Tahoe from the 6-9 month 20% strain 0.1 mm/s Group.
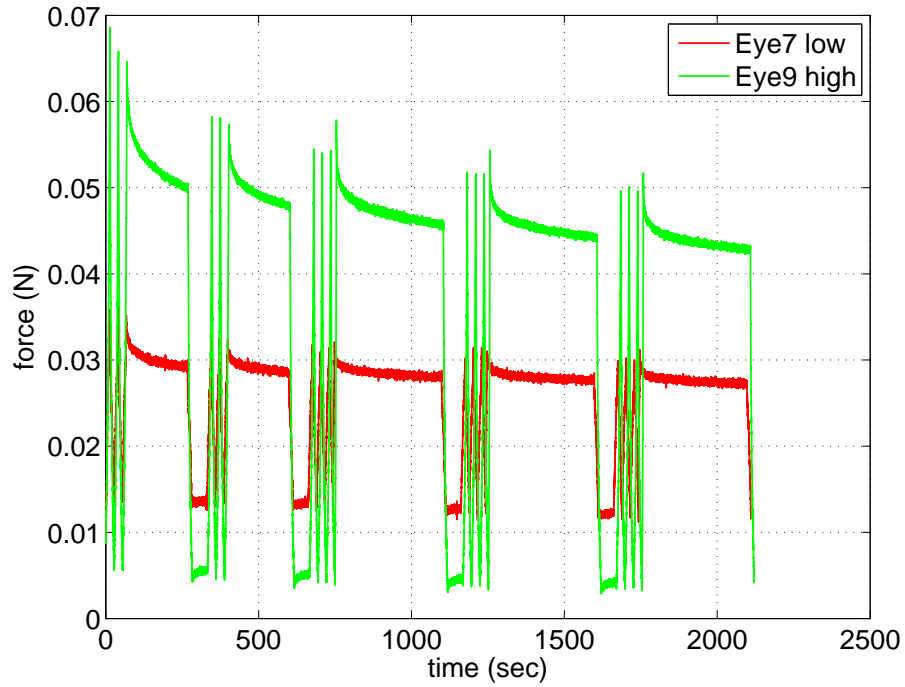
Figure 3.30: Graph of Eye7 and Eye9 from the 6-9 month 20% strain 0.3 mm/s Group.
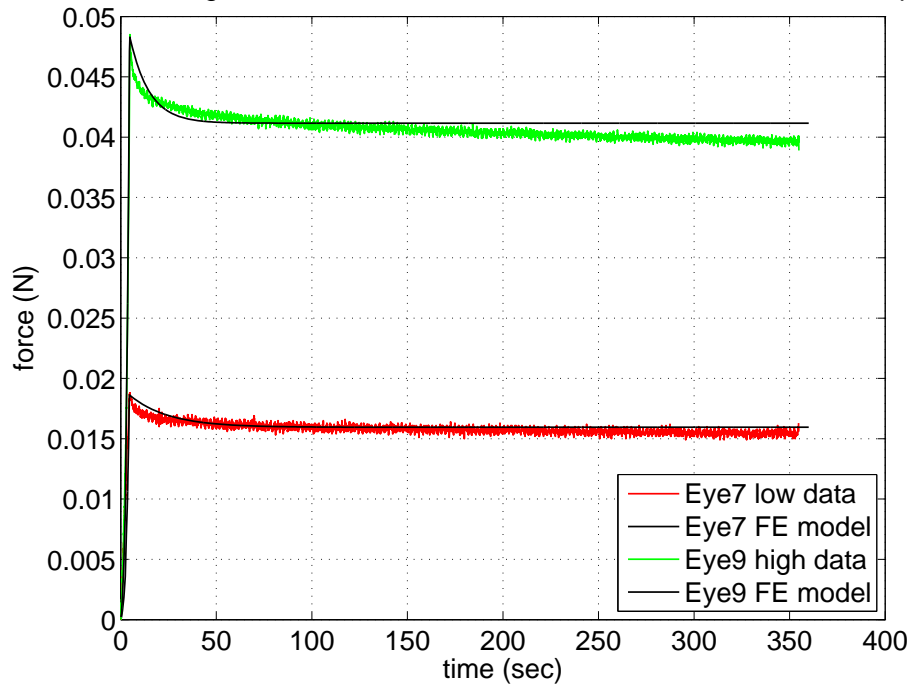
Figure 3.31: Graph of Eye7 and Eye9 vs Tahoe from the 6-9 month 20% strain 0.3 mm/s Group.

Below are graphs of the whole porcine ocular lenses tested in unconfined compression without preconditioning. Reviewing the test data, noise is apparent during some of the tests. The cause of this is unknown and another set of tests are currently being run to see if the noise still exists or not. These data are currently being fitted.
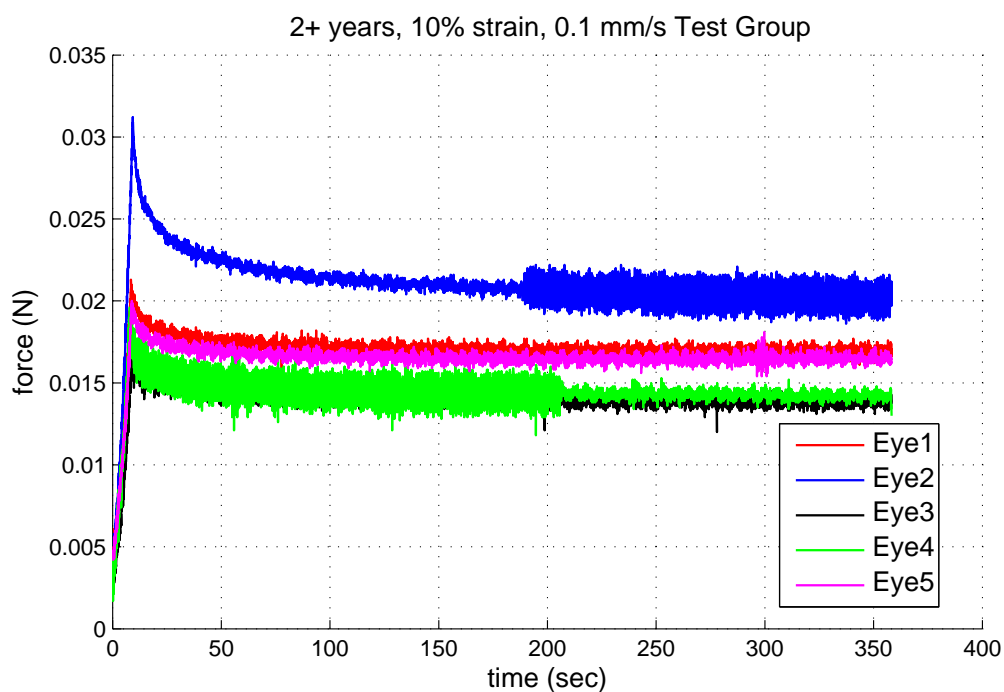
Figure 3.32: Graph of all eyes from the 2+ year 10% strain 0.1 mm/s with no Preconditioning Group.
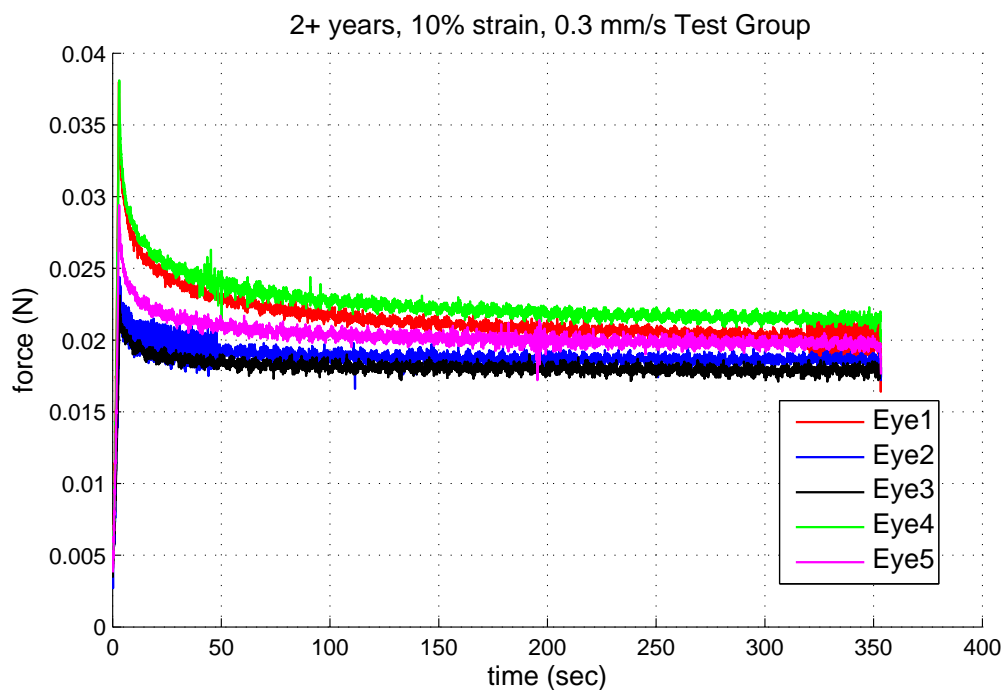
Figure 3.33: Graph of all eyes from the 2+ year 10% strain 0.3 mm/s with no Preconditioning Group.
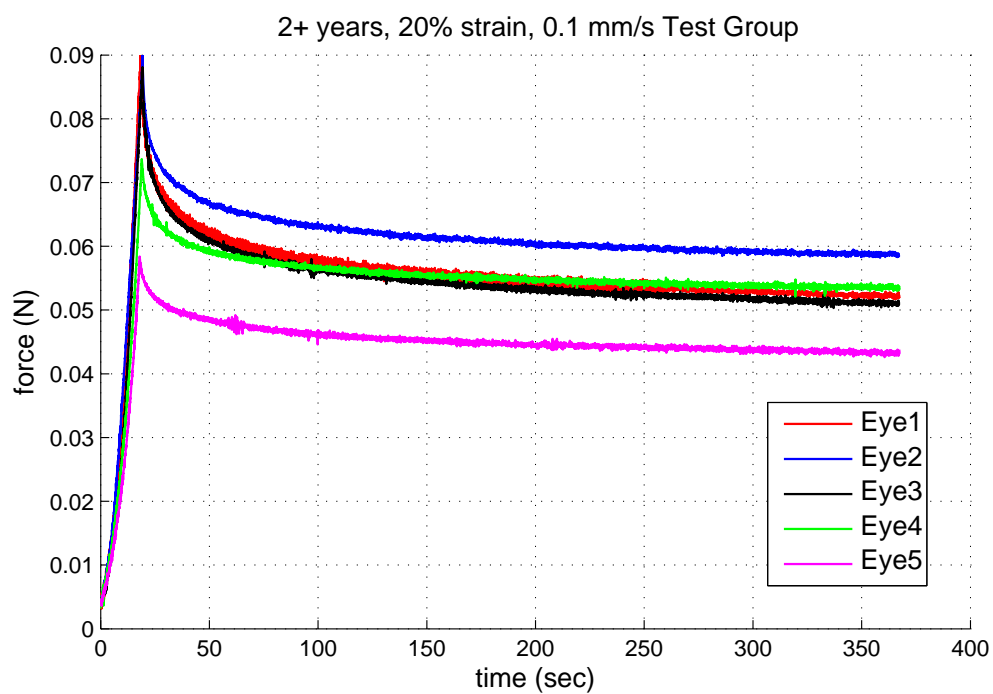
Figure 3.34: Graph of all eyes from the 2+ year 20% strain 0.1 mm/s with no Preconditioning Group.
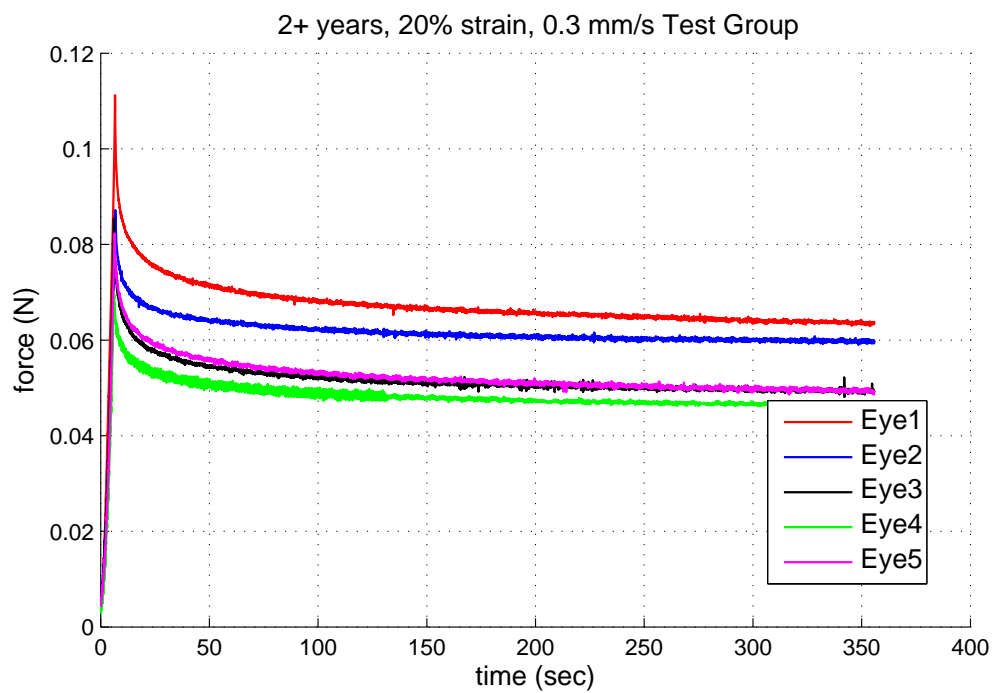
Figure 3.35: Graph of all eyes from the 2+ year 20% strain 0.3 mm/s with no Preconditioning Group.
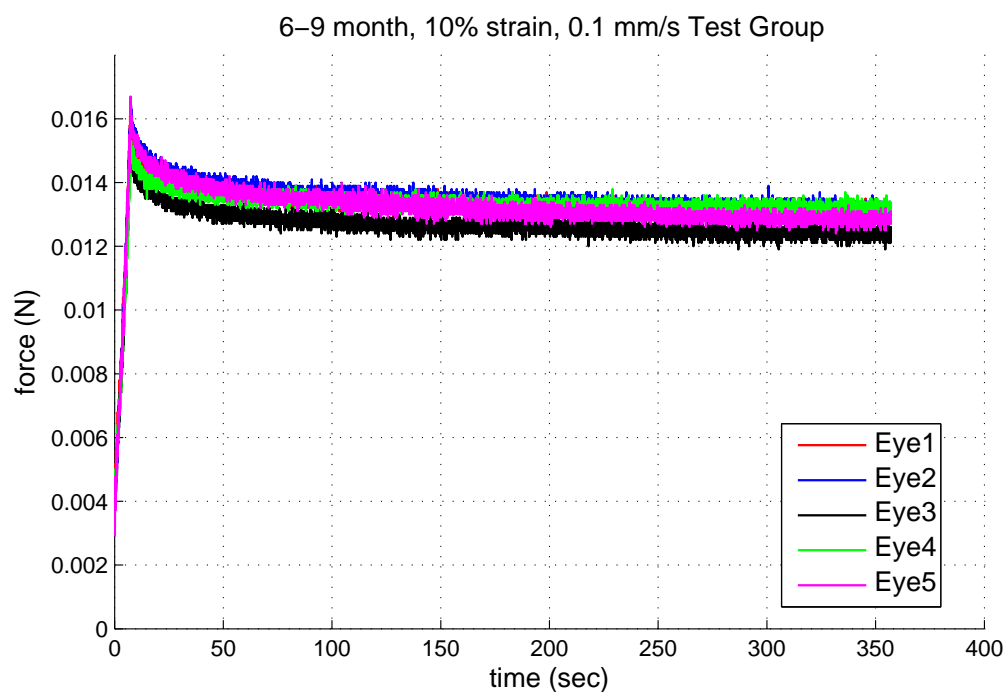
Figure 3.36: Graph of all eyes from the 6-9 month 10% strain 0.1 mm/s with no Preconditioning Group.
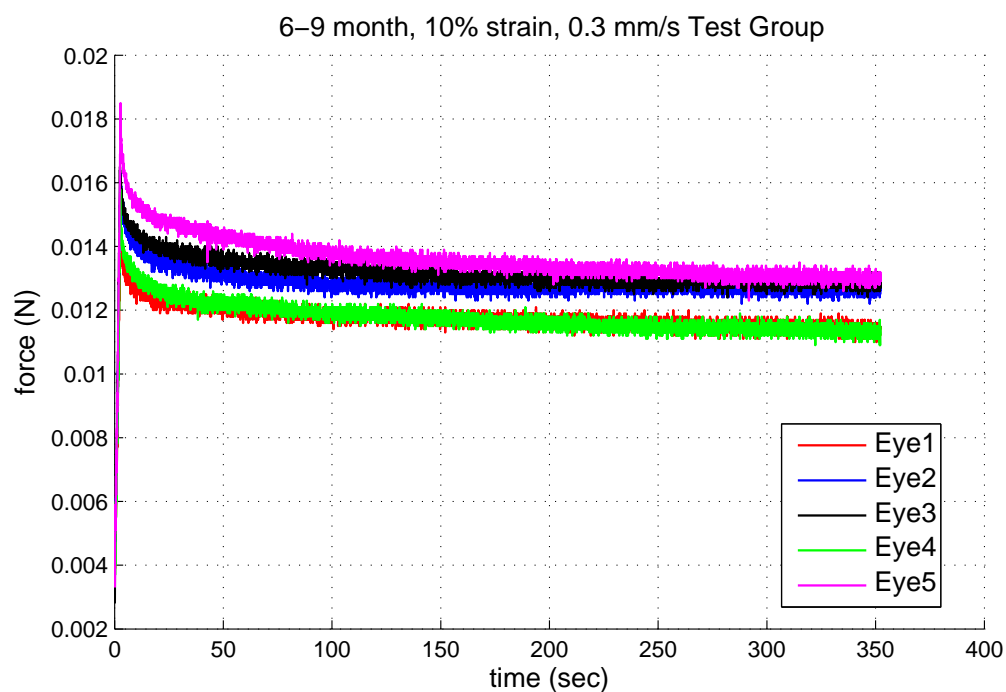
Figure 3.37: Graph of all eyes from the 6-9 month 10% strain 0.3 mm/s with no Preconditioning Group.
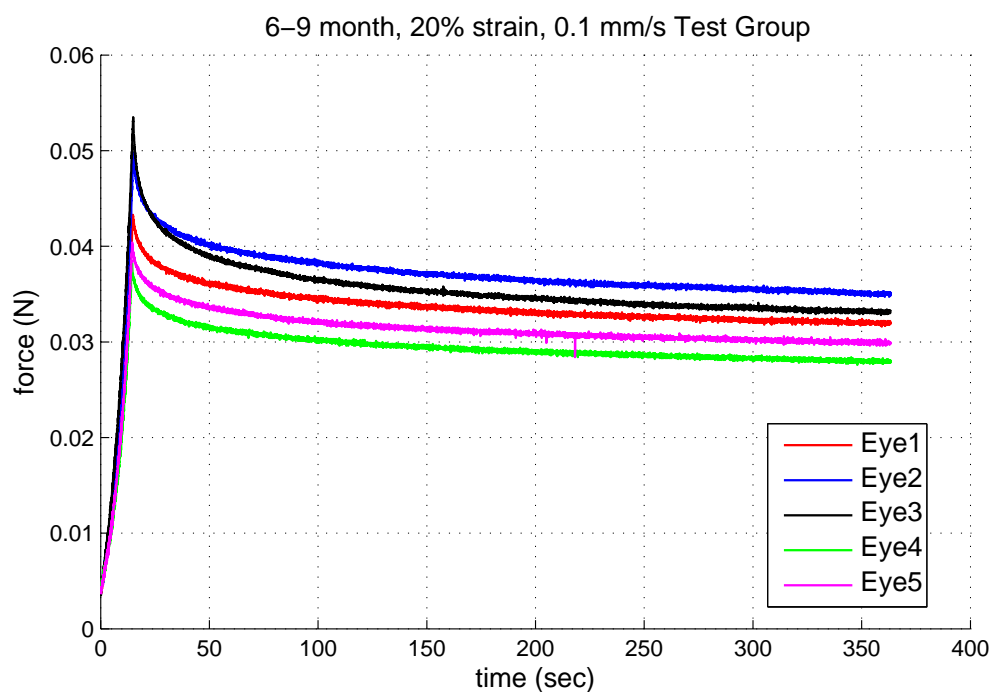
Figure 3.38: Graph of all eyes from the 6-9 month 20% strain 0.1 mm/s with no Preconditioning Group.
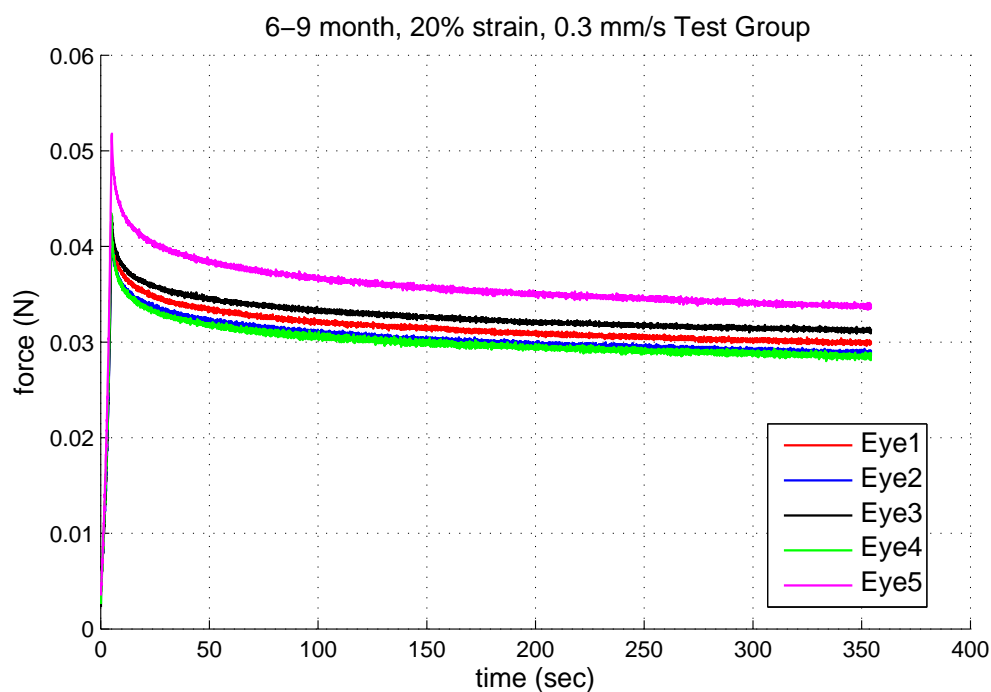
Figure 3.39: Graph of all eyes from the 6-9 month 20% strain 0.3 mm/s with no Preconditioning Group.

3.7   Discussion

As can be seen in the overall testing history for each lens that was fitted, the preconditioning resulted in a lower force in the last loading curve, with the exception of the high load curve for the 6-9 month, 10% strain, 0.3 mm/s loading rate test group. As for why the lens force became greater after more cycles, we are unsure. The viscoelasticity of the whole porcine ocular lens can also be seen in the testing history of each lens, showing a relaxation in the force over the hold time after each loading. This supports our reasoning that viscoelastic properties of the lens need to be included in ocular lens computational models as opposed to assuming the tissue is purely elastic or that the viscoelastic forces are negligible.

For each test group from the first round of testing, approximate fits were achieved. In order to get better fits for the initial drop of the curve, adjustments will need to be made to the constitutive model within Tahoe. The average parameters for the two different age test groups were calculated and are shown below. Table 3.3 shows the average values for the test group of tissue aged 2 years or more. Table 3.4 shows the average values for the test group of tissue aged 6-9 months. While these fits are just preliminary and not enough to determine significantly accurate material properties, it can be seen between the two age groups' viscosities that the older test group lenses are more viscous. This complies with the theory that the lens stiffens as we age, resulting in the loss of accommodation seen in presbyopia.

Table 3.3: Average Parameters Fitted of Tissue 2 Years or Older

	τ (s)	μ_{EQ} (MPa)	μ_{NEQ} (MPa)	κ_{EQ} (MPa)	κ_{NEQ} (MPa)	η_{D} (MPa.s)	η_{V} (MPa.s)
Capsule	11.1	0.84	0.29	84.0	29.4	3.27	327
Substance	11.1	8.4e-5	2.94e-5	0.084	0.0294	3.27e-4	0.327

Reviewing the no-preconditioning test groups, no immediate trend or difference can be seen between the test groups with preconditioning. It seems the force values of the no-preconditioning group generally fall within the range seen in the preconditioning test group. More data is needed to determine a difference in forces. It will be interesting to see the difference in material properties

Table 3.4: Average Parameters Fitted of Tissue 6-9 Months Old

	τ (s)	μ_{EQ} (MPa)	μ_{NEQ} (MPa)	κ_{EQ} (MPa)	κ_{NEQ} (MPa)	η_{D} (MPa.s)	η_{V} (MPa.s)
Capsule	13.1	0.71	0.135	71.0	13.5	1.77	177
Substance	13.1	7.1e-5	1.35e-5	0.071	0.0135	1.77e-4	0.177

when the fits are completed for the no-preconditioning test groups.

Some preliminary modeling of the unconfined compression of the whole porcine ocular lens has been completed in Abaqus. Figures 3.40, 3.41, and 3.42 show the various stages of the Abaqus simulation of Lens 3 (high load case) of the 2+ year, 10% strain, 0.1 mm/s loading rate test group. Figure 3.40 shows the beginning of the simulation, with the lens positioned with the anterior surface downward, the fixed platen at the bottom representing the testing pedestal, and the load platen at the top. In Figure 3.41 we can see the lens flattening against both the load platen and bottom surface and the stress in the lens capsule along the top and bottom surfaces of the lens. This image shows the simulation at the point where the lens has been deformed to the defined strain of 10%. When comparing Figure 3.42 at the end of the simulation to Figure 3.41 at the height of the force, the stress relaxation can be noticed in the lens capsule. Comparing Figure 3.43 and Figure 3.44 the relaxation of the stress in the lens fiber cells can be seen. The maximum stresses in the lens fiber cells can be seen located near the contact point of the platen. Figure 3.45 shows an overlay of the Abaqus model with an image of the compressed lens. The compressed model appears to match well with the actual compressed lens.
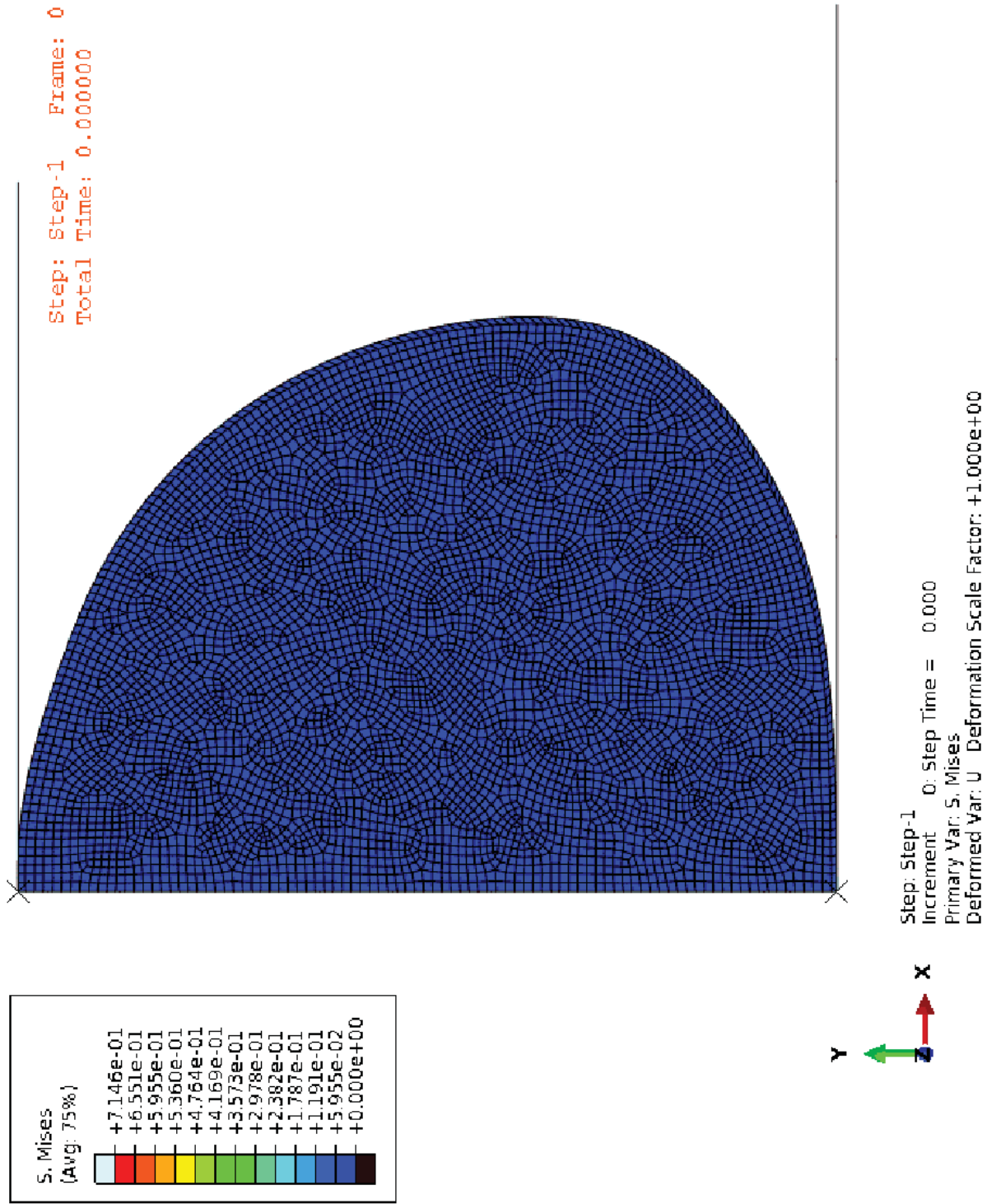
Figure 3.40: Simulation of Unconfined Compression on Whole Porcine Ocular Lens - Beginning of simulation.
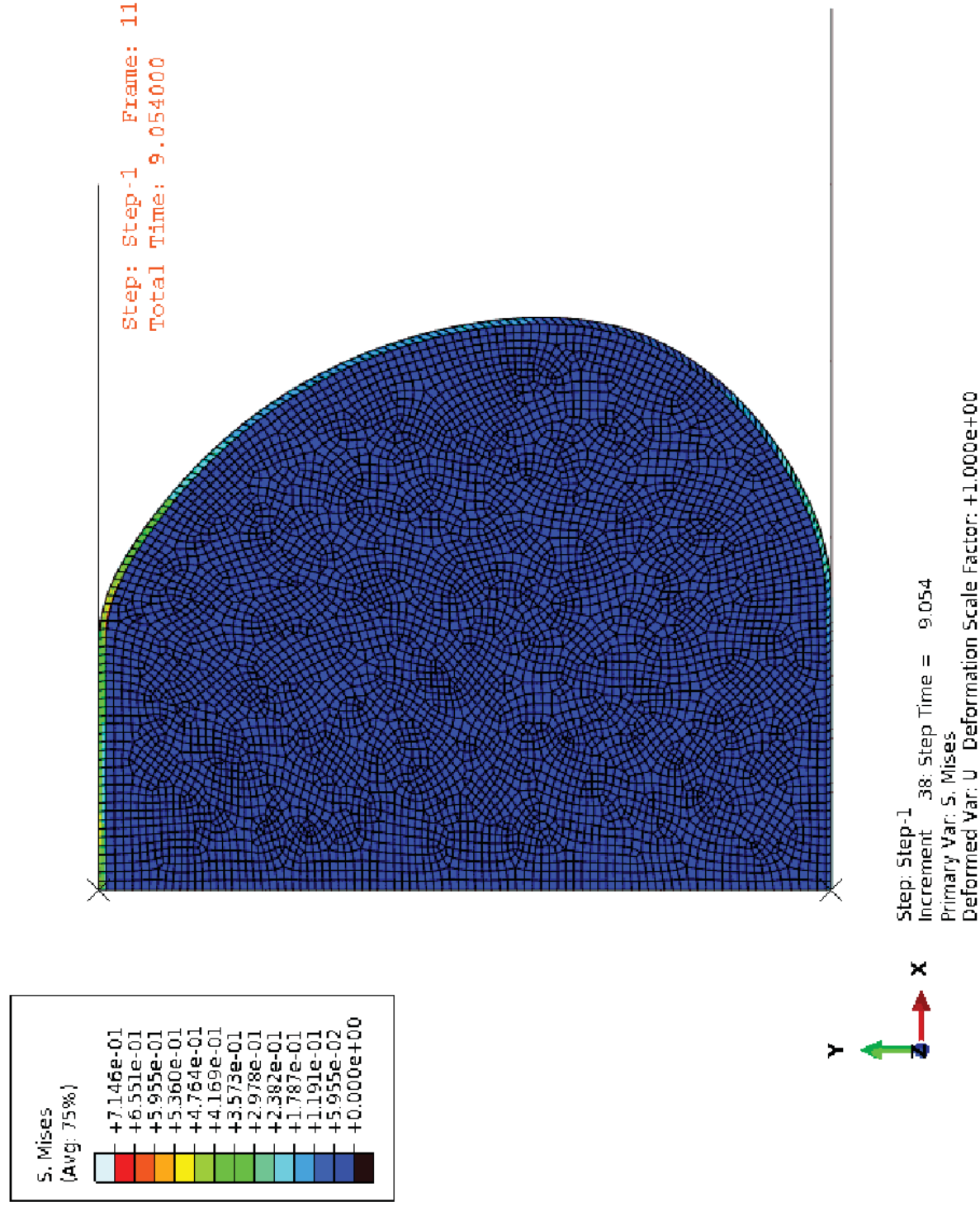
Figure 3.41: Abaqus Simulation of Unconfined Compression on Whole Porcine Ocular Lens - Full loading has been reached; can see stress in the capsule along the top and bottom.
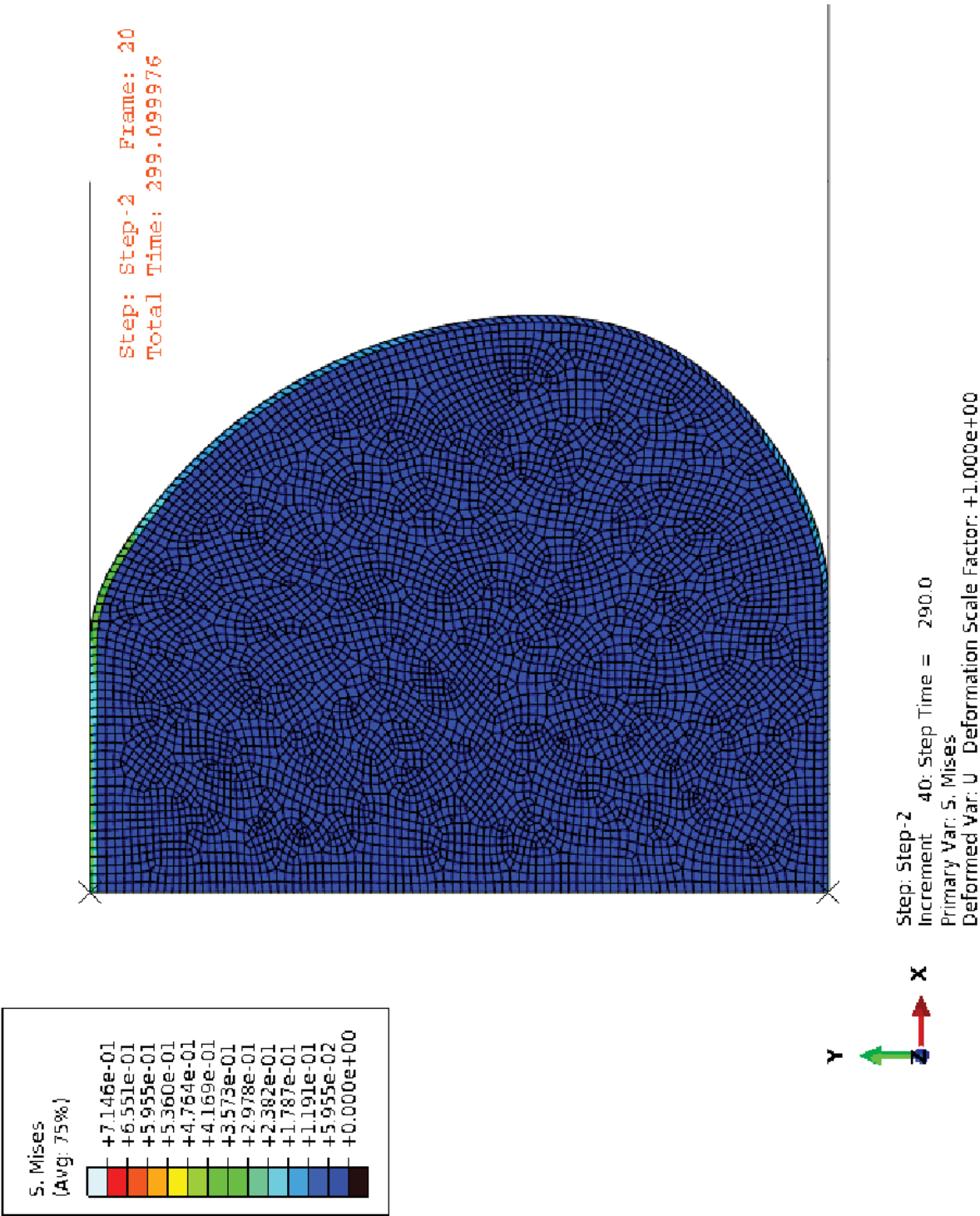
Figure 3.42: Abaqus Simulation of Unconfined Compression on Whole Porcine Ocular Lens - End of simulation; stress has gradually relaxed in capsule.

Figure 3.43: Scaled contour of the Abaqus simulation showing the maximum stressed state of the lens fiber cells.
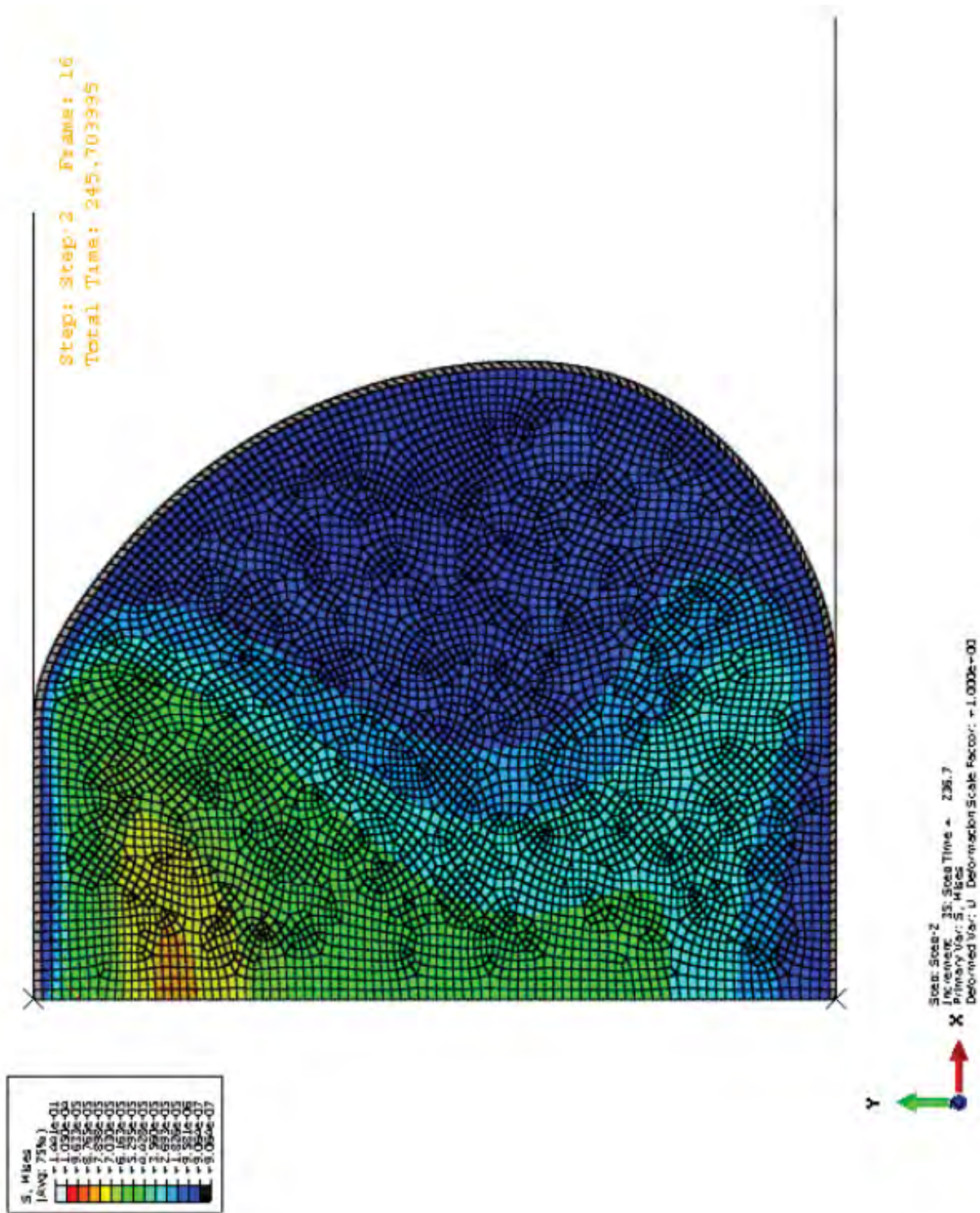
Figure 3.44: Scaled contour of the Abaqus simulation showing the stressed state of the lens fiber cells at the end of the simulation.
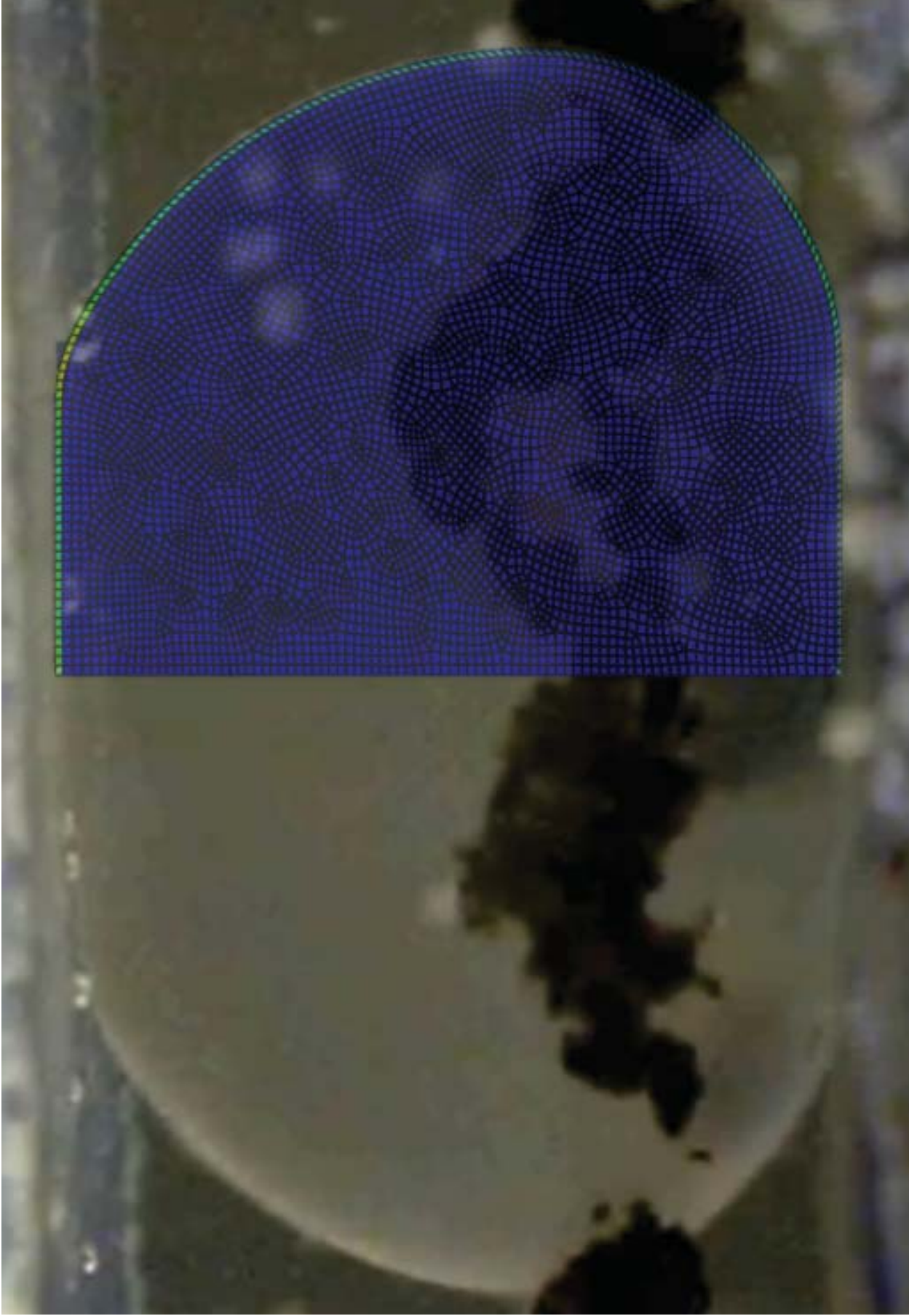
Figure 3.45: Overlay of the Abaqus simulation with an image of the compressed lens.

Figure 3.46 compares the theoretical data produced from Tahoe using the fitted parameters and the theoretical data produced by the simulation within Abaqus. In order to get the 2 sets of data to match, the material properties for Abaqus had to be slightly adjusted. This is likely due to the differences in constitutive governing equations used between the model implemented in Tahoe and the model in Abaqus. The Abaqus model properties were setup as isotropic viscoelastic. The 2 sets of parameters are shown below in Table 3.5. The difference in parameters are small and the data matching between the two simulations is encouraging towards the ends of determine the viscoelastic properties of the whole porcine ocular lens.
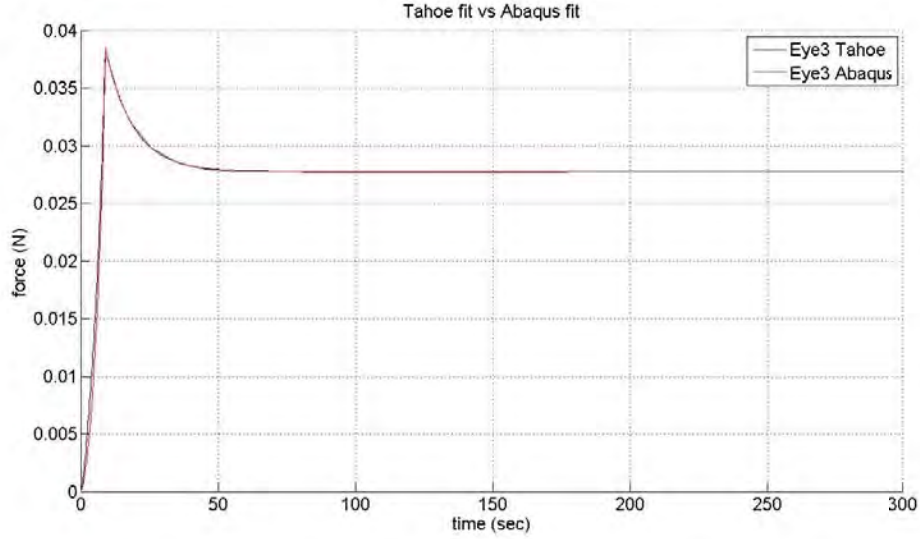
Figure 3.46: Graph of Data Produced From Tahoe Simulation and Abaqus Simulation

Table 3.5: Tahoe Parameters vs Abaqus Parameters

	τ (s)	μ_{EQ} (MPa)	μ_{NEQ} (MPa)	κ_{EQ} (MPa)	κ_{NEQ} (MPa)
Capsule (Tahoe)	10	1.275	0.65	127.5	65
Capsule (Abaqus)	10	1.479	0.49	147.9	49
Substance (Tahoe)	10	7.1e-5	1.35e-5	0.071	0.0135
Substance (Abaqus)	10	1.479e-4	4.9e-5	0.1479	0.049

Chapter 4

Puncture Testing of the Whole Lens

Puncture testing was completed to provide data that would be useful in modeling the interaction between the ocular lens and intraocular foreign bodies (IOFBs). This data will also allow for the calculation of material properties (similar to the method described in the Parameter Fitting of Unconfined Compression Testing Data Chapter at large deformations). Additionally, using the puncture testing protocol, tissue will be fixed and imaged using confocal LASER scanning microscopy to study the deformation/damage of the lens fibers after loading/puncture. Whole porcine ocular lenses were loaded past puncture using a MTS Insight II electromechanical testing system with 6 different puncture tip geometries, described below. The tests were recorded to gain information of the gross deformation of the lens under puncture. Force and displacement were recorded and the data were exported for future analysis and modeling. Preliminary modeling was done using Abaqus (www.simulia.com), described in more detail below.

4.1   Sample Preparation

Whole porcine globes were shipped on wet ice from Animal Technologies, Inc. in Tyler, TX. Tissue came from one age group: pigs aged 2 or more years. For puncture testing, the whole ocular lens was removed by excising the cornea and cutting through the iris and zonules. This was done by making a small incision with a diamond-head blade at the edge of the cornea and using curved microsurgery scissors to cut around the cornea. The same process is used to cut through the zonules. Excess zonules were removed by rolling the lens along its equator on tissue paper. Excess

vitreous was also removed by rolling the lens end over end on tissue paper and trimming away the vitreous that stuck to the paper. Lens were then placed in Alcon Laboratories, Inc. Balanced Salt Solution (BSS) for transport to the MTS Insight II for testing.

4.2   Experimental Setup

All puncture tests were completed on a MTS Insight II Electromechanical testing system. The Insight II is screw-driven machine. The tests utilized a 2N load cell (sensitivity: 2.04 mv/V) to measure the small force response of the ocular lens (see Figure 4.1). The puncture tip was connected to the load cell by a piece of polycarbonate designed so that tips could be interchanged (see Figure 4.1). Lenses were loaded and punctured with six different puncture geometries: 1) a 1 mm diameter cylindrical tip, 2) a 2 mm diameter cylindrical tip, 3) a 1 mm diameter spherical tip, 4) a 2 mm diameter spherical tip, 5) a 30 degree conical tip, 6)and a 45 degree conical tip. The geometries and dimensions can be seen in Figure 4.2.

Table 4.1: Testing Configurations and Number of Lenses Tested

Tip Geometry (d,Θ)	Loading Rate (mm/s)	Anterior Surface	Posterior Surface
1mm spherical	0.5	5	5
2mm spherical	0.5	5	5
1mm cylindrical	0.5	5	5
2mm cylindrical	0.5	5	5
30 deg conical	0.5	5	5
45 deg conical	0.5	5	5

The ocular lenses were tested at a single loading rate of 0.5 mm/s to 80% nominal axial strain. Test groups and samples per group can be seen in Table 4.1. All tests were performed in Alcon BSS. The overall test setup can be seen in Figure 4.3. The lens was placed in the Alcon BSS in a testing pedestal. The testing pedestal was situated inside of a water bath contained by an environmental testing chamber. The water bath was heated to 37 ℃. The lenses were imaged before testing and recorded during testing using an Aven Hand-Held Digital Microscope
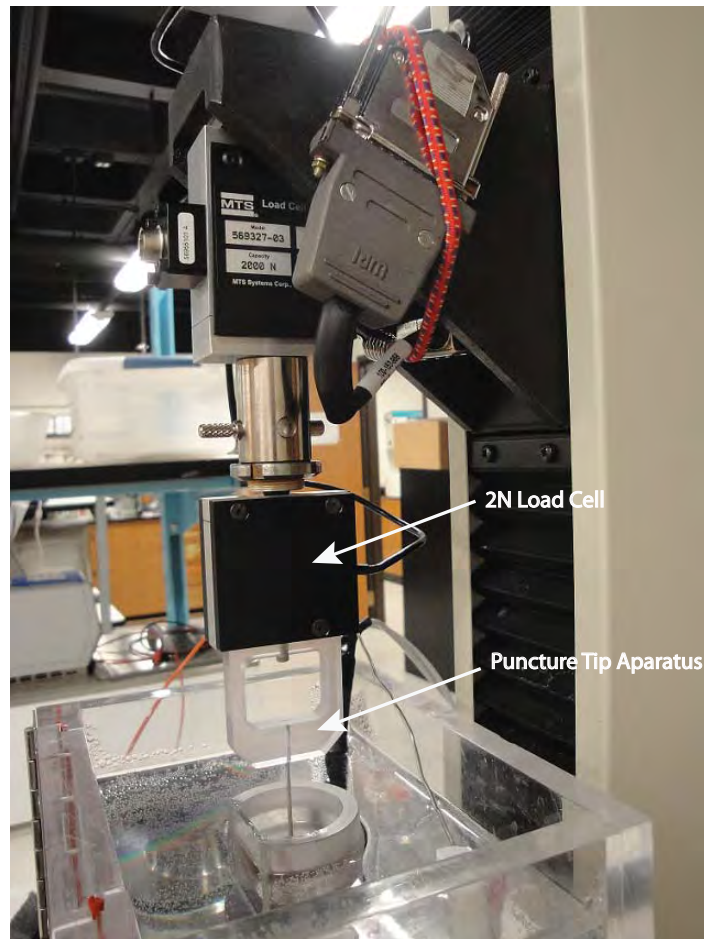
Figure 4.1: 2N Load Cell and Puncture Tip Apparatus Attached to MTS Insight II.
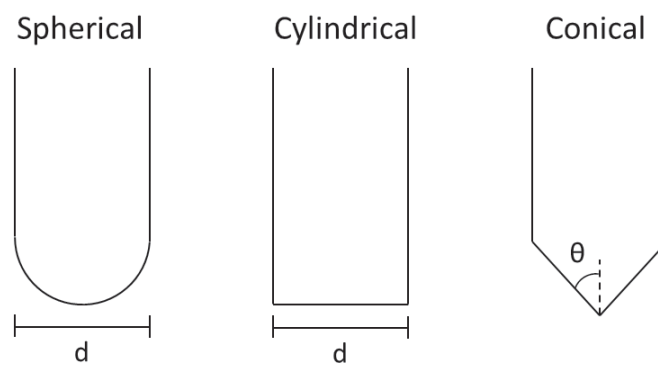
Figure 4.2: Puncture Loading Tip Geometries with Various Diameters d and Angles Θ.
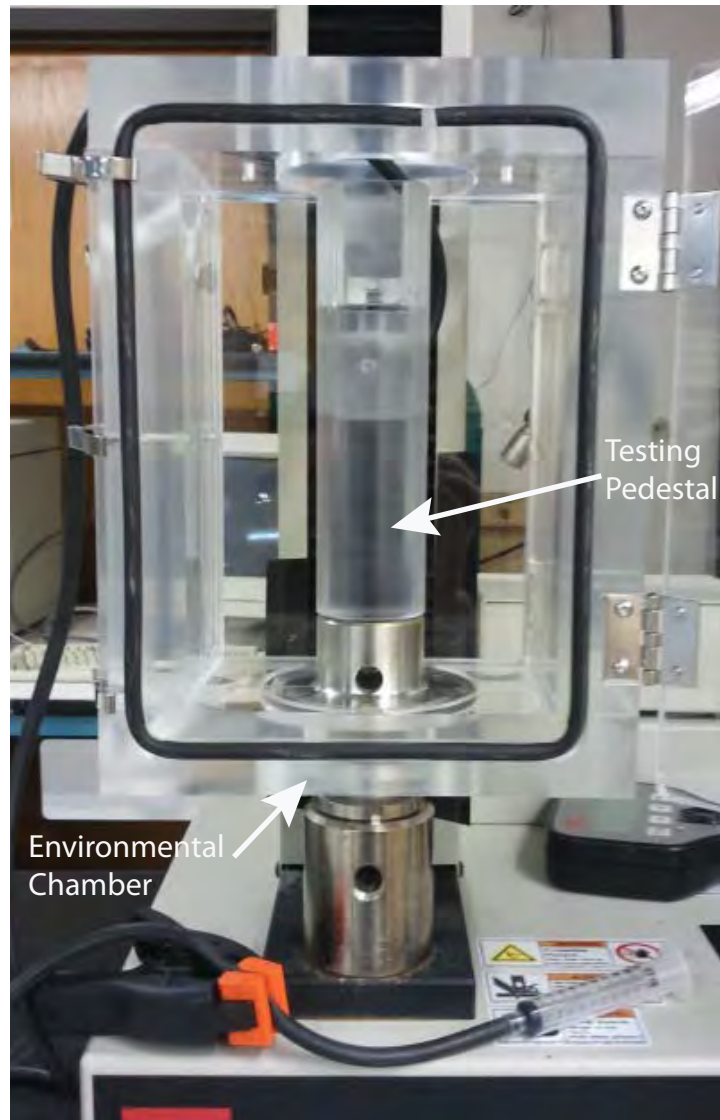
Figure 4.3: Environmental Chamber with Testing Pedestal Placed Inside.

(1.3 Megapixel)(see Figure4.4). For posterior tests, the lens was centered in the pedestal and rested freely on it's anterior surface. For anterior tests, it was required to manufacture a well to hold the lens with the anterior surface pointed up (see Figure 4.5).

Figure 4.4: Example of Image Taken Before Each Test to get Geometry Data.

This well was made out of acrylic and made to have the approximate shape of posterior surface of the lens. The software TestWorks 4 (www.mts.com) was used in all of the tests to control the Insight II and collect all the data.

4.3   Experimental Method

A testing program was developed in TestWorks 4 allowing specification of displacement speed, strain to displace to, whether the anterior or posterior surface is being punctured, lens height, test date, test time, any observational notes about the lens pre-test, and how the lens failed post-test. Initially the puncture tip was brought into contact to determine where the testing pedestal or puncture well surface was, for calculating the lens height. The lens was then placed in the testing pedestal reservoir, either anterior surface up (with puncture well) or posterior surface up. The puncture tip was lowered to approximately 1 mm above the lens. The load cell was then zeroed and began approaching the lens. Once the pre-load force of 0.05 N was reached, the program displayed
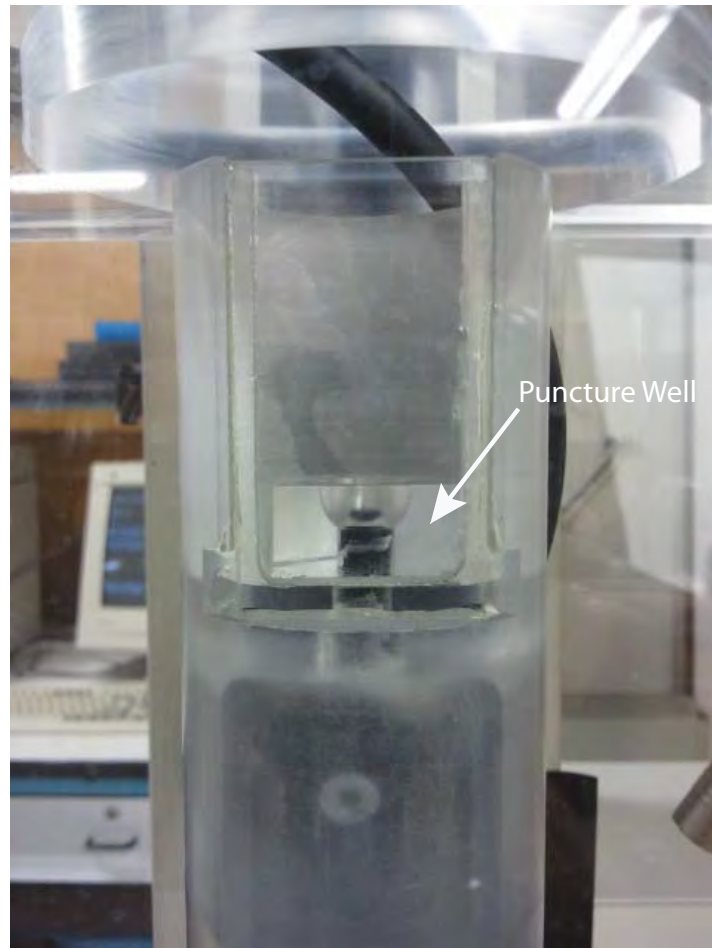
Figure 4.5: Sample Holder inside of Environmental Chamber.

the lens height for the user to record. An image was taken of the lens using the digital microscope before testing. The user then entered all testing information (lens height, displacement speed, strain to displace to, puncture tip being used, surface being punctured, and any observational notes about the lens). Once all information was entered, video recording and the test began, collecting force and displacement data at a rate of 20 Hz. The lens was loaded at the specified testing rate (0.5 mm/s for all tests) to the desired strain (80%). Upon reaching 80%, the machine paused 3 seconds to ensure complete data collection and then the test ended. The user stopped the video recording and then entered how the lens failed (anterior puncture, posterior puncture, side blow-out, other), supplying any additional notes on the test/failure mode. The machine was then retracted and the punctured lens was removed. The Alcon BSS in the pedestal reservoir was removed after 5 consecutive tests in order to provide better imaging conditions. The Alcon BSS was allowed to acclimate to temperature after it was changed.

4.4   Theoretical Modeling

Preliminary modeling was completed in the commercially available modeling software Abaqus (www.simulia.com). A 2-D, axisymmetric simulation was set up based off the geometry of a 2+ year aged porcine ocular lens from the 1 mm spherical posterior test group. The model of the lens was divided into 2 parts: the lens capsule and the interior lens fibers, each with separate material properties. Both sections were modeled using Abaqus' hyperelastic, isotropic, Neo-hookean material, which requires the definition of $g_1 = \mu_{\text{NEQ}} \div \mu_{\text{EQ}}$ (shear modulus ratio), $\kappa_1 = \kappa_{\text{NEQ}} \div \kappa_{\text{EQ}}$ (bulk modulus ratio), τ_1 (relaxation time constant), $C10 = \mu_{\text{EQ}} \div 2$, and $D1 = 2 \div \kappa_{\text{EQ}}$. Average material properties (μ_{EQ}, μ_{NEQ}, κ_{EQ}, κ_{NEQ}, and τ) were calculated from the parameters given from the fitted experimental data from the unconfined compression testing as parameter fitting on the puncture testing data has not been completed. Both sections were meshed with quad elements. The 1 mm spherical puncture tip was modeled as a solid, incompressible surface. Contact was defined as frictionless. The puncture tip was fixed in the U1 = 0 (x) and U3 = 0 (rotational) direction. The lens was fixed at the bottom in the U1 = 0, U2 = 0 (y), and U3 = 0 directions and

at the top in the U2 = 0 and U3 = 0 directions. A boundary condition was set up along the x-axis at the bottom to represent the testing pedestal surface. The simulation was set to run at 0.5 mm/s displacement to 80% strain.

4.5   Results

Below are graphs of each test group, showing the 5 whole ocular lenses in each group.
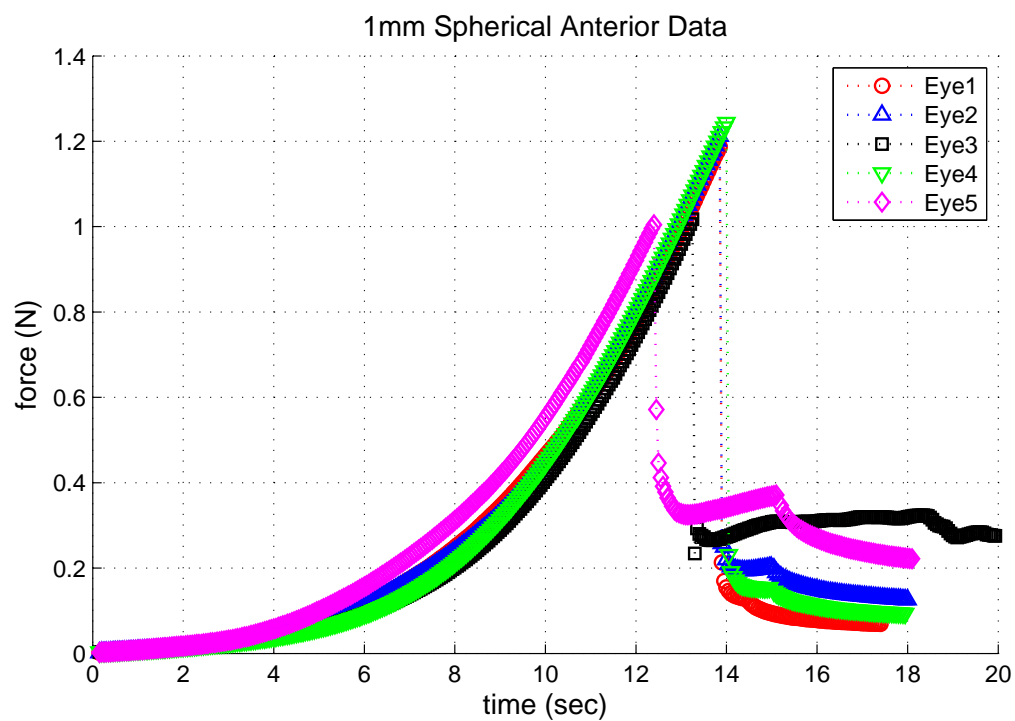
Figure 4.6: Graph of 1 mm Spherical Anterior Data.
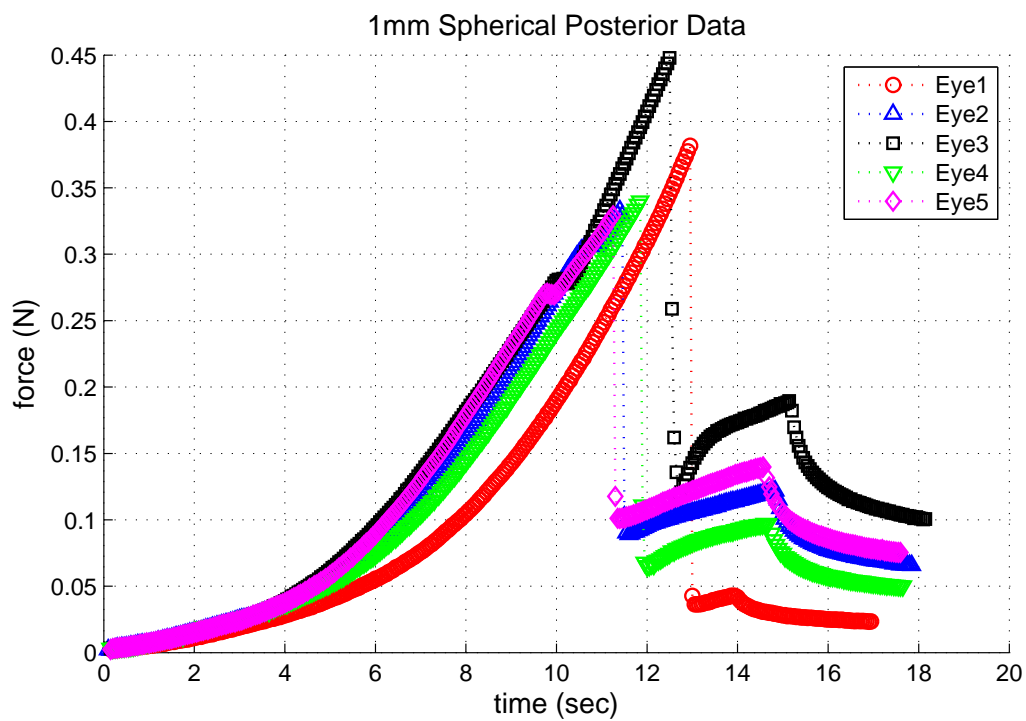
Figure 4.7: Graph of 1 mm Spherical Posterior Data.
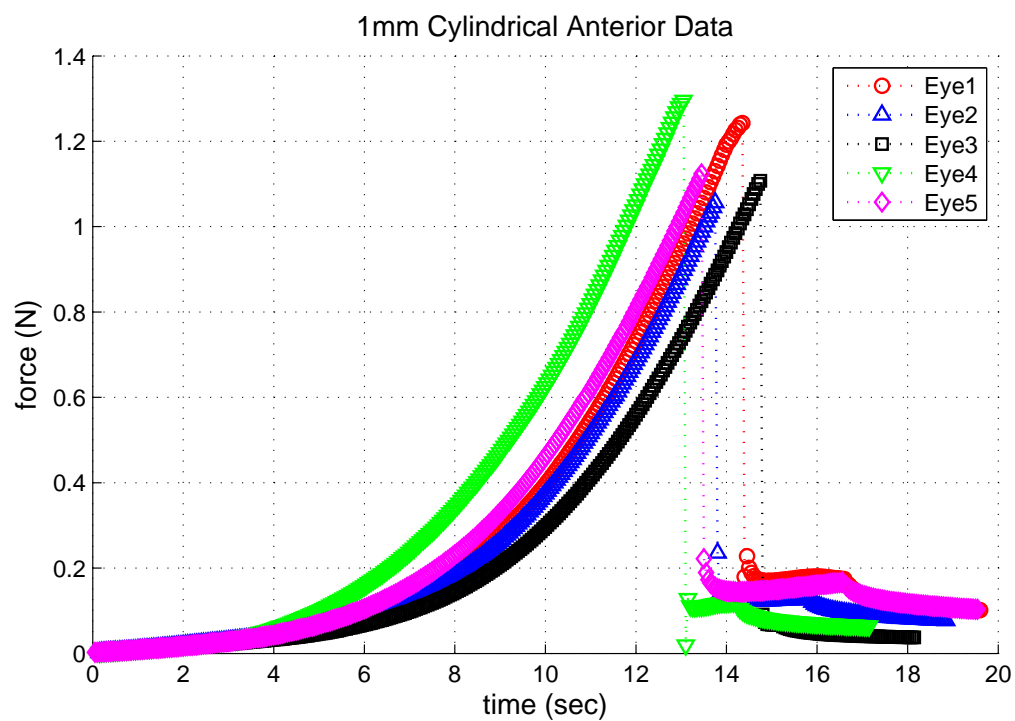
Figure 4.8: Graph of 1 mm Cylindrical Anterior Data.
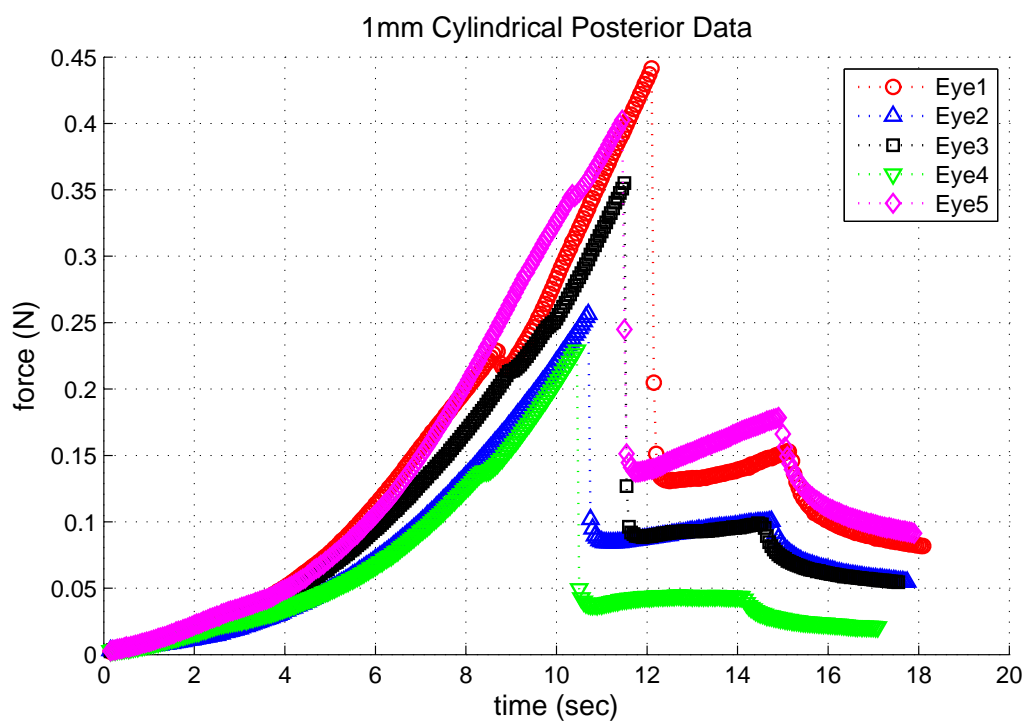
Figure 4.9: Graph of 1 mm Cylindrical Posterior Data.
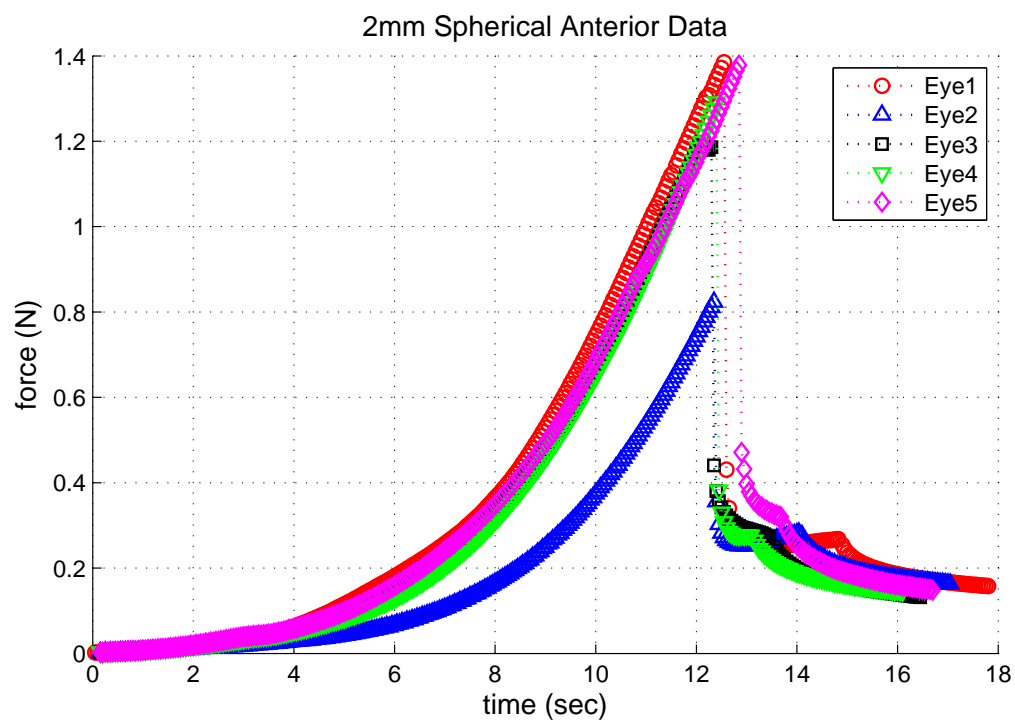
Figure 4.10: Graph of 2 mm Spherical Anterior Data.
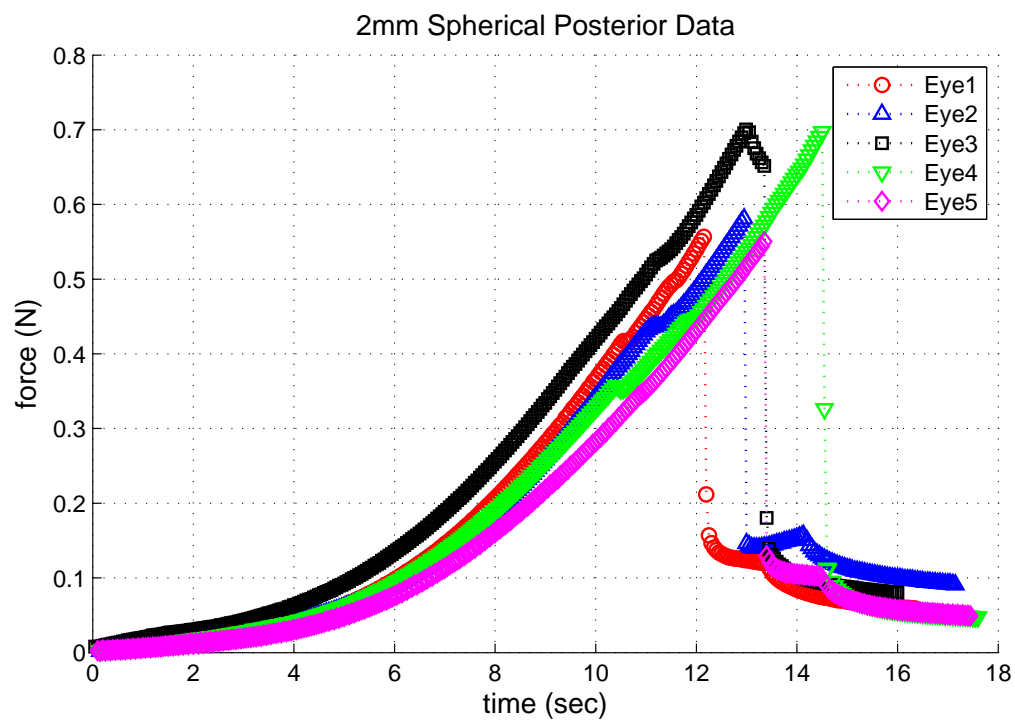
Figure 4.11: Graph of 2 mm Spherical Posterior Data.
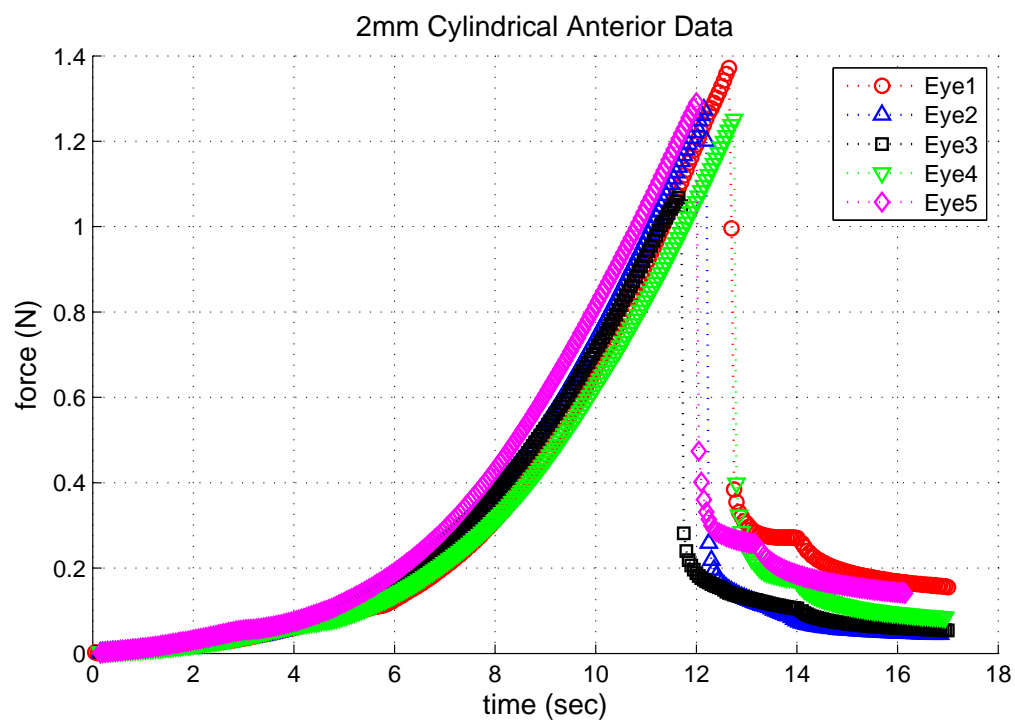
Figure 4.12: Graph of 2 mm Cylindrical Anterior Data.
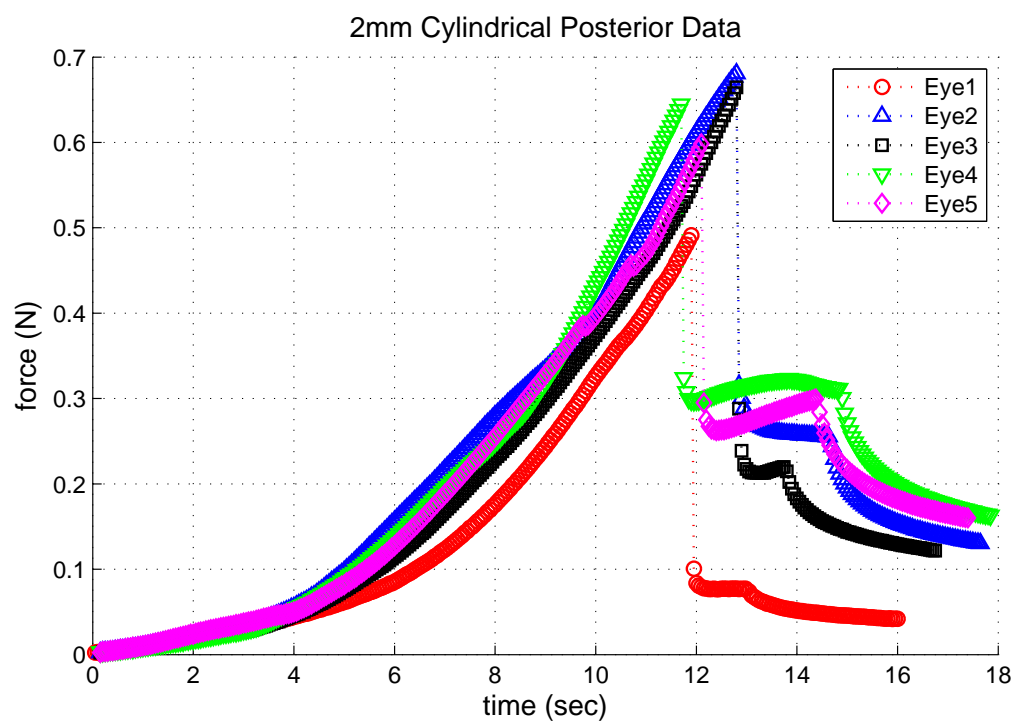
Figure 4.13: Graph of 2 mm Cylindrical Posterior Data.
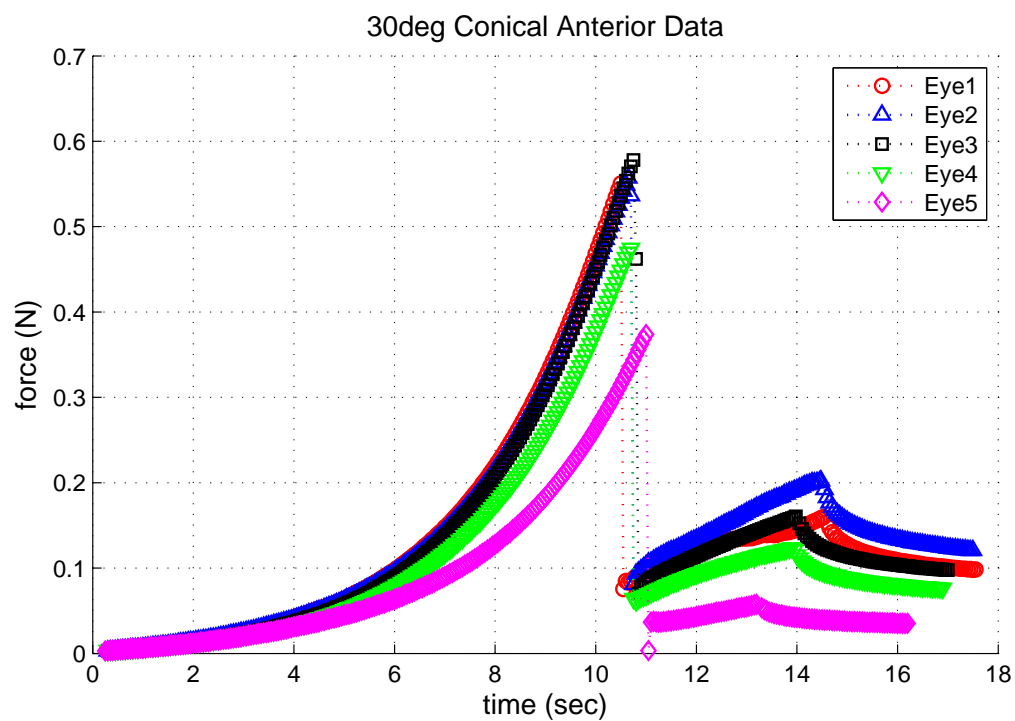
Figure 4.14: Graph of 30 deg Conical Anterior Data.
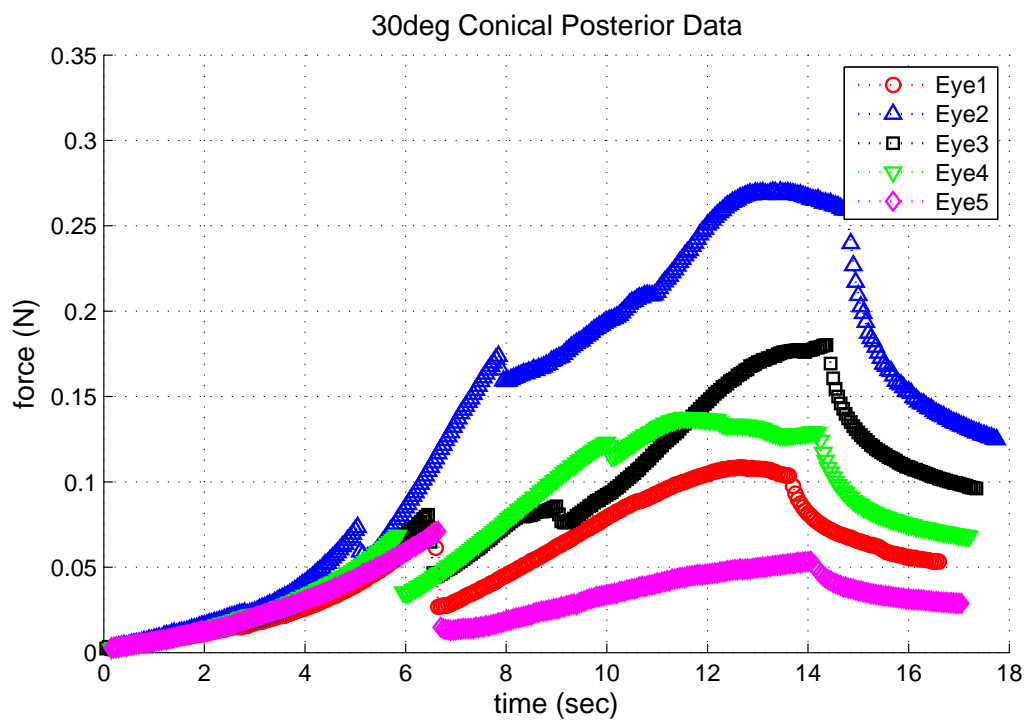
Figure 4.15: Graph of 30 deg Conical Posterior Data.
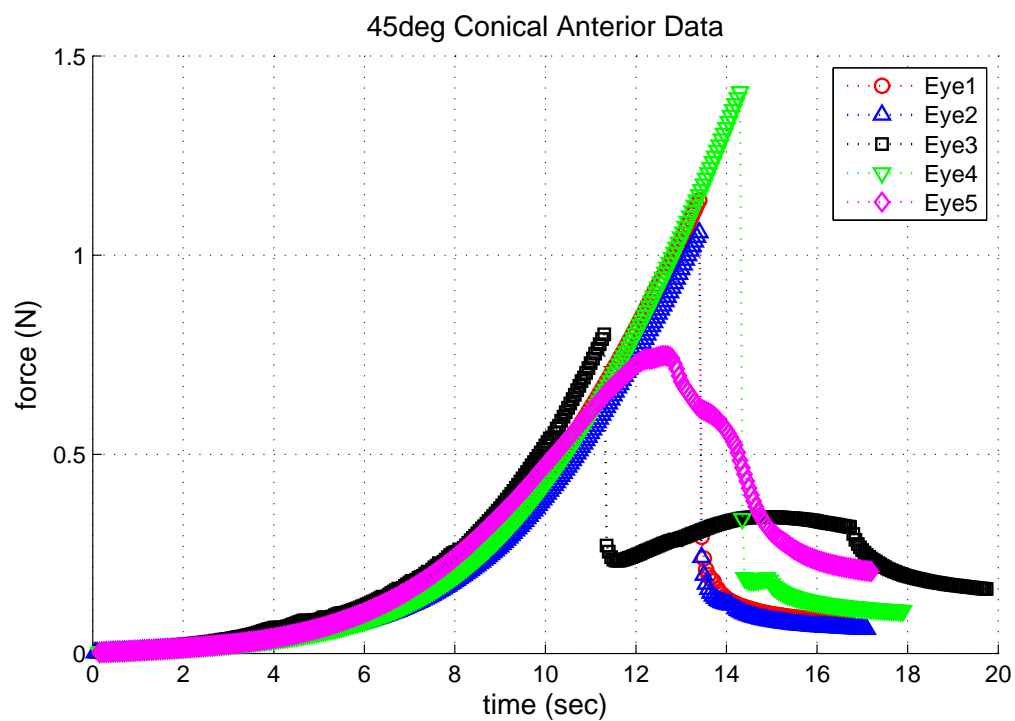
Figure 4.16: Graph of 45 deg Conical Anterior Data.
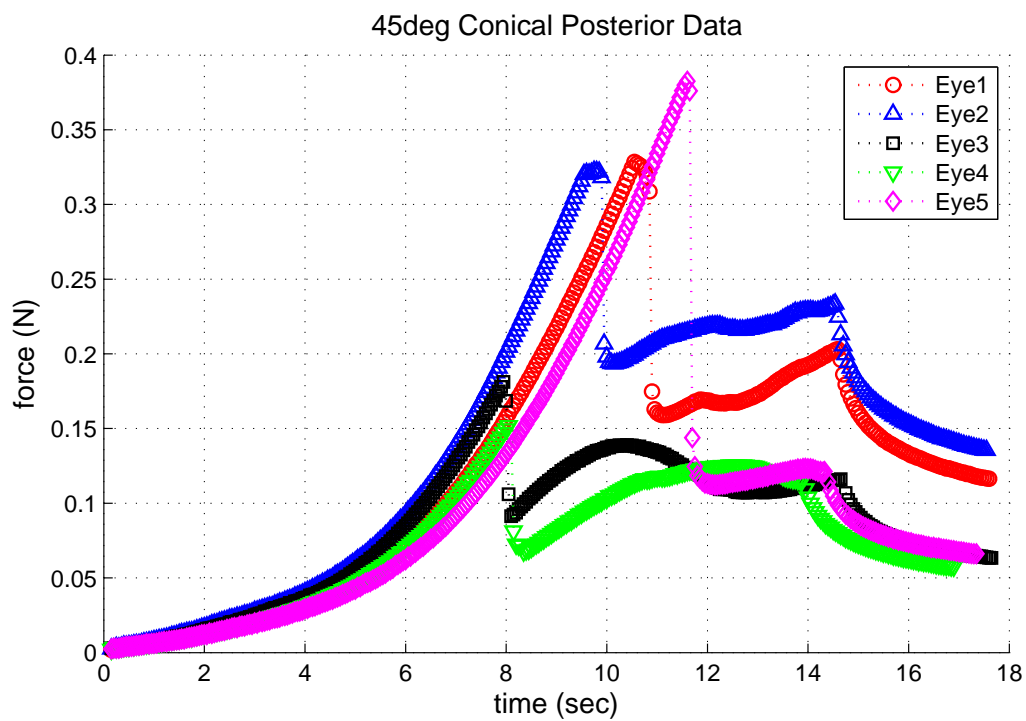
Figure 4.17: Graph of 45 deg Conical Posterior Data.

4.6   Discussion

Looking at the graphs for each test configuration, the data appear to have grouped well. All tests look similar with the exception of the 30 degree conical posterior test group. The tests show a very early puncture force, followed by a slight decrease in force, and then an increase in force to values greater than the puncture force by the end of the test. Upon further investigation of the data by reviewing the recorded video of the tests, it can be seen that after the initial puncture as the puncture tip continues downward, the capsule tears in addition to the original puncture (see Figure 4.18). The tears appear to go from the original puncture site down to the equator. After the tears, the lens shifts from being centrally located under the puncture tip as the puncture tip moves through the exposed lens fibers. We believe the puncture to occur earlier than the others due to the sharper nature of the 30 degree conical tip and that the posterior lens is weaker and thinner than the anterior lens [Krag et al., 1997, Yang et al., 1998a].
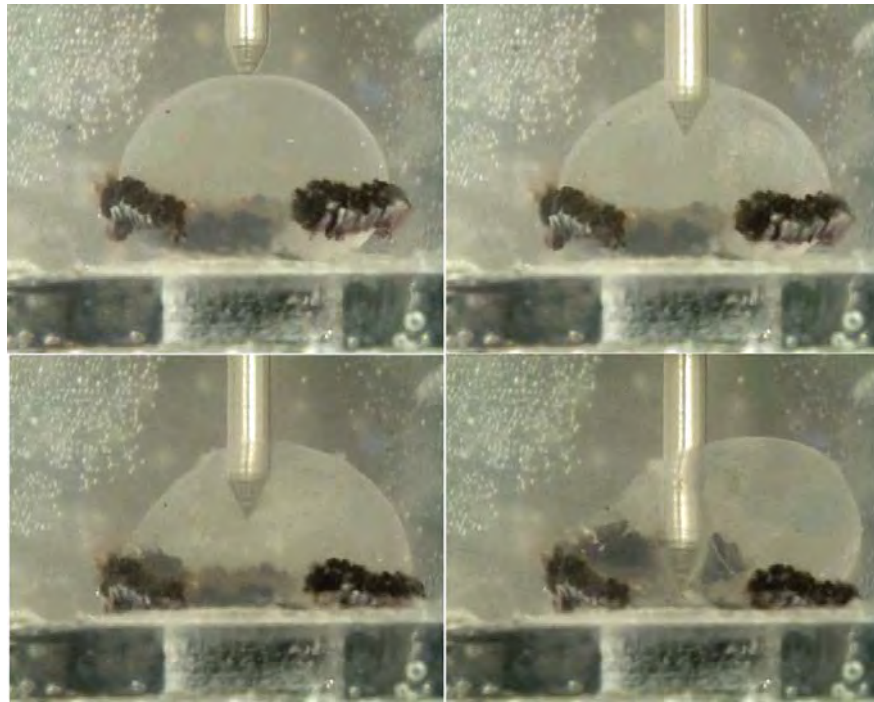
Figure 4.18: Image series showing the lens at the begining of the test (top left), after the initial puncture (top right,) and subsequent tearing (bottom left and right) during a 30 degree conical puncture test.

Average puncture forces and the average time to puncture were calculated for each test group and can be seen in Table 4.2. It can be seen from the average values that the sharper (30 degree) and smaller diameter (1 mm) puncture tips had a smaller puncture force than their more blunt (45 degree) and larger (2 mm) counterparts. Also, the puncture forces for posterior tests are smaller than the puncture forces for the anterior tests for all groups. This supports Yang's findings that the anterior lens capsule is stronger than the posterior lens capsule [Yang et al., 1998a]. The puncture forces between the respective spherical and cylindrical tip sizes were approximately the same, with the 45 degree conical tip landing somewhere in between anteriorly and slightly below posteriorly. The 30 degree conical tip puncture force was much lower than all the others, due to its sharpness. Puncture times for the tips were longer on anterior tests than posterior tests except for the 2 mm cylindrical group and the 2 mm spherical group. In the 2 mm cylindrical tip group times were approximately the same between anterior and posterior tests. In the 2 mm spherical tip group, the average anterior time was lower than the average posterior time by 0.73 seconds. Although the posterior lens capsule is weaker than the anterior, perhaps the average puncture time for the 2 mm spherical posterior group was longer than the anterior group because of the non-sharp nature of the tip and the greater surface area of the posterior lens capsule (allowing for more deformation before failure with the non-sharp tip).

Table 4.2: Average Puncture Force & Average Time to Puncture.

| Tip Geometry | Anterior | | Posterior | |
(d,Θ)	Force (N)	Time (s)	Force (N)	Time (s)
1 mm spherical	1.1329	13.47	0.3663	12.00
2 mm spherical	1.2929	12.48	0.6171	13.21
1 mm cylindrical	1.1651	13.89	0.3508	11.03
2 mm cylindrical	1.2510	12.16	0.6159	12.18
30 deg conical	0.5067	10.73	0.0672	5.61
45 deg conical	1.2399	13.18	0.2928	9.25

Preliminary modeling is being completed in Abaqus. Below Figures 4.19 and 4.20 show an Abaqus simulation for a 1 mm spherical posterior puncture test with a loading rate of 0.1 mm/s (we

started with a lower loading rate than actual to get the simulation to run the longest). Figure 4.19 shows the beginning of the simulation and Figure 4.20 shows as far as the simulation will run. The simulation is setup as a 2-D axisymmetric mesh with a fixed bottom platen and and incompressible 1 mm spherical puncture tip. The interactions between the lens and the tip and the lens and the bottom platen are frictionless. In Figure 4.20 the stress can be seen in the lens capsule near the contact point of the puncture tip. Figure 4.21 better shows the stresses in the lens fiber cells, with the highest stresses being located near the puncture tip contact point. We are trying to model the puncture test up to puncture (approximately 70% strain). Unfortunately, with Abaqus the simulation only runs to approximately 17% strain before failing to converge. Work is currently being done to model the lens capsule as a shell element and the interior lens fibers as a viscous incompressible fluid in hopes of getting the simulation to run to higher strains.

While modeling has been difficult, our data support Yang's findings that the anterior lens capsule is stronger than the posterior lens capsule [Yang et al., 1998a]. More importantly, the data gathered will be useful in calculating material properties of the whole porcine ocular lens with parameter fitting in Tahoe to compare with the properties calculated from the unconfined compression testing data. Additionally, the data will be useful when the model is developed enough begin modeling the interaction between intraocular foreign bodies and the ocular lens.

62
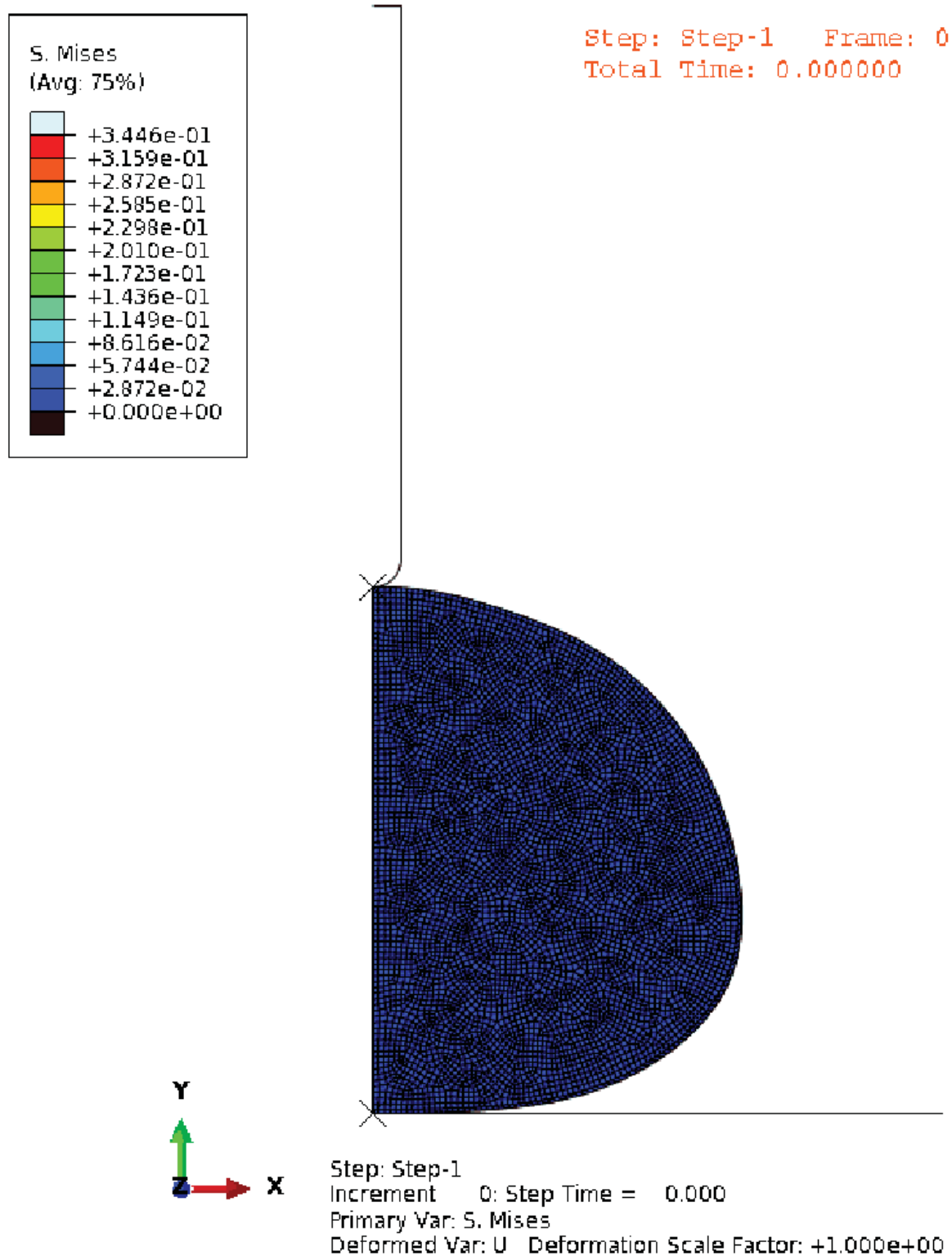
Figure 4.19: Abaqus Simulation of Puncture Testing of Whole Porcine Ocular Lens - Beginning of simulation.

S. Mises
(Avg: 75%)

+3.446e-01
+3.159e-01
+2.872e-01
+2.585e-01
+2.298e-01
+2.010e-01
+1.723e-01
+1.436e-01
+1.149e-01
+8.616e-02
+5.744e-02
+2.872e-02
+0.000e+00

Step: Step-1   Frame: 3
Total Time: 2.192533

Y

Z   X

Step: Step-1
Increment   32: Step Time =   2.193
Primary Var: S. Mises
Deformed Var: U   Deformation Scale Factor: +1.000e+00
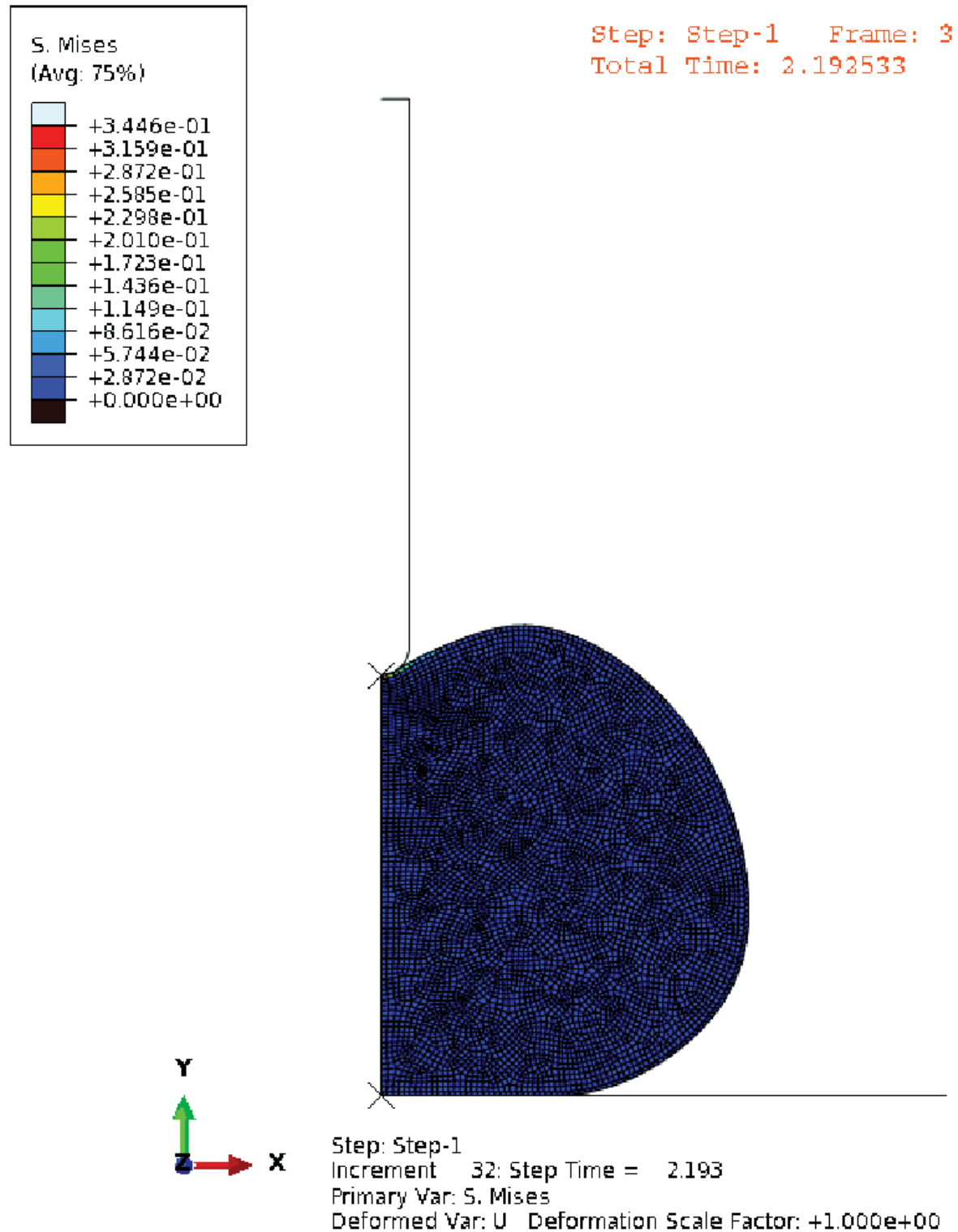
Figure 4.20: Abaqus Simulation of Puncture Testing of Whole Porcine Ocular Lens - As far as simulation will complete.
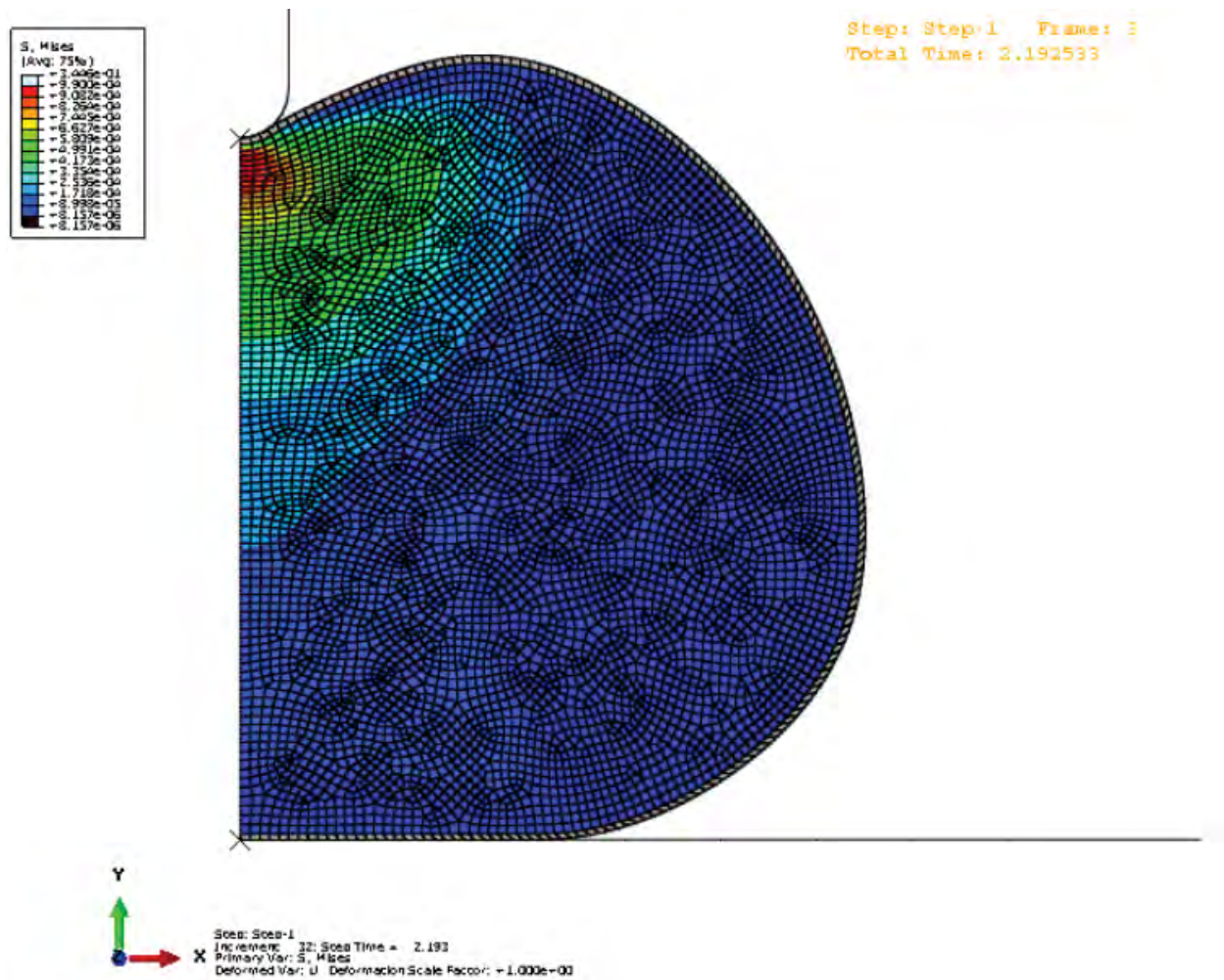
Figure 4.21: Abaqus Simulation of Puncture Testing of Whole Porcine Ocular Lens - Scaled contour to better show stresses in lens fibers.

Chapter 5

Nanoindentation of the Capsule

Nanoindentation can be used to determine the material properties of samples. This is done by indenting a material with known properties (the indentation tip) into a material's surface with unknown properties. The force and displacement are recorded during the test and later used with the tip geometry and indentation area to calculate the unknown material properties. For viscoelastic materials, frequently a stress-relaxation test or a creep test are used to determine material properties. In a stress-relaxation test, the indentation tip is lowered into the sample to a pre-defined depth at which the tip stops displacing and the material is allowed to relax over a pre-defined hold time, after which the indentation tip will retract. In a creep test, the indentation tip is lowered into the sample until a pre-defined force is reached. Once this force is reached, the indentation tip will continue to indent into the sample as it relaxes, maintaining that pre-defined force for a certain length of time, after which the indentation tip will retract. Nanoindentation is being used on the lens capsule to determine the capsules material properties (specifically τ (relaxation time constant), μ_{EQ} (equilibrium shear modulus), and μ_{NEQ} (nonequilibrium shear modulus)). Because of the size of the indentation tips used in nanoindentation, very small volumes of material can be tested. This fits well with the lens capsule as the porcine anterior lens capsule is approximately 60 μm thick. Calculation of the parameters will be done using the same method employed in the parameter fitting of the unconfined compression data, described in detail in the previous Parameter Fitting of Unconfined Compression Testing Data Chapter. Determination of just the lens capsule properties will allow for the back calculation of the interior lens fiber material

properties from the whole lens data gathered from the unconfined compression data. The two material property sets will be used for the different materials in the computational model.

5.1   Sample Preparation

Anterior lens capsule tissue was collected by first removing the cornea as previously described in the Puncture Testing of the Whole Lens Chapter. Then, while applying slight pressure to the whole globe, a small incision was made with a diamond-head scalpel in the anterior surface of the ocular lens, near the attachment of the zonules. By gently widening this incision with the scalpel, the interior lens fibers slide out, intact, from the slight pressure being applied to the globe. With the interior lens fibers removed, the anterior portion of the capsule was then lifted by a pair of tweezers inserted through the previously made incision. Once lifted, the anterior capsule was collected by using a pair of micro scissors to cut the capsule near the zonule attachments around the perimeter. Once extracted, the anterior lens capsule tissue was placed in vials containing Alcon BSS and transported to the nanoindenter (at the Colorado School of Mines in Golden, CO) on wet-ice.

5.2   Experimental Setup

A TI-950 TriboIndenter made by Hysitron was used to perform the nanoindentation (see Figure 5.1). The machine was located at the Colorado School of Mines in Golden, CO under the direction of Assistant Professor Corrine Packard. A 1 μm diameter, spherical fluid cell tip was used to test the lens capsule in Alcon BSS at room temperature (approximately 21 ℃). The anterior lens capsule tissue was placed on a polycarbonate substrate with the approximate curved shape of the anterior surface of the lens (see Figure 5.2). The substrate has a surrounding wall to contain the Alcon BSS that the lens capsule is immersed in. The lens capsule was held in place by a small metallic washer, preventing slippage of the tissue while being indented (see Figure 5.3).

Figure 5.1: Hysitron TI-950 TriboIndenter Nanoindenter Located at the Colorado School of Mines.

5.3   Experimental Method

TriboScan 9 software was utilized to perform the tests and export the data. After ensuring the correct calibration file was loaded, an air indent was performed to calibrate the indentation tip and system. This was followed by tip-to-optic calibration. The boundary was defined for an aluminium standard and an h-pattern indentation series was used to align the indentation tip with the optics. The sample tissue was then placed on the substrate, held in place by the small metallic washer, and immersed in Alcon BSS that had acclimated to the room temperature for at least 24 hours. The substrate and sample were then placed in the machine. After defining the boundary of the testing substrate, the indentation tip was positioned over the center of the testing substrate and lowered into the fluid so that the Alcon BSS could no longer be seen being pulled up the sides of the indentation tip but without contacting the lens capsule. A single tip-to-optic calibration indent
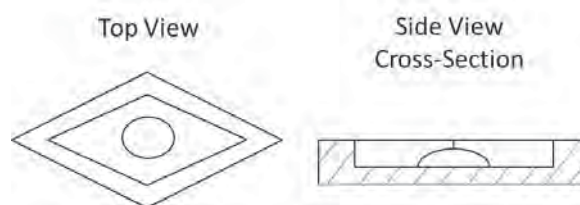
Figure 5.2: Drawing of Nanoindentation Substrate with Dome-Shaped Surface and Liquid Well.
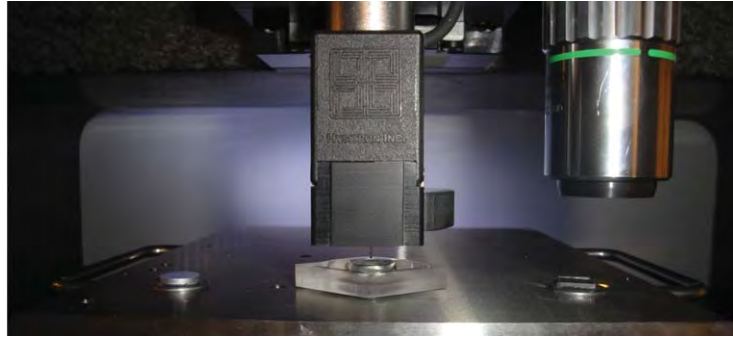
Figure 5.3: Image of Lens Capsule Being Held in Place by a Small Metallic Washer Within the Nanoindenter.

was performed on the lens capsule tissue to determine the height of the sample. The software was then switched into Imaging mode (normally used to create a 3-D image of a material's surface using the indentation tip). Single indents in Imaging mode were used to indent the sample. This allowed for more reliable finding of the surface of the lens capsule as the tip remains in constant contact with the lens capsule. Creep tests were performed with a hold load of 5 μN. The tip loaded for 10 seconds, held the load for 30 seconds, and unloaded over 10 seconds. Test locations were separated by 60 μm in the positive x-direction (to avoid any plastic deformation from previous indents) until 4 indents were completed. The test locations then moved 60 μm in the negative y-direction and resumed testing, moving 60 μm in the negative x-direction until 4 tests were completed. This process was repeated for all tests. Depth, load, and time were recorded for each test. Once the test was completed, the data were exported in text files for later analysis.

5.4   Results

Below are graphs showing creep test data from nanoindentation of the anterior porcine lens capsule and the anterior human lens capsule. The non-zero starting force on each graph is a product of the pre-load force necessary for the indentation tip to find contact. It was hard to avoid with such a small holding load.
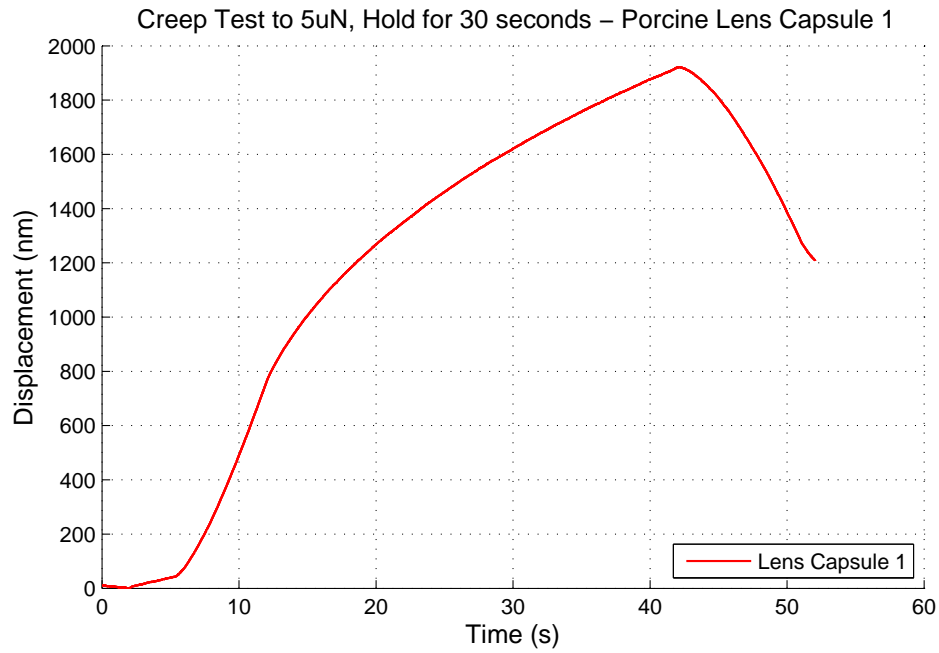
Figure 5.4: Graph of Nanoindentation Creep Test Porcine Lens Capsule 1 - Load to 5 μN, Hold for 30 seconds. The pre-load force necessary to get contact with the lens capsule is the cause of the non-zero starting force.

Figure 5.5: Graph of Nanoindentation Creep Test Porcine Lens Capsule 2 - Load to 5 μN, Hold for 30 seconds. The pre-load force necessary to get contact with the lens capsule is the cause of the non-zero starting force.
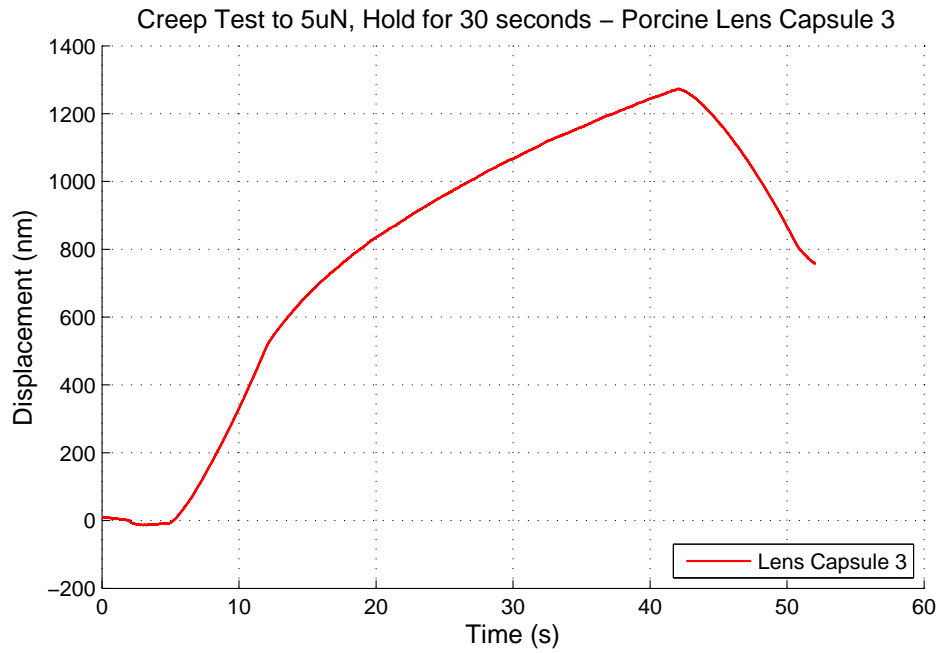
Figure 5.6: Graph of Nanoindentation Creep Test Porcine Lens Capsule 3 - Load to 5 μN, Hold for 30 seconds. The pre-load force necessary to get contact with the lens capsule is the cause of the non-zero starting force.
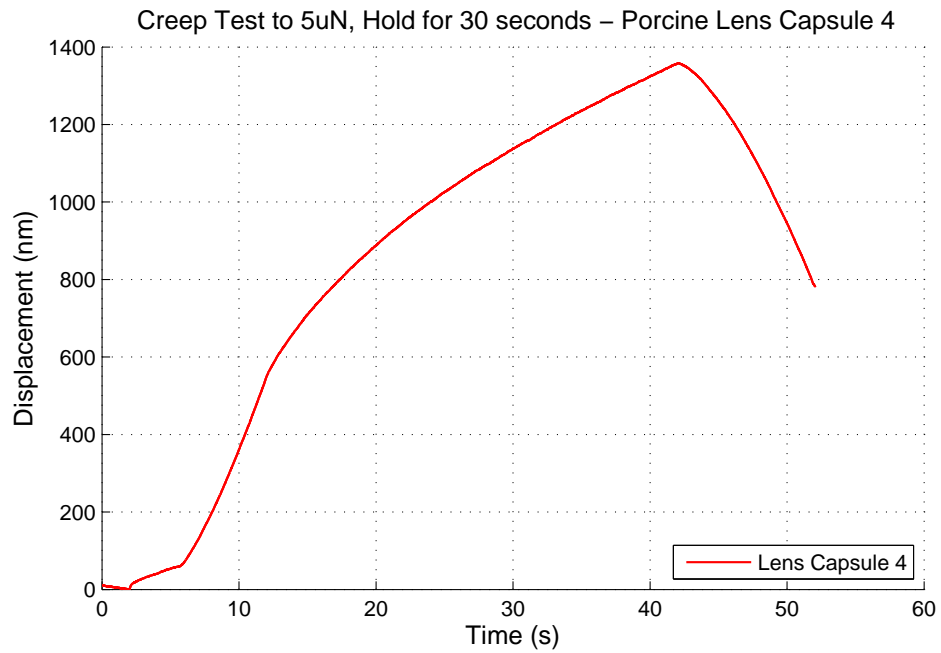
Figure 5.7: Graph of Nanoindentation Creep Test Porcine Lens Capsule 4 - Load to 5 μN, Hold for 30 seconds. The pre-load force necessary to get contact with the lens capsule is the cause of the non-zero starting force.
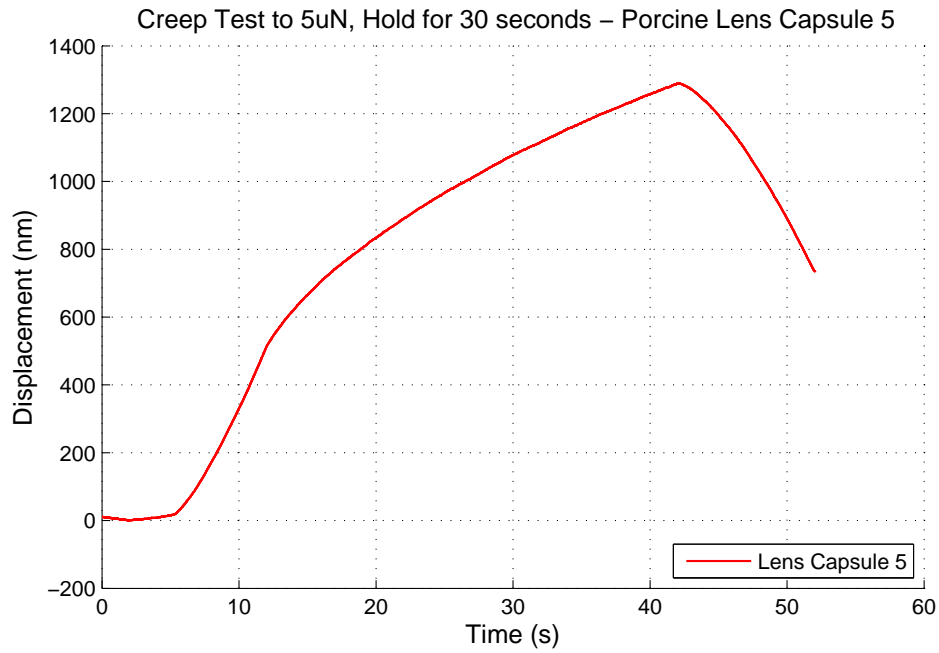
Figure 5.8: Graph of Nanoindentation Creep Test Porcine Lens Capsule 5 - Load to 5 μN, Hold for 30 seconds. The pre-load force necessary to get contact with the lens capsule is the cause of the non-zero starting force.
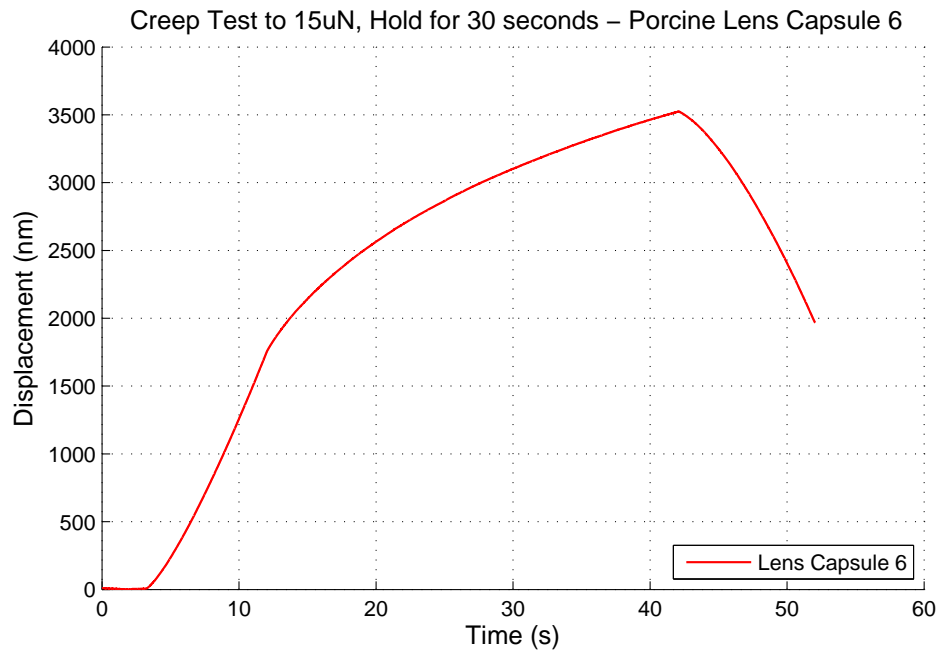
Figure 5.9: Graph of Nanoindentation Creep Test Porcine Lens Capsule 6 - Load to 15 μN, Hold for 30 seconds. The pre-load force necessary to get contact with the lens capsule is the cause of the non-zero starting force.
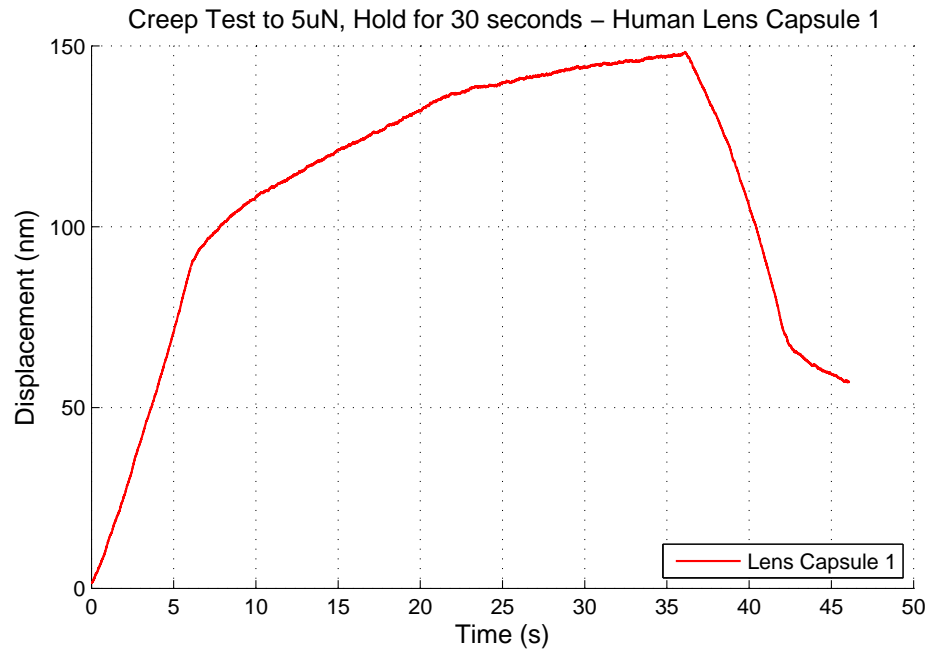
Figure 5.10: Graph of Nanoindentation Creep Test Human Lens Capsule 1 - Load to 5 μN, Hold for 30 seconds. The pre-load force necessary to get contact with the lens capsule is the cause of the non-zero starting force.
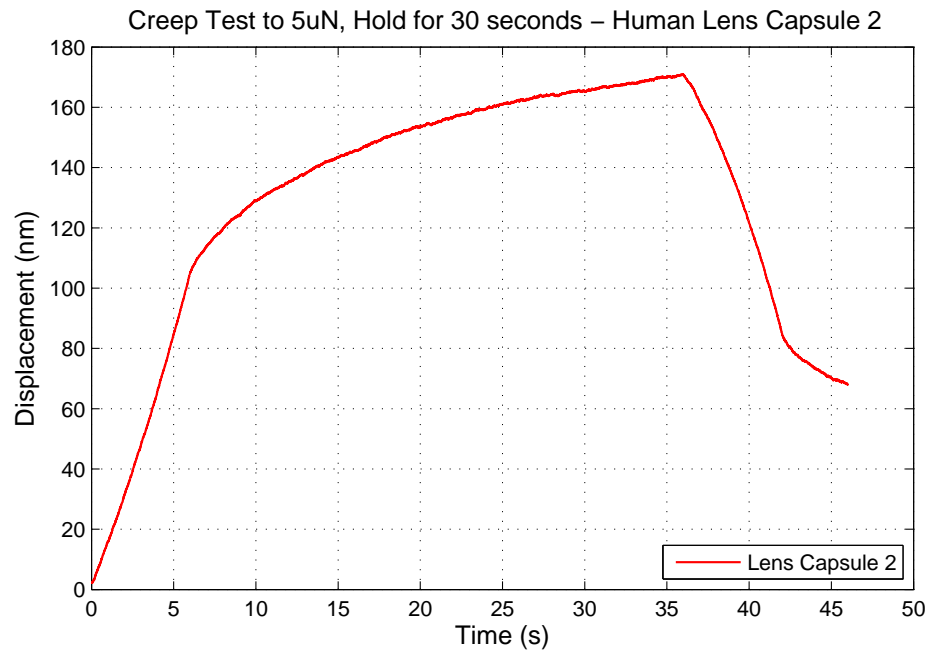
Figure 5.11: Graph of Nanoindentation Creep Test Human Lens Capsule 2 - Load to 5 μN, Hold for 30 seconds. The pre-load force necessary to get contact with the lens capsule is the cause of the non-zero starting force.
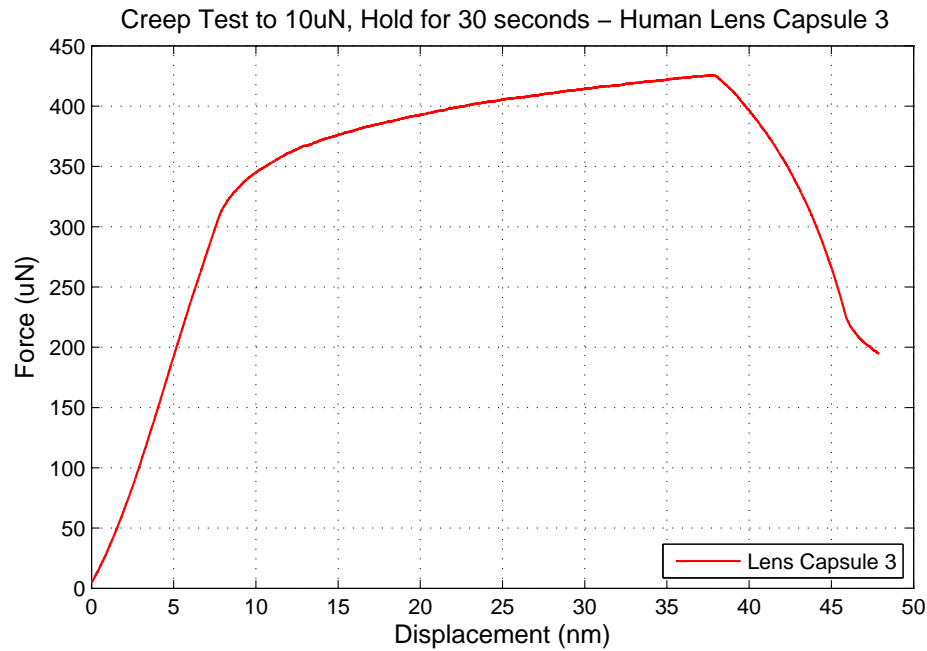
Figure 5.12: Graph of Nanoindentation Creep Test Human Lens Capsule 3 - Load to 10 μN, Hold for 30 seconds. The pre-load force necessary to get contact with the lens capsule is the cause of the non-zero starting force.
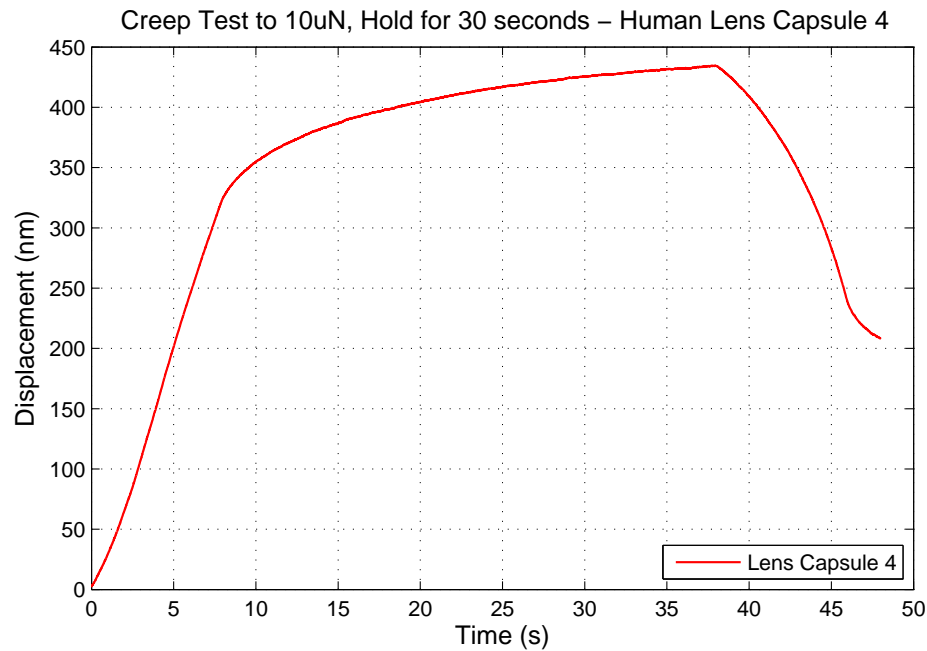
Figure 5.13: Graph of Nanoindentation Creep Test Human Lens Capsule 4 - Load to 10 μN, Hold for 30 seconds. The pre-load force necessary to get contact with the lens capsule is the cause of the non-zero starting force.
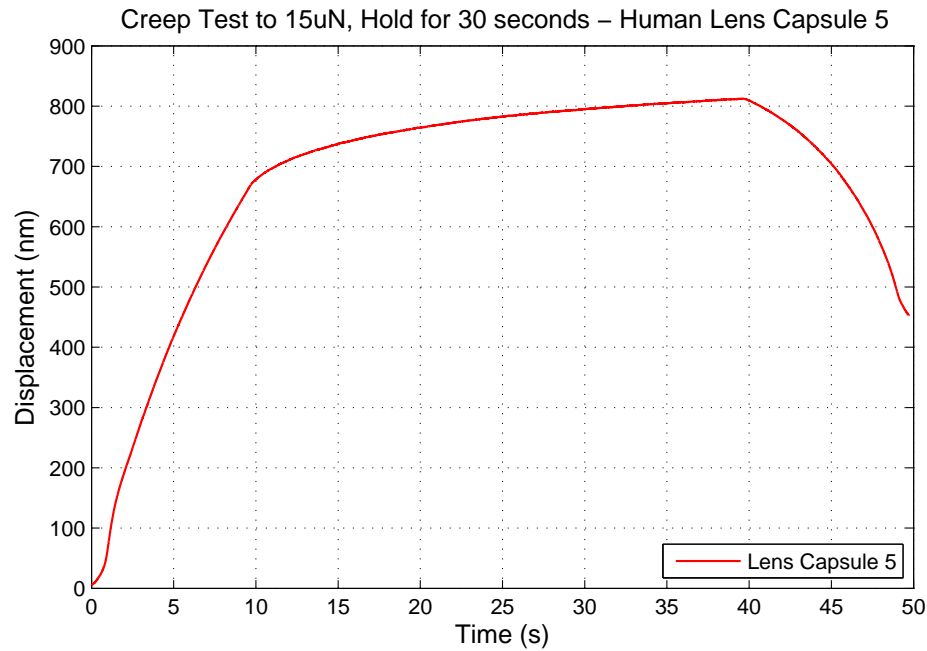
Figure 5.14: Graph of Nanoindentation Creep Test Human Lens Capsule 5 - Load to 15 μN, Hold for 30 seconds. The pre-load force necessary to get contact with the lens capsule is the cause of the non-zero starting force.
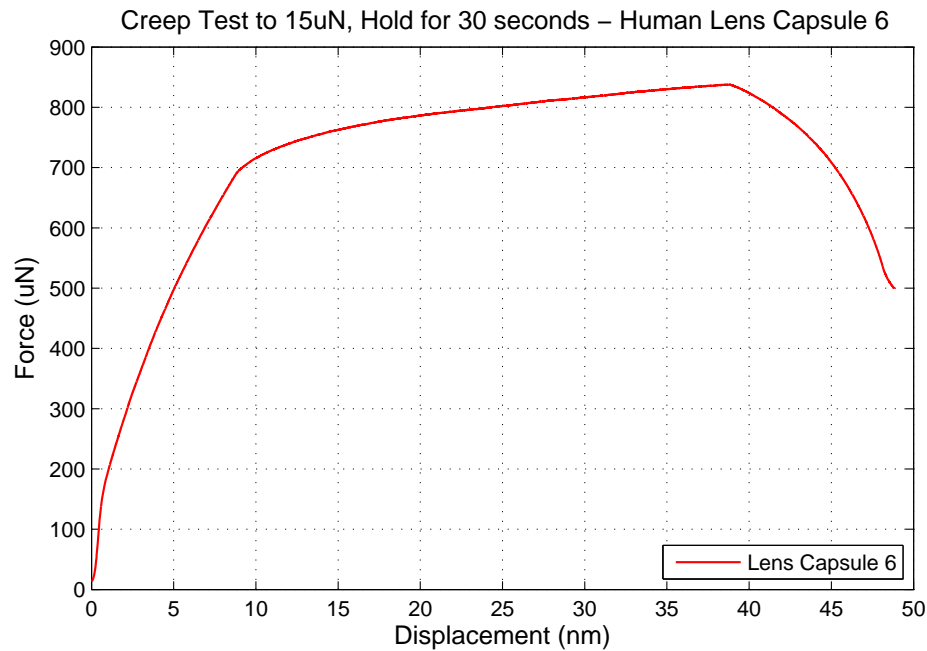
Figure 5.15: Graph of Nanoindentation Creep Test Human Lens Capsule 6 - Load to 15 μN, Hold for 30 seconds. The pre-load force necessary to get contact with the lens capsule is the cause of the non-zero starting force.
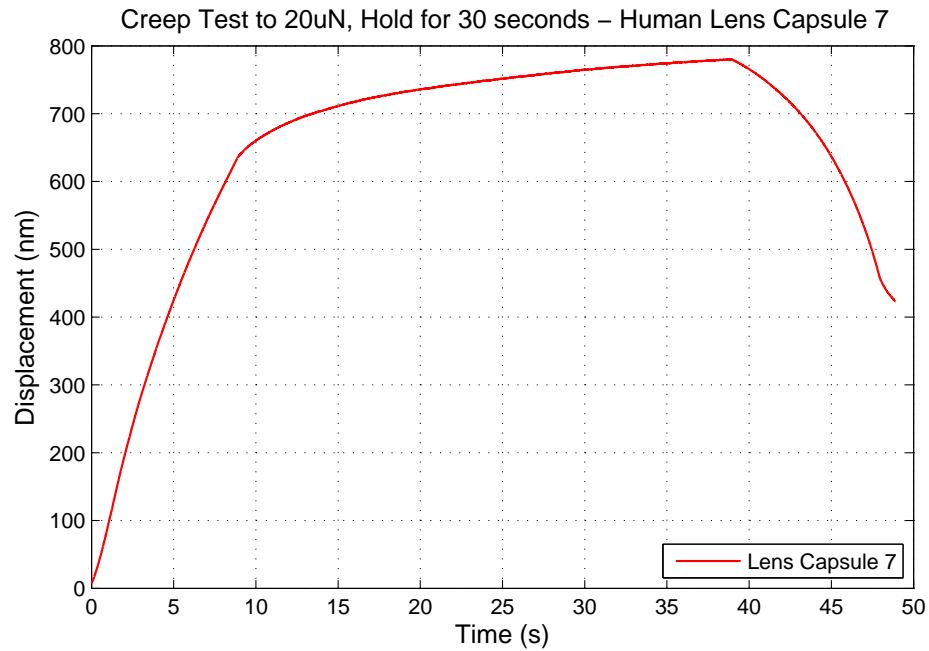
Figure 5.16: Graph of Nanoindentation Creep Test Human Lens Capsule 7 - Load to 20 μN, Hold for 30 seconds. The pre-load force necessary to get contact with the lens capsule is the cause of the non-zero starting force.
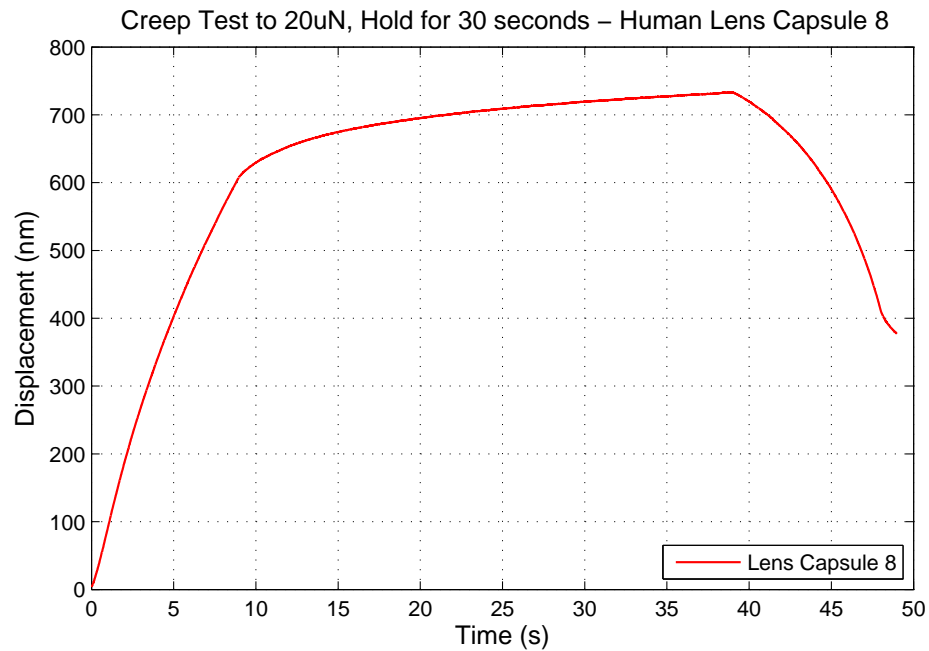
Figure 5.17: Graph of Nanoindentation Creep Test Human Lens Capsule 8 - Load to 20 μN, Hold for 30 seconds. The pre-load force necessary to get contact with the lens capsule is the cause of the non-zero starting force.
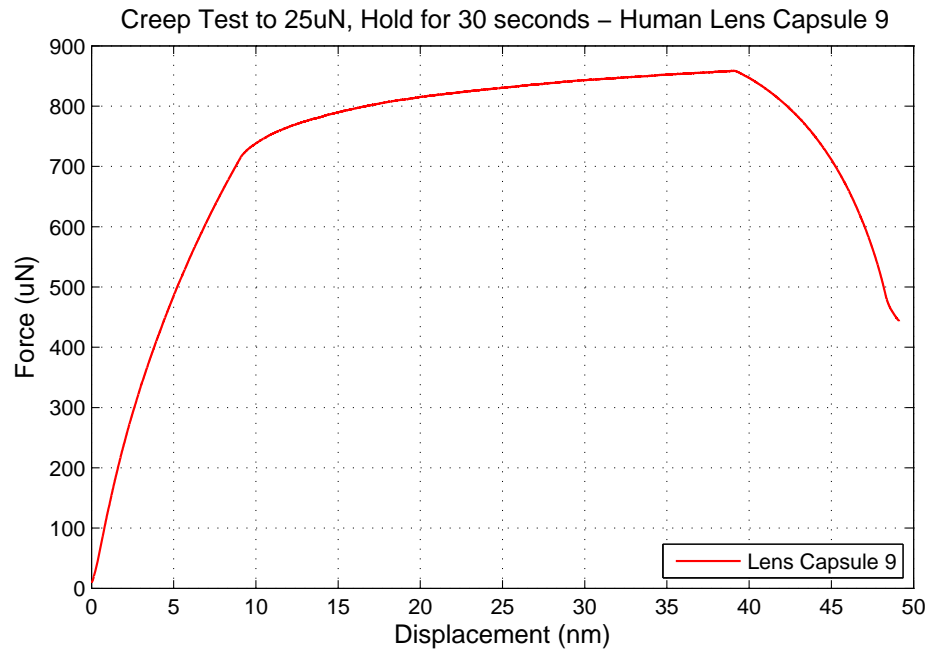
Figure 5.18: Graph of Nanoindentation Creep Test Human Lens Capsule 9 - Load to 25 μN, Hold for 30 seconds. The pre-load force necessary to get contact with the lens capsule is the cause of the non-zero starting force.
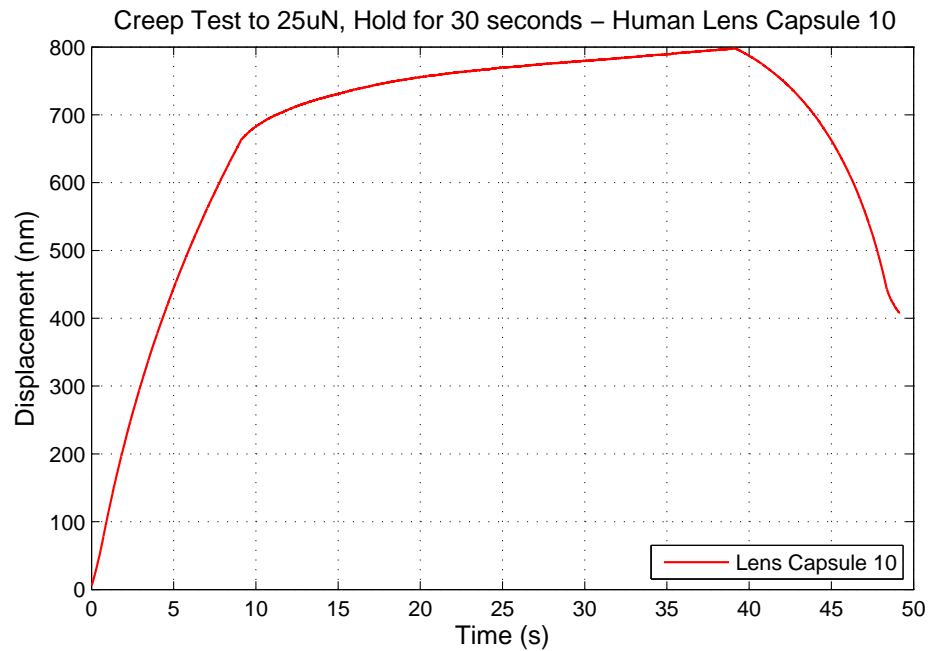
Figure 5.19: Graph of Nanoindentation Creep Test Human Lens Capsule 10 - Load to 25 μN, Hold for 30 seconds. The pre-load force necessary to get contact with the lens capsule is the cause of the non-zero starting force.
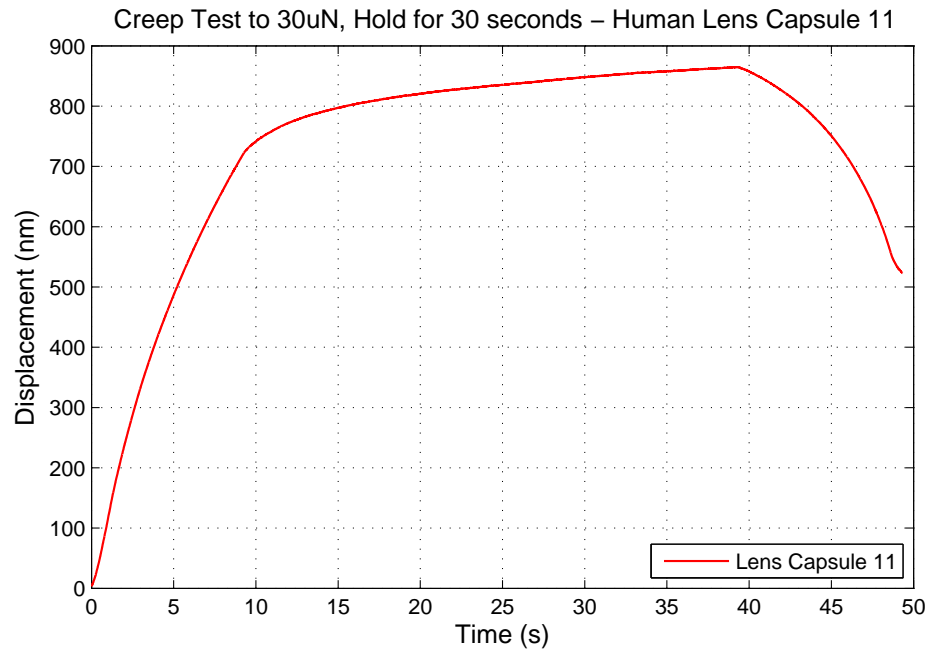
Figure 5.20: Graph of Nanoindentation Creep Test Human Lens Capsule 11 - Load to 30 μN, Hold for 30 seconds. The pre-load force necessary to get contact with the lens capsule is the cause of the non-zero starting force.
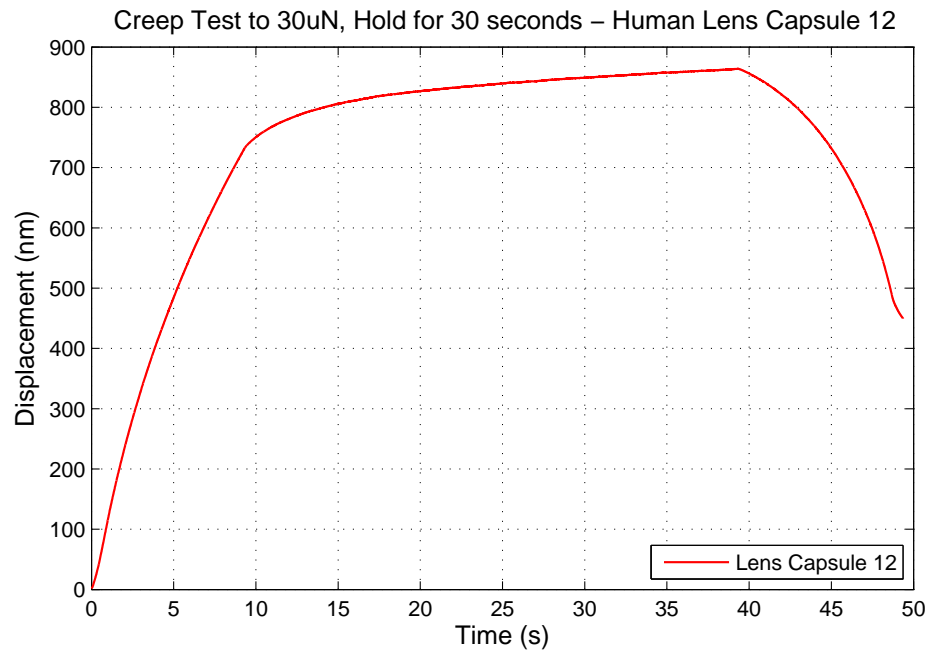
Figure 5.21: Graph of Nanoindentation Creep Test Human Lens Capsule 12 - Load to 30 μN, Hold for 30 seconds. The pre-load force necessary to get contact with the lens capsule is the cause of the non-zero starting force.
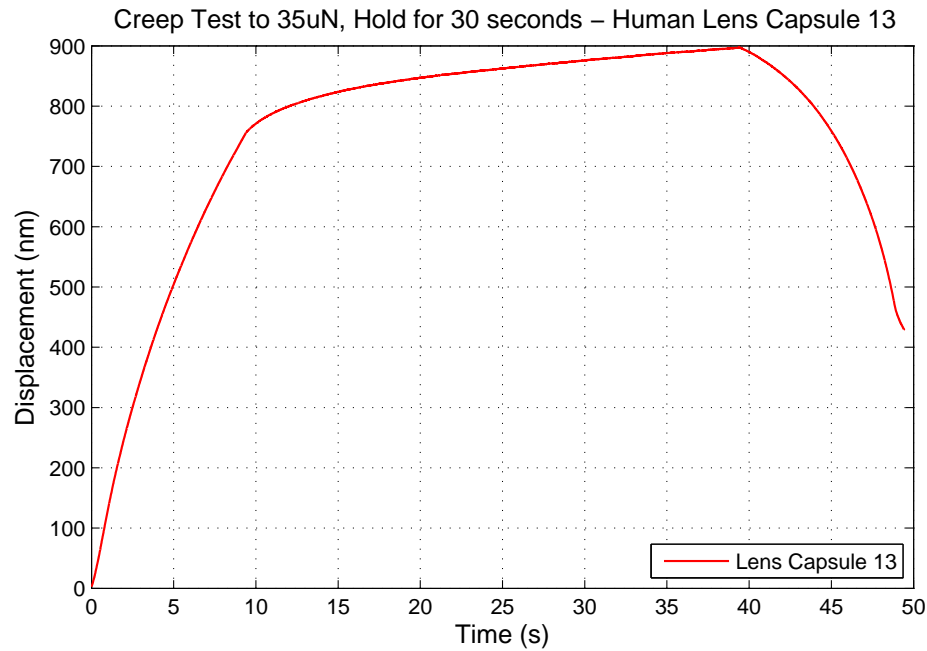
Figure 5.22: Graph of Nanoindentation Creep Test Human Lens Capsule 13 - Load to 35 μN, Hold for 30 seconds. The pre-load force necessary to get contact with the lens capsule is the cause of the non-zero starting force.
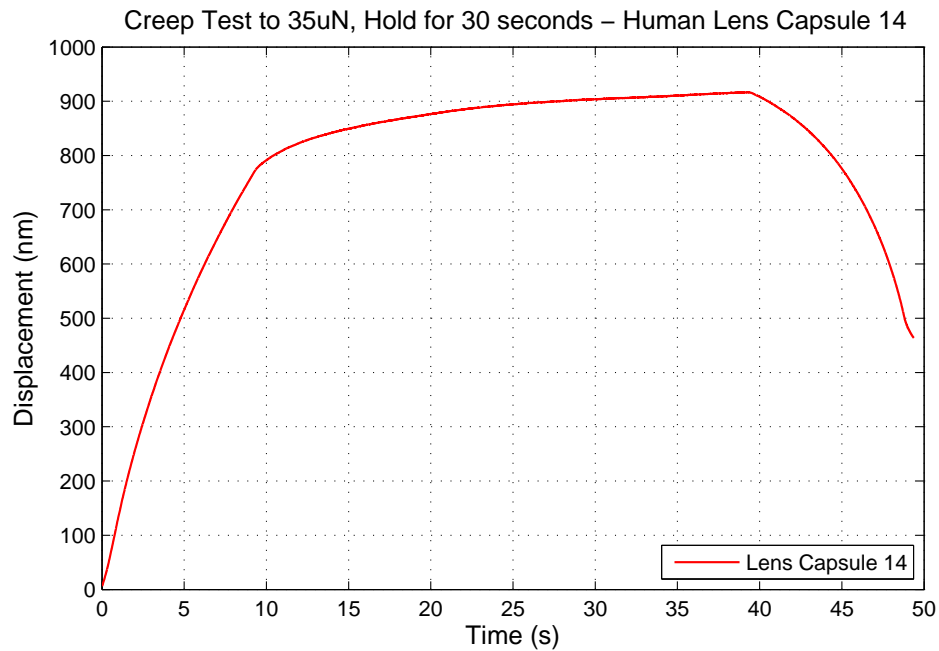
Figure 5.23: Graph of Nanoindentation Creep Test Human Lens Capsule 14 - Load to 35 μN, Hold for 30 seconds. The pre-load force necessary to get contact with the lens capsule is the cause of the non-zero starting force.
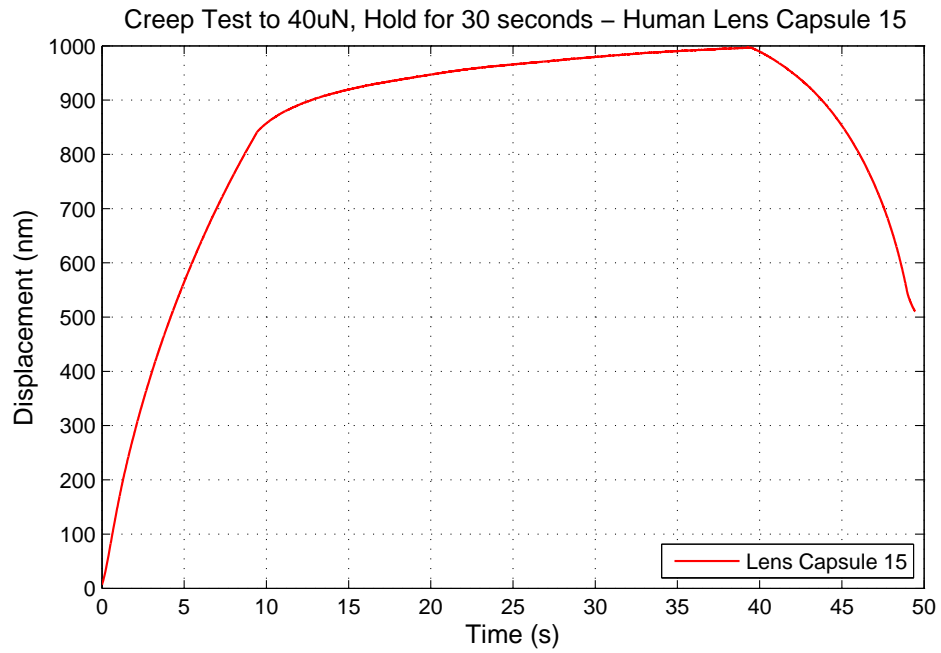
Figure 5.24: Graph of Nanoindentation Creep Test Human Lens Capsule 15 - Load to 40 μN, Hold for 30 seconds. The pre-load force necessary to get contact with the lens capsule is the cause of the non-zero starting force.
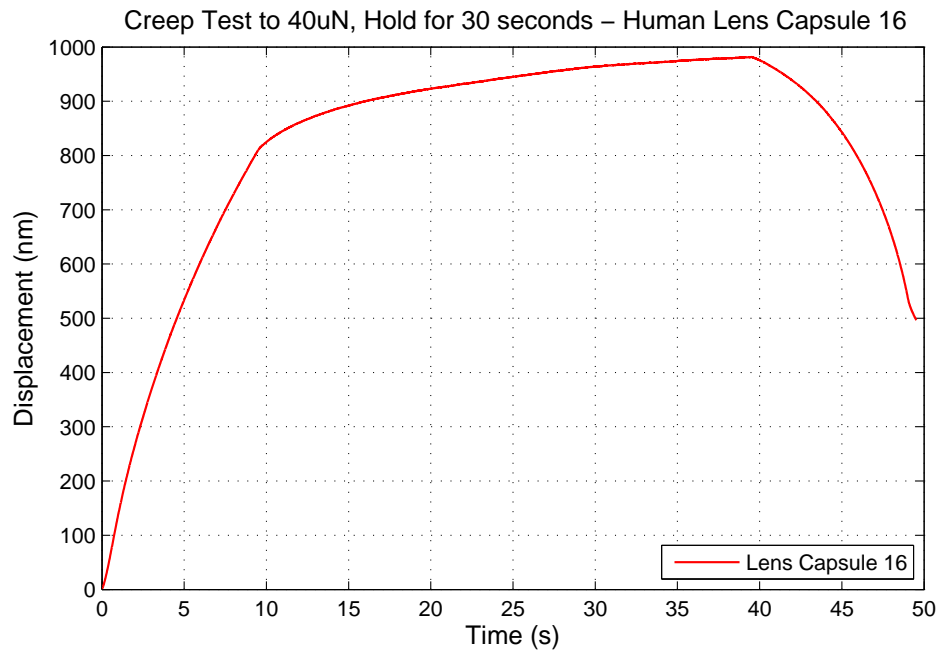
Figure 5.25: Graph of Nanoindentation Creep Test Human Lens Capsule 16 - Load to 40 μN, Hold for 30 seconds. The pre-load force necessary to get contact with the lens capsule is the cause of the non-zero starting force.
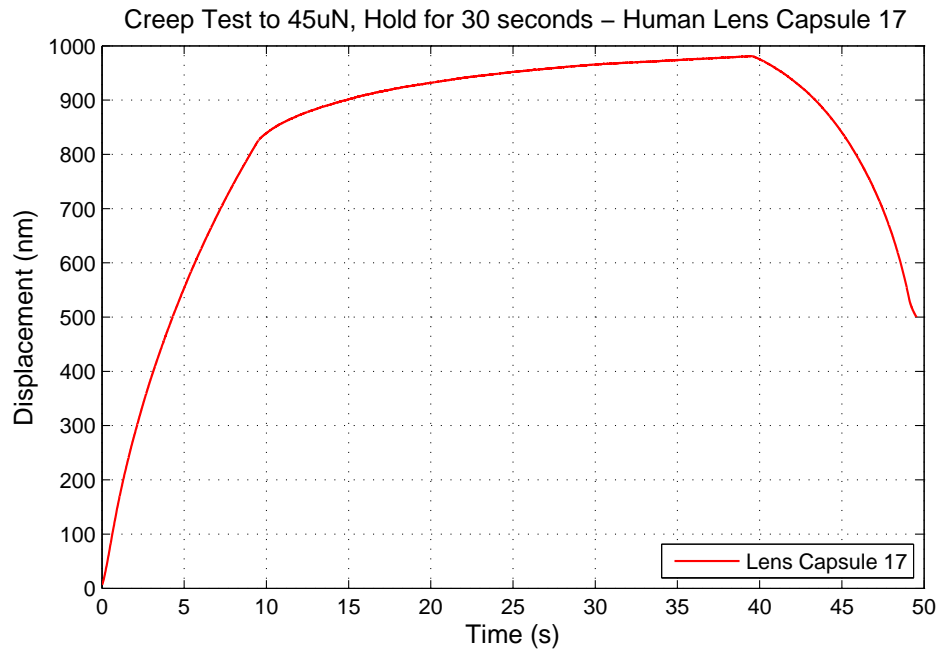
Figure 5.26: Graph of Nanoindentation Creep Test Human Lens Capsule 17 - Load to 45 μN, Hold for 30 seconds. The pre-load force necessary to get contact with the lens capsule is the cause of the non-zero starting force.
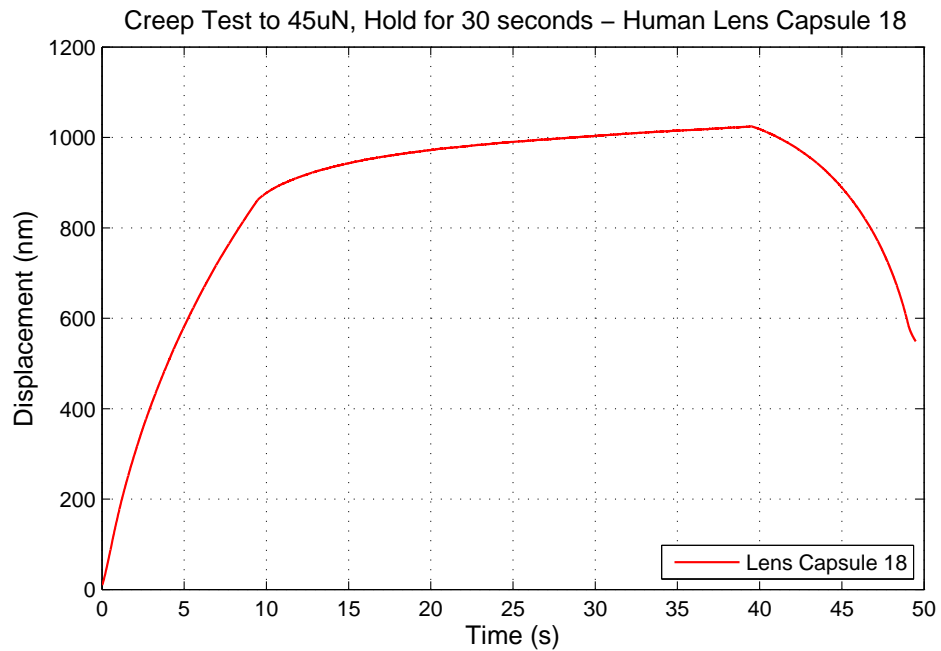
Figure 5.27: Graph of Nanoindentation Creep Test Human Lens Capsule 18 - Load to 45 μN, Hold for 30 seconds. The pre-load force necessary to get contact with the lens capsule is the cause of the non-zero starting force.

5.5   Discussion

Overall, the creep test data from nanoindentation of the both the anterior porcine lens capsule and anterior human lens capsule looks promising. However, this data is just preliminary. The data would be improved with a longer hold section to better capture the viscoelastic dissipation of the force response. For the holding force of 5 μN, the total creep for each porcine test fell approximately within the range of 800-1100 nm (see Figures 5.4-5.8). Additionally, the porcine creep test to 15 μN had a total creep of approximately 1750 nm (see Figure 5.9). The fact that the total creep from the 15 μN porcine creep test is greater than the total creep from any 5 μN porcine test helps to validate that the test is working properly and we are indenting the porcine lens capsule and not just the fluid. Also, the loading curve for the 15 μN porcine creep test looks smoother. This is due to the smaller proportion of the pre-load force to hold force compared to the 5 μN porcine tests.

Looking at the human test data, we see a similar progression of smoother curves as the peak force is increased. Average (2 tests/peak force) total displacement as well as initial and final displacements can be seen in Table 5.1. As the peak force increased, the displacement into the tissue generally increased as well. The total displacement varied with each test, and more data is needed before an overall trend can be determined. At 45 μN peak force, we achieved an indentation depth of approximately 5% strain, assuming the human anterior lens capsule to be approximately 11-33 μm [Krag et al., 1997]. These data are usable and will be fit with Tahoe or Abaqus using methods similar to the fitting of the unconfined compression data.

Table 5.1: Average Displacment Values from Human Anterior Lens Capsule Creep Tests

Peak Force (μN)	Depth at Initial Peak Force (nm)	Depth After Creep (nm)	Total Displacement During Creep (nm)
5	96.9	159.7	62.8
10	317.5	429.8	112.3
15	680.3	824.7	144.4
20	620.6	756.7	136.1
25	689.4	828.3	138.9
30	727.8	864.3	136.5
35	764.8	906.9	142.1
40	825.6	989.1	163.5
45	843.4	1002.5	159.2

Chapter 6

Electron Microscopy and Tomography of the Lens Capsule

Electron Microscopy (EM) is used to image samples at very small scales (down to the nm scale in our research). Electron Tomography (ET) refers to imaging a sample by slices, allowing the collection of images in the z-axis resulting in a "stack" of images. Through EM and ET, the ultra-structure of the lens capsule can be determined for use in a computational model. To image the lens capsule, transmission electron microscopy (TEM) was used. A transmission electron microscope works by utilizing an electron gun to generate a beam of electrons which is then focused through a series of electrostatic and electromagnetic lenses onto the sample. The sample then allows electrons to pass through and scatters others, based upon its composition and structure. The resulting beam of electrons is then, in our case, collected by a CCD camera. Images are then post-processed with software to measure structure and other characteristics. In order to create stacks of images to allow for the 3-dimensional reconstruction of the sample, ET is employed. This is done by taking 2 tilt-series of the sample, along the x and y axis. During a tilt-series, the sample is rotated by a set amount along an axis to positive and negative limit of tilt. This allows images to be taken through the sample section at different angles. With the addition of the tilt-series along a perpendicular axis, the two data sets can then be combined with software to create a 3-D reconstruction of the sample. ET is used to image the lens capsule and, more specifically, the type-IV collagen mesh-work of the lens capsule.

Sample preparation for EM and ET involved one method of cryofixation. The cryofixation for cryo-ET differs from the process used for EM and ET. Both are described in detail below. Briefly,

for ET and EM the samples are frozen using a high pressure freezer (HPF). By using a HPF, the sample is frozen under approximately 30,000 PSI to the temperature of liquid nitrogen (-196 ℃) in a few milliseconds. This process is used to prevent the formation of ice crystals, which would disrupt the native structure of the tissue and show up as artifacts in imaging. The samples then undergo freeze-substitution, described below, are embedded in resin, and sectioned. The difference from EM/ET to cryo-EM/cryo-ET is that instead of undergoing freeze-substitution, embedding, sectioning, and imaging (the last three being done at room temperature), the samples are kept at very low temperatures during sectioning and imaging, resulting in no need for freeze-substitution and embedding in resin. This allows for the imaging of a hydrated sample in its native state without possible alteration of the sample's structure. Cryo-EM/cryo-ET is a difficult technique and the process for our samples is still being figured out. The progress so far is presented below.

6.1   Sample Preparation

Anterior lens capsule was collected to be used for ET. This was done by first removing the cornea as previously described in the Puncture Testing of the Whole Lens Chapter. Then, while applying slight pressure to the whole globe, a small incision was made with a diamond-head scalpel in the anterior surface of the ocular lens, near the attachment of the zonules. By gently widening this incision with the scalpel, the interior lens fibers slide out, intact, from the slight pressure being applied to the globe. With the interior lens fibers removed, the anterior portion of the capsule is then lifted by a pair of tweezers inserted through the previously made incision. Once lifted, the anterior capsule is collected by using a pair of micro scissors to cut the capsule near the zonule attachments around the perimeter.

For EM/ET, the anterior lens capsule was then transported to the BalTec HPM 010 HPF (see Figure 6.1) in a vial of Alcon BSS.

At the HPF, a circular sample was cut out with a 2 mm diameter dermal punch. The sample was then placed in 150 mM mannitol in Alcon BSS for several minutes prior to freezing. The HPF specimen carrier (100 μm circular stainless steel well) was then filled with the same solution. The

Figure 6.1: BalTec HPM 010 High Pressure Freezer.

sample was then placed in the carrier and frozen in the HPF. The sample was then immediately transferred to a container of liquid nitrogen in which the carrier was removed. The sample was kept in liquid nitrogen as it was transported to the freeze-substitution vessel. The freeze-substitution process was done with an acetone solution including 2% osmium tetroxide and 0.1% uranyl acetate. The sample and solution were kept at -90 ℃ over 36 hours while the substitution took place. The samples were then warmed to room temperature over 18 to 24 hours and washed with acetone before being fixed in epoxy resin for sectioning. The samples were sectioned on a Microtome to a thickness of 60-80 nm for EM and 150 nm for ET. Sections were placed in EM grids and taken to the scope for imaging.

For cryo-ET, dome-shaped carriers were used during high pressure freezing. These carriers were then mounted using a special chuck into the cryochamber of an Ultracut UCT microtome (Leica Inc., Vienna, Austria). Here they were cut into sections approximately 100 nm thick at -155 ℃. After being placed on a grid, the sections were transported in liquid nitrogen to the cryo-transmission electron microscope. A cryo-holder (Gatan Inc., Warrendale, PA, USA) was used in the scope which kept the temperature of the sample at -180 ℃.

6.2   Experimental Setup

For the initial EM images, a Phillips CM-100 Transmission Electron Microscope (see Figure 6.2) was used in the Molecular, Cellular, and Developmental Biology (MCDB) department at CU Boulder. The Phillips CM-100 TEM is equipped with a 100kV electron gun. It is setup to image plastic sections.

For the ET images, a FEI Tecnai TF30 300kV IVEM microscope (see Figure 6.3) was used in the The Boulder Laboratory For 3-D Electron Microscopy of Cells at CU (bio3d.colorado.edu). In its function at Boulder, this scope is used for both plastic and frozen-hydrated (cryo) electron tomography.

Figure 6.2: Phillips CM-100 Transmission Electron Microscope.

Figure 6.3: FEI Tecnai TF30 300kV IVEM Microscope.

6.3   Experimental Method

On the Phillips CM-100 TEM, images were taken at various magnifications (shown on each image in the results) of the initial samples to help provide an idea of what was visible with EM. The electron gun was set at 80kV for imaging of the thin, transparent samples to provide the most

contrast. The power of the electron beam was adjusted based off of the magnification to limit damage to the sample. Images were saved in .tiff format.

On the FEI Tecnai TF30 300kV IVEM microscope, the software SerialEM was used to take tilt-series (developed by The Boulder Laboratory For 3-D Electron Microscopy of Cells). Tilt-series were taken at 23,000x magnification and from -60° to 60° on each axis in steps of 1°. The tilt-series were then aligned and assembled using IMOD (a software package developed by The Boulder Laboratory For 3-D Electron Microscopy of Cells). IMOD contains image processing, modeling and display programs specifically designed for tomographic and 3D reconstruction of EM images. In the reconstructed data, the space between images/slices was 1 nm. IMOD was also used for some preliminary modeling of the type-IV collagen mesh-work, shown in the results. "Nodes" of the mesh-work were selected manually based off of the darkness compared to the surrounding area of the image and apparent fibers coming into the node. Node coordinates and connectivity were exported from IMOD to be used in a future model in Tahoe.

6.4   Results

Below are images of the lens capsule taken with both EM and ET. Figure 6.4 is a picture from our initial attempts with EM. We aimed for a comparable settings that were used by Barnard [Barnard et al., 1992] in their images of a lens capsule replica. Figure 6.5 shows one of our initial ET attempts. The sample imaged was approximately 150 nm thick taken from the anterior portion of the porcine lens capsule. Figure 6.6 is a zoomed-in view of a section of the image in Figure 6.5. It has a scale bar of 100 nm. Figure 6.7 shows another sample that was imaged with ET with a scale bar of 100 nm.

60.00 nm
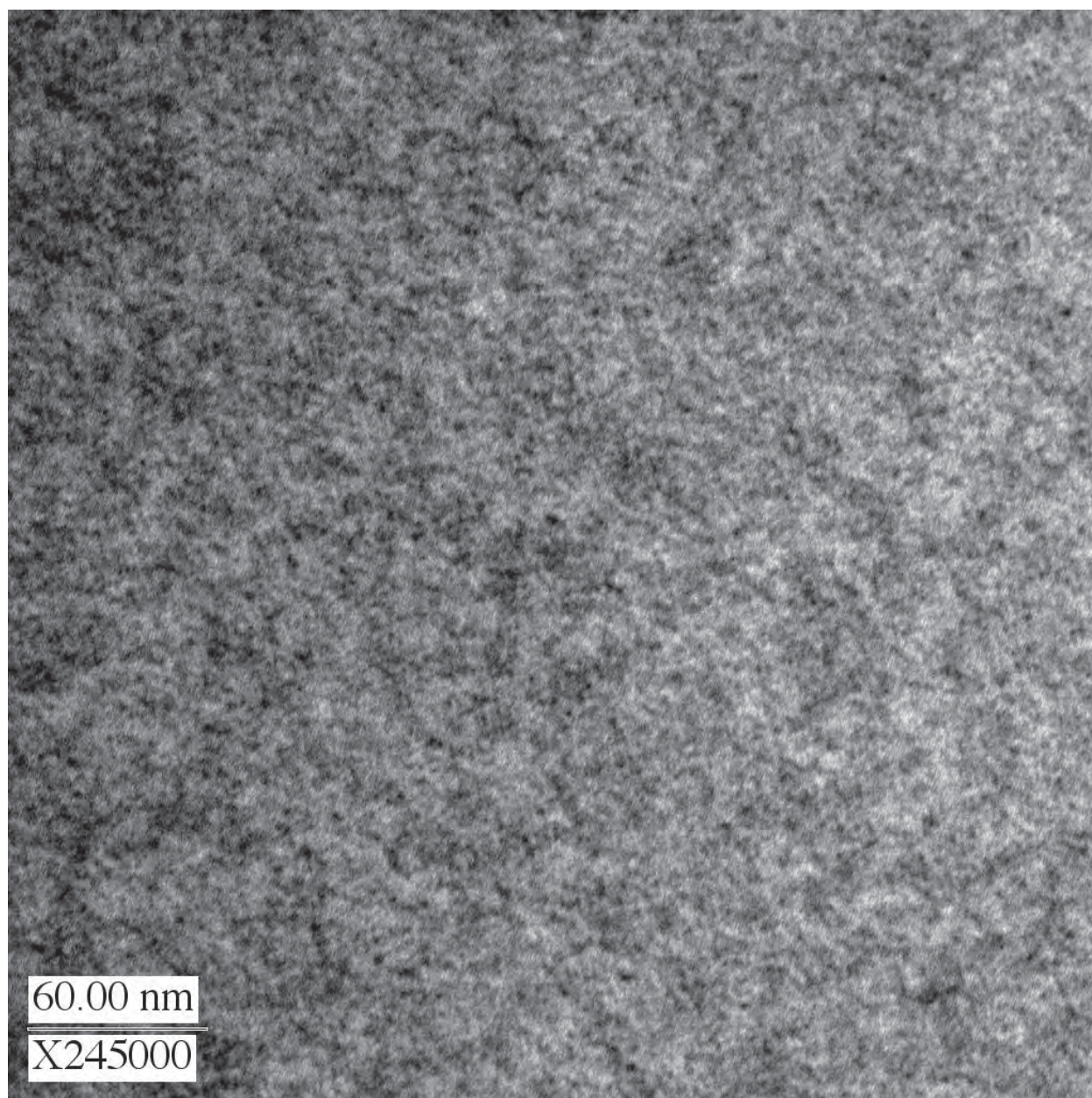
X245000

Figure 6.4: Initial Image Collected on Phillips CM-100 at 245,000X with 60 nm scale bar.
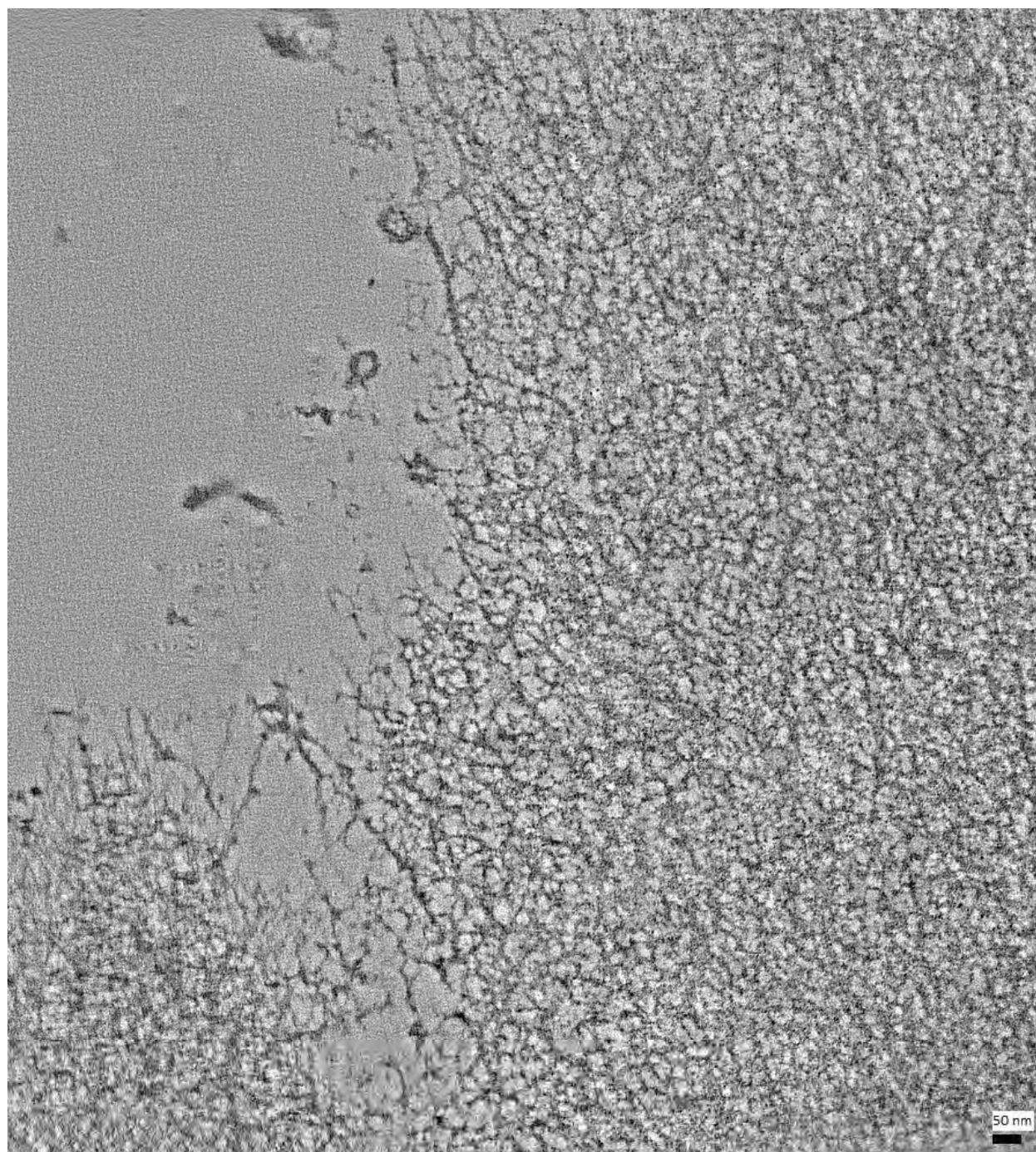
Figure 6.5: Reconstructed Image from Tilt-Series: taken at 23,000X, 1 image per degree from -60° to 60° with 50 nm scale bar.
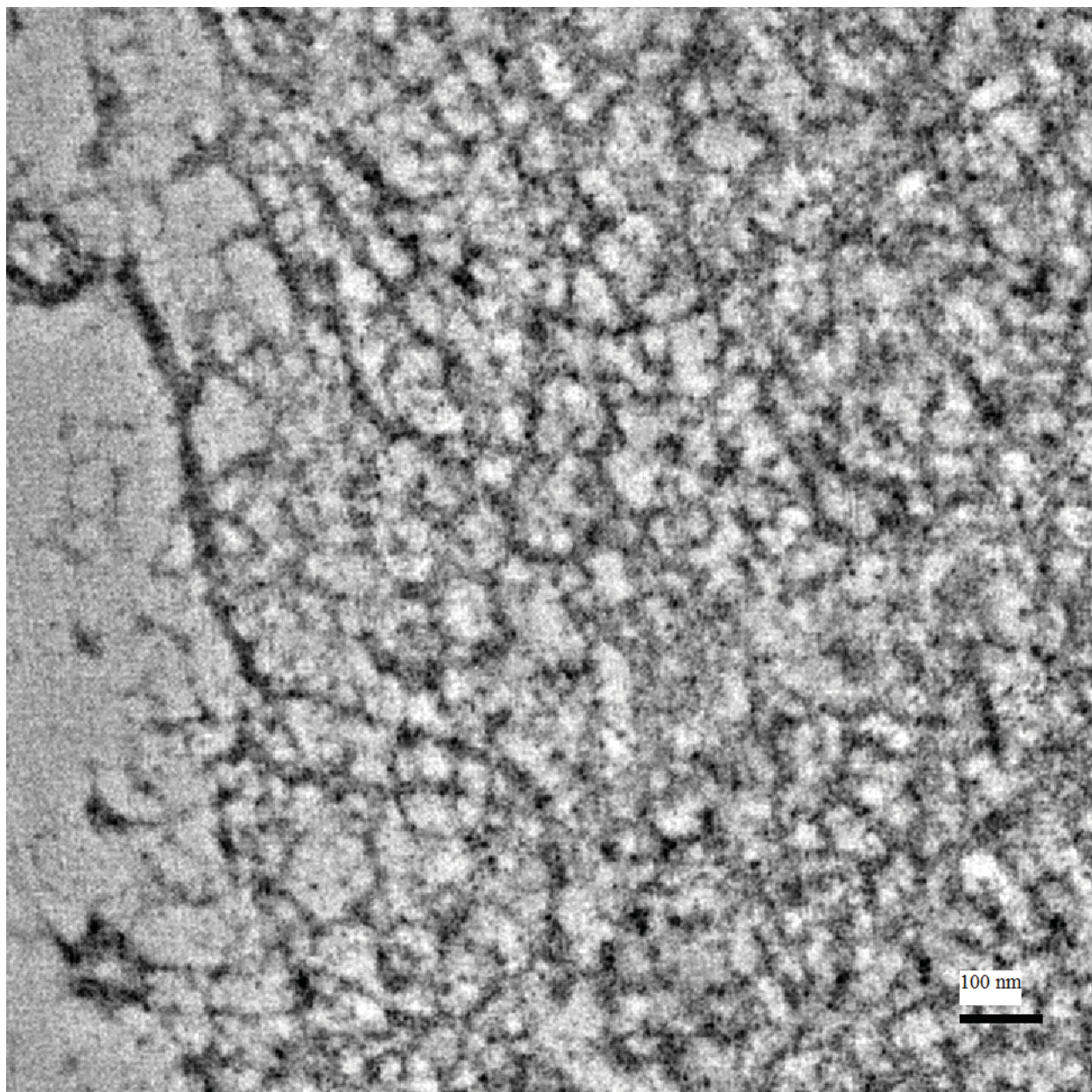
Figure 6.6: Zoomed in Region of Reconstructed Image from Tilt-Series: taken at 23,000X, 1 image per degree from -60° to 60° with 100 nm scale bar.
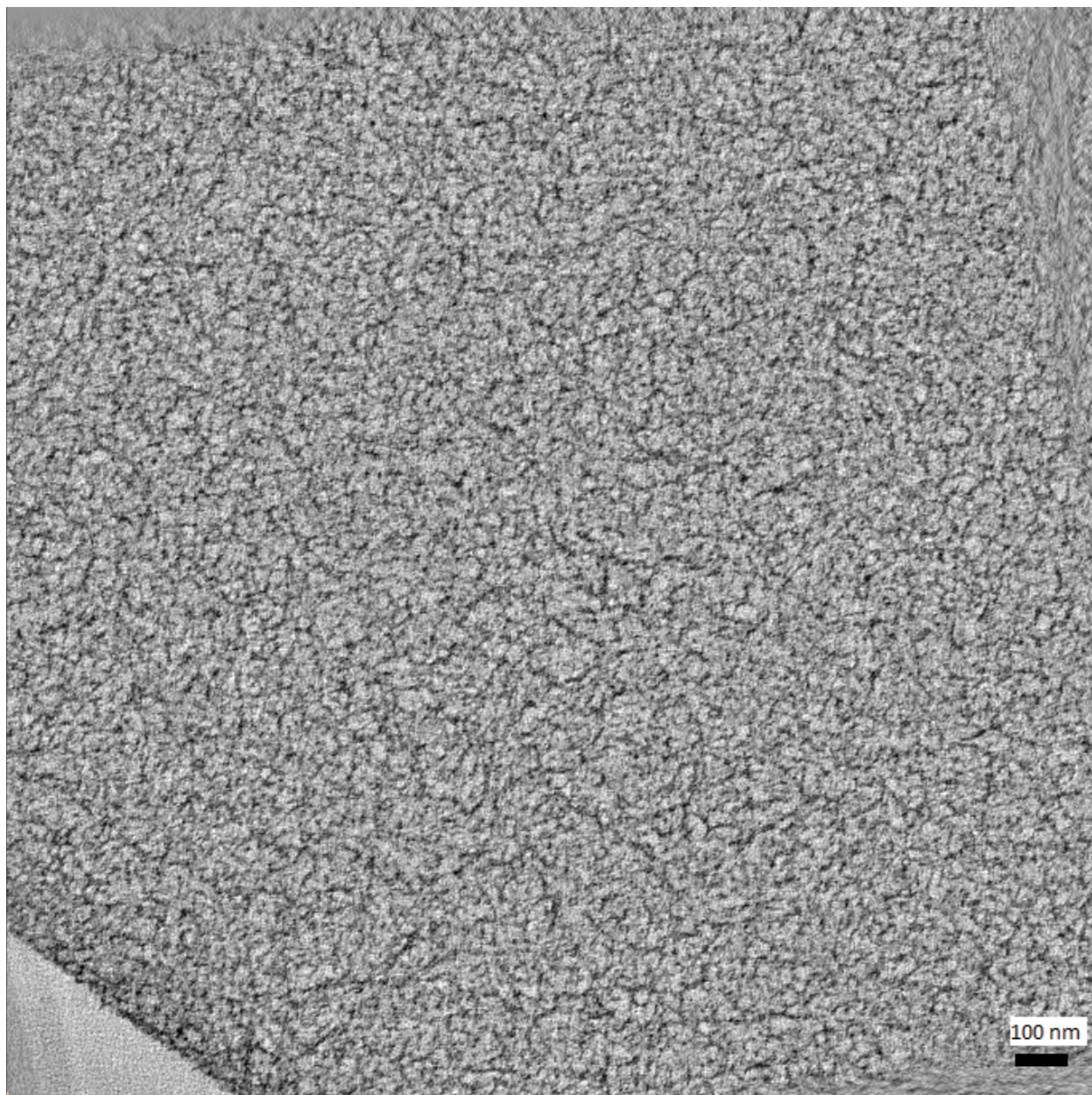
Figure 6.7: Reconstructed Image from Tilt-Series: taken at 23,000X, 1 image per degree from -60° to 60° with 50 nm scale bar.

6.5   Discussion

Looking at Figure 6.4, there is little to no definition and no apparent structure visible. While we did mimic Barnard's [Barnard et al., 1992] imaging settings, we opted to not perform the extraction and platinum deposition that was done to their samples so we could better preserve the native structure. It appears that without extraction, no visible structure can be seen using 2-D TEM. These results led us to trying ET to image the lens capsule. Upon the initial examination of our ET results in Figure 6.5, we were inclined to believe that we had successfully imaged the type-IV collagen mesh-work structure of the porcine lens capsule. Furthermore, the comparison of the size of the fibers and gaps seen in our images to those of Barnard [Barnard et al., 1992] bolstered our belief that we had imaged the mesh-work structure. We imaged another sample and again, saw similar results (see Figure 6.7). However, after consulting with additional microscopists within the The Boulder Laboratory For 3-D Electron Microscopy of Cells, we cannot yet positively determine whether what we are seeing in the images is structure or artifact from the freezing/freeze-substitution process. Currently, work is being done to image more samples using the same process as well as using cryo-ET, which will hopefully provide us samples with the least possible artifacts in a nearest native state as we can achieve. Preliminary modeling work is being done using IMOD on the current images (see Figure 6.8). Whether the current images are showing structure or not, they are good practice for streamlining the modeling process. The nodes of the mesh-work are selected manually and the user searches for connections in both the x-y plane and through the stack in the z-axis. The node coordinates and connectivity are exported from IMOD to be processed by FEA simulation software.
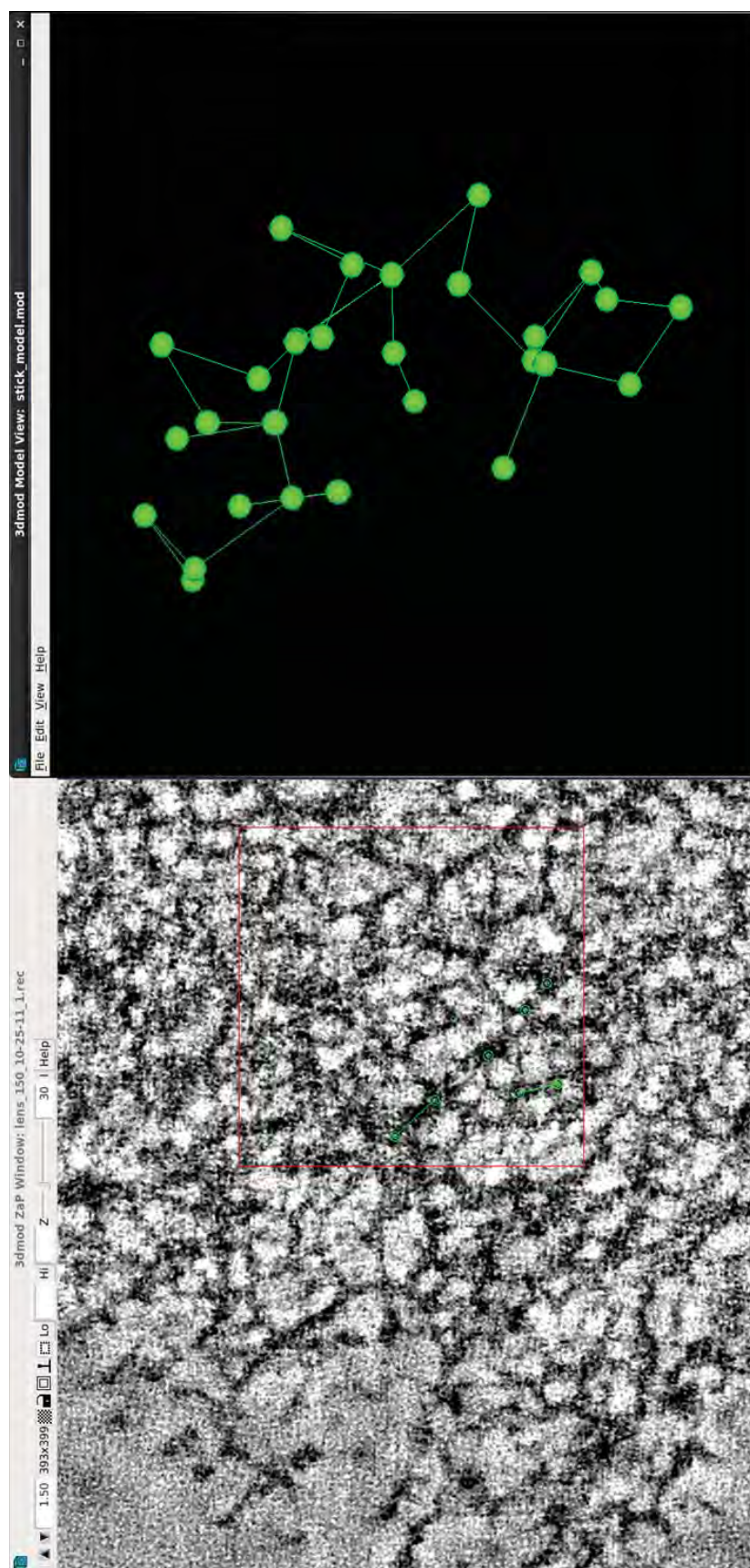
Figure 6.8: Modeling of Perceived Structure from ET Images using IMOD.

Chapter 7

Confocal Scanning Laser Microscopy of the Lens Fiber Cells

As mentioned earlier, the reason for using confocal LASER scanning microscopy (CLSM) is to image the ultra-structure of the interior lens fibers in 3 dimensions. The confocal images can be processed with software to recreate the structure of the lens fibers, which can then be employed in the computational mechanical model. CLSM works by staining a sample with binding-specific fluorescent molecules. These agents are then stimulated by LASER light and the resulting luminance is recorded. Since multiple wavelengths of LASER can be used, multiple agents bound to different sites can be imaged on one sample. Images of each fluorophore are taken on separate channels (see Figure 7.1).

Using post-processing software, the color can be added to the channels to help view the different structures and the channels can be combined into one image (see Figure 7.2 and Figure 7.3). Of interest for the project were imaging the actin that is found in the structure of the crystalline lens fibers (to model the lens fiber shape and size) and the nuclei found in the epithelial cells along the anterior portion of the lens (to help orient the images and provide a landmark to reference).

7.1   Sample Preparation

Upon receipt of eyes from Animal Technologies, Inc., the whole ocular lens was removed, as described previously in the Puncture Testing of the Whole Lens Chapter. The lenses were then placed in a sample tray and fixed with 4% paraformaldehyde for 36 hours at room temperature. After fixation, the lenses were washed in phosphate-buffered saline (PBS) and sectioned using a
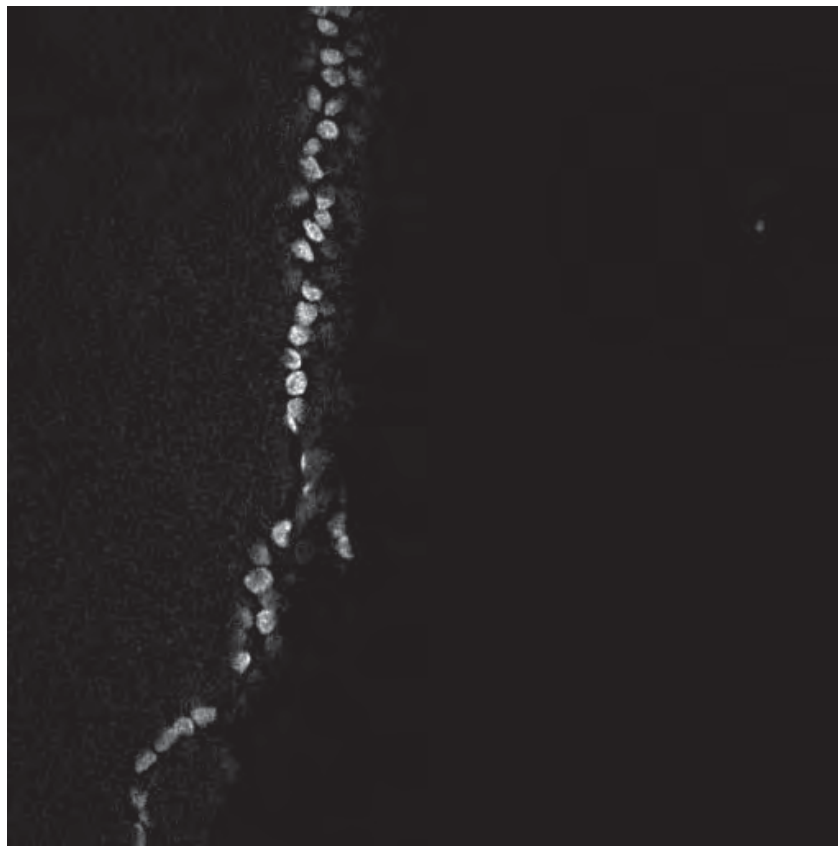
(a) Channel 1 Showing DAPI Staining of Porcine Lens Capsule.
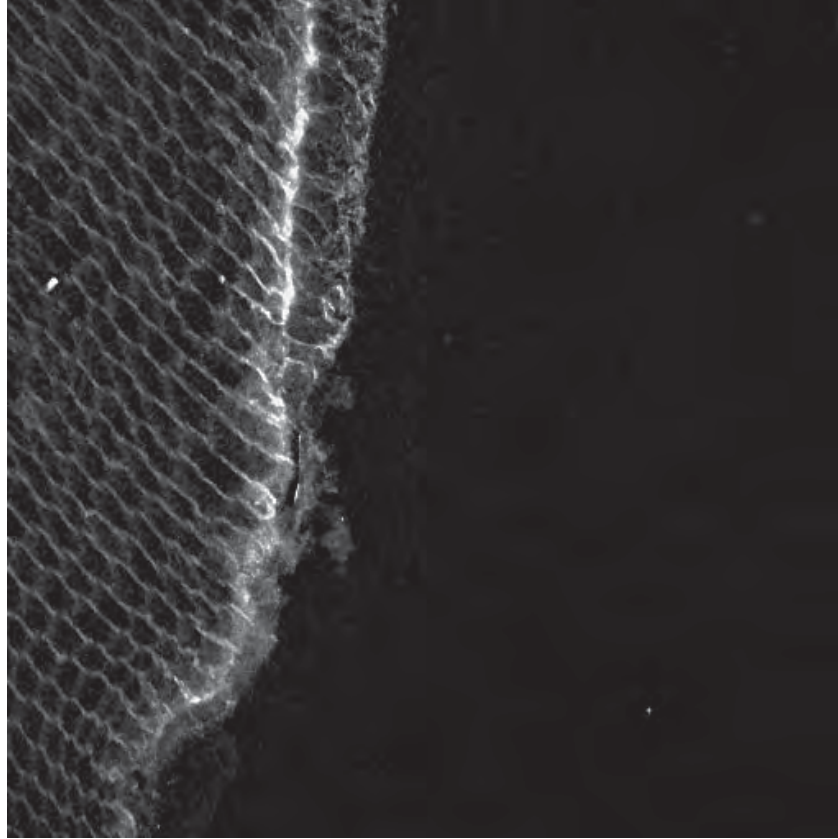
(b) Channel 2 Showing Phalloidin Staining of Porcine Lens Capsule.

Figure 7.1: Confocal LASER Scanning Microscopy Images of Porcine Lens Capsule.
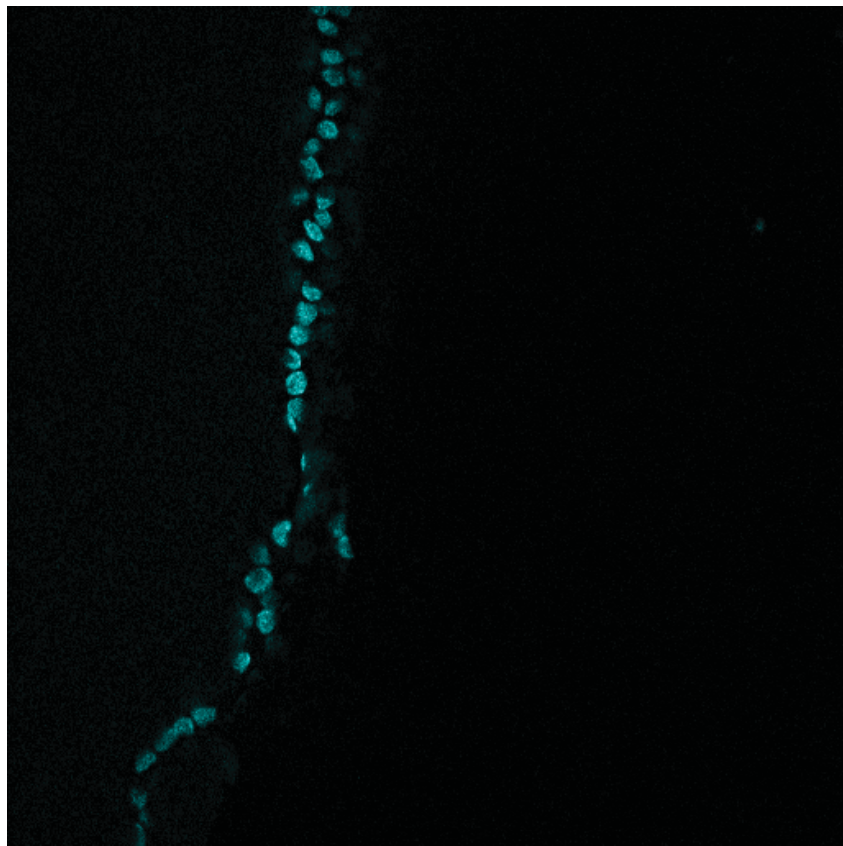
(a) Channel 1 Showing DAPI Staining of Porcine Lens Capsule After Color Addition Through Post-Processing.
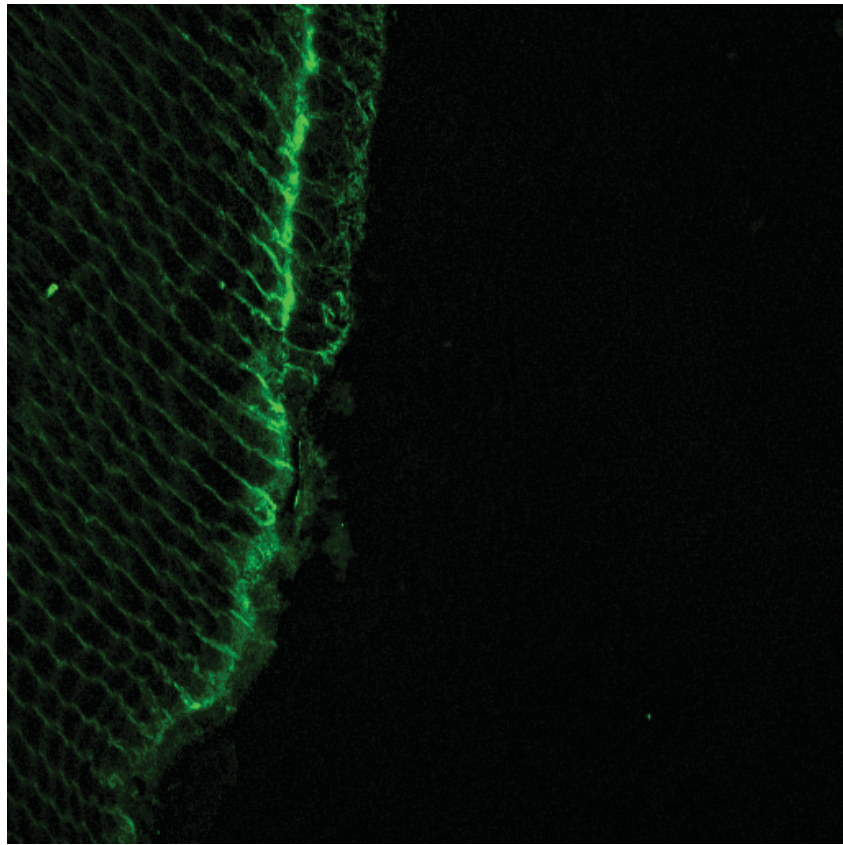
(b) Channel 2 Showing Phalloidin Staining of Porcine Lens Capsule After Color Addition Through Post-Processing.

Figure 7.2: Confocal LASER Scanning Microscopy Images of Porcine Lens Capsule After Color Addition Through Post-Processing.
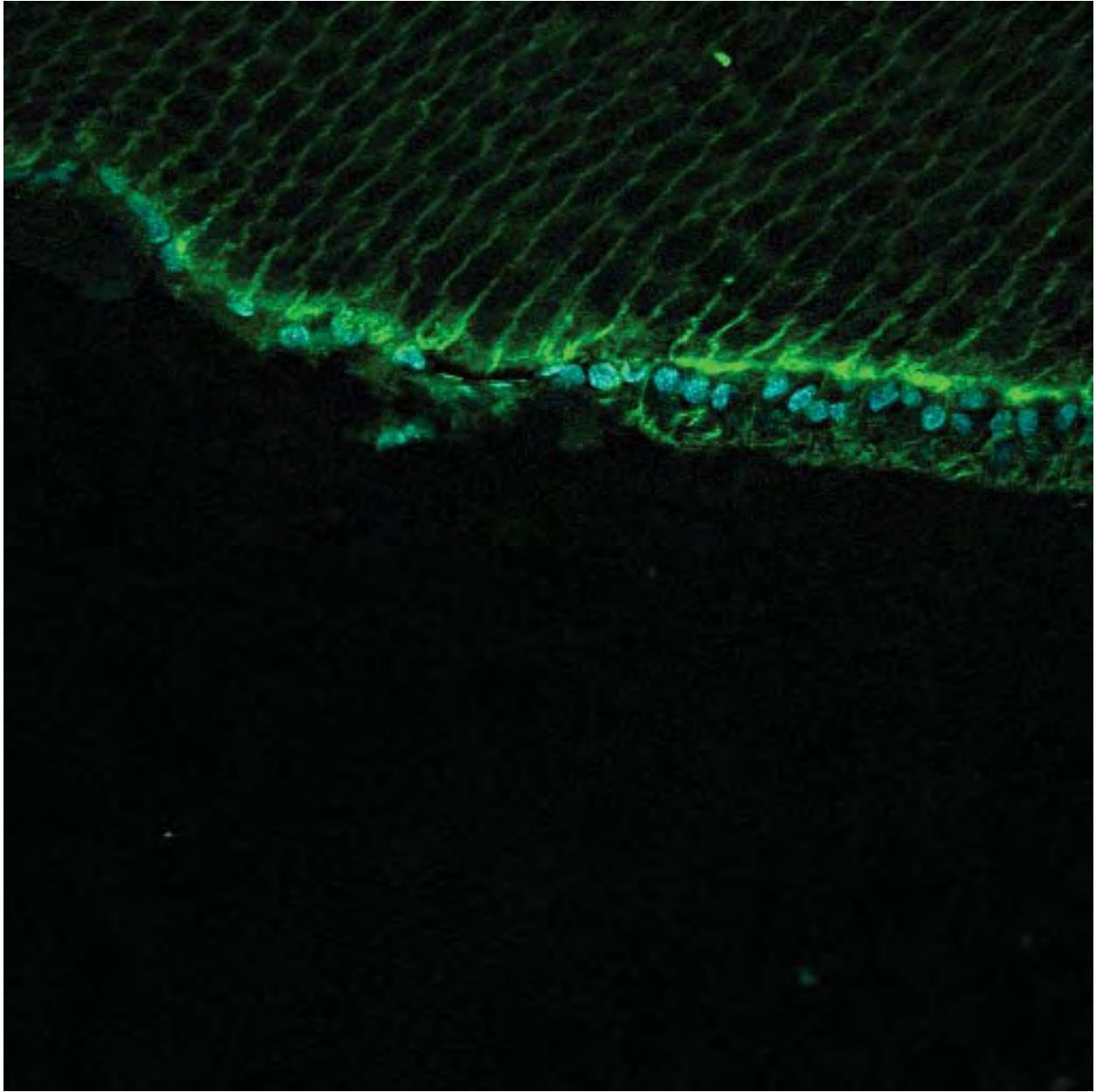
Figure 7.3: Channels 1 & 2 of Confocal LASER Scanning Microscopy Images of Porcine Lens Capsule Combined Into Composite Image With Post-Processing.

Vibratome to sections approximately 70 μm thick. To permeabilize the cells, the lens sections were blocked with phosphate-buffered saline Triton X-100 (PBST, 0.2% Triton X-100) for 12-18 hours at room temperature. The sections were then stained with Alexa Fluor® 488 Phalloidin from Life Technologies (www.lifetechnologies.com) in PBST (dilution 1:200). Sections were stained for 12-18 hours and then washed with PBST 5 times for 20 minutes each wash on an orbital shaker table. This was followed by one wash of PBS for 10 minutes on an orbital shaker table. Next, the sections were stained with DAPI (4',6-Diamidino-2-Phenylindole, Dihydrochloride) from Life Technologies (www.lifetechnologies.com) diluted in PBS (1:1000) for 15 minutes on an orbital shaker table. After the DAPI staining, the sections were washed 4 times in PBS for 10 minutes each on an orbital shaker table. The sections were then mounted on Fisherbrand Super Frost Plus microscope slides with Fluormount-G from Southern Biotech for imaging.

7.2   Experimental Setup

For imaging, an Olympus Fluoview FV1000 Confocal Microscope with a motorized stage was used (see Figure 7.4). Three lenses were used for imaging: 20X in air with a numerical aperture (NA) of 0.75, 40X in oil with a NA of 1.30, and 100X in oil with a NA of 1.40. Excitation LASERs of wavelengths 405 nm and 488 nm were used for the DAPI and Phalloidin, respectively.

Figure 7.4: Olympus Fluoview FV1000 Confocal Microscope.

7.3 Experimental Method

Olympus' FV1000 ASW software was used to take the images. Details for each image are included in the captions. Images were exported from the FV1000 ASW software and were processed using ImageJ (rsbweb.nih.gov/ij/) and Fiji (fiji.sc).

7.4 Results

Below are the confocal images of the anterior porcine lens capsule. For purposed of determining the orientation of the samples, the cells stained with DAPI (cyan in the images) are located along the anterior surface of the lens capsule. These sections were cut parallel with the anterior pole/posterior-pole axis.
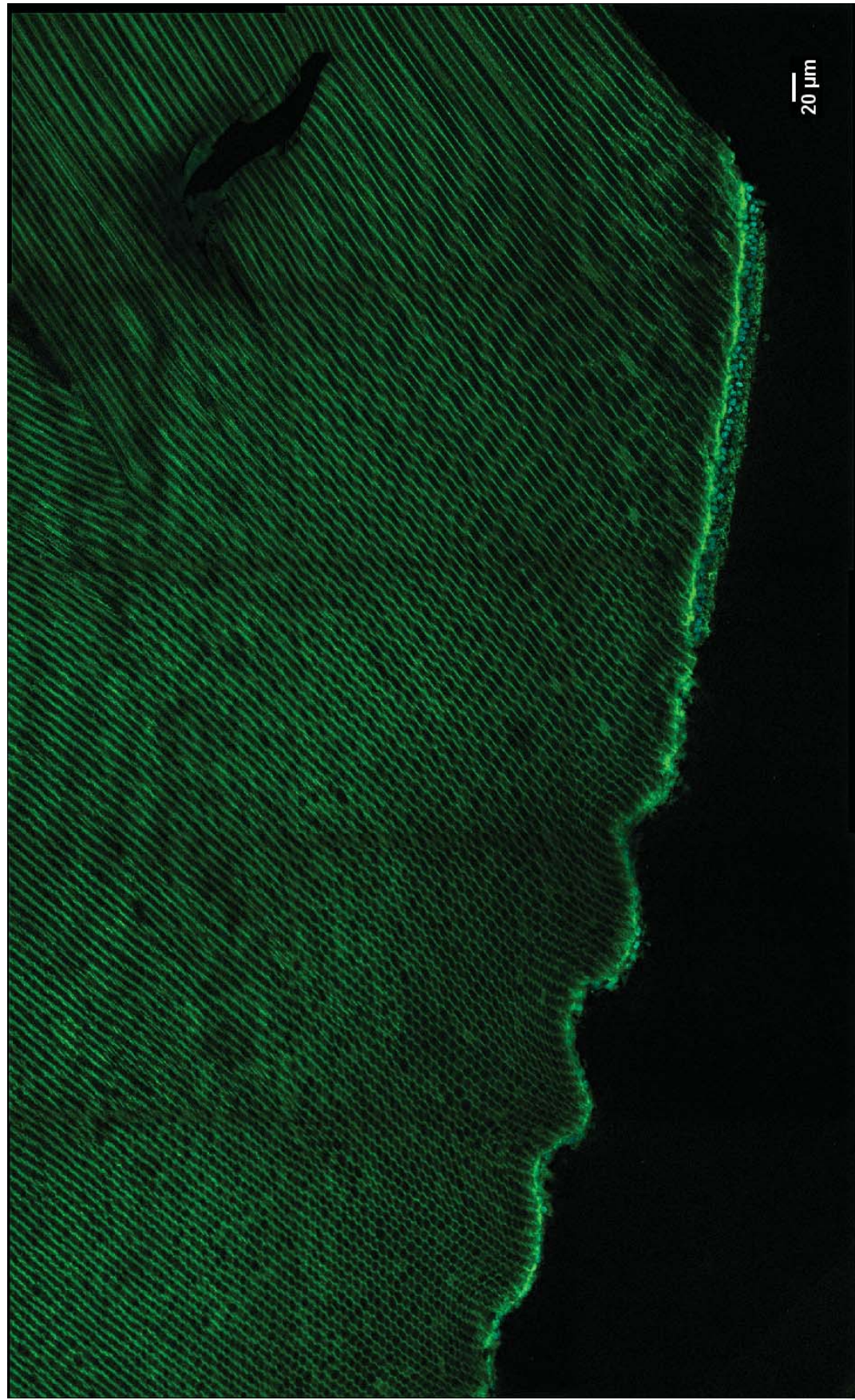
Figure 7.5: Confocal Image of Lens Fibers: 3x5 stitched image, each individual image was taken with the 40x(NA=1.30) objective in oil. Each image is 512 x 512 pixels and 317.331 x 317.331 μm, resulting in an overall image size of 1586.655 x 951.993 μm. The anterior surface can be identified at the bottom of the image by the nuclei stained with DAPI shown in cyan. The waves seen on the bottom of the sample are artifacts from the sectioning process. Notice the fine, honeycomb-like structure of the lens fibers in the bottom left area of the tissue.
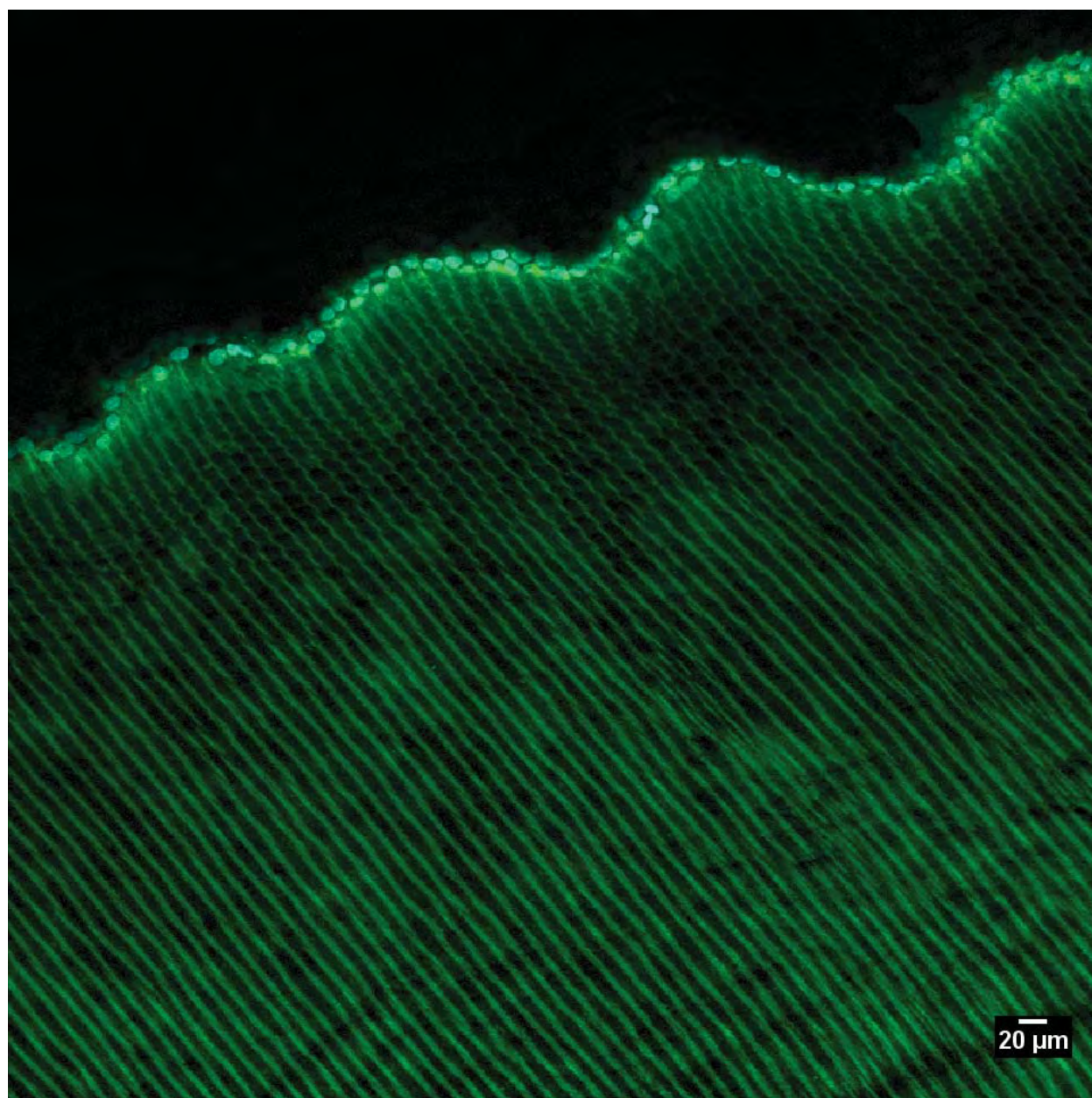
Figure 7.6: Confocal Image of Lens Fibers: Image was taken with the 20x(NA=0.75) objective in air. The image size is 800 x 800 pixels, or 635.205 x 635.205 μm. Again, the anterior surface of the samples is identified by the stained nuclei in cyan. The fine structure of the lens fibers can be seen in the upper portion of the of the sample.
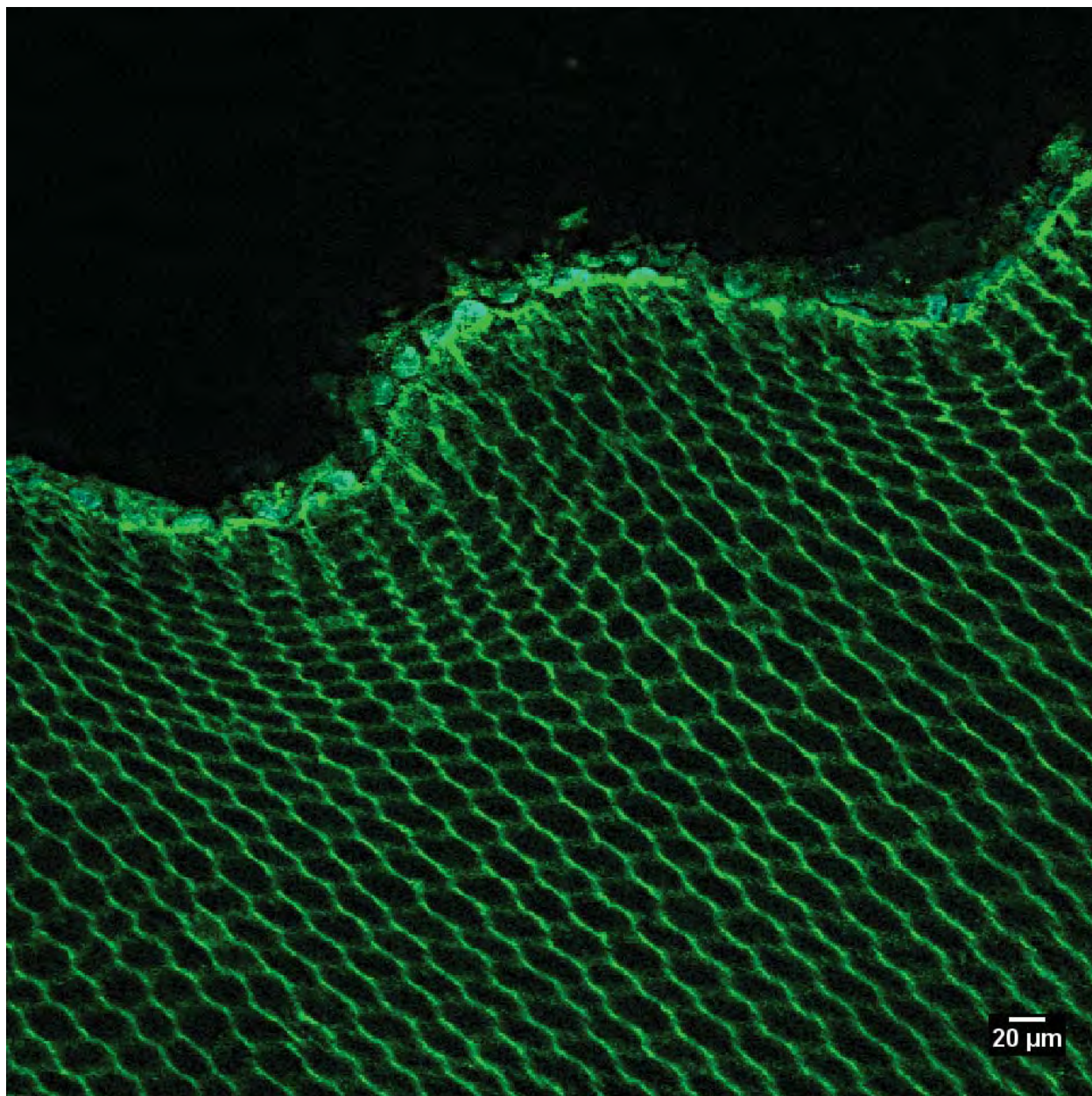
Figure 7.7: Confocal Image of Lens Fibers: Image was taken with the 40x(NA=1.30) objective in oil. The image is 512 x 512 pixels and has a size of 317.331 x 317.331 μm. The the lens fiber structure appears to be somewhat regular, with an exception along the anterior surface. This could be due to deformation of the tissue during the sectioning process.
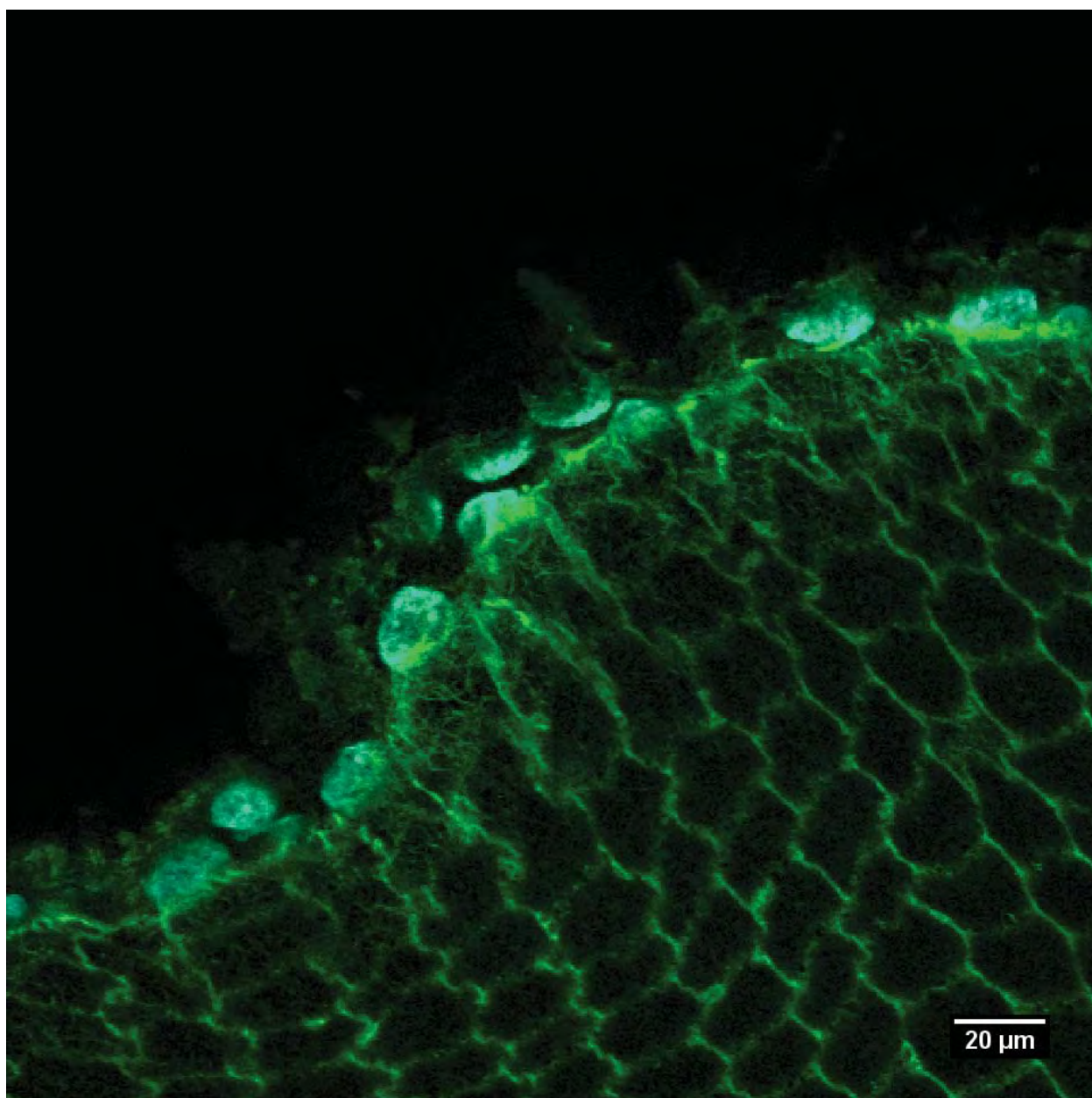
Figure 7.8: Confocal Image of Lens Fibers: Image was taken with the 100x(NA=1.40) objective in oil. The image is 512 x 512 pixels and has a size of 126.728 x 126.728 μm. This image provides a detailed view of the lens fiber cells near the anterior surface.
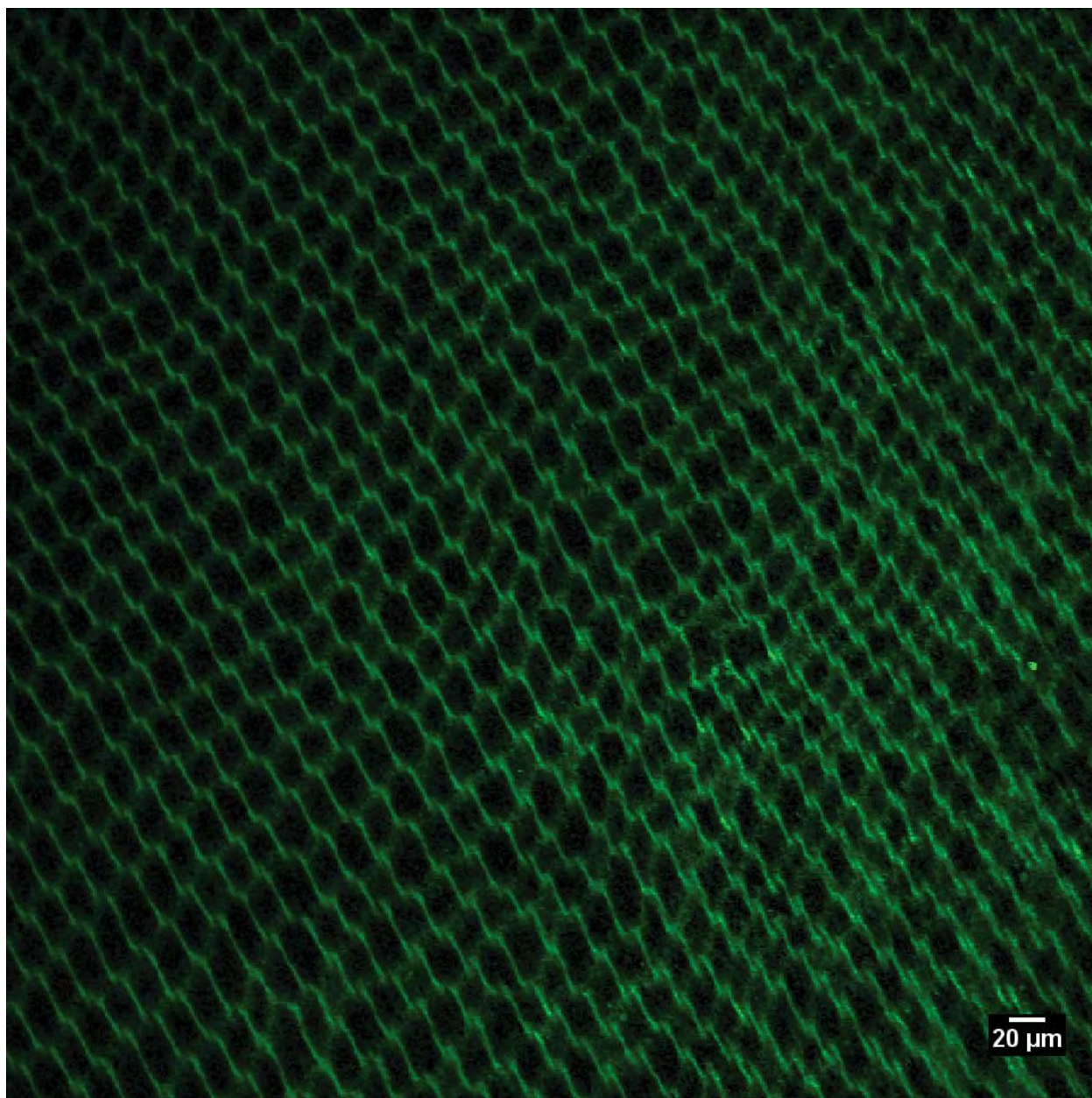
Figure 7.9: Confocal Image of Lens Fibers: Image was taken with the 40x(NA=1.30) objective in oil. The image is 512 x 512 pixels and has a size of 317.331 x 317.331 μm. Lens fiber structure moving towards the middle of the section.

Figure 7.10: Confocal Image of Lens Fibers: Image was taken with the 40x(NA=1.30) objective in oil. The image is 512 x 512 pixels and has a size of 317.331 x 317.331 μm. The structure of the lens fibers is harder to distinguish. This could be due to inadequate staining in the middle of the sample.
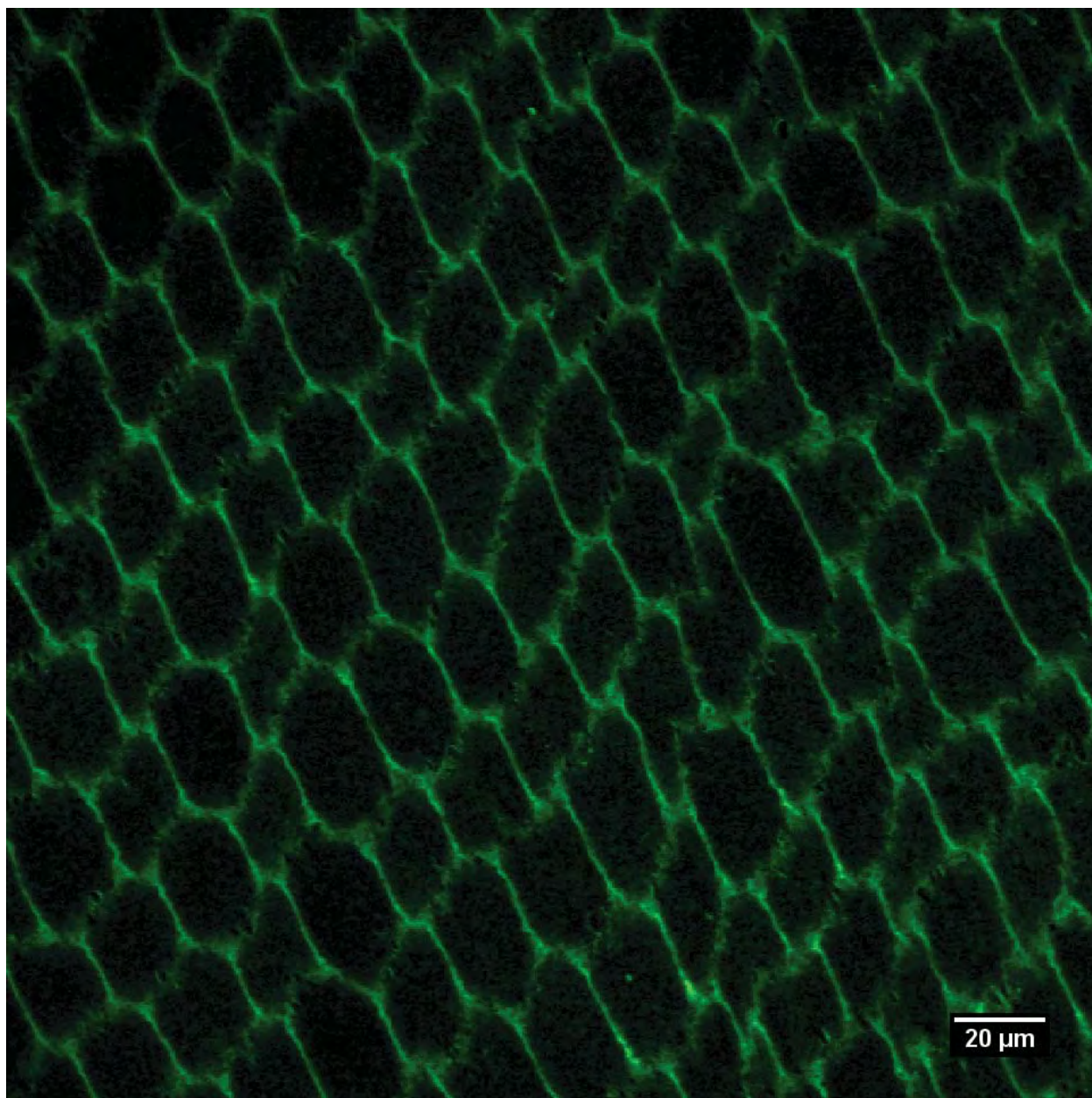
Figure 7.11: Confocal Image of Lens Fibers: Image was taken with the 100x(NA=1.40) objective in oil. The image is 512 x 512 pixels and has a size of 126.728 x 126.728 μm. This image provides a detailed view of the lens fiber cells towards the middle of the section.
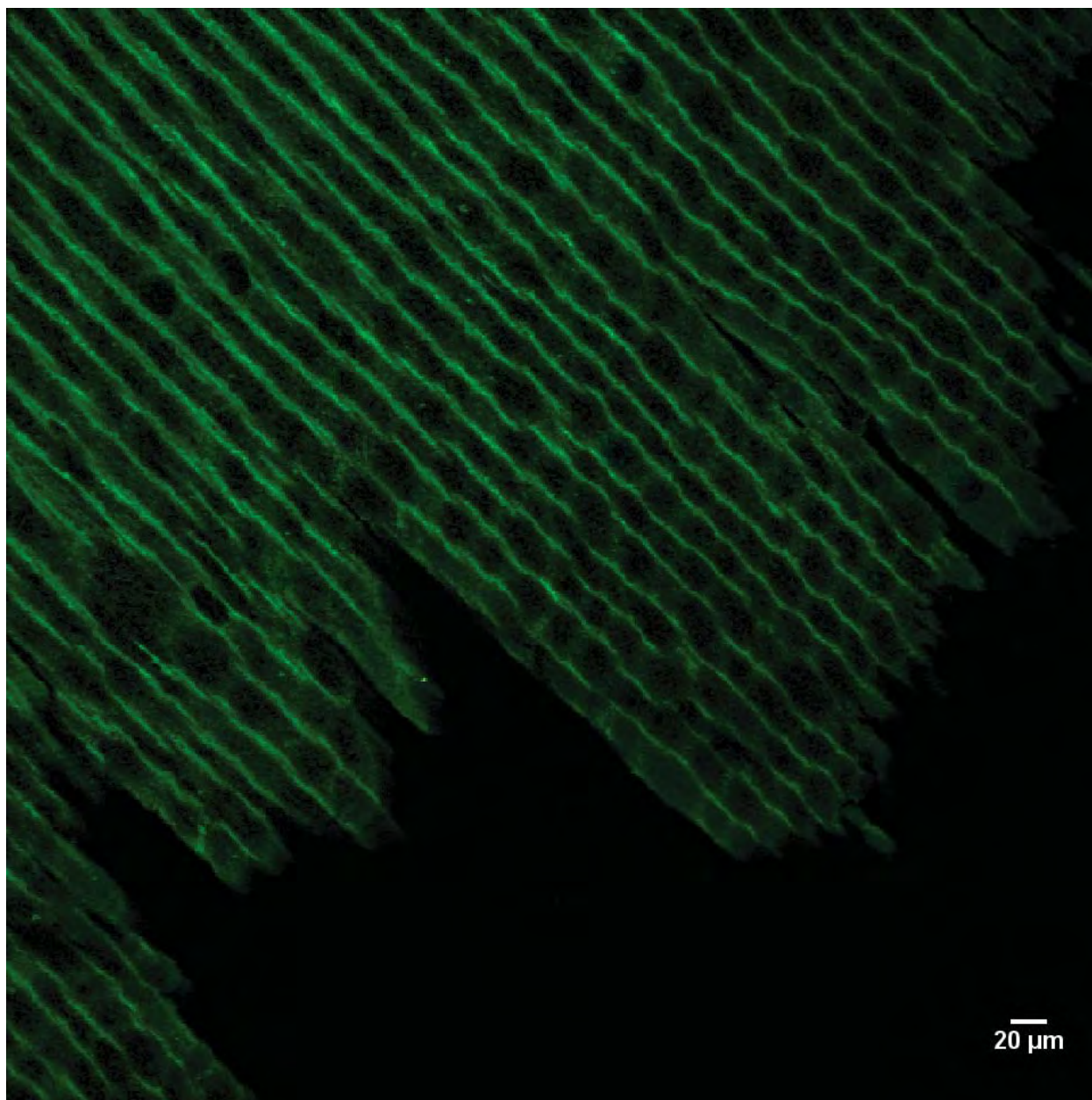
Figure 7.12: Confocal Image of Lens Fibers: Image was taken with the 40x(NA=1.30) objective in oil. The image is 512 x 512 pixels and has a size of 317.331 x 317.331 μm. Image shows area where lens fibers were torn, near edge of sample.
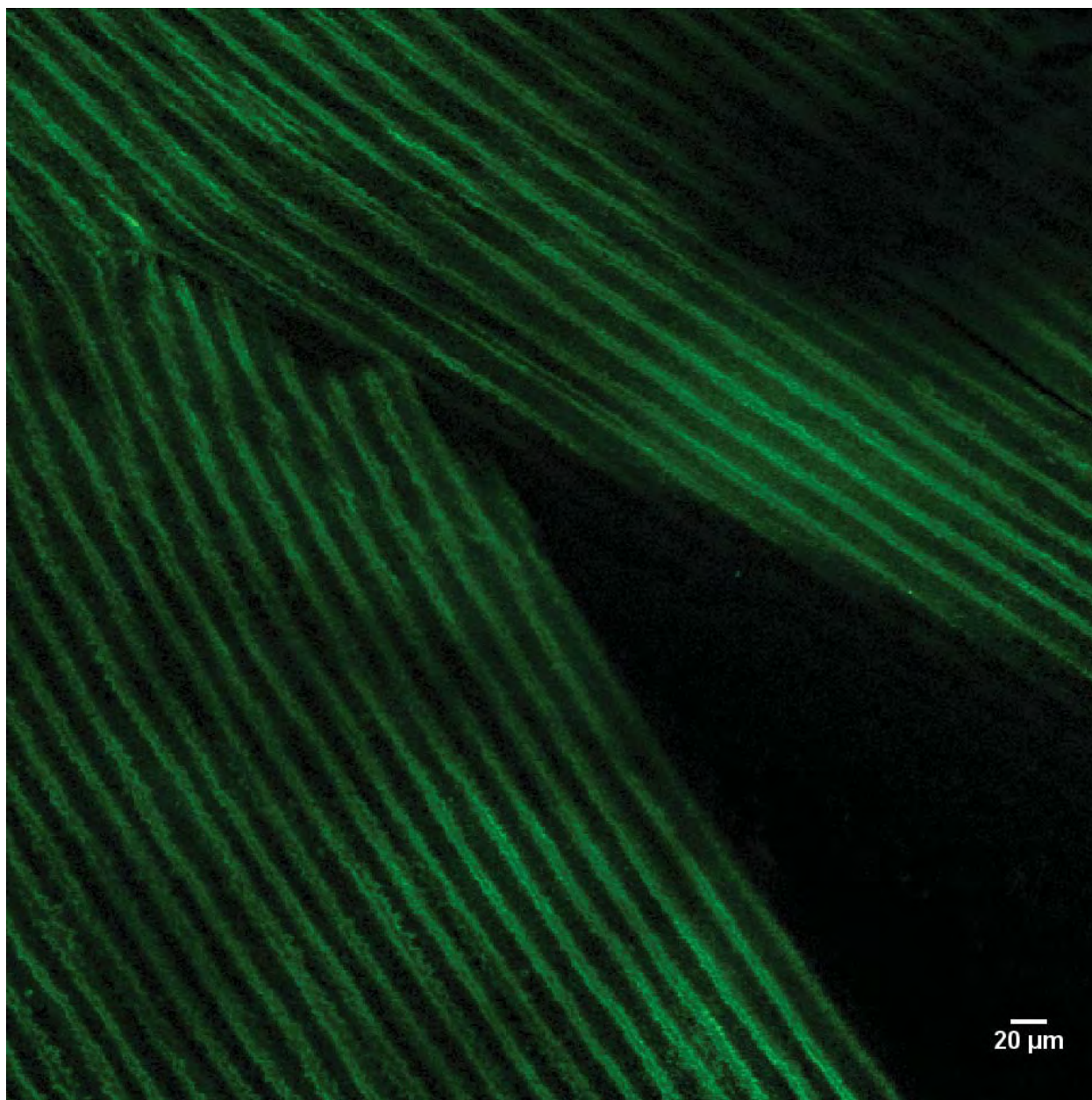
Figure 7.13: Confocal Image of Lens Fibers: Image was taken with the 40x(NA=1.30) objective in oil. The image is 512 x 512 pixels and has a size of 317.331 x 317.331 μm. Potentially another tear in the sample, cleaner than in Figure 7.12.

7.5   Discussion

Looking at Figure 7.5, the structure of the lens fibers is easily observed. The lens fibers appear to be arranged in a fine honeycomb-like pattern, especially near the bottom of the tissue section. The waviness of the anterior surface of the section is believed to be caused by the sectioning process. The little definition of the honeycomb-like structure further from the edge of the sample could be from inadequate staining of the more interior lens fiber cells. It could also be from the angle of the lens fibers in relation to the plane of sectioning. If the fibers are more aligned with the plane of sectioning, they can appear as long channels, instead of hexagonal cross-sections. Figure 7.6 provides a better view of the structure near the anterior surface of the sample. In Figure 7.7 the honeycomb-like structure of the lens fiber cells appears rather regular in size and spacing, with exception of the cells near the anterior surface. Figure 7.8 shows the non-regular cells near the anterior surface. The different size of these cells could be a result of compression and deformation from the sectioning process. On the other hand, the size difference could be attributed to the formation of new fiber cells which occurs along the anterior lens capsule surface.

The area imaged by Figures 7.9, 7.10, and 7.11 were taken towards the middle of the section. The semi-regularity of the lens fiber structure can be seen in Figure 7.9 and the approximate diameter of 20 μm can be see in Figure 7.11. It appears there is little difference in the lens fibers from the more exterior regions to the more interior regions. It is important to note that these images are of sections from the cortex and do not include the nucleus of the lens fiber cells.

Figure 7.12 shows an area of the section that appears to be torn away. This is of significant interest with regard to understanding how the lens, and specifically lens fibers are damaged. Figure 7.13 is an image of a potential tear in the section. Again, this is of interest in studying lens trauma and injury.

A method has been developed to begin gathering geometrical data from the confocal images of the lens fiber cells for use in the generation of an ocular model. The structure is manually identified by selecting apparent intersections of the lens fibers (nodes) and the connectivity between the nodes

(see Figure 7.14). These coordinates and connectivity are then exported for use in the finite element

modeling program Tahoe.
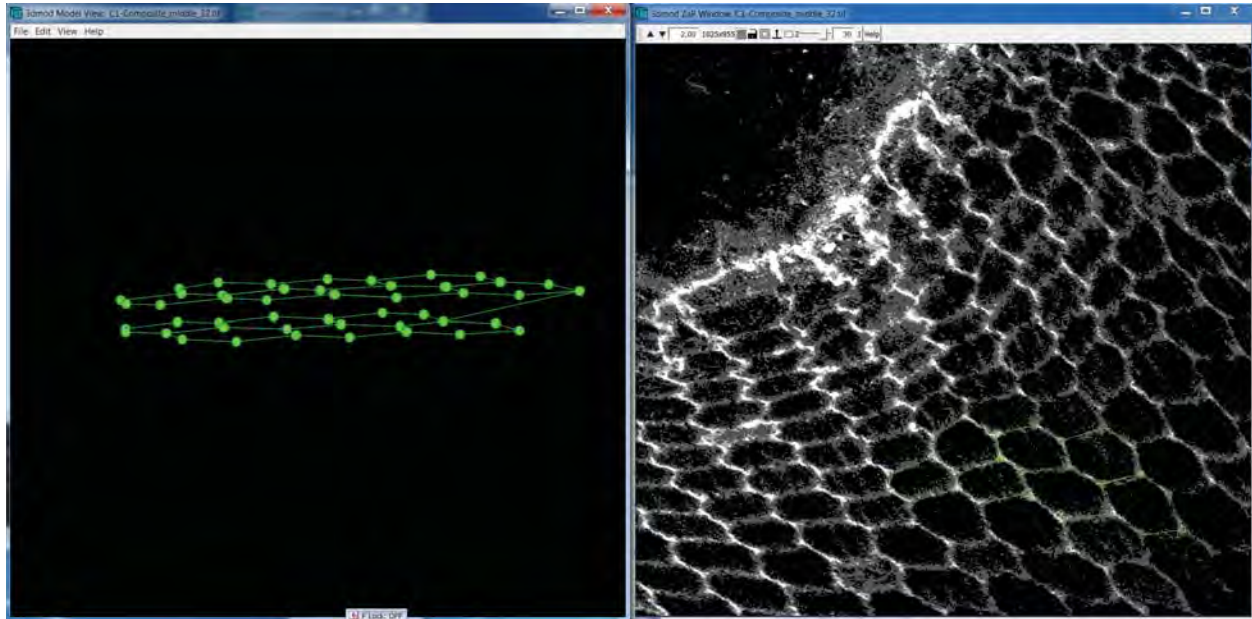
Figure 7.14: Modeling of Lens Fiber Ultrastructure using IMOD.

Chapter 8

Discussion

Progress has been made in regards to the determination of the material properties of the ocular lens. Our method for unconfined compression testing has produced good data. Preliminary fits have been completed for the preconditioned data. The calculated parameters show the older porcine lenses to be more viscous than the younger lenses that were tested. This complies with the theory that material properties of the lens change over time, possibly contributing to presbyopia. This change over time is supported by other research as well [Krag and Andreassen, 2003a]. We also noticed viscoelastic behavior in the whole porcine ocular lens. Additionally, data of lenses that did not undergo preconditioning has been generated to be fit and compare with the previous data. Preliminary models have been generated in Abaqus and Tahoe and will serve as a stepping stone to the creation of an ultrastructurally based computational finite element model. We also have developed a puncture testing method that has produced data that can be fitted from which to calculate material properties. A result of the testing is damaged tissue under controlled conditions that can be imaged and studied to investigate the mechanics of cutting, puncture, and IOFBs with regards to the lens. Our results support Yang's findings that the anterior lens capsule is stronger than the posterior lens capsule [Yang et al., 1998a]. A preliminary model of the puncture test has been developed in Abaqus as well. The nanoindentation of the anterior lens capsule in fluid is promising. The creep test data can be fit using Dakota and Tahoe, which will lead to the calculation of the material properties of the anterior lens capsule separate from the lens fiber cells. These calculations can then be used to verify the parameters from the compression and puncture

testing and allow back-calculation of the properties of the lens fibers. With additional testing, a strong data set can be developed, providing confidence in our material parameters for our model.

In terms of structure identification and geometrical data, the first steps have been made and with more work, we will have good data on which to base the model. The structure in the electron tomography images still remains to be confirmed. While they do look similar to the results produced by Barnard et al.'s imaging [Barnard et al., 1992], we want to be confident in our structure identification. A method has been developed to extract the coordinate data of the structure to include in our model. The confocal imaging has produced good images of the lens fiber structure. Our initial results show structure similar to that imaged by other work [Taylor et al., 1996]. A similar method for extracting the 3-dimensional coordinate data has been developed and the gathering of these data is currently in progress.

While more work remains to be done, much experimental progress has been made towards the generation of an ultrastructurally based computational finite element model. The work presented here is part of a larger project with the following research tasks: (1) the development of a model for type IV collagen mesh-work of lens capsule tissue; (2) the development of a multiscale model of the lens capsule in regards to its poromechanical characteristics; (3) the development of a multiscale lens fiber cell equivalent soft viscoelastic constitutive model of the internal lens substance; (4) unconfined compression testing of whole porcine lenses to estimate whole lens mechanical response; (5) nanoindentation testing on porcine lenses to approximate lens capsule parameters; and (6) imaging of lens fiber cell geometry using confocal laser scanning microscopy, and type IV collagen network ultrastructure in lens capsule using cryo-electron tomography. Significant work has been completed on tasks (4), (5), and (6) as well as limited preliminary modeling on tasks (1) and (2). The research described here contributes to the development of an ultrastructurally based computational finite element model that will contribute to the greater task of accurately modeling the lens to better understand accommodation, presbyopia, and ocular lens related injuries.

Chapter 9

Recommendations

9.1   Determine Material Properties from Data

While some parameter fitting has been completed, the data from the unconfined compression tests with no preconditioning and the puncture test data need to be fit as well. The same process used for the unconfined compression data with preconditioning can be used, with slight changes to the Tahoe setup. On top of fitting the other data, the constitutive framework should be adjusted and fine-tuned to better account for the lens's viscoelastic behavior, providing better fits and more accurate material properties or range of properties.

9.2   Additional Imaging and Modeling

More analysis needs to be done with the confocal images to provide more data on the structure of the lens fibers. This can be done with IMOD. Additional images of the lens should be taken to provide regional structure data throughout the lens. The lens fibers are already divided into 2 areas: the nucleus and the cortex. The structural differences of the two need to be found to include in a truly ultrastructurally based computational model.

With the ET images of the lens capsule, confirmation of whether what the images show are structure or artifact is needed. This can be accomplished through additional imaging and varying the freezing/preparation process, such as cryo-ET. Once the structure is identified, those images will need to be analyzed with IMOD to provide the structural data in a useful format to input into Tahoe. Again, the identification of the type-IV collagen mesh-work is important to accurately

model the lens capsule.

A large amount of work remains to be done in the modeling aspects of this research. Meshes of the lenses need to be generated with the information gathered from imaging. The sections of the model need to be decided on, such as anterior capsule, posterior capsule, lens fiber nucleus, and lens fiber cortex. The equations of the constitutive models for these different sections need to be adjusted and finalized. This can be done through further development of Tahoe, and is part of the current research.

9.3   Confocal Imaging of Deformed/Damaged Lenses

It would be of interest to image a deformed lens, whether in compression or being indented (not to failure), potentially from one of the puncture tips. This could be done by utilizing the existing compression and puncture testing setups to deform the lens. Once deformed, the lens could be held in that state with the MTS Insight II, and fixed with the paraformaldehyde used in the confocal specimen preparation. Imaging the lens in a deformed state could lead to increased understanding of how the lens fibers interact as the lens accommodates. This imaging could also provide information on how lens fibers respond to trauma, either from blunt force contact or by blast wave loading (percussive waves generated by explosions that load the eye).

Punctured lenses should also be imaged, specifically around the puncture site and along any tears that occur. The damaged lens capsule could be imaged using a similar process as described in the EM/ET chapter. The damaged lens fibers could be imaged using the same process used to take confocal images of the normal lens fiber cells. Data from these images could lead to increased understanding of the interaction between the lens and intraocular foreign bodies (IOFBs), potentially resulting in improved treatment options for IOFB injuries.

9.4   Posterior Lens Capsule Testing

Due to the differences between the anterior and posterior lens capsules, mainly thickness, curvature, and the lack of epithelial cells on the posterior lens capsule, the posterior lens capsule

needs to be tested as it's material properties may be different from those of the anterior lens capsule. This can be done through nanoindentation and ET. Nanoindentation can provide the material properties of the posterior lens capsule through creep testing similar to the testing done on the anterior lens capsule. This is important to include in the ultrastructurally based computational model to accurately predict the reactions of the lens.

9.5   Human Tissue Testing

While tests can be calibrated on animal tissue, testing of human tissue is the ultimate goal. All tests and imaging processes should be repeated for human tissue in order to identify the structure and material properties of the human ocular lens. The processes and testing fixtures should not need to be modified, with the exception of the puncture well for anterior puncture tests due to the smaller size of the human lens when compared to the porcine lens. Additionally, the use of human data can provide insight into structure and material property differences between gender, something not provided with the porcine tissue. Also, with the range of age of human tissue, a better understanding of accommodation in different ages as well as presbyopia can be achieved.

9.6   Higher Strain Rate Testing

In regards to the compression and puncture testing, higher strain testing should be performed. At higher loading rates, the lens may respond differently, resulting in different material properties. With the goal of being able to model blast wave loading on the eye, test data from high strain rate testing will ensure that the correct material properties are being used in the model. Currently a partnership is being formed with Dr. Tusit Weerasooriya at the Army Research Laboratory (ARL) in Aberdeen, Maryland, to utilize some of their high strain rate testing equipment. Intermediate strain rate (0.0125/s to 125/s) testing can be performed with their Bose Electroforce TestBench Instrument. Figure 9.1 shows a CAD drawing of a water bath and fixtures to allow for intermediate strain rate testing in fluid (Alcon BSS). To achieve high strain (greater than 125/s) testing, ARL has several split Hopkinson bar systems that could be utilized.
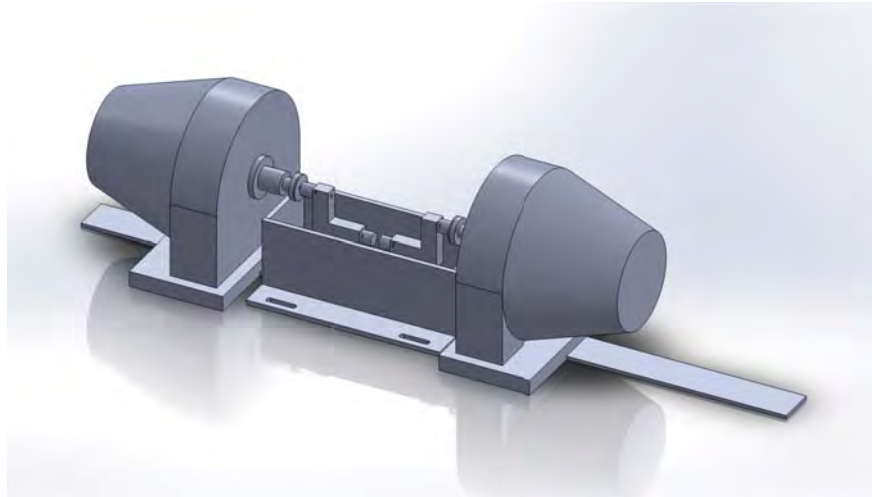
Figure 9.1: CAD Drawing of Environmental Bath and Test Fixtures Adapted to a Bose Electroforce TestBench System to Allow for Intermediate Strain Rate Testing in Fluid.

9.7 Determine Properties/Structure of Zonules/Ciliary Body

In order to create a model of the eye, the structure and material properties of all parts of the eye need to be known. To initially expand the model, parts of the eye that interact with the lens should be focussed on, specifically the suspensory zonules and the ciliary body. Testing opportunities for the zonules include using a lens stretcher clamped at the edges of the ciliary body, near the attachment of the zonules. The force would be recorded as the lens was stretched. With the force response of the lens/zonule assembly, the properties of the zonules could be back-calculated using the data from the whole lens tests performed (compression and puncture). Additionally, a fixture could be made to clamp and hold the ciliary body, suspending the lens in free air. The lens would then be displaced by a flat platen connected to a load cell measuring the force response, similar to the unconfined compressing testing procedure. A back-calculation of the properties of the zonules would again be necessary. A similar approach could possibly be used for the ciliary body, making sure to clamp at the exterior edge of the ciliary body. As for structure identification of the zonules and ciliary body, imaging processes would need to be investigated. With the material properties and structure of the zonules and ciliary body, the model could be coupled with other models and data on the other parts of the eye to further progress towards a complete computational model of the eye.

Chapter 10

Conclusion

There is much motivation to better understand the biomechanics of the ocular lens. The process of accommodation (the lens adjusting in optical power to focus an image) and presbyopia (the loss of accommodation over time) are not well understood. While the lens is an important part of the visual system, there has not been much focus until recently on the mechanics of accommodation and the mechanical characteristics of the ocular lens. This is mainly due to the possibility of the restoration of accommodation through surgical treatment (intraocular lens replacement surgery) and the improvement of cataract surgery. Through an increased understanding of the mechanics of the lens, IOLs and cataract surgery can be improved. Additionally, with recent military tours, an increase in ocular injuries has been recorded. This is largely due to the widespread use of improvised explosive devices (IEDs) and improved survival rates [Mader et al., 1993, Mader et al., 2006]. Management of ocular injuries in both soldiers and civilians as well as improved surgical treatments of the eye can be achieved with the development of an ultrastructurally based computational finite element model of the ocular lens.

In order to create such a model, the material properties and the ultrastructure of the components of the lens must be determined. While previous work has been done to understand the lens, more is needed for a consensus to be had. The work described above entailed mechanical testing as well as structure identification of the ocular lens with regard to the development of an accurate model. Data were analyzed from previous unconfined compression tests, producing material parameters by fitting the previous data curves. Additional data was generated through unconfined

compression tests without preconditioning, to provide more fitting data and the opportunity to compare the effects of preconditioning to those of lenses tested with none. Alongside compression testing, a puncture testing method was developed and data produced that can also be fit and allow the investigation of lens failure and the interaction between the ocular lens and intraocular foreign bodies (IOFBs). Both of these mechanical tests have provided data that will result in the determination of material properties of the whole porcine ocular lens. Nanoindentation was performed on the anterior porcine lens capsule to isolate the properties of the lens capsule. With said properties, the mechanical properties of the interior lens fibers can be back-calculated for the whole lens testing data.

The identification of the ultrastructure of the lens was also pursued. The type-IV collagen mesh-work that comprises the support structure of the lens capsule was imaged using electron tomography. More imaging is needed to confirm the observed structure, but a preliminary method (in need of some refining) has been developed to extract the geometrical data from the 3-dimensional reconstruction of the lens capsule samples. Confocal LASER scanning microscopy was employed to image the ultrastructure of the lens fiber cells. This was successful and many images of the fiber cell structure were obtained. A similar method has been developed to extract the geometrical data and that work is currently being completed.

This thesis is a presentation of results that are part of a larger research goal, that goal being the generation of an ultrastructurally based computational finite element model of the ocular lens. The results from this research are great progress towards that goal and will hopefully have lasting effects for soldiers, civilians, and anyone with visual impairment or injury involving the ocular lens.

Bibliography

[Abolmaali et al., 2007] Abolmaali, A., Schachar, R., and Le, T. (2007). Sensitivity study of human crystalline lens accommodation. Computer Methods and Programs in Biomedicine, 85(1):77–90.

[Aggarwal et al., 2012] Aggarwal, P., Garg, P., Sidhu, H., and Mehta, S. (2012). Post-traumatic endophthalmitis with retained intraocular foreign body – a case report with review of literature. Nepalese Journal of Ophthalmology, 4(1).

[Al-Amoudi et al., 2005a] Al-Amoudi, A., Dubochet, J., and Norl, L. (2005a). Nanostructure of the epidermal extracellular space as observed by Cryo-Electron microscopy of vitreous sections of human skin. Journal of Investigative Dermatology, 124(4):764–777.

[Al-Amoudi et al., 2004] Al-Amoudi, A., Norlen, L. P., and Dubochet, J. (2004). Cryo-electron microscopy of vitreous sections of native biological cells and tissues. Journal of Structural Biology, 148(1):131 – 135.

[Al-Amoudi et al., 2005b] Al-Amoudi, A., Studer, D., and Dubochet, J. (2005b). Cutting artefacts and cutting process in vitreous sections for cryo-electron microscopy. Journal of Structural Biology, 150(1):109 – 121.

[Bailey et al., 1993] Bailey, A., Sims, T., Avery, N., and Miles, C. (1993). Chemistry of collagen cross-links: glucose-mediated covalent cross-linking of type-IV collagen in lens capsules. The Biochemical Journal, 296(2):489–496.

[Bantseev and Sivak, 2005] Bantseev, V. and Sivak, J. G. (2005). Confocal laser scanning microscopy imaging of dynamic TMRE movement in the mitochondria of epithelial and superficial cortical fiber cells of bovine lenses. Molecular Vision, 11(December 2004):518–523.

[Barnard et al., 1992] Barnard, K., Burgess, S., Carter, D., and Woolley, D. (1992). Three-dimensional structure of type IV collagen in the mammalian lens capsule. Journal of Structural Biology, 108(1):6–13.

[Beers and van der Heijde, 1996] Beers, A. P. and van der Heijde, G. L. (1996). Age-related changes in the accommodation mechanism. Optometry and Vision Science: Official Publication of the American Academy of Optometry, 73(4):235–242. PMID: 8728490.

[Bond et al., 1996] Bond, J., Green, C., Donaldson, P., and Kistler, J. (1996). Liquefaction of cortical tissue in diabetic and galactosemic rat lenses defined by confocal laser scanning microscopy. Investigative Ophthalmology & Visual Science, 37(8):1557–65.

[Breitenfeld et al., 2005] Breitenfeld, P., Ripken, T., and Lubatschowski, H. (2005). Finite element method-simulation of the human lens during accommodation. In Bergh, H. v. d. and Vogel, A., editors, Therapeutic Laser Applications and Laser-Tissue Interactions II, volume 5863, page 586302. SPIE.

[Burd, 2009] Burd, H. (2009). A structural constitutive model for the human lens capsule. Biomechanics and Modeling in Mechanobiology, 8(3):217–231. 10.1007/s10237-008-0130-5.

[Burd et al., 2002] Burd, H., Judge, S., and Cross, J. (2002). Numerical modelling of the accommodating lens. Vision Research, 42(18):2235 – 2251.

[Burd et al., 1999] Burd, H. J., Judge, S. J., and Flavell, M. J. (1999). Mechanics of accommodation of the human eye. Vision Research, 39(9):1591 – 1595.

[Chen et al., 2007] Chen, X., Dunn, A. C., Sawyer, W. G., and Sarntinoranont, M. (2007). A biphasic model for Micro-Indentation of a Hydrogel-Based contact lens. Journal of Biomechanical Engineering, 129(2):156–163.

[Chien et al., 2006] Chien, C. M., Huang, T., and Schachar, R. A. (2006). Analysis of human crystalline lens accommodation. Journal of Biomechanics, 39(4):672 – 680.

[Colyer et al., 2008] Colyer, M. H., Chun, D. W., Bower, K. S., Dick, J. S. B., and Weichel, E. D. (2008). Perforating globe injuries during operation iraqi freedom. Ophthalmology, 115(11):2087–2093. PMID: 18672293.

[David et al., 2007] David, G., Pedrigi, R. M., Heistand, M. R., and Humphrey, J. D. (2007). Regional multiaxial mechanical properties of the porcine anterior lens capsule. Journal of Biomechanical Engineering, 129(1):97–104.

[Dhawahir-Scala and Kamal, 2005] Dhawahir-Scala, F. E. and Kamal, A. (2005). Intralenticular foreign body: a D-Day reminder. Clinical & Experimental Ophthalmology, 33(6):659–660.

[Erpelding et al., 2005] Erpelding, T., Hollman, K., and O'Donnell, M. (2005). Spatially mapping the elastic properties of the lens using bubble-based acoustic radiation force. In Ultrasonics Symposium, 2005 IEEE, volume 1, page 613 – 616.

[Fineman et al., 2000] Fineman, M. S., Fischer, D. H., Jeffers, J. B., Buerger, D. G., and Repke, C. (2000). Changing trends in paintball sport-related ocular injuries. Archives of Ophthalmology, 118(1):60–64. PMID: 10636415.

[Fung, 1993] Fung, Y. (1993). Biomechanics: Mechanical Properties of Living Tissues. Springer.

[Glasser and Campbell, 1998] Glasser, A. and Campbell, M. C. (1998). Presbyopia and the optical changes in the human crystalline lens with age. Vision Research, 38(2):209 – 229.

[Glasser and Campbell, 1999] Glasser, A. and Campbell, M. C. (1999). Biometric, optical and physical changes in the isolated human crystalline lens with age in relation to presbyopia. Vision Research, 39(11):1991–2015.

[Heistand et al., 2005] Heistand, M., Pedrigi, R., Delange, S., Dziezyc, J., and Humphrey, J. (2005). Multiaxial mechanical behavior of the porcine anterior lens capsule. Biomechanics and Modeling in Mechanobiology, 4(2):168–177. 10.1007/s10237-005-0073-z.

[Helmholz, 1855] Helmholz, H. (1855). U. ber die accommodationes des auges. Arch. fur Ophthalmol., 1:1–74.

[Hermans et al., 2006] Hermans, E., Dubbelman, M., Heijde, G. v. d., and Heethaar, R. (2006). Estimating the external force acting on the human eye lens during accommodation by finite element modelling. Vision Research, 46(21):3642 – 3650.

[Heys et al., 2004a] Heys, K. R., Cram, S. L., and Truscott, R. J. W. (2004a). Massive increase in the stiffness of the human lens nucleus with age: the basis for presbyopia? Molecular Vision, 10:956–963. PMID: 15616482.

[Heys et al., 2004b] Heys, K. R., Cram, S. L., and Truscott, R. J. W. (2004b). Massive increase in the stiffness of the human lens nucleus with age: the basis for presbyopia? Molecular Vision, 10:956–963. PMID: 15616482.

[Hsieh et al., 2006] Hsieh, C., Leith, A., Mannella, C. A., Frank, J., and Marko, M. (2006). Towards high-resolution three-dimensional imaging of native mammalian tissue: Electron tomography of frozen-hydrated rat liver sections. Journal of Structural Biology, 153(1):1–13.

[Hsieh et al., 2002] Hsieh, C., Marko, M., Frank, J., and Mannella, C. A. (2002). Electron tomographic analysis of frozen-hydrated tissue sections. Journal of Structural Biology, 138(1–2):63 – 73.

[Jain et al., 2004] Jain, S. S., Rao, P., Nayak, P., and Kothari, K. (2004). Posterior capsular dehiscence following blunt injury causing delayed onset lens particle glaucoma. Indian Journal of Ophthalmology, 52(4):325–327. PMID: 15693327.

[Kaufman and Alm, 2003] Kaufman, P. L. and Alm, A. (2003). Adler's Physiology of the Eye. Mosby, St. Louis, MO, tenth edition edition.

[Kessel and Kardon, 1979] Kessel, R. G. and Kardon, R. H. (1979). Tissues and Organs: a text-atlas of scanning electron microscopy. W.H. Freenman and Co., San Francisco, CA, first edition edition.

[Kim et al., 2009] Kim, T. H., Kim, S. J., Kim, E., Chung, I. Y., Park, J. M., Yoo, J. M., Song, J. K., and Seo, S. W. (2009). Spontaneous anterior lens capsular dehiscence causing lens particle glaucoma. Yonsei Medical Journal, 50(3):452–454. PMID: 19568612 PMCID: PMC2703773.

[Krag and Andreassen, 1996] Krag, S. and Andreassen, T. T. (1996). Biomechanical measurements of the porcine lens capsule. Experimental Eye Research, 62(3):253 – 260.

[Krag and Andreassen, 2003a] Krag, S. and Andreassen, T. T. (2003a). Mechanical properties of the human lens capsule. Progress in Retinal and Eye Research, 22(6):749 – 767.

[Krag and Andreassen, 2003b] Krag, S. and Andreassen, T. T. (2003b). Mechanical properties of the human posterior lens capsule. Investigative Ophthalmology & Visual Science, 44(2):691–696.

[Krag et al., 1997] Krag, S., Olsen, T., and Andreassen, T. T. (1997). Biomechanical characteristics of the human anterior lens capsule in relation to age. Investigative Ophthalmology & Visual Science, 38(2):357–63.

[Kremer et al., 1996] Kremer, J. R., Mastronarde, D. N., and McIntosh, J. R. (1996). Computer visualization of three-dimensional image data using IMOD. Journal of Structural Biology, 116(1):71–76. PMID: 8742726.

[Kumar et al., 2005] Kumar, A., Kumar, V., and Dapling, R. B. (2005). Traumatic cataract and intralenticular foreign body. Clinical & Experimental Ophthalmology, 33(6):660–661.

[Lam et al., 1998] Lam, D. S. C., Tham, C. C. Y., Kwok, A. K. H., and Gopal, L. (1998). Combined phacoemulsification, pars plana vitrectomy, removal of intraocular foreign body (IOFB), and primary intraocular lens implantation for patients with IOFB and traumatic cataract. Eye, 12:395–398.

[Lee and Song, 2001] Lee, S. I. and Song, H. C. (2001). A case of isolated posterior capsule rupture and traumatic cataract caused by blunt ocular trauma. Korean Journal of Ophthalmology: KJO, 15(2):140–144. PMID: 11811583.

[Liu et al., 2006] Liu, Z., Wang, B., Xu, X., and Wang, C. (2006). A study for accommodating the human crystalline lens by finite element simulation. Computerized Medical Imaging and Graphics, 30(6–7):371 – 376.

[Ljubimova et al., 2008] Ljubimova, D., Eriksson, A., and Bauer, S. (2008). Aspects of eye accommodation evaluated by finite elements. Biomechanics and Modeling in Mechanobiology, 7(2):139–150. 10.1007/s10237-007-0081-2.

[Mader et al., 1993] Mader, T. H., Aragones, J. V., Chandler, A. C., Hazlehurst, J. A., Heier, J., Kingham, J. D., and Stein, E. (1993). Ocular and ocular adnexal injuries treated by united states military ophthalmologists during operations desert shield and desert storm. Ophthalmology, 100(10):1462–1467.

[Mader et al., 2006] Mader, T. H., Carroll, R. D., Slade, C. S., George, R. K., Ritchey, J. P., and Neville, S. P. (2006). Ocular war injuries of the iraqi insurgency, January–September 2004. Ophthalmology, 113(1):97–104.

[Martin et al., 2005] Martin, H., Guthoff, R., Terwee, T., and Schmitz, K. (2005). Comparison of the accommodation theories of coleman and of helmholtz by finite element simulations. Vision Research, 45(22):2910 – 2915.

[Massig et al., 1994] Massig, J. H., Preissler, M., Wegener, A. R., and Gaida, G. (1994). Real-time confocal laser scan microscope for examination and diagnosis of the eye in vivo. Applied Optics, 33(4):690–694.

[Masters, 1998] Masters, B. (1998). Three-dimensional microscopic tomographic imagings of the cataract in a human lens in vivo. Optics Express, 3(9):332–338.

[Masters and Bohnke, 2002] Masters, B. R. and Bohnke, M. (2002). Three-dimensional confocal microscopy of the living human eye. Annual Review of Biomedical Engineering, 4:69–91. PMID: 12117751.

[McCauley et al., 2008] McCauley, M. B., Anderson, D. M., and Johnson, A. J. (2008). Posterior chamber visian implantable collamer lens: stability and evaluation following traumatic grenade explosion. Journal of Refractive Surgery (Thorofare, N.J.: 1995), 24(6):648–651. PMID: 18581794.

[McLeod et al., 2003] McLeod, S. D., Portney, V., and Ting, A. (2003). A dual optic accommodating foldable intraocular lens. British Journal of Ophthalmology, 87(9):1083–1085.

[Muzaffar et al., 2000] Muzaffar, W., Khan, M. D., Akbar, M. K., Khan, M. D., Malik, A. M., and Durrani, O. M. (2000). Mine blast injuries: ocular and social aspects. British Journal of Ophthalmology, 84(6):626–630.

[Nguyen et al., 2002] Nguyen, Q. D., Kruger, E. F., Kim, A. J., Lashkari, M. H., and Lashkari, K. (2002). Combat eye trauma: intraocular foreign body injuries during the Iran-Iraq war (1980-1988). International Ophthalmology Clinics, 42(3):167–177. PMID: 12131593.

[O'Connor et al., 2008] O'Connor, M. D., Wederell, E. D., Iongh, R. d., Lovicu, F. J., and McAvoy, J. W. (2008). Generation of transparency and cellular organization in lens explants. Experimental Eye Research, 86(5):734 – 745.

[Parver et al., 1993] Parver, L. M., Dannenberg, A. L., Blacklow, B., Fowler, C. J., Brechner, R. J., and Tielsch, J. M. (1993). Characteristics and causes of penetrating eye injuries reported to the national eye trauma system registry, 1985-91. Public Health Reports, 108(5):625–632. PMID: 8210260 PMCID: 1403438.

[Pau and Kranz, 1991] Pau, H. and Kranz, J. (1991). The increasing sclerosis of the human lens with age and its relevance to accommodation and presbyopia. Graefe's Archive for Clinical and Experimental Ophthalmology, 229(3):294–296. PMID: 1869070.

[Pedrigi et al., 2007] Pedrigi, R., David, G., Dziezyc, J., and Humphrey, J. (2007). Regional mechanical properties and stress analysis of the human anterior lens capsule. Vision Research, 47(13):1781 – 1789.

[Pedrigi and Humphrey, 2011] Pedrigi, R. and Humphrey, J. (2011). Computational model of evolving lens capsule biomechanics following Cataract-Like surgery. Annals of Biomedical Engineering, 39(1):537–548. 10.1007/s10439-010-0133-0.

[Powell et al., 2010] Powell, T. A., Amini, R., Oltean, A., Barnett, V. A., Dorfman, K. D., Segal, Y., and Barocas, V. H. (2010). Elasticity of the porcine lens capsule as measured by osmotic swelling. Journal of Biomechanical Engineering, 132(9):091008.

[Ravi et al., 2006] Ravi, N., Wan, K., Swindle, K., Hamilton, P., and Duan, G. (2006). Development of techniques to compare mechanical properties of reversible hydrogels with spherical, square columnar and ocular lens geometry. Polymer, 47(11):4203 – 4209.

[Reese and Govindjee, 1998] Reese, S. and Govindjee, S. (1998). A theory of finite viscoelasticity and numerical aspects. International Journal of Solids and Structures, 35(26–27):3455–3482.

[Reilly and Ravi, 2009] Reilly, M. and Ravi, N. (2009). Microindentation of the young porcine ocular lens. Journal of Biomechanical Engineering, 131(4):044502.

[Reilly et al., 2009] Reilly, M. A., Hamilton, P. D., Perry, G., and Ravi, N. (2009). Comparison of the behavior of natural and refilled porcine lenses in a robotic lens stretcher. Experimental Eye Research, 88(3):483 – 494.

[Reilly et al., 2008] Reilly, M. A., Hamilton, P. D., and Ravi, N. (2008). Dynamic multi-arm radial lens stretcher: A robotic analog of the ciliary body. Experimental Eye Research, 86(1):157 – 164.

[Richdale et al., 2008] Richdale, K., Bullimore, M. A., and Zadnik, K. (2008). Lens thickness with age and accommodation by optical coherence tomography. Ophthalmic & physiological optics : the journal of the British College of Ophthalmic Opticians (Optometrists), 28(5):441–447. PMID: 18761481 PMCID: PMC2857534.

[Rofagha et al., 2008] Rofagha, S., Day, S., Winn, B. J., Ou, J. I., Bhisitkul, R. B., and Chiu, C. S. (2008). Spontaneous resolution of a traumatic cataract caused by an intralenticular foreign body. Journal of Cataract & Refractive Surgery, 34(6):1033–1035.

[Shestopalov and Bassnett, 2000] Shestopalov, V. I. and Bassnett, S. (2000). Three-Dimensional organization of primary lens fiber cells. Investigative Ophthalmology & Visual Science, 41(3):859–863.

[Stachs et al., 2005] Stachs, O., Martin, H., Behrend, D., Schmitz, K., and Guthoff, R. (2005). Three-dimensional ultrasound biomicroscopy, environmental and conventional scanning electron microscopy investigations of the human zonula ciliaris for numerical modelling of accommodation. Graefe's Archive for Clinical and Experimental Ophthalmology, 244(7):836–844.

[Stachs et al., 2007] Stachs, O., Zhivov, A., Kraak, R., Stave, J., and Guthoff, R. (2007). In vivo three-dimensional confocal laser scanning microscopy of the epithelial nerve structure in the human cornea. Graefe's Archive for Clinical and Experimental Ophthalmology, 245(4):569–575. 10.1007/s00417-006-0387-2.

[Strenk et al., 2004] Strenk, S. A., Strenk, L. M., Semmlow, J. L., and DeMarco, J. K. (2004). Magnetic resonance imaging study of the effects of age and accommodation on the human lens Cross-Sectional area. Investigative Ophthalmology & Visual Science, 45(2):539–545.

[Szijarto et al., 2007] Szijarto, Z., Gaal, V., Kovacs, B., and Kuhn, F. (2007). Prognosis of penetrating eye injuries with posterior segment intraocular foreign body. Graefe's Archive for Clinical and Experimental Ophthalmology, 246(1):161–165.

[Taylor et al., 1996] Taylor, V. L., al-Ghoul, K. J., Lane, C. W., Davis, V. A., Kuszak, J. R., and Costello, M. J. (1996). Morphology of the normal human lens. Investigative Ophthalmology & Visual Science, 37(7):1396–1410.

[Thim et al., 1993] Thim, K., Krag, S., and Corydon, L. (1993). Hydroexpression and viscoexpression of the nucleus through a continuous circular capsulorhexis. Journal of Cataract and Refractive Surgery, 19(2):209–212. PMID: 8487162.

[WALTER, 1962] WALTER, W. L. (1962). Intralenticular foreign body as a cause of traumatic cataract. American Journal of Ophthalmology, 54:856–858. PMID: 13998693.

[Weeber et al., 2005] Weeber, H. A., Eckert, G., Soergel, F., Meyer, C. H., Pechhold, W., and Van Der Heijde, R. G. L. (2005). Dynamic mechanical properties of human lenses. Experimental Eye Research, 80(3):425–434.

[Weeber and Van Der Heijde, 2008] Weeber, H. A. and Van Der Heijde, R. G. L. (2008). Internal deformation of the human crystalline lens during accommodation. Acta Ophthalmologica, 86(6):642–647.

[Weichel and Colyer, 2008] Weichel, E. D. and Colyer, M. H. (2008). Combat ocular trauma and systemic injury. Current Opinion in Ophthalmology, 19(6):519–525.

[Weichel et al., 2008] Weichel, E. D., Colyer, M. H., Ludlow, S. E., Bower, K. S., and Eiseman, A. S. (2008). Combat ocular trauma visual outcomes during operations iraqi and enduring freedom. Ophthalmology, 115(12):2235–2245. PMID: 19041478.

[Wong et al., 1997] Wong, T. Y., Seet, M. B., and Ang, C. (1997). Eye injuries in twentieth century warfare: A historical perspective. Survey of Ophthalmology, 41(6):433–459.

[Yang et al., 1998a] Yang, X., Zou, L., Binrong, M., Dong, D., Dai, H., and Lu, X. (1998a). Tensile strength of lens capsules in eye-bank eyes. Journal of Cataract and Refractive Surgery, 24(4):543–546. PMID: 9584253.

[Yang et al., 1998b] Yang, X., Zou, L., Binrong, M., Dong, D., Dai, H., and Lu, X. (1998b). Tensile strength of lens capsules in eye-bank eyes. Journal of Cataract and Refractive Surgery, 24(4):543–546. PMID: 9584253.

[Ziebarth et al., 2011] Ziebarth, N. M., Arrieta, E., Feuer, W. J., Moy, V. T., Manns, F., and Parel, J. (2011). Primate lens capsule elasticity assessed using atomic force microscopy. Experimental Eye Research, 92(6):490–494.

[Ziebarth et al., 2008] Ziebarth, N. M., Borja, D., Arrieta, E., Aly, M., Manns, F., Dortonne, I., Nankivil, D., Jain, R., and Parel, J. (2008). Role of the lens capsule on the mechanical accommodative response in a lens stretcher. Investigative Ophthalmology & Visual Science, 49(10):4490–4496.

[Ziebarth et al., 2010] Ziebarth, N. M., Rico, F., and Moy, V. T. (2010). Structural and mechanical mechanisms of ocular tissues probed by AFM. In Bhushan, B., editor, Scanning Probe Microscopy in Nanoscience and Nanotechnology, page 363–393. Springer Berlin Heidelberg, Berlin, Heidelberg.

B Senior Thesis

The appendix includes the Senior Thesis of Ms. Srinidhi Radhakrishnan, 2012, *Ultrastructural Identification of the Internal Fiber Cells of the Mammalian Ocular Lens*, to which is referred in early sections of this Final Report.

Ultrastructural Identification of the Internal Fiber Cells of the Mammalian Ocular Lens

by

Srinidhi Radhakrishnan

Department of Chemical and Biological Engineering

Senior Thesis Advisor

Dr. Richard Regueiro

Department of Civil, Environmental, and Architectural Engineering

University of Colorado- Boulder

College of Engineering and Applied Sciences

April 2014

Abstract

 Cataract formation occurs when the lens becomes opaque and cloudy, therefore limiting the refractive capabilities of the lens. Current treatments for mitigating cataracts involve removing the internal fiber cells and implanting an intraocular lens (IOL). A limitation with the use of these intraocular lenses is the loss in accommodation features, or the inability to fully restore accommodative vision, which is normally present in healthy internal fiber cells. Also, by understanding the native structure of the ocular lens, researchers can estimate through computational mechanical modeling how the change in structure from trauma contributes to deficiencies in function.

 This paper identifies the ultrastructure of the internal fiber cells of a porcine lens using confocal laser scanning microscopy. With this information, a three-dimensional model of the lens, incorporating the ultrastructural images as well as its mechanical properties, will be generated. This model can then be applied to devise effective mechanisms to rectify the internal lens fiber cells and retain the accommodative capabilities of the eye.

1

Acknowledgments

First and foremost, I would like to thank Professor Richard Regueiro for his continued support throughout my journey at the University of Colorado at Boulder. I was introduced to this project in the fall of 2012, through the Discovery Learning Apprenticeship Program. Since this time, you have provided generous mentorship. Furthermore, you have helped me achieve many memorable academic milestones in CU Boulder. I sincerely appreciate your continual encouragement and confidence in my research potential.

I would also like to acknowledge Dr. Christopher English for his invaluable assistance and training throughout my work on this project. Your multitalented abilities and willing to share your knowledge has helped develop this project from its initial stages. Additionally, your kindness and patience with teaching have yielded a lasting impact on me.

Lastly, I would like to thank Christopher Bay, Chad Hotimsky, and Saikripa Radhakrishnan for helping me develop the skills needed to achieve the various objectives of this project. I thank you all for providing support that was essential for my progress in research.

Contents

I. Introduction

Motivation

The crystalline lens is one of the simpler, yet heavily relied upon systems in the human body. Consequently, the natural function served by the lens has been developed for a variety of applications. Nevertheless, the accommodative capabilities as well as the transparent properties of the lens remain at the forefront of clinically relevant research challenges. In part, this is attributed to the lack of structural understanding of the lens. At present, cataracts are treated by replacing the affected internal lens substance with an intraocular lens (IOL) (McLeod, Portney, & Ting, 2003). IOLs are placed into the capsule through a small incision. Subsequently, the IOL expands through the anterior area to then restore the conditions needed for visualization. Although IOL treatment options for traumatic cataract are effective for partially restoring vision, there are multiple facets of visualization, including accommodation, that are limited post-surgery. Finite element models of the lens have the potential to estimate lens accommodation upon different mechanical loads (Burd, Judge, & Cross, 2002). The development of these models can help develop prophylactic measures to reduce the onset of cataract as well as treatments that will most effectively restore accommodation. By understanding the molecular mechanisms that result in cataract formation as well as the ultrastructural characteristics of the normal and cataractous lens, many of these features may be incorporated in treatment protocols. Consequently, this study focuses on understanding more of the collective structural characteristics of the lens by utilizing confocal laser scanning microscopy (CLSM).

Previous Research

A previous approach to imaging the lens fiber cells applied transmission electron microscopy (TEM) and scanning electron microscopy (SEM) using human lenses gathered 24

hours post-mortem (Taylor, et al., 1996). For the TEM images, the lens fiber cells were cut in sections parallel to the optic axis using a vibratome. The samples were placed in a fixative comprising of 2.5% glutaraldedehyde, 2% paraformaldehyde, 1% tannic acid in cacodylate buffer and subsequently imaged. The images demonstrated distorted hexagonal shapes and no organelles. Additionally, the cell membranes demonstrated the classic ball-and-socket loops. For the SEM images, they were placed in two fixatives and mounted for imaging. The primary fixative contained 10% neutral buffered formalin prepared in 0.1 M phosphate buffer. The secondary fixative comprised of 2.5% glutaraldehyde prepared in 0.12 M cacodylate buffer. The morphology of the lens fiber cells gathered through SEM appeared similar to the TEM images (Taylor, et al., 1996). The images highlight the radial positioning of fiber cells in particular regions, as seen in Figure 1.1. The crystallins are cross-linked into a 3D network, and the packing of proteins appears very close.
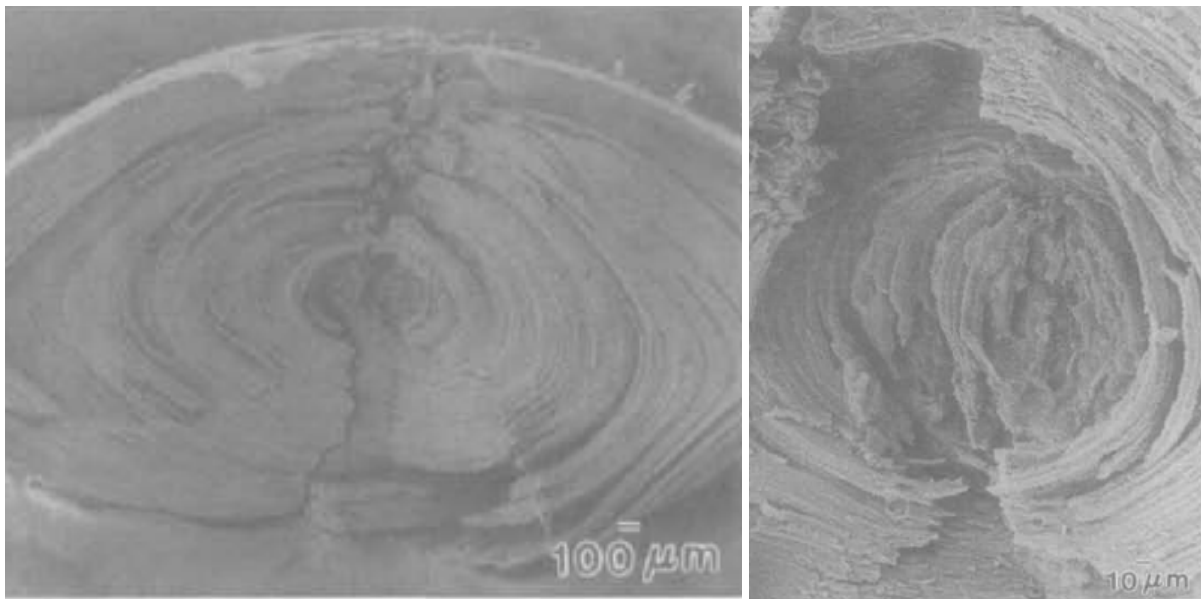
Figure 1.1: Images of the embryonic nuclei of the human lens fiber cells (Taylor, et al., 1996)

Another approach for imaging the lens fiber cells also used confocal laser scanning microscopy (CLSM). Thin sectioning of the lens fiber cells helped describe the differentiation

process of lens epithelial cells (Bassnett & Beebe, 1992); see Figure 1.2. While the integrity of

the tissue was maintained through sectioning, the equatorial epithelial cells were at a higher

likelihood of damage due to the sectioning procedure. Similarly, near the sectioned regions,

damage was visible though the interior appeared undisturbed. Furthermore, the staining process

failed to stain the nucleus and superficially stained the rest of the cytoplasm, though the staining

was uniform. The confocal images showed that the cells contained mitochondria that were tightly

coiled, while the newly-formed cells had more elongated and branched mitochondria, which

corresponded with previous research results. A significant finding was that the mitochondria and

nuclei appeared to disappear abruptly and concurrently in the deep lens cortex. Actin under the

fiber cell membranes was also seen in the images (Bassnett & Beebe, 1992).
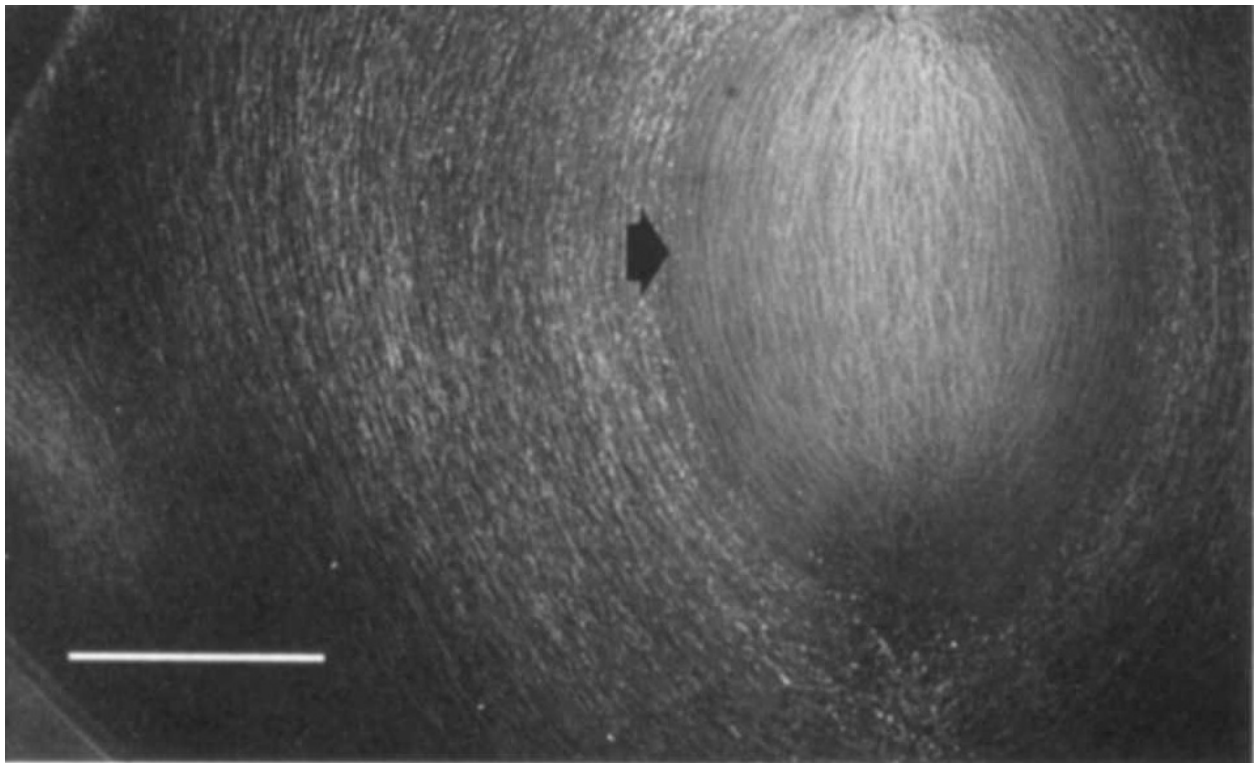
Figure 1.2: Organelle-free CLSM image of the lens fiber cells; scale bar is 250μm (Bassnett & Beebe, 1992)

Current Challenges

The challenge with gathering images of the internal fiber cells includes the natural distortion and damage induced through fixing and sectioning. Furthermore, although CLSM has produced better lens fiber cell images in comparison to SEM and TEM, there are difficulties in imaging the central region of the lens fiber cell sections due to limitations in stain permeation and fragility induced by fixatives. Although this problem was not entirely circumvented, the section thickness was adjusted to mitigate this issue in the research. While a large sample hinders the stain penetration, a thinly sectioned sample is more prone to damage and distortion. Since a full reconstruction of the internal lens fiber cells will ultimately be developed, this will also improve the approximations made in regions of the structure that were distorted.

Contribution

To more accurately model the lens, there are four main objectives embedded in this project. These include (i) identification of the three-dimensional (3-D) ultrastructure of the porcine internal lens fiber cells using confocal laser scanning microscopy; (ii) isolation and imaging of the posterior and anterior lens capsule's type IV collagen using cryo-electron tomography; (iii) gathering data pertaining to the mechanical properties of these fiber cells and lens capsule using the material testing system (MTS) and nanoindenter respectively; and (iv) generation of a constitutive mechanical model of the ocular lens and behavior upon exposure to external forces.

The focus of this project is to develop the 3- D ultrastructure of the lens fiber cells, while other members of the research group are gathering mechanical data and lens capsule images. This 3-D lens fiber cell ultrastructural arrangement as well as the other components of the objectives will be incorporated into a structurally based computational model. The purpose of

this model is to simulate the trauma that can occur to the ocular lens. These include, but are not limited to blunt force contact, blast-wave loading, or perforation by an intraocular foreign body. Due to the fragile nature of the lens, small deformations can lead to severe and permanent consequences. The high onset of blindness as a result of any of these forms of trauma, frequently faced by the personnel of the armed forces and also observed in workplace accidents and field jobs, motivates the creation of a model that provides a better understanding of the ocular response to trauma (Weichel & Colyer, 2008). This model can be applied to advance protective technologies that mitigate ocular trauma. To develop a comprehensive computational model of the lens, both the material and mechanical properties of the lens as well as the ultrastructure of the lens are necessary. A better understanding of these characteristics of the lens also has the potential to explain the causes for the loss of accommodative features in the lens with time in addition to other lens-centered diseases.

II. Background

The crystalline lens is a transparent structure formed primarily of lens fiber cells. The lens is suspended between the aqueous humor and vitreous humor by zonules that attach at the lens equator, as indicated in Figure 2.1. The lens capsule, comprised of a meshwork of type IV collagen, holds the lens fiber cells. The posterior of the lens is suspended by the vitreous humor, a gelatinous and stagnant substance comprised primarily of water. The anterior of the lens is protected by the transparent cornea, which also covers the iris and pupil. The cornea is continuous with the sclera which is the opaque, white, and protective outer layer of the eye. The iris, directly anterior to the lens, regulates the amount of light that enters the eye. On the other hand, the pupil is a hole at the center of the iris that allows light to enter the eye. The light entering the eye is closely dependent on the alignment of the lens fibers as well as the refractive index of the vitreous. The light captured from the surroundings produces an image by patterned excitation of the rods and cones in the retina. The lens is a specialized epithelial tissue that is responsible for fine-tuning the image projected onto the retina (Alm & Kaufman, 2003).
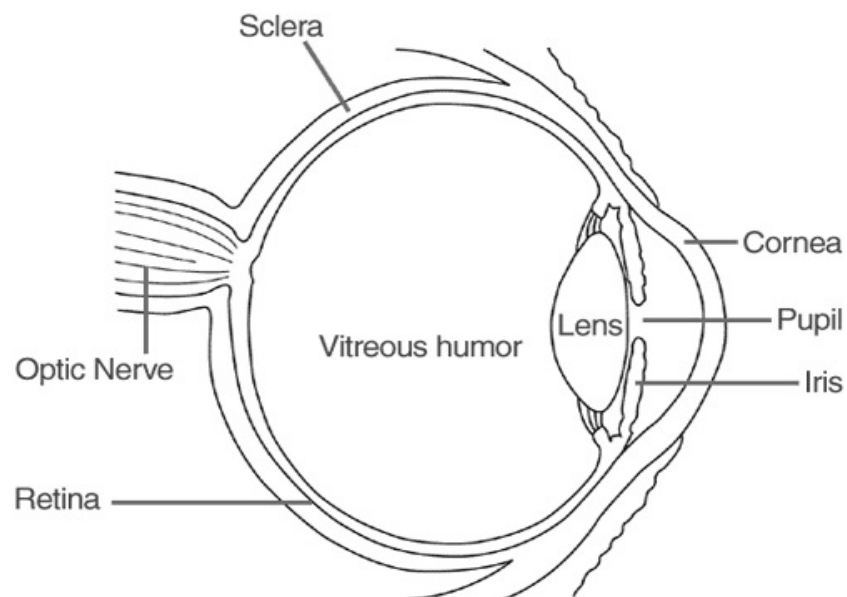
Figure 2.1: Anatomy of the Human Eye (nei.nih.gov)

Although densely arranged with cells, the lens maintains transparency and a high refractive index. This is largely attributed to the precise alignment of lens fiber cells with their neighbors and subsequent high concentration of crystallin accumulation. The differentiation of fiber cells is propagated and characterized by the synthesis and accumulation of these crystallin proteins. The exoskeleton of the lens fiber cells is stabilized by an abundance of microtubules. Although the exact function of these microtubules is unknown, it is predicted that these microtubules play a role in elongating the fiber cells as the lens ages and new layers form at the periphery of the lens. In addition to the microtubules, there is a stable network of actin-containing microfilaments that form the sub-membrane meshwork. To provide the accommodative features of the lens, the ciliary zonules interweave with the capsule along the equator of the lens capsule, as indicated in Figure 2.2.
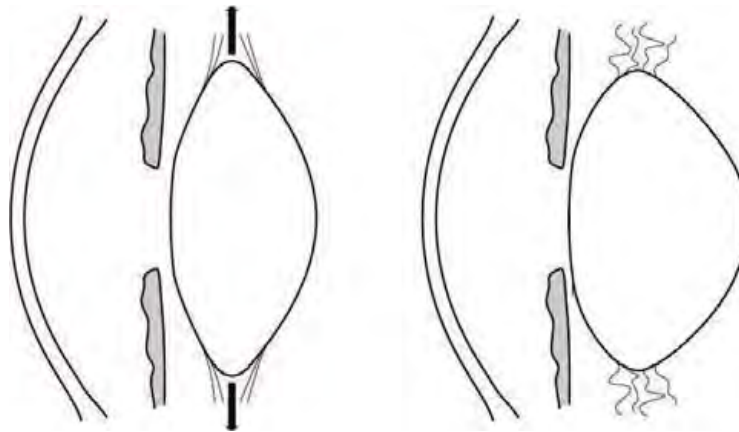
Figure 2.2: Lens Accommodation Schematic (McLeod, Portney, & Ting, 2003)
(a) Unaccommodated state- zonules are in tension,
(b) Accommodated state- zonules are relaxed due to contraction of the ciliary muscles

The internal lens fiber cells are comprised of two main regions: the inner nucleus and the outer cortex, as shown in Figure 2.3. As the cells age, the new fibers are proposed to divide at the equator of the cell and push older cells toward the central nucleus, thus increasing the overall cell

volume as the lens ages. As new cells continue to differentiate and the lens matures, it is more

susceptible to mechanical modification. The cumulative modification affects the functional

capabilities of the crystallin protein structure, thus causing the lens to lose its transparency,

inadequately scatter light onto the retina, and yield the onset of cataract (Sharmaa &

Santhoshkumar, 2009).
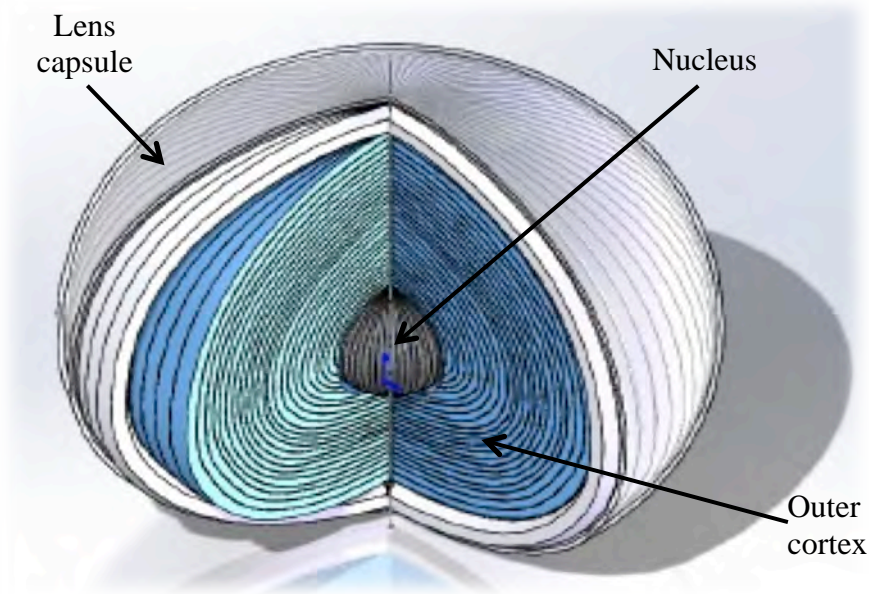
Figure 2.3: SolidWorks Model of the Human Lens (courtesy of Chad Hotimsky)

III. Materials and Methods

As a starting point for this research project, porcine lenses were imaged due to its similar morphological properties and size as compared to the human lens. Several sessions of dissecting and imaging the porcine eyes were conducted to determine the optimal extraction procedure for the internal fiber cells. The most effective method for extraction involved removing the cornea, by cutting along the interface of the sclera and cornea. Afterward, the iris was removed by clipping along the interface of the sclera and the iris. Due to the proximity of the iris to the lens it is crucial to perform this clipping carefully. Following this, the lens was scooped out of the remaining sclera pocket containing the vitreous, which also slightly pulls the lens. The removal was performed slowly to

Figure 3.1: Porcine Lens

avoid potential alterations that result from the tension that the vitreous exerts on the lens. The removed lens, photographed in Figure 3.1, will generally also have zonules and ciliary muscle still attached along its equator.

Extraction and Fixation

The six to nine month porcine eyes, pictured in Figure 3.2, were received from Animal Technologies and dissected within 24 hours of acquisition. To perform the dissection, the cornea and aqueous humor were carefully removed, while retaining the pressure held by the vitreous humor, such that the lens as well as the iris is visible and

Figure 3.2: Porcine Eye

undisrupted. By pressing the sclera and gradually increasing the pressure exerted on the eye after

12

the cornea and aqueous humor are removed, the lens will detach from the zonule fibers and can be wholly extracted. After isolating the lenses, they were immediately fixed in four percent paraformaldehyde (PFA) in 1X PBS for two days. An identical procedure was followed for extracting the human lens, obtained from the Colorado Eye Bank from a 66-year old deceased male.

Sectioning

After two days in fixative, each lens was sectioned using a vibratome, which is presented in Figure 3.3. In addition to the required protocol for the vibratome, the following procedure was followed. The lens was sliced such that the resulting sections were parallel to the optical axis. Initially, the lens was cut in half in order to create two samples with flat sides that can then be mounted, as seen in Figure 3.4. Each sample was separately mounted onto the vibratome and the sectioning platform was immersed in an ice bath. The lens samples were sectioned to a thickness of 200μm at an amplitude setting of one, a speed setting of five, and a frequency setting of seven. The amplitude adjusts the arcuate path of the blade and is generally set at low values (<3) for fixed/ harder samples or high values (>8) for soft samples. The speed adjusts the rate at which the blade advances and is set at low values (1-2) for softer samples and higher values (7-8) for fixed/ harder samples. The frequency adjusts the blades' lateral movement rate and is generally low (1-2) for softer samples and high (>10) for fixed/ harder samples. In particular, the settings used for the lens fiber cells were determined by observing the motion of the blade in accordance with the fragility of the sample. When using the vibratome it is essential to choose a blade movement that is not too slow or fast for sample sectioning as these extremes will damage the sample. Samples were immediately placed in 1X PBS at room temperature after being sectioned.

Figure 3.3: Leica Vibratome used to section internal lens fiber cell samples (in MCDB facility)
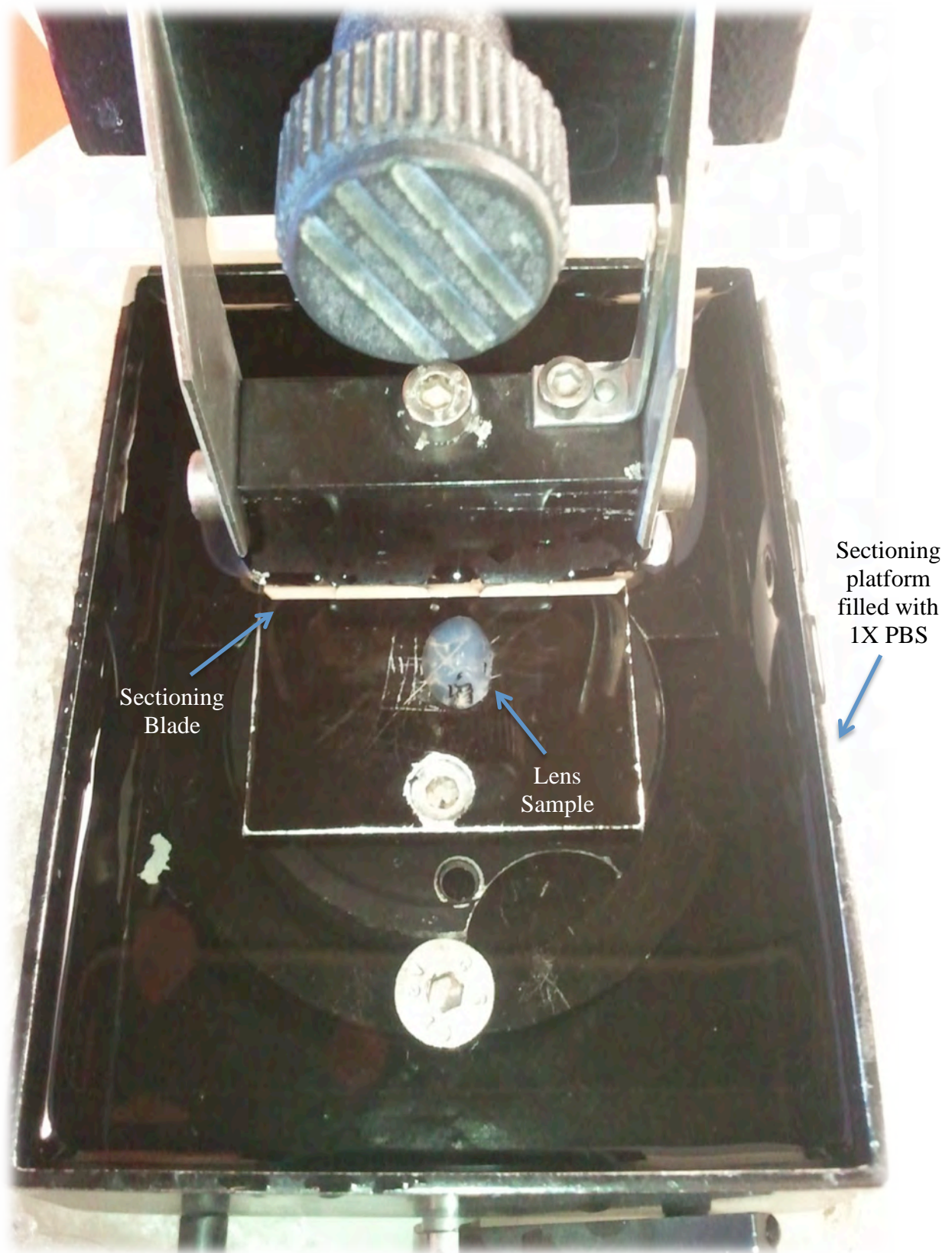
Figure 3.4: Closer view of the sectioning mechanism of the vibratome (in MCDB facility)

After sectioning the samples and prior to staining the samples, they were placed in a blocking agent prepared with 1X phosphate buffered saline (PBS) and Triton X-100 (PBST), bovine serum, bovine serum albumin (BSA), normal goat serum, and sodium-azide. Blocking agent permeabilizes the cell walls and reduces non-specific binding of stains in order to open the channels for stains to enter the tissue. The samples were placed in a blocking agent containing 1X PBST for 12-15 hours at room temperature. Subsequently, the samples were stained with Life Technologies' Alexa Fluor 555 Phalloidin diluted 1:200 in block. Phalloidin was chosen since it stains actin, the structural protein in the cytoskeleton of internal fiber cells. The samples were placed in Phalloidin for three days at room temperature. Afterward, the samples were washed five times with 1X PBST for time intervals gradually increasing from five minutes to one hour. This process removes the residual Phalloidin that was not bound to the actin of the internal fiber cells. The samples were then stained with Life Technologies' 4',6-Diamidino-2-Phenylindole, Dihydrochloride (DAPI), which was diluted 1:1000 in 1X PBS. DAPI attaches to the nucleus of the epithelial cells, which are present in the anterior of the lens. Specifically, DAPI was used to determine the orientation of the lens, in order to generate the three-dimensional composite of the lens that appropriately distinguishes the anterior and posterior parts of the lens. The samples were placed in DAPI for one hour at room temperature. Once again, the samples were washed five times with 1X PBST for time intervals gradually increasing from five minutes to one hour. Prior to mounting, the samples were washed once with 1X PBS.

Mounting

The samples were mounted on Fisherbrand glass slides using Southern Biotech's Fluoromount liquid mounting medium. The slides were placed at room temperature until the

Fluoromount hardened. The slides were subsequently left in the cold room, at a temperature of 5°C for storage to preserve stain positioning and excitation effectiveness. The mounted sections are shown below in Figure 3.5.

Figure 3.5: Lens sections mounted on Fisherbrand glass slides

Imaging and Processing

Ultimately, CLSM was used to determine the ultrastructure of the lens, since this form of microscopy has the capability to form 3-D stacks of the sample. The Zeiss 510 confocal laser scanning microscope at the light microscopy facility, managed by the Molecular, Cellular, and Development Biology (MCDB) department at CU Boulder, was used to acquire the images. The orientation of the sections that were imaged has been demonstrated below in Figure 3.6 with respect to position in the whole lens. The images have been sectioned and imaged parallel to the

optical axis, which is represented by the z-axis in Figure 3.6. The nuclei of the epithelial cells,

which are located on the anterior portion of the lens capsule, have also been stained to

distinguish the anterior and posterior of the lens. To prevent excess photobleaching of the sample

and retain the excitation resolution, the higher resolution images were gathered prior to gathering

the 5X images. Images were exported from Zeiss Zen 2009 software, and post-processing was

conducted using ImageJ and FIJI software (FIJI, 2013).
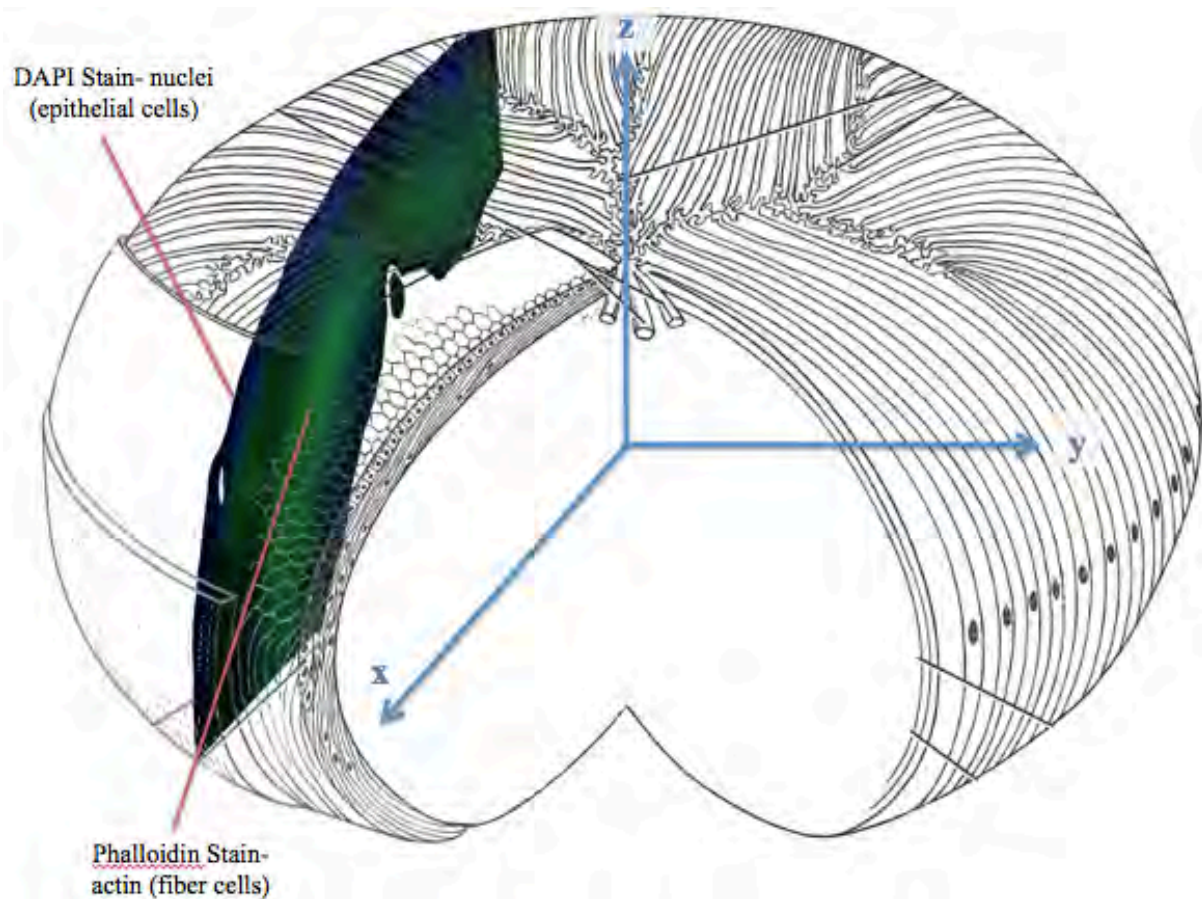
Figure 3.6: Sectioning orientation with respect to the whole lens ultrastructure, showing human adult lens sutures from Kessel and Kardon (Kessel & Kardon, 1979)

IV. Results

The confocal images gathered for the porcine lenses as well as the human lenses have been included below. Colors shown were added during image post-processing to distinguish the epithelial cells (indicated by blue DAPI stain) and lens fiber cells (indicated by gray or green phalloidin stain). The objective used to gather each image will be included in the respective figure caption. The 405 nm diode laser was used to excite DAPI and the helium-neon laser was used to excite phalloidin.

Part I: Porcine Lens
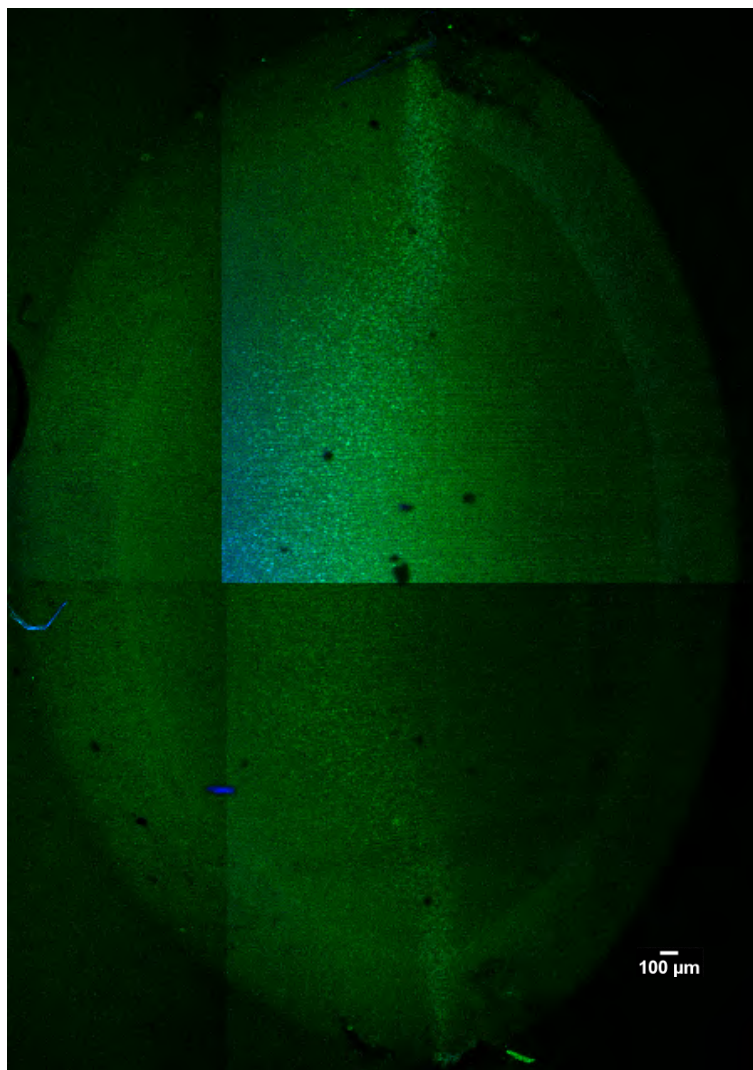
Figure 4.1: Fully stitched cross-section of the lens imaged with 5X objective
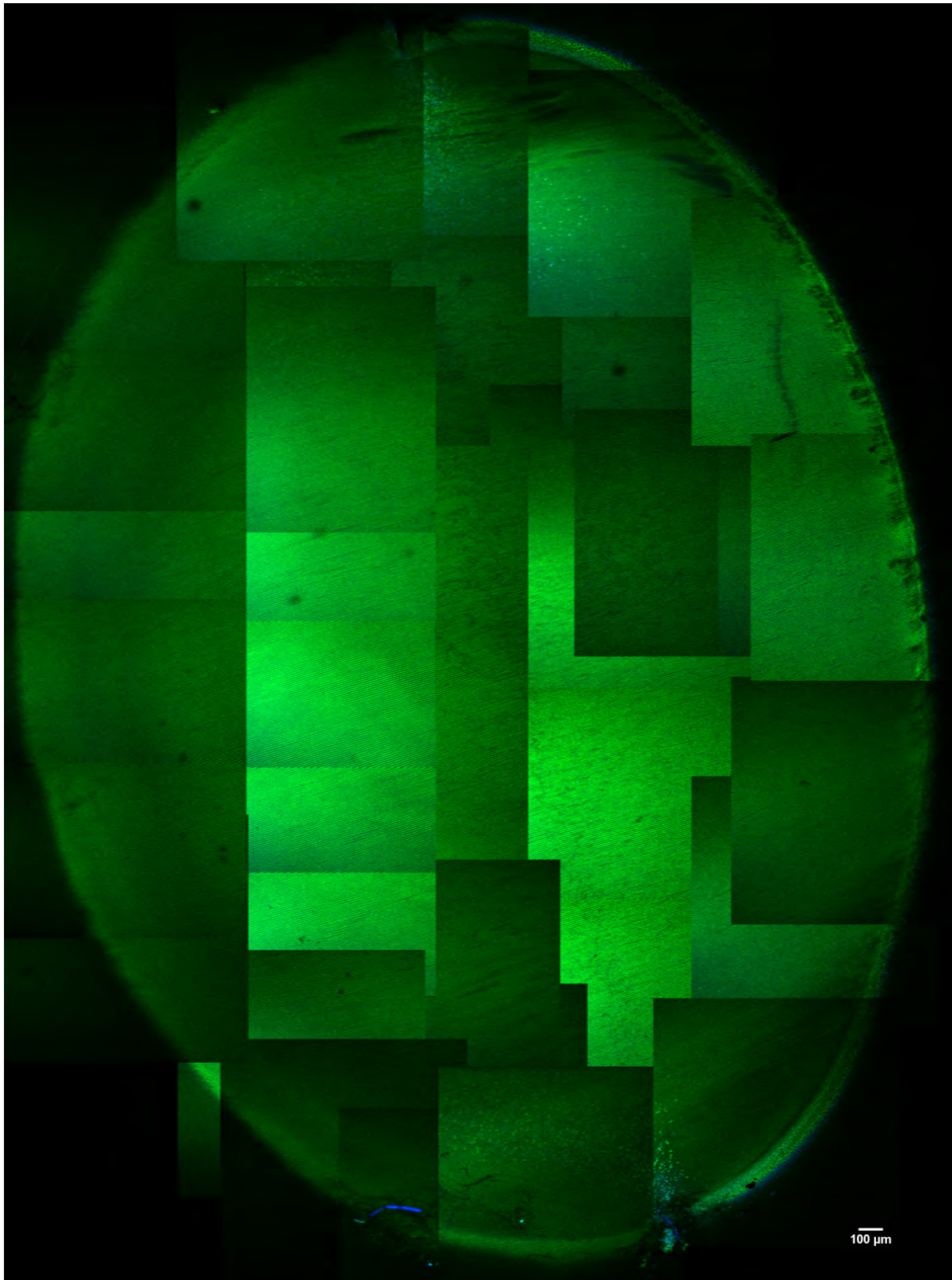
Figure 4.2: Fully stitched cross-section of the lens imaged with 10X objective

The following image, Figure 4.3, is the same tear that is at the upper right of the stitched lens cross-section shown in Figure 4.2, at the same resolution (10X). This was included in order provide context regarding the resolution of the image above. Information provided in the fully stitched lens above has been lost when printed, due to the limitations in page size.
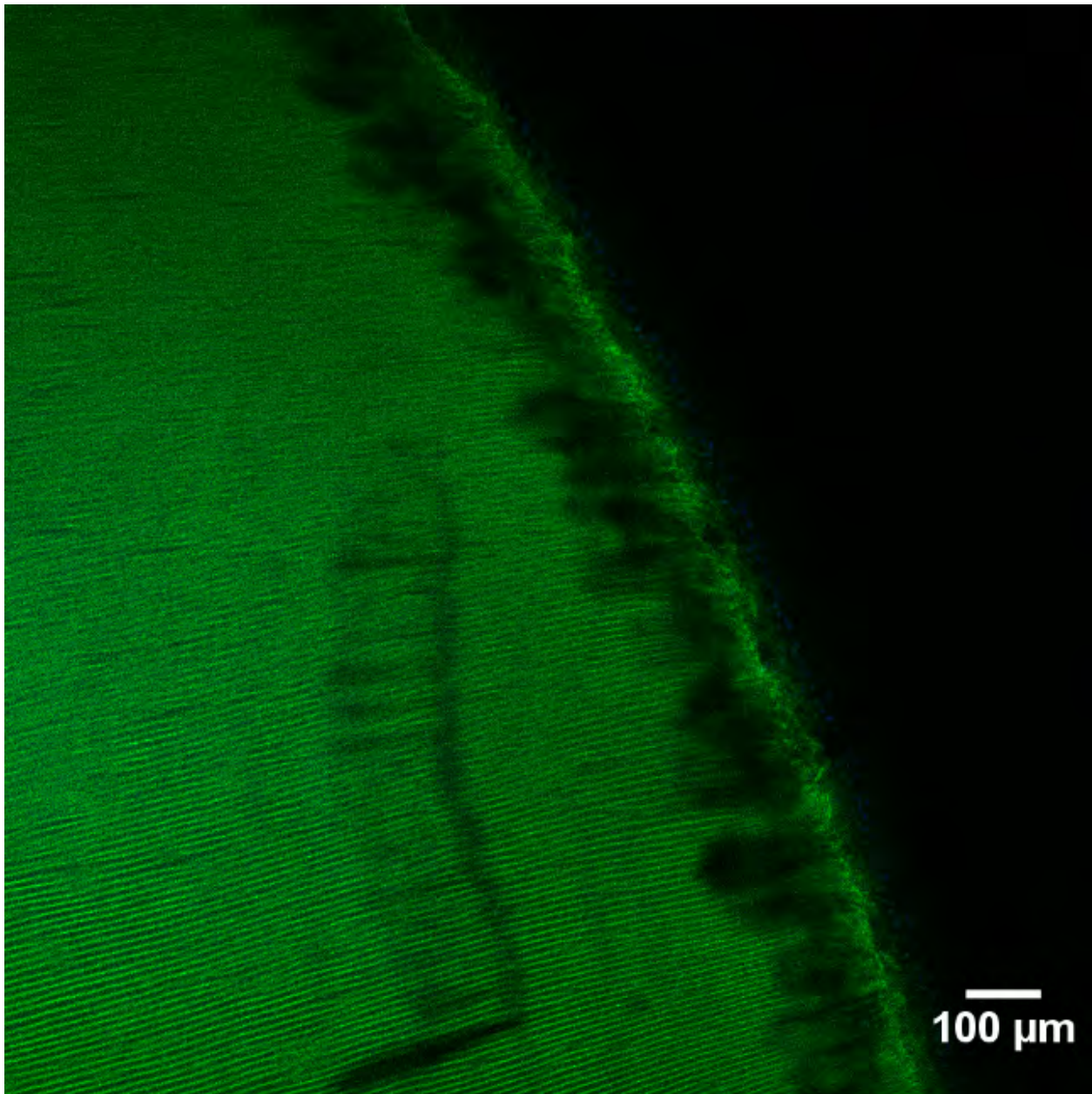
Figure 4.3: 10X confocal image of a porcine lens section

Figure 4.4 utilizes a feature of the ImageJ software, which allows the stacks of images, collected with the confocal laser scanning microscope, to be layered over one another. With respect to Figure 3.6, the depth of this stacked image is in the direction of the y-axis.
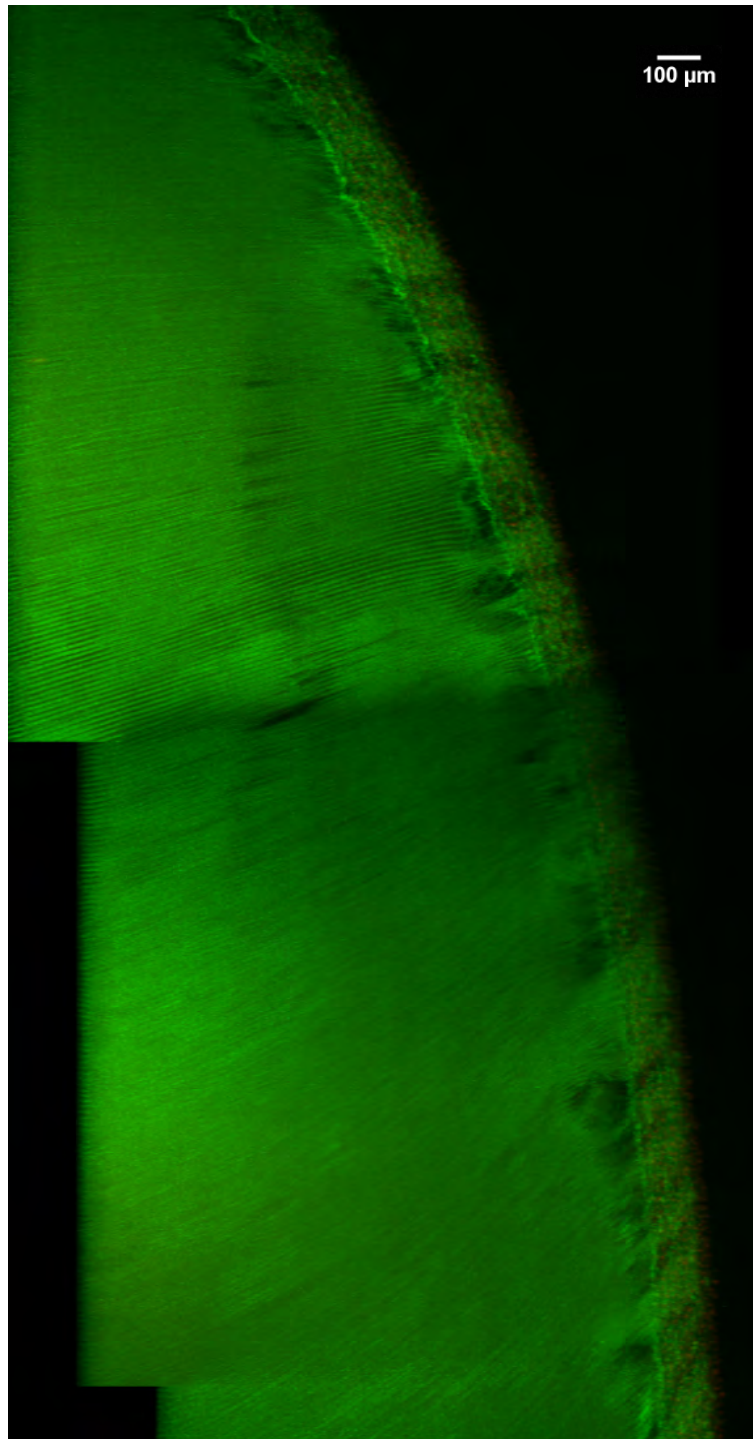
Figure 4.4: 3-D projection of 10X image stack
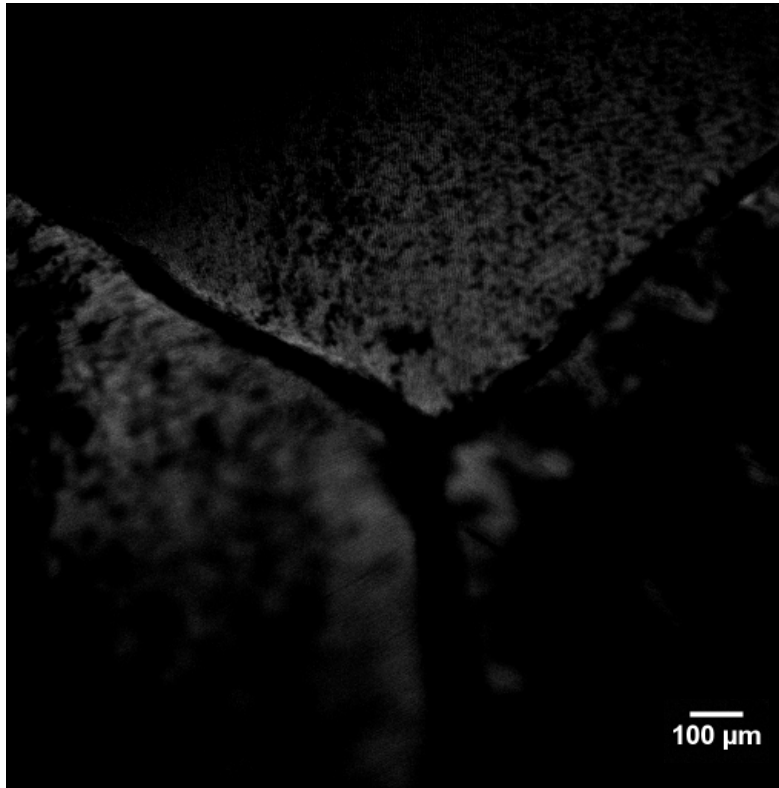
Figure 4.5: 10X images of lens sectioned perpendicular to the optical axis at suture point
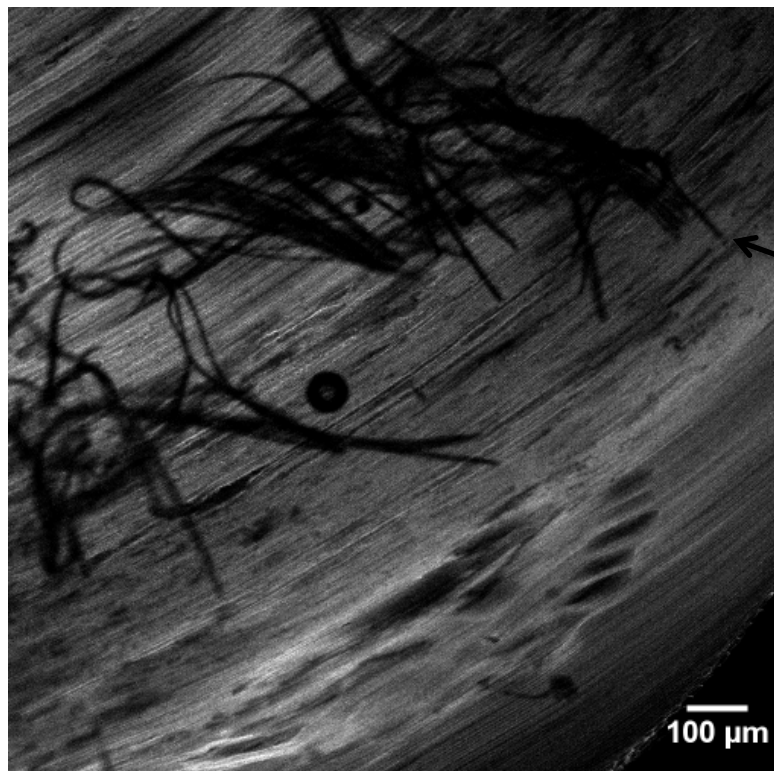
Strands of fiber cells displaced outside of the imaging plane demonstrate shadowed effect, known as birefringence

Figure 4.6: 10X confocal image demonstrating birefringence
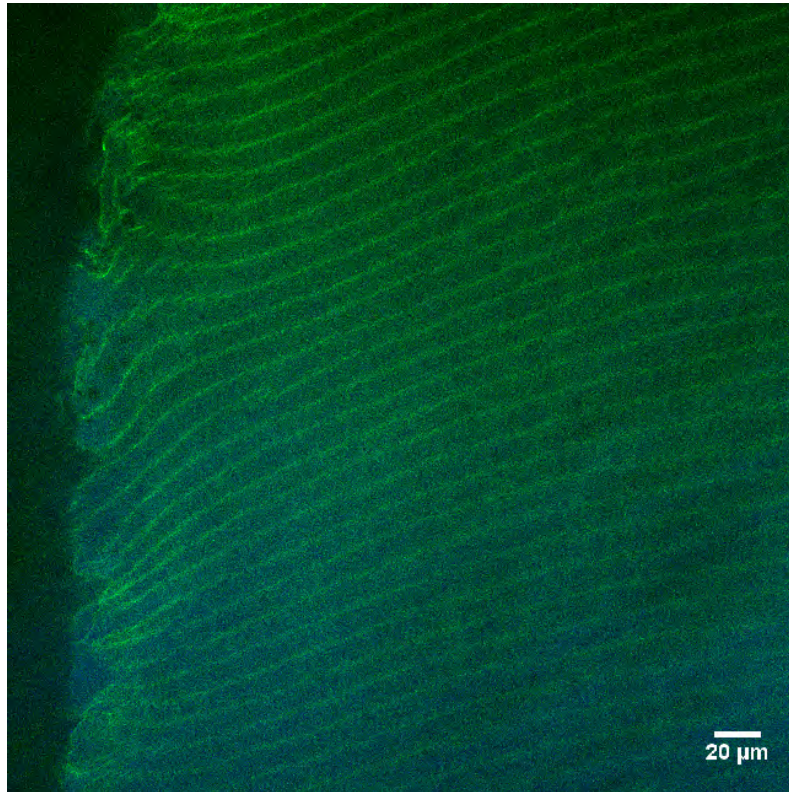
Figure 4.7: 40X image of porcine lens
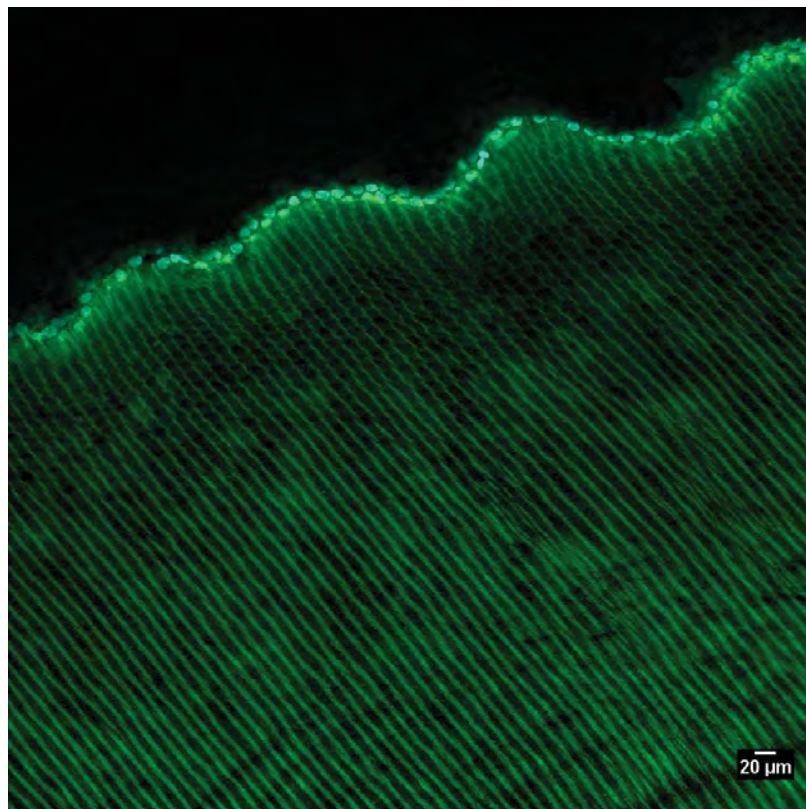
Figure 4.8: 20X porcine lens image highlighting hexagonal pattern (courtesy of Christopher Bay)
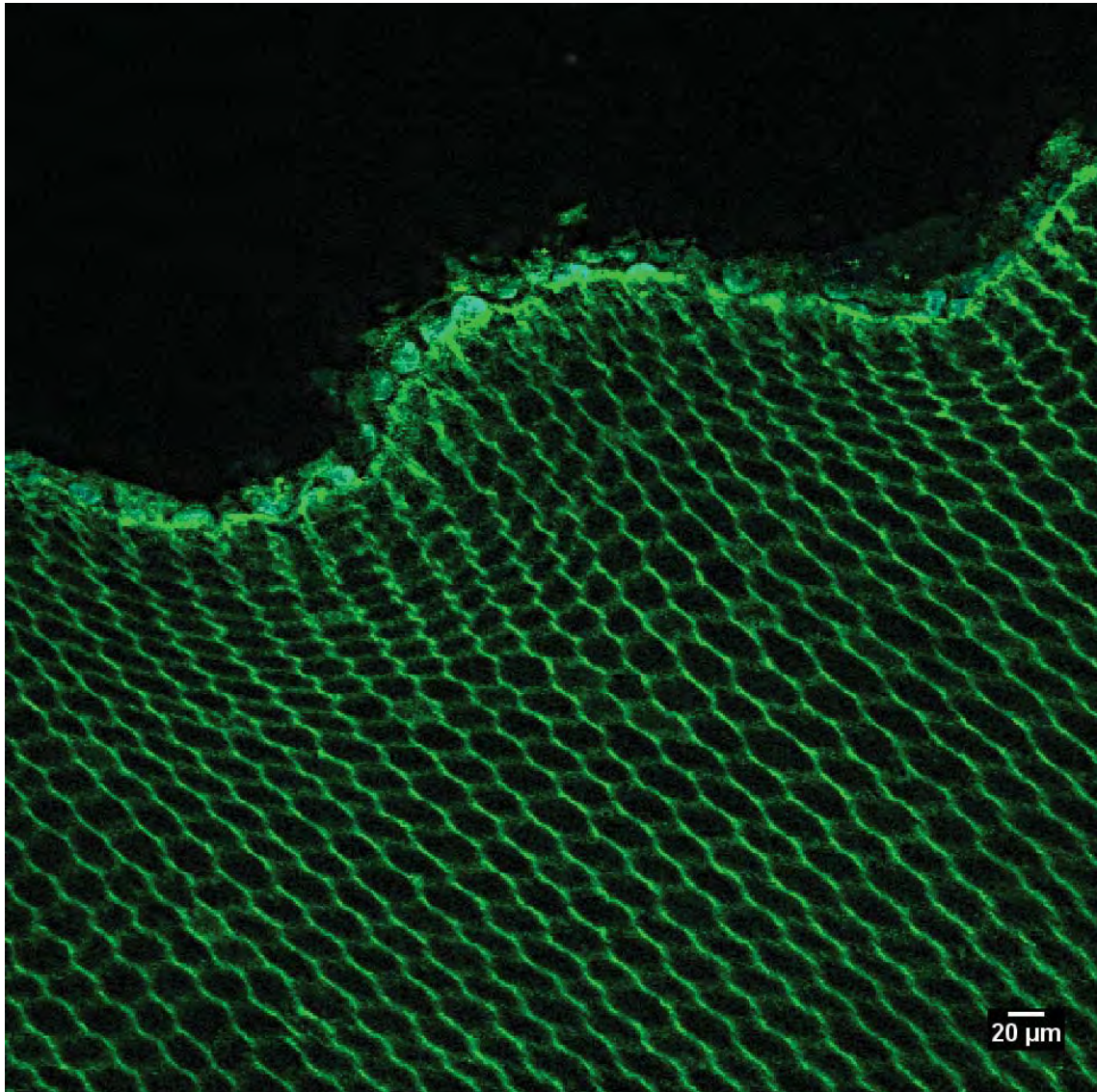
Figure 4.9: 40X porcine lens image highlighting hexagon pattern (courtesy of Christopher Bay)
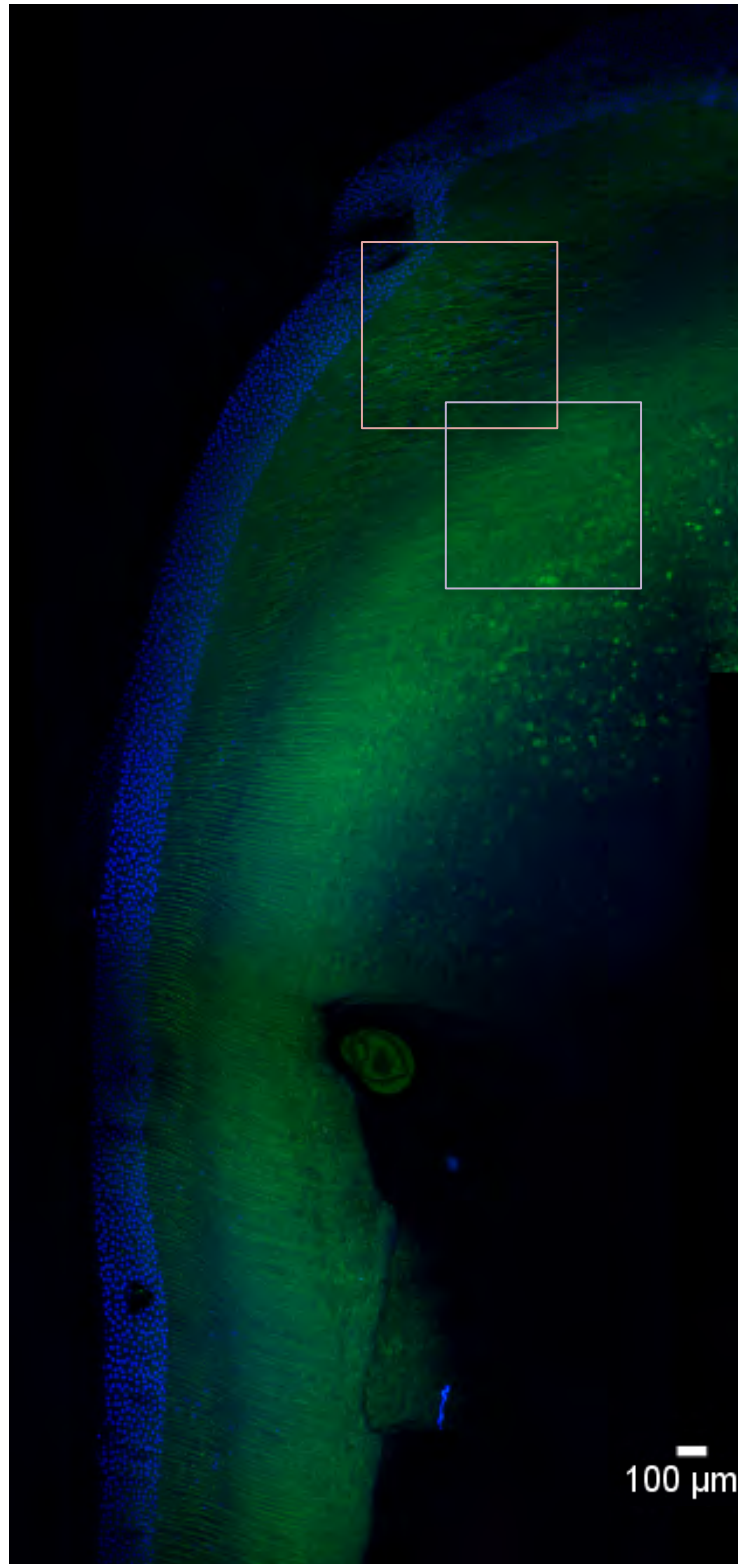
Figure 4.10: Stitched 10X confocal image of human lens fiber cells and epithelial cells

Bright spots indicating auto-fluorescence of sample

100 µm
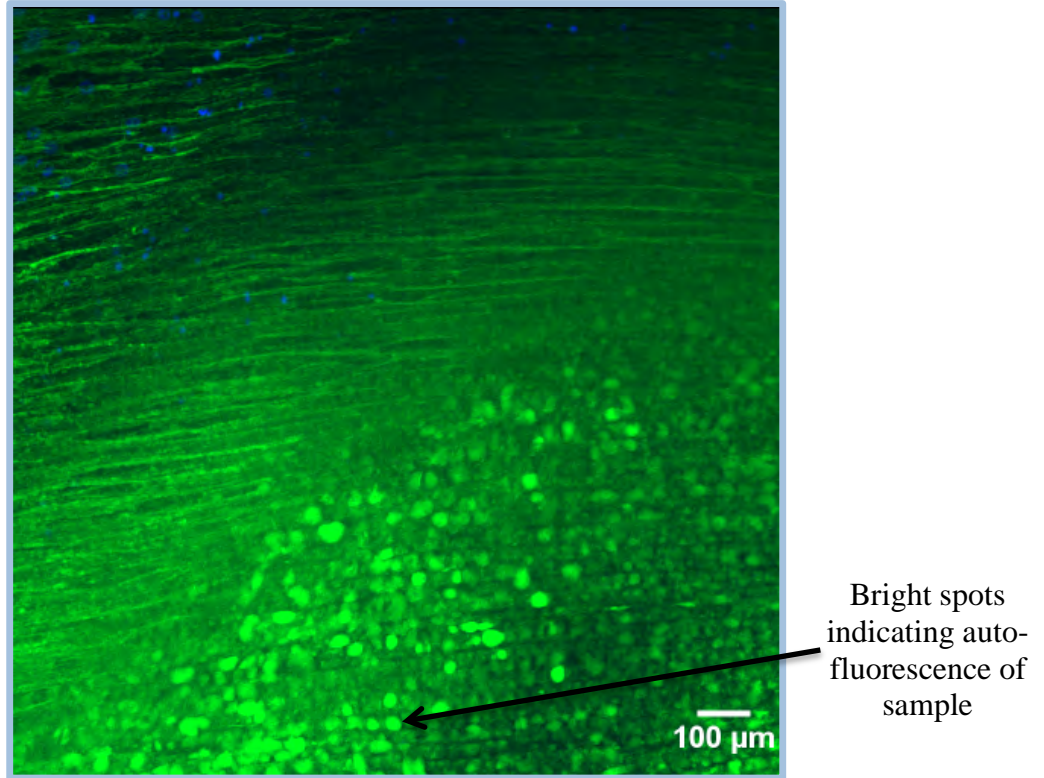
Figure 4.11: 20X region of section outlined by blue square in Figure 10

100 µm
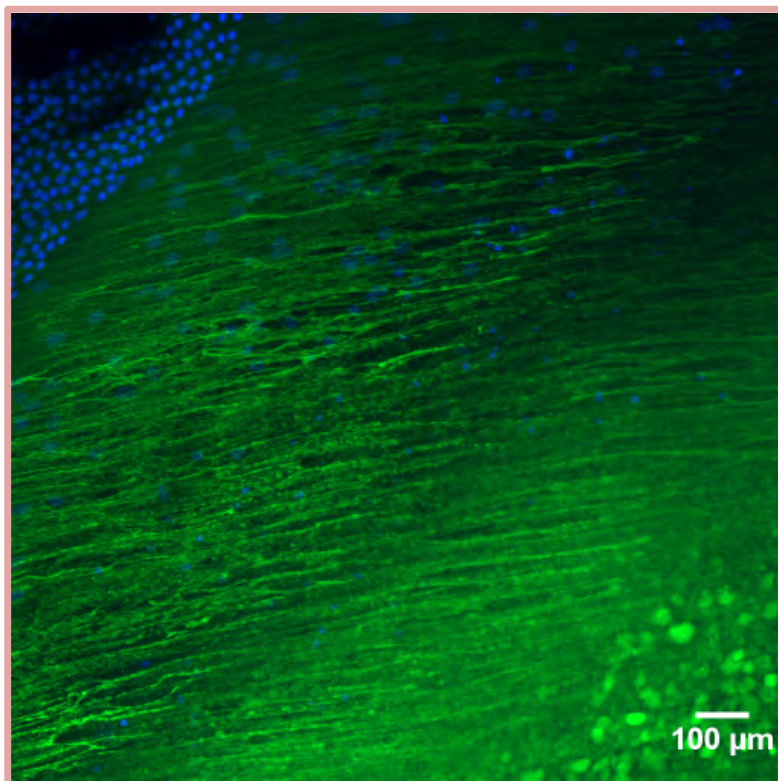
Figure 4.12: 20X region of section outline by red square in Figure 10

Figures 4.13 and 4.15, once again, utilize a feature of the ImageJ software enabling the

projection of these 20X and 40X images through the z-axis.
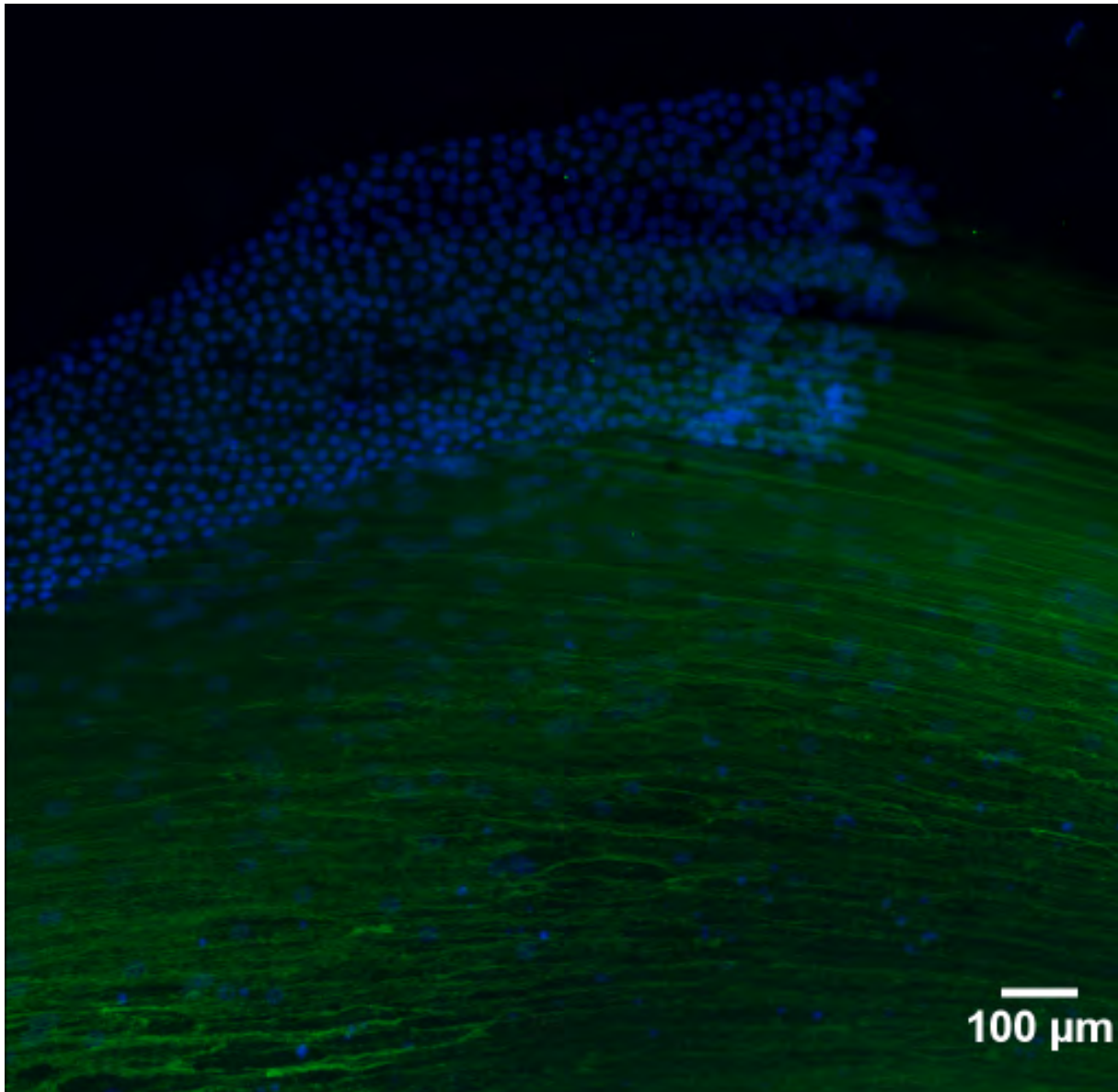
Figure 4.13: 3-D projection of 20X image stack

Figure 4.14, below, is included alongside Figure 4.15 in order to provide a comparison between a single layer image (4.14) and projected imaged (4.15), when processed with FIJI.
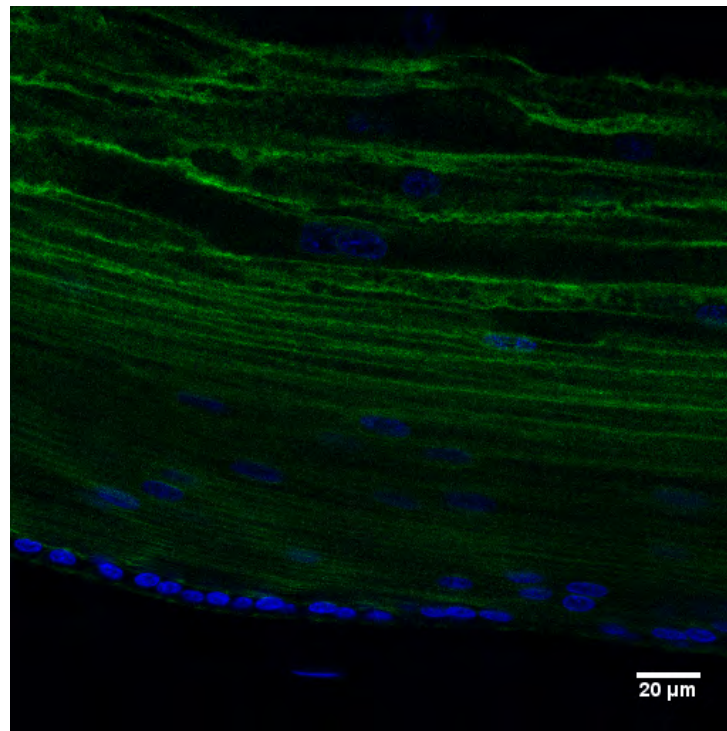
Figure 4.14: 40X image of human lens cortex
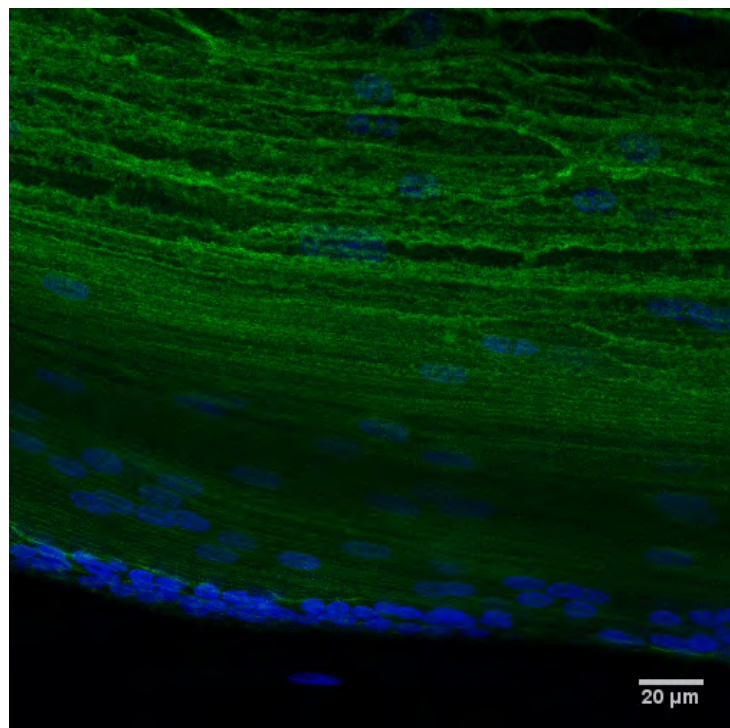
Figure 4.15: 3-D projection of 40X image of human lens cortex

V. Discussion

It was noted that the thicker lens sections appeared cloudy and stain permeation was minimal. A possible cause for this was excess usage of Triton-X 100. Although Triton-X 100 is an essential chemical for permeabilizing the cell wall, it is also a viscous detergent. Detergents remove the membrane of the cell (making holes on the cell membrane surface), thus increasing the permeability of the membrane to stains akin to Phalloidin or DAPI. Increasing the concentration of Triton, however, yields more holes in the cell membrane surface; therefore creating more tears in the lens fiber cell. Consequently, a short experiment was conducted to determine the appropriate concentration of PBST that yielded the best permeability without causing tissue damage. Ultimately, for thicker sections (300-500µm), 0.8X PBST generated better imaging results. On the other hand, for thinner section, similar to the samples presented in this study, 1X PBST produced better images. For this reason, all of the samples shown in the results were permeabilized with 1X PBST.

Ranges of sectioning thickness, which included 70µm – 500µm sections, were also attempted prior to determining the optimal thickness for the lens samples. For thinner samples, stain permeation was better, however the fragility of the sample resulted in the loss of the lens nuclei and subsequent damage of the tissue during the washing steps of staining. On the other hand, for larger sections, the stain could not penetrate through the sample and a very cloudy layer formed around the sample, as mentioned above. Ultimately, 200µm sections were used, as the samples did not form a cloudy layer and the stain was able to permeate through the sample. Although the centers fell out of these samples when approaching the nucleus of the lens, for the most part, the lens sections stayed intact. In particular, porcine tissue was gathered from young 6-9 month old pigs, since the starting model was to be void of any age-related cataract, which

was more prevalent in porcine samples obtained from pigs that were over two years old. Although the centers became more fragile as the layers were sectioned, significantly less of the cortex fell apart, in comparison to that of the human sample. This difference may be a function of the age as well as the innate characteristics of the porcine tissue, which appears to be more robust than the human lens, which was obtained from a 66-year old male.

As seen in a comparison between Figures 4.1 and 4.2, the 5X images demonstrate some linear trends of the fiber cells; however the 10X images, as seen in Figure 4.3, are preferred due to the clarity present in the images collected, in terms of identifying the ultrastructure of the lens fibers cells. For this reason, the full model will be gathered with a higher resolution. Ideally, the full structure should be gathered with the 40X objective; however each image stack takes approximately 40 minutes to position and obtain. For one cross-section, hundreds of 40X images must be collected. Then, this process must be repeated for each of 20-30 collected cross-sections to image the full 3-D ultrastructure of the fiber cells of one porcine lens. Due to time limitations, developing a full 40X model is not practical/ plausible. Consequently, the full lens will be imaged with the 10X objective. Within the stitched Figures 4.1 and 4.2, different intensities of the imaged samples were observed, thus yielding brighter or darker images. These variations in stitching samples of the 5X and 10X porcine lens sections arise from discrepancies in the imaging confocal microscope on different days. Furthermore, the images were gathered and stitched from a stack of images; therefore error in the software interpolation may have also contributed to the inconsistencies between samples being stitched together. The cross-section presented in Figures 4.2 and 4.3 is taken toward the middle of the lens. Specifically, this was the seventh-200μm section when sectioned sequentially and parallel to the optical axis. The 3-D

projection of this sample was also included, in Figure 4.4, to provide a glimpse of the eventual

goal for this project, which involves forming a 3-D projection of the full lens.

The 10X images, specifically Figures 4.2-4.6 demonstrate a linear pattern of cell

alignment that is consistent throughout the section. On the other hand, when resolving these

images with the 20X and 40X objectives in Figures 4.7, 4.8, and 4.9, the lens fibers follow a

hexagonal pattern when sectioned parallel to the optical axis, or along the x-z plane of Figure

3.6. Figure 4.5, however, was obtained from a sample that was sectioned perpendicular to the

optical plane, or along the x-y plane of Figure 3.6. As seen in this figure, the 3 suture planes

form at "Y" at the place of intersection. As the lens grows, these suture planes become increasing

complex, eventually forming a star suture with 12 suture planes at the anterior and posterior of

the human lens (Levin, et al., 2011). Figure 4.6 demonstrates lens fiber cells exhibiting

birefringence. This property refers to a material having a refractive index that depends on the

polarization and propagation direction of the light, resulting from anisotropic material

characteristics. In Figure 4.6, the fiber cells that are aligned with one another polarize the light

along a different plane than that of the fiber cells that were rearranged during the sectioning

procedure; therefore creating the shadowed effect as shown by the dark, displaced fiber cell

strands. In order to minimize light-scattering and maintain low total birefringence, the

supramolecular organization along with the parallel alignment of the lens fiber cells must be

precise (Mcdevitt, 2012). As seen in Figure 4.6, disturbance in this alignment results in severe

birefringence, which will greatly impair the refraction of light rays.

The human lens sections were ranging from 70-100μm. Imaging the inner cortex and

nucleus of the human lens was difficult, as cells fell apart easily as layers were sectioned. This

observation indicates that there may be a correlation between the denseness of the cells near the

nucleus and the age of individual. Additionally, auto-fluorescence, seen in Figures 4.10, 4.11, and 4.12 , was observed when approaching the cell interior; therefore indicating that the cells are either dead or densely packed, such that the stain cannot penetrate the cells. There is a very clear transition between the periphery of the sample, which was easier to section, and the center of the sample, which was fragile and peeling. This observation is in accordance with the current understanding of the manner in which the lens fiber cells grow: newer cells grow at the periphery of the lens and older cells are gradually pushed toward the center of the lens. With time, the center of the lens becomes denser as older cells continue to be pushed toward the nucleus, thus leading to age-related cataract (Yanoff & Duker, 2013).

Three-dimensional projections of the human lens sample are provided in Figures 4.13 and 4.15. Additionally, Figure 4.14 has been provided to show the differences between a single image and z-projection of the same region. More information about the lens through several planes is seen in 4.14. This detail reinforces the patterns observed through the lens sample. The linear patterns are, once again, observed in the human lens sample. However, the linearity is more consistent in the porcine lens sample. The age of each tissue is a likely cause for the differences observed. Since the porcine samples were gathered from younger pigs, not only were the samples easier to section, they also retained their natively parallel patterns during sectioning. On the other hand, imaging of the human lens was limited to the periphery of the sample. After this, since cells were denser and more difficult to section, the arrangement of the cells was distorted by the fragility of central fiber cells and lens nucleus.

VI. Conclusion

The protocol that is necessary for imaging the lens tissue using CLSM was determined. The optimal thickness for the porcine lens samples, which balances the effectiveness of stain permeation and lens fragility, was observed to be approximately 200μm. Furthermore, the appropriate concentration of blocking agent was 1X PBST for the sample thicknesses imaged for this study. Ultimately, the 3-D reconstruction of the lens will be created with images using the 10X objective, as the 5X objective does not provide enough detail to see the structure, while the full 40X reconstruction will not be feasible with time limitations. The 40X objective will, however, be used to gain a better understanding of regions of interest within the lens, for example, near the cells that are rearranged after exerting a load with the material testing system (MTS). The 10X images of the porcine lens indicated a uniformly parallel arrangement of the lens fiber cells. A disturbance in this alignment indicated birefringence, which will greatly impair vision in an in vivo environment. When observed with the 20X and 40X objectives, the hexagonal patterns of the lens fiber cells became apparent.

In comparison, the human lens fiber cells also followed a linear pattern. This pattern, however, was disrupted by the loss of the cells in the inner cortex and nucleus of the sample. Additionally, auto-fluorescence was observed in regions of the inner cortex that were retained after sectioning the sample. This auto-fluorescence is likely attributed to the dense arrangement of cells or the death of cells in this region. As a whole, there are significant differences between the robustness of the porcine and human lenses which may be due to the age of the respective samples. However, the linear arrangement and parallel alignment of the lens fiber cells is consistent between the porcine and human lens samples.

Future Work

There are also several smaller objectives that must be accomplished prior to compiling the information gathered into a finite element model. At present, sections must continue to be imaged to develop the three-dimensional model of the unmodified porcine lens, but there are also potential methods of optimizing the images obtained.

Changing the fixative can potentially mitigate the consistent loss of sample that is observed as sectioning approaches the nucleus. Specifically, the concentration of crosslinking formaldehyde in PFA can be adjusted and the fixation procedure can be modified to use alcohols, like methanol, to react the formaldehyde monomers. Formaldehyde covalently modifies certain bonds (C=O is the reactive side) while methanol decreases the solubility and disrupts hydrophobia, thus yielding better permeation of stains into the sample.

With regards to image post-processing, in order to improve interpolation conducted by the ImageJ program and ensure its accuracy in approximations made through the z-axis, a similar 3-D model for a sample that is perpendicular to the optical axis should be generated. This will resolve images collected by the current images in the z-direction and provide information regarding the suture points of the lens fiber cells.

Currently, porcine lenses are being used to gather these images and determine a thorough protocol to follow for subsequent 3-D reconstructions. Since there are clear differences between the human lens and the porcine lens, ultimately a 3-D arrangement of human lenses both intact and deformed must be imaged to develop a computational model that is most directly applicable to humans. In the future, thicker human lens samples will also need to be tested in order to determine a similar optimal thickness that will enable effective permeation of the stain and maintain the robustness of the lens through the washing and staining procedure.

Ultimately, the collected images will be used to initialize microstructural computational finite element meshes or other numerical discretization models. This model will provide useful information about relatively undistorted lens fiber cells. However, to gain a thorough understanding of the effects of trauma on these fiber cells, a 3-D model should be generated for a lens that has been loaded dynamically, punctured, or distorted in a form similar to ocular deformations observed in workplace accidents or military injuries. This will provide information regarding the range and limitations of lens fiber cell movement and make proposed solutions to this trauma more effective. Furthermore, if time studies are eventually conducted, more information about the nature of lens realignment post-trauma can be understood.

VII. References

Alm, A., & Kaufman, P. L. (2003). *Adler's Physiology of the Eye* (Tenth ed.). St. Louis , Missouri: Mosby Elsevier.

Bassnett, S., & Beebe, D. C. (1992). Coincident Loss of Mitochondria and Nuclei During Lens Fiber Cell Differentiation. *194*, 85-93.

Burd, H., Judge, S., & Cross, J. (2002). Numerical modelling of the accommodating lens. *Vision Research, 42*, 2235-2251.

FIJI. (2013). *Fiji Is Just ImageJ*. Retrieved from FIJI: http://fiji.sc/Fiji

Kessel, R. G., & Kardon, R. H. (1979). *Tissues and Organs: a text-atlas of scanning electron microscopy.* San Francisco, CA: W.H. Freenman and Co.

Levin, L. A., Nilsson, S. F., Ver Hoeve, J., Wu, S., Kaufman, P. L., & Alm, A. (2011). *Adler's Physiology of the Eye: Expert Consult.* Elsevier Health Sciences.

Mcdevitt, D. (2012). *Cell biology of the eye.* Elsevier.

McLeod, S., Portney, V., & Ting, A. (2003). A dual optic accommodating foldable intraocular lens. *British Journal of Opthalmology, 87*, 1083-1085.

nei.nih.gov. (n.d.). *Diagram of the Eye*. Retrieved from National Institutes of Health- National Eye Institute: http://www.nei.nih.gov/index.asp

Sharmaa, K. K., & Santhoshkumar, P. (2009, October). Lens aging: Effects of crystallins. *Biochimica et Biophysica Acta, Volume 1790,*(10), 1095–1108.

Taylor, V. L., Al-Ghoul, K. J., Lane, W., Davis, A., Kiszak, J. R., & Costello, M. J. (1996, June). Morphology of the Normal Human Lens. *Investigative Ophthalmology & Visual Science, 37*(7), 1396-1410.

Weichel, E. D., & Colyer, M. H. (2008). Combat ocular trauma and systemic injury. *Current*

    Opinion in Opthalmology, 19, 519-525.

Yanoff, M., & Duker, J. S. (2013). *Ophthalmology: Expert Consult: Online and Print.* Elsevier

    Health Sciences.

C   Journal Paper

The appendix includes a journal paper, to which is referred in early sections of this Final Report: Regueiro, R.A., Zhang, B., Wozniak, S.L. (2014) Large deformation dynamic three-dimensional coupled finite element analysis of soft biological tissues treated as biphasic porous media, *Comp. Model. Eng. Sci.*, 98(1):1-39.

Large Deformation Dynamic Three-Dimensional Coupled Finite Element Analysis of Soft Biological Tissues Treated as Biphasic Porous Media

R.A. Regueiro[1,2]**, B. Zhang**[2]**, S.L. Wozniak**[3]

Abstract: The paper presents three-dimensional, large deformation, coupled finite element analysis (FEA) of dynamic loading on soft biological tissues treated as biphasic (solid-fluid) porous media. An overview is presented of the biphasic solid-fluid mixture theory at finite strain, including inertia terms. The solid skeleton is modeled as an isotropic, compressible, hyperelastic material. FEA simulations include: (1) compressive uniaxial strain loading on a column of lung parenchyma with either pore air or water fluid, (2) out-of-plane pressure loading on a thin slab of lung parenchyma with either pore air or water fluid, and (3) pressure loading on a 1/8th symmetry vertebral disc (nucleus and annulus) with pore water. For the simulations, mixed formulation Q27P8 and stabilized Q8P8 finite elements are compared ("Q" indicates the number of solid skeleton displacement nodes, and "P" the number of pore fluid pressure nodes). The FEA results demonstrate the interplay of dynamics (wave propagation through solid skeleton and pore fluid), large deformations, effective stress and pore fluid pressure coupling, compressibility and viscosity of pore fluid, and three-dimensional effects for soft biological tissues treated as biphasic porous media.

Keywords: soft biological tissues; biphasic mixture theory; dynamics; large deformations; coupled three-dimensional finite element analysis

1   Introduction

It is well-known that soft biological tissues are multiphase (oftentimes treated as a biphasic mixture of solid and fluid phases (Holmes, 1986; Suh, Spilker, and

---

[1] richard.regueiro@colorado.edu

[2] Department of Civil, Environmental, and Architectural Engineering, University of Colorado, Boulder, Boulder, CO 80309

[3] Bowhead Science and Technology, LLC., U.S. Army Research Laboratory, Aberdeen Proving Ground, MD 21005

Holmes, 1991; Almeida and Spilker, 1998; Levenston, Frank, and Grodzinsky, 1998)) and can undergo large deformations. Few researchers have considered inertia terms in the biphasic theory in studying wave propagation through soft biological tissues (Zhu and Suh, 2000, 2001). The flow of pore fluid relative to solid skeleton deformation (such as squeezing a saturated sponge) must be handled properly within a finite strain context, as well as considering inertia terms for dynamic loading when necessary, and implemented properly within a mixed Lagrangian finite element (FE) formulation, or other large deformation numerical method. For typical physiological dynamic loading such as encountered during normal athletic activities (e.g., running, jumping), the relative acceleration of the fluid phase $\boldsymbol{a}_\mathrm{f}$ with respect to solid phase $\boldsymbol{a}_\mathrm{s}$ may be approximated as zero: $\tilde{\boldsymbol{a}}_\mathrm{f} = \boldsymbol{a}_\mathrm{f} - \boldsymbol{a}_\mathrm{s} \approx \boldsymbol{0}$. At higher strain rates, however, such as encountered during shock loading and head impact (e.g., leading to traumatic brain injury (TBI)), the relative acceleration of the fluid phase with respect to solid phase may not be zero ($\tilde{\boldsymbol{a}}_\mathrm{f} \neq \boldsymbol{0}$), requiring reformulation of the balance equations originally formulated for lower rate loading (such as normal athletic activities). Such extension is discussed in the paper, but all FE results currently assume $\tilde{\boldsymbol{a}}_\mathrm{f} \approx \boldsymbol{0}$. The mixed FE formulation and three-dimensional (3D) Q27P8 hexahedral FE implementation (27 solid skeleton displacement nodes, 8 pore fluid pressure nodes, Fig.4) leads to a stable finite element method even for undrained loading conditions, such as those encountered at the initial transient of dynamic loading. A stabilized mixed formulation (Brezzi and Pitkaranta, 1984; Truty and Zimmermann, 2006; White and Borja, 2008; Sun, Ostien, and Salinger, 2013) Q8P8 hexahedral element is also implemented within the coupled dynamics framework, and results are compared with the Q27P8 element. The formulation for biphasic mixture theory at finite strain naturally calculates the build up of pore fluid pressure, and thus properly calculates, through the effective stress principle, the change in solid skeleton stress (i.e., the "effective" stress) over time, when a biphasic soft tissue is subjected to dynamic loading. Also, after the initial transient, the variation of solid skeleton stresses will be naturally calculated as the fluid phase pressure dissipates over time. This is important for developing physiologically-relevant degradation/damage hyperelastic, anisotropic constitutive models for soft biological tissues (Pena, 2011; Balzani, Brinkhues, and Holzapfel, 2012) within the context of biphasic mixture theory. The 3D FE implementation is conducted in Tahoe (`tahoe.sourceforge.net`), an opensource C++ FE code, with more details provided in Ebrahimi (2007); Regueiro and Ebrahimi (2010), and formulation details in Li, Borja, and Regueiro (2004).

An outline of the remainder of the paper is as follows: Section 2 presents a brief overview of the theory of biphasic solid-fluid mixtures at finite strain, including kinematics, balance equations (linear momentum, and mass), and thermodynamics

for constitutive equation forms. Section 3 also presents the stabilization term on the balance of mass for stabilized Q8P8 implementation. Section 4 presents numerical examples to test the performance of the Q27P8 versus Q8P8 elements, and also to study the importance of including inertia terms for simulating dynamic loading of soft biological tissues treated as porous media. Section 5 summarizes the results, conclusions, and future work.

Index notation will be used wherever needed to clarify the presentation. Cartesian coordinates are assumed, so all indices are subscripts, and the partial spatial derivative is the same as covariant spatial derivative (Eringen, 1962). Some symbolic/direct notation is also given, such that $(\boldsymbol{F}^T \cdot \boldsymbol{F})_{IJ} = F_{iI}F_{iJ}$, where $\boldsymbol{F}$ is the deformation gradient. Boldface denotes a tensor or vector. Subscript $(\bullet)_{,i}$ implies a partial spatial derivative. Lowercase subscript i denotes a leg of the tensor in the current configuration $\mathscr{B}$, and capital subscript $I(\text{s})$ denotes a leg of the tensor in the reference configuration $\mathscr{B}_0^{\text{s}}$ of the solid skeleton. Superposed dot $(\dot{\Box}) \overset{\text{def}}{=} D^{\text{s}}(\Box)/Dt$ denotes material time derivative with respect to the solid skeleton motion. The symbol $\overset{\text{def}}{=}$ implies a definition.

2 Biphasic (solid-fluid) mixture theory at finite strain: overview of theory and 3D FE implementation

The background for the theory of porous media at finite strain may be found primarily in Bowen (1980, 1982); Coussy (2004); de Boer (2005), and originally in Truesdell and Toupin (1960). For other details on nonlinear solid mechanics, refer to Holzapfel (2000) and references therein. We follow the notation of Holzapfel (2000); de Boer (2005), and to some extent also Bowen (1980, 1982).

2.1 Concept of volume fraction and mixture theory

The concept of volume fraction is illustrated in Fig.1 for the lung parenchyma (alveolar tissue for solid skeleton). The volume fractions n^{α} for a biphasic mixture (solid (s) and fluid (f)) relate "real" quantities with respect to the differential volume dv_{α} of constituent α in the current configuration, versus the smeared quantity over the total differential volume dv, where $n^{\alpha} = dv_{\alpha}/dv$, or $dv_{\alpha} = n^{\alpha}dv$. For example, the partial mass density of the α constituent is calculated as $\rho^{\alpha} = \rho^{\alpha R}n^{\alpha}$ (see Fig.1), where $\rho^{\alpha R}$ is the real mass density of constituent α. Similarly, mass of constituent α, m_{α}, over the total body $\mathscr{B}$ can be defined (see Fig.1).

2.2 Motion and kinematics, material time derivative

The kinematics of a biphasic solid-fluid mixture theory are shown in Fig.2. The vector $\boldsymbol{x}$ is the spatial position vector, which is simultaneously occupied by all

$$n^\alpha(\boldsymbol{x},t) = dv_\alpha/dv$$

$$\sum_\alpha n^\alpha = 1 , \quad n^{\mathrm{f}} + n^{\mathrm{s}} = 1$$

$$dv = \sum_\alpha dv_\alpha$$

- n^α = volume fraction of constituent α in $dv \subset \mathscr{B}$, where $\mathscr{B} = \mathscr{B}^{\mathrm{s}}$

- dv_α = differential volume of constituent α in dv

$$m_\alpha = \int_{\mathscr{B}^\alpha} \rho^{\alpha R} dv_\alpha = \int_{\mathscr{B}} \rho^{\alpha R} n^\alpha dv = \int_{\mathscr{B}} \rho^\alpha dv$$

$$\rho^{\alpha R} = dm_\alpha/dv_\alpha$$

$$\rho^\alpha = dm_\alpha/dv = \rho^{\alpha R} n^\alpha$$

- dm_α = differential mass of constituent α

- $\rho^{\alpha R}$ = real mass density of constituent α

- ρ^α = partial mass density of constituent α
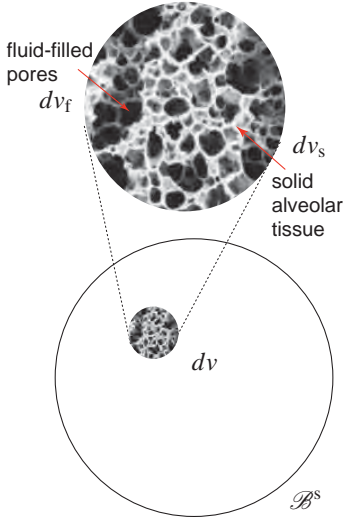
*theory of porous media assumes control space is that of the solid phase $\mathscr{B} \stackrel{\mathrm{def}}{=} \mathscr{B}^{\mathrm{s}}$

Figure 1: Concept of volume fraction for biphasic (solid(s)-fluid(f)) mixture theory, showing solid skeleton composed of alveolar tissue, and definitions of mass and density.

constituent material points $X_{\mathrm{s}}, X_{\mathrm{f}}$ of the mixture (homogenized, or smeared), such that $\boldsymbol{x} = \boldsymbol{\chi}_{\mathrm{f}}(\boldsymbol{X}_{\mathrm{f}}, t) = \boldsymbol{\chi}_{\mathrm{s}}(\boldsymbol{X}_{\mathrm{s}}, t)$, where the material point of the solid skeleton X_{s} is mapped from the reference position $\boldsymbol{X}_{\mathrm{s}}$ to the current position $\boldsymbol{x}$ through mapping χ_{s} (and similarly for the material point of pore fluid X_{f} which maps through χ_{f}, Fig.2). We define the inverse map $\boldsymbol{X}_\alpha = \boldsymbol{\chi}_\alpha^{-1}(\boldsymbol{x}, t)$ $(X_{I(\alpha)} = \chi_{I(\alpha)}^{-1}(\boldsymbol{x}, t))$, assuming smoothly differentiable fields. The deformation gradient and its inverse are written for each phase α as,

$$\boldsymbol{F}_\alpha = \frac{\partial \boldsymbol{\chi}_\alpha}{\partial \boldsymbol{X}_\alpha}, \quad \boldsymbol{F}_\alpha^{-1} = \frac{\partial \boldsymbol{X}_\alpha}{\partial \boldsymbol{x}}$$
$$F_{iI(\alpha)} = \frac{\partial \chi_{i(\alpha)}}{\partial X_{I(\alpha)}}, \quad F_{Ii(\alpha)}^{-1} = \frac{\partial X_{I(\alpha)}}{\partial x_i} \tag{1}$$

Likewise, the volumetric deformation of a solid-fluid mixture, that is smeared in the current configuration at spatial position vector $\boldsymbol{x}$, is shown in Fig.3. The differential
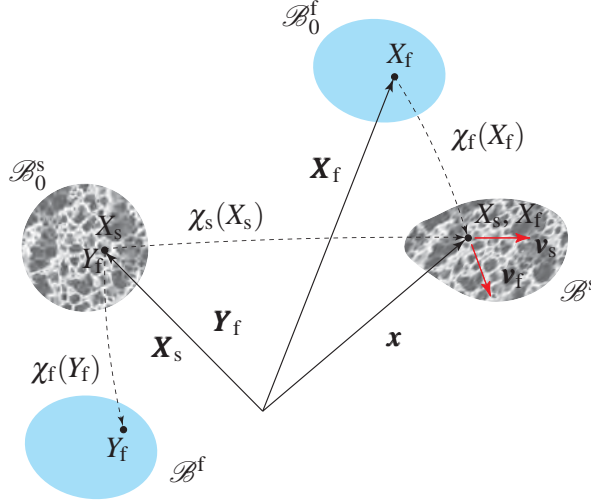
Figure 2: Kinematics of a biphasic (solid-fluid) mixture theory, showing solid skeleton composed of alveolar tissue. The continuum assumption of mixture theory is evident in the assumption that solid (s) and fluid (f) constituents coexist at the current position $\boldsymbol{x}$, although their velocities $\boldsymbol{v}_s$ and $\boldsymbol{v}_f$ may be different; i.e., $\boldsymbol{v}_f \neq \boldsymbol{v}_s$, in general.

volumes dV_f and dV_s in their respective reference configurations $\mathscr{B}_0^f$ and $\mathscr{B}_0^s$, both map to the same differential volume dv in the current configuration $\mathscr{B}$, through their deformation gradients $\boldsymbol{F}_f$ and $\boldsymbol{F}_s$.

The Jacobian of deformation for the two constituents is written as,

$$J_s = \det\boldsymbol{F}_s > 0 \;; \quad J_f = \det\boldsymbol{F}_f > 0 \tag{2}$$

$$dv = J_s dV_s = J_f dV_f \tag{3}$$

$$dv_\alpha = n^\alpha dv = n^\alpha J_\alpha dV_\alpha \tag{4}$$

$$dV_f \subset \mathscr{B}_0^f \,, \quad dV_s \subset \mathscr{B}_0^s \tag{5}$$

where we will typically drop the s superscripts and subscripts because the theory of porous media assumes we follow the motion of the solid skeleton.
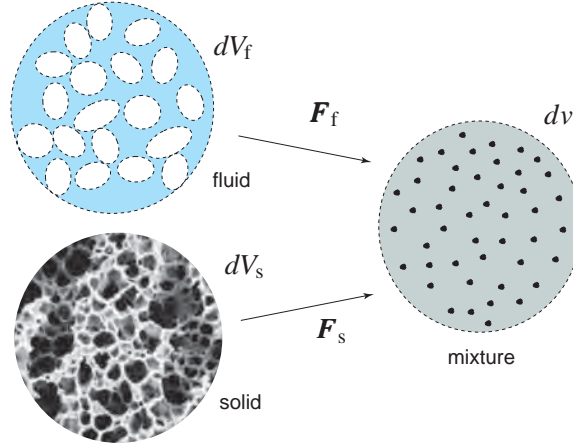
Figure 3: Volumetric deformation of solid and fluid constituents in a biphasic mixture (solid skeleton composed of alveolar tissue of the lung parenchyma).

We convert all material time derivatives with respect to the solid phase motion $((\dot{\square}) \stackrel{\text{def}}{=} D^s(\square)/Dt)$, such that for phase α, the material time derivative is,

$$\frac{D^\alpha(\square)}{Dt} = \frac{D^s(\square)}{Dt} + \frac{\partial(\square)}{\partial \boldsymbol{x}} \cdot \tilde{\boldsymbol{v}}_\alpha \tag{6}$$

$$\tilde{\boldsymbol{v}}_\alpha = \boldsymbol{v}_\alpha - \boldsymbol{v}_s \tag{7}$$

$$\frac{D^s(\square)}{Dt} = \frac{\partial(\square)}{\partial t} + \frac{\partial(\square)}{\partial \boldsymbol{x}} \cdot \boldsymbol{v}_s \tag{8}$$

where $\tilde{\boldsymbol{v}}_\alpha$ is the relative velocity vector of the α phase with respect to the solid (s) phase motion. The material time derivative will be used in deriving the balance equations in the following sections.

2.3 Balance of mass (spatial and material descriptions)

For the balance of mass of the mixture, we write separately the balance of mass of each constituent, solid and fluid, expressing all material time derivatives in terms of the solid skeleton motion, and then add the two equations together to obtain the balance of mass of the mixture. The total mass of constituent α in $\mathscr{B}$ is written as (cf. Fig.1)

$$m_\alpha = \int_{\mathscr{B}} \rho^\alpha dv = \int_{\mathscr{B}_0^\alpha} \rho^\alpha J_\alpha dV_\alpha \tag{9}$$

Taking the material time derivative of this spatial field m_α with respect to the motion of constituent α, we can express the balance of mass of constituent α as

$$\frac{D^\alpha m_\alpha}{Dt} = \int_{\mathscr{B}} \left(\frac{D^\alpha \rho^\alpha}{Dt} + \rho^\alpha \text{div} \boldsymbol{v}_\alpha \right) dv = \int_{\mathscr{B}} \gamma^\alpha dv \tag{10}$$

where γ^α is the mass supply rate for constituent α. If we assume compressibility of constituent α, assuming temperature is constant, we may write (Li, Borja, and Regueiro, 2004)

$$\frac{1}{\rho^{\alpha R}} \frac{D^\alpha \rho^{\alpha R}}{Dt} = \frac{1}{K_\alpha} \frac{D^\alpha p_\alpha}{Dt} \tag{11}$$

where p_α is the mean Cauchy stress of constituent α, and K_α is the bulk modulus. Then balance of mass for constituent α becomes:

$$\frac{D^\alpha n^\alpha}{Dt} + \frac{n^\alpha}{K_\alpha} \frac{D^\alpha p_\alpha}{Dt} + n^\alpha \text{div} \boldsymbol{v}_\alpha = \frac{\gamma^\alpha}{\rho^{\alpha R}} \tag{12}$$

We assume that the solid constituent is nearly incompressible, such that $n^s/K_s \rightarrow 0$, and also that there is no supply of solid mass, such that $\gamma^s = 0$. Using these assumptions, we can solve for the volume fraction of the solid phase as $n^s = n_0^s/J_s$ in closed form from the balance of mass equation for the solid phase by itself (Li, Borja, and Regueiro, 2004). The volume fraction of fluid is then solved as $n^f = 1 - n^s$. The simplified form of the balance of mass of the biphasic (solid-fluid) mixture (to solve for Cauchy pore fluid pressure p_f) then results as, when adding Eq.(12) for $\alpha = f, s$,

$$\frac{n^f}{K_f} \frac{D^s p_f}{Dt} + \text{div} \boldsymbol{v}_s + \frac{1}{K_f} \frac{\partial p_f}{\partial \boldsymbol{x}} \cdot (n^f \tilde{\boldsymbol{v}}_f) + \text{div}(n^f \tilde{\boldsymbol{v}}_f) = \frac{\gamma^f}{\rho^{fR}} \tag{13}$$

We can map Eq.(13) back to the reference configuration of the solid phase $\mathscr{B}_0^s$ to obtain the following,

$$\frac{J_s n^f}{K_f} \frac{D^s p_f}{Dt} + \frac{D^s J_s}{Dt} + \frac{J_s}{K_f} \frac{\partial p_f}{\partial \boldsymbol{X}_s} \cdot \boldsymbol{F}_s^{-1} \cdot (n^f \tilde{\boldsymbol{v}}_f) + J_s \left[\frac{\partial (n^f \tilde{\boldsymbol{v}}_f)}{\partial \boldsymbol{X}_s} \right] : \boldsymbol{F}_s^{-T} = \frac{J_s \gamma^f}{\rho^{fR}} \tag{14}$$

For a Total Lagrangian FE implementation, this is the equation from which we derive our variational equation for the weak form.

2.4 Balance of linear momentum (material and spatial descriptions)

Here, the balance of linear momentum of the biphasic solid-fluid mixture is presented. Carrying out the material time derivative of the linear momentum with respect to the α phase motion, applying the balance of mass of constituent α, and using the divergence theorem on the traction term $\boldsymbol{t}^{\alpha}$, we can localize the integral to obtain the balance of linear momentum for phase α in the current configuration as,

$$\text{div}\boldsymbol{\sigma}^{\alpha} + \rho^{\alpha}\boldsymbol{b}^{\alpha} + \boldsymbol{h}^{\alpha} = \rho^{\alpha}\boldsymbol{a}_{\alpha} + \gamma^{\alpha}\boldsymbol{v}_{\alpha} \tag{15}$$

where $\boldsymbol{\sigma}^{\alpha}$ is the partial Cauchy stress, such that the total Cauchy stress $\boldsymbol{\sigma} = \boldsymbol{\sigma}^{s} + \boldsymbol{\sigma}^{f}$, ρ^{α} is the partial mass density, such that total mass density $\rho = \rho^{s} + \rho^{f}$, $\boldsymbol{b}^{\alpha}$ is the body force per unit mass on constituent α (we will assume the same body force per unit mass for each constituent, such as acceleration of gravity, $\boldsymbol{b}^{\alpha} = \boldsymbol{g}$), $\boldsymbol{h}^{\alpha}$ is the interaction body force from all other constituents on constituent α, $\boldsymbol{a}_{\alpha}$ is the acceleration vector, and $\gamma^{\alpha}\boldsymbol{v}_{\alpha}$ is the mass supply momentum (usually negligible). We note that the internal body forces due to drag between constituents sum to zero (equal and opposite), and thus do not affect the mixture as a whole, such that $\boldsymbol{h}^{s} + \boldsymbol{h}^{f} = \boldsymbol{0}$. The balance of angular momentum for non-polar constituents states that the respective partial stresses (and, in turn, the total Cauchy stress, and effective stress) are symmetric: $\boldsymbol{\sigma}^{\alpha} = (\boldsymbol{\sigma}^{\alpha})^{T}$.

It is now relevant to discuss a principle that allows us to distinguish stress acting on the solid skeleton, and the pressure acting on the pore fluid (assuming the fluid is nearly inviscid, such as water). We apply the effective stress principle, which can be credited to Terzaghi (1943) (pg12) for saturated condition of soils, that states[1]

$$\boldsymbol{\sigma} = \boldsymbol{\sigma}' - p_{f}\left(1 - \frac{K^{\text{skel}}}{K_{s}}\right)\boldsymbol{1} \tag{16}$$

where the real pore fluid pressure $p_{f} = \frac{1}{3n^{f}}\text{tr}(\boldsymbol{\sigma}^{f})$ is positive in compression, and the mean effective stress is positive in tension $p' = \frac{1}{3}\text{tr}(\boldsymbol{\sigma}')$, where $\boldsymbol{\sigma}'$ is the "effective" Cauchy stress, or the stress acting on the solid skeleton, for which we will apply our solid skeleton constitutive equations. $B = \left(1 - \frac{K^{\text{skel}}}{K_{s}}\right)$ is the Biot coefficient (Coussy, 2004), and K^{skel} is the solid skeleton bulk modulus. For soils and soft biological tissues, $K^{\text{skel}}/K_{s} \to 0$, whereas for rocks and bone K^{skel}/K_{s} is finite. We

---

[1] The application of the effective stress principle to soft biological tissues has not been completely tested to date, but it is applied here for theoretical and numerical convenience. This is a topic of further research.

assume a nearly inviscid (no shear stress) isotropic fluid (e.g., water), where then

$$\boldsymbol{\sigma}^{\mathrm{f}} = -p^{\mathrm{f}} \mathbf{1} \implies p_{\mathrm{f}} = \frac{p^{\mathrm{f}}}{n^{\mathrm{f}}} \tag{17}$$

and

$$\boldsymbol{\sigma}^{\mathrm{s}} = \boldsymbol{\sigma}' - p^{\mathrm{f}} \left(\frac{1}{n^{\mathrm{f}}} - 1 \right) \mathbf{1} \tag{18}$$

Thus, we note that the partial solid stress $\boldsymbol{\sigma}^{\mathrm{s}}$ is not equal to the effective stress $\boldsymbol{\sigma}'$, $\boldsymbol{\sigma}^{\mathrm{s}} \neq \boldsymbol{\sigma}'$, unless the pore fluid pressure $p_{\mathrm{f}} = 0$. The effective stress principle is useful for introducing constitutive equations for the solid skeleton separate from the pore fluid.

Starting with Eq.(15), we can map the balance of linear momentum of phase α back to the reference configuration of the solid phase $\mathscr{B}_0^{\mathrm{s}}$. The partial first Piola-Kirchhoff stress α with respect to solid phase reference configuration is written as,

$$\boldsymbol{P}_{\mathrm{s}}^{\alpha} = J_{\mathrm{s}} \boldsymbol{\sigma}^{\alpha} \cdot \boldsymbol{F}_{\mathrm{s}}^{-T} \ , \ P_{iI(\mathrm{s})}^{\alpha} = J_{\mathrm{s}} \sigma_{ij}^{\alpha} F_{I(\mathrm{s})j}^{-1} \tag{19}$$

where subscript s denotes the reference configuration $\mathscr{B}_0^{\mathrm{s}}$ to which the j leg of σ_{ij}^{α} is mapped. It is then possible to arrive at the balance of linear momentum in the reference configuration of the solid phase (s) for phase α as,

$$\mathrm{DIV}_{\mathrm{s}} \boldsymbol{P}_{\mathrm{s}}^{\alpha} + \rho_{0(\mathrm{s})}^{\alpha} \boldsymbol{b}^{\alpha} + J_{\mathrm{s}} \boldsymbol{h}^{\alpha} = \rho_{0(\mathrm{s})}^{\alpha} \boldsymbol{a}_{\alpha} + \gamma_{0(\mathrm{s})}^{\alpha} \boldsymbol{v}_{\alpha} \tag{20}$$

Starting with Eq.(20), we can write each balance of linear momentum equation for solid (s) and fluid (f) phases, and use the following information to derive the balance of linear momentum of the solid-fluid mixture (s)+(f) in the reference configuration of the solid phase $\mathscr{B}_0^{\mathrm{s}}$:

1. total Cauchy stress, and first Piola-Kirchhoff stress with respect to $\mathscr{B}_0^{\mathrm{s}}$:

$$\boldsymbol{\sigma} = \boldsymbol{\sigma}^{\mathrm{s}} + \boldsymbol{\sigma}^{\mathrm{f}} \ , \ \boldsymbol{P}_{\mathrm{s}} = \boldsymbol{P}_{\mathrm{s}}^{\mathrm{s}} + \boldsymbol{P}_{\mathrm{s}}^{\mathrm{f}} \tag{21}$$

2. effective stress equation for Cauchy stress:

$$\boldsymbol{\sigma} = \boldsymbol{\sigma}' - p_{\mathrm{f}} \left(1 - \frac{K^{\mathrm{skel}}}{K_{\mathrm{s}}} \right) \mathbf{1} \tag{22}$$

3. assume solid and fluid phase accelerations are nearly the same (for now): $\boldsymbol{a}_f \approx \boldsymbol{a}_s = \boldsymbol{a}$, which may be appropriate for longer period motions like earthquakes and athletic activities, but likely not appropriate for high impact events experienced during car crash, or blast loading

4. assume all mass supplies are negligible: $\gamma^\alpha = 0$

5. assume body forces per unit mass are only due to gravity: $\boldsymbol{b}^\alpha = \boldsymbol{g}$, where $\boldsymbol{g}$ is the acceleration vector of gravity

The resulting balance of linear momentum of the solid-fluid mixture (s)+(f) in the reference configuration of the solid phase $\mathscr{B}_0^s$ is then written as,

$$\text{DIV}_s \boldsymbol{P}_s + \rho_{0(s)} \boldsymbol{g} = \rho_{0(s)} \boldsymbol{a} \tag{23}$$

$$\boldsymbol{P}_s = \boldsymbol{P}_s' - J_s p_f B \boldsymbol{F}_s^{-T} \tag{24}$$

Eventually, for the Total Lagrangian finite element formulation, we will drop the s designation because the reference configuration will always be that of the solid skeleton (phase), such that,

$$\text{DIV} \boldsymbol{P} + \rho_0 \boldsymbol{g} = \rho_0 \boldsymbol{a} \tag{25}$$

$$\boldsymbol{P} = \boldsymbol{P}' - J p_f B \boldsymbol{F}^{-T} \tag{26}$$

Remark 1: balance of linear momentum (spatial description) for $\boldsymbol{a}_s \neq \boldsymbol{a}_f$. Let us revisit the balance of linear momentum for the solid-fluid mixture in the current configuration $\mathscr{B}$, assuming $\boldsymbol{a}_s \neq \boldsymbol{a}_f$, such that,

$$\text{div} \boldsymbol{\sigma} + \rho \boldsymbol{g} = \rho^s \boldsymbol{a}_s + \rho^f \boldsymbol{a}_f \tag{27}$$

The question becomes how to handle $\boldsymbol{a}_f$. One way is to write the balance of linear momentum specifically for the fluid phase as,

$$\text{div} \boldsymbol{\sigma}^f + \rho^f \boldsymbol{b}^f + \boldsymbol{h}^f = \rho^f \boldsymbol{a}_f \tag{28}$$

where for an inviscid fluid phase, $\boldsymbol{\sigma}^f = -n^f p_f \mathbf{1}$, we can express the interaction fluid body force as,

$$\boldsymbol{h}^f = p_f \frac{\partial n^f}{\partial \boldsymbol{x}} - \left(\frac{n^f}{\hat{k}}\right)(n^f \tilde{\boldsymbol{v}}_f) \tag{29}$$

where the superficial fluid velocity vector $(n^{\mathrm{f}} \tilde{\boldsymbol{v}}_{\mathrm{f}})$ (a.k.a., the Darcy velocity) is defined constitutively in Eq.(41). Then, upon substituting Eq.(29) into Eq.(28), we can write the balance of linear momentum for the fluid phase as,

$$\rho^{\mathrm{f}} \boldsymbol{a}_{\mathrm{f}} + n^{\mathrm{f}} \frac{\partial p_{\mathrm{f}}}{\partial \boldsymbol{x}} + \left(\frac{n^{\mathrm{f}}}{\hat{k}} \right) (n^{\mathrm{f}} \tilde{\boldsymbol{v}}_{\mathrm{f}}) - \rho^{\mathrm{f}} \boldsymbol{g} = \boldsymbol{0} \tag{30}$$

Then, Eq.(30), upon mapping back to the solid skeleton reference configuration, including Eqs.(14),(23), we have three coupled balance equations to solve for three unknown fields: solid skeleton displacement $\boldsymbol{u}_{\mathrm{s}}$, fluid phase displacement $\boldsymbol{u}_{\mathrm{f}}$, and Cauchy pore fluid pressure p_{f}. A similar procedure was followed for small strain by Jeremic, Cheng, Taiebat, and Dafalias (2008). This is left for future work.

2.5 *Thermodynamics (first and second laws, constitutive equation forms)*

Before we introduce constitutive equations, we briefly present the thermodynamics for a biphasic mixture. Using the first and second laws of thermodynamics, and assuming the existence of a Helmholtz free energy per unit mass of the α phase ψ^{α}, we derive the Clausius-Duhem inequality, which will be useful for defining constitutive model forms.

Applying the material time derivative to the total internal energy of phase α, using the balance of mass for α, divergence theorem on the traction term, and balance of linear momentum on α, and localizing the integral, we can derive the balance of energy of phase α in the current configuration $\mathscr{B}$ as,

$$
\underbrace{\rho^{\alpha} \frac{D^{\alpha} e^{\alpha}}{Dt}}_{\text{internal energy density rate}} - \underbrace{\boldsymbol{\ell}_{\alpha} : \boldsymbol{\sigma}^{\alpha}}_{\text{stress power}} + \underbrace{\operatorname{div} \boldsymbol{q}^{\alpha}}_{\text{internal heat flux}} - \underbrace{\rho^{\alpha} r^{\alpha}}_{\text{internal heat supply rate}}
$$

$$
= \underbrace{\gamma^{\alpha} \left(\frac{1}{2} \boldsymbol{v}_{\alpha} \cdot \boldsymbol{v}_{\alpha} - e^{\alpha} \right)}_{\text{mass supply power}} - \underbrace{\boldsymbol{v}_{\alpha} \cdot \boldsymbol{h}^{\alpha}}_{\text{interphase power}} + \underbrace{\hat{e}^{\alpha}}_{\text{phase } \alpha \text{ power}} \tag{31}
$$

where e^{α} is the internal energy per unit mass of α, $\boldsymbol{q}^{\alpha}$ is the heat flux vector, r^{α} is the heat input rate per unit mass, and $\hat{e}^{\alpha}$ is the power density supply to phase α by other phases. The second law of thermodynamics for phase α is written in the current configuration $\mathscr{B}$ as,

$$\theta^{\alpha} \gamma^{\alpha} \eta^{\alpha} + \rho^{\alpha} \frac{D^{\alpha} \eta^{\alpha}}{Dt} \theta^{\alpha} - \rho^{\alpha} r^{\alpha} - \frac{1}{\theta^{\alpha}} \frac{\partial \theta^{\alpha}}{\partial \boldsymbol{x}} \cdot \boldsymbol{q}^{\alpha} + \operatorname{div} \boldsymbol{q}^{\alpha} \geq 0 \tag{32}$$

where η^α is the entropy per unit mass, and θ^α is the temperature of phase α. To obtain the Clausius-Duhem inequality in the current configuration for phase α, we consider the existence of the Helmholtz free energy per unit mass for phase α in the current configuration ψ^α as,

$$\psi^\alpha = e^\alpha - \theta^\alpha \eta^\alpha \tag{33}$$

Taking the material time derivative of Eq.(33), using the first law in Eq.(31), and substituting into the second law in Eq.(32), we arrive at the Clausius-Duhem inequality for phase α as,

$$\underbrace{\gamma^\alpha \left(\theta^\alpha \eta^\alpha + \frac{1}{2} \boldsymbol{v}_\alpha \cdot \boldsymbol{v}_\alpha - e^\alpha \right)}_{\text{mass supply power}} + \underbrace{\boldsymbol{\ell}_\alpha : \boldsymbol{\sigma}^\alpha}_{\text{stress power}} - \underbrace{\boldsymbol{v}_\alpha \cdot \boldsymbol{h}^\alpha}_{\text{interphase power}} + \underbrace{\hat{e}^\alpha}_{\text{phase } \alpha \text{ power}}$$

$$- \underbrace{\rho^\alpha \frac{D^\alpha \psi^\alpha}{Dt}}_{\text{Helmholtz free energy density rate}} - \underbrace{(\rho^\alpha \eta^\alpha) \frac{D^\alpha \theta^\alpha}{Dt}}_{\text{temperature rate power}} - \underbrace{\frac{1}{\theta^\alpha} \frac{\partial \theta^\alpha}{\partial \boldsymbol{x}} \cdot \boldsymbol{q}^\alpha}_{\text{heat flux power}} \geq 0 \tag{34}$$

We assume the solid constituent is nearly incompressible (ρ^{sR} is constant) and the fluid phase is compressible, such that the Helmholtz free energy per unit mass for the solid skeleton (s) in $\mathscr{B}_0^s$ and fluid phase (f) in $\mathscr{B}$ are written as,

$$\rho_0^s \psi^s (\boldsymbol{C}_s, \theta^s) \; ; \; \rho^f \psi^f (\rho^{fR}, \theta^f) \tag{35}$$

where $\boldsymbol{C}_s = \boldsymbol{F}_s^T \cdot \boldsymbol{F}_s$ is the right Cauchy-Green tensor for the solid skeleton deformation. We assume the fluid partial stress $\boldsymbol{\sigma}^f$ consists only of a pressure term (inviscid, such as water), such that $\boldsymbol{\sigma}^f = -p^f \boldsymbol{1}$, where the partial fluid pressure p^f is related to the Cauchy fluid pressure p_f through $p^f = n^f p_f$. Recall the total Cauchy stress written in terms of the partial stresses and solid skeleton effective stress as,

$$\boldsymbol{\sigma} = \boldsymbol{\sigma}^s + \boldsymbol{\sigma}^f = \boldsymbol{\sigma}' - p_f B \boldsymbol{1} \tag{36}$$

We write the Clausius-Duhem inequality for each phase ($\alpha =$ s,f) in Eq.(34), add them together, account for the functional forms of the Helmholtz free energy functions in their respective configurations in Eq.(35) ($\mathscr{B}_0^s$ and $\mathscr{B}$, respectively), and then derive the Clausius-Duhem inequality for the solid-fluid mixture as (all terms

pushed forward to the current configuration $\mathscr{B}$, and localizing the integral),

$$
\left[\frac{1}{2J_s} \boldsymbol{S}_s' - \frac{1}{J_s} \frac{\partial(\rho_0^s \psi^s)}{\partial \boldsymbol{C}_s} \right] : \frac{D^s \boldsymbol{C}_s}{Dt} + \left[p_f B \frac{n^f}{\rho^{fR}} - \frac{\partial(\rho^f \psi^f)}{\partial \rho^{fR}} \right] \frac{D^f \rho^{fR}}{Dt}
$$

$$
+ \left[-\frac{\partial p_f}{\partial \boldsymbol{x}} - \rho^{fR}(\boldsymbol{a}_f - \boldsymbol{b}^f) \right] \cdot (n^f \tilde{\boldsymbol{v}}_f)
$$

$$
- \left[\frac{1}{J_s} \frac{\partial(\rho_0^s \psi^s)}{\partial \theta^s} + \frac{1}{J_s}(\rho_0^s \eta^s) \right] \frac{D^s \theta^s}{Dt} - \left[\frac{\partial(\rho^f \psi^f)}{\partial \theta^f} + (\rho^f \eta^f) \right] \frac{D^f \theta^f}{Dt}
$$

$$
- \frac{1}{\theta^s} \frac{\partial \theta^s}{\partial \boldsymbol{x}} \cdot \boldsymbol{q}^s - \frac{1}{\theta^f} \frac{\partial \theta^f}{\partial \boldsymbol{x}} \cdot \boldsymbol{q}^f \geq 0 \tag{37}
$$

Applying the Coleman and Noll (1963) argument for independent rate processes $\frac{D^s \boldsymbol{C}_s}{Dt}$, $\frac{D^f \rho^{fR}}{Dt}$, $\frac{D^s \theta^s}{Dt}$, and $\frac{D^f \theta^f}{Dt}$, then for Eq.(37) to be satisfied (and hence, the 2nd law), the following constitutive equations must hold:

$$
\boldsymbol{S}_s' = 2\frac{\partial(\rho_0^s \psi^s)}{\partial \boldsymbol{C}_s} \;,\; p_f = \frac{\rho^{fR}}{Bn^f} \frac{\partial(\rho^f \psi^f)}{\partial \rho^{fR}} \tag{38}
$$

$$
\rho_0^s \eta^s = -\frac{\partial(\rho_0^s \psi^s)}{\partial \theta^s} \;,\; \rho^f \eta^f = -\frac{\partial(\rho^f \psi^f)}{\partial \theta^f} \tag{39}
$$

The remaining terms in Eq.(37) comprise the reduced dissipation inequality as,

$$
- \left[\frac{\partial p_f}{\partial \boldsymbol{x}} + \rho^{fR}(\boldsymbol{a}_f - \boldsymbol{b}^f) \right] \cdot (n^f \tilde{\boldsymbol{v}}_f)
$$

$$
- \frac{1}{\theta^s} \frac{\partial \theta^s}{\partial \boldsymbol{x}} \cdot \boldsymbol{q}^s - \frac{1}{\theta^f} \frac{\partial \theta^f}{\partial \boldsymbol{x}} \cdot \boldsymbol{q}^f \geq 0 \tag{40}
$$

Furthermore, we assume thermodynamic conjugacy through proportionality parameters (permeability $\hat{k}$, and thermal conductivities k^{θ^s} and k^{θ^f}), such that the following constitutive forms hold for generalized Darcy's law, and Fourier's law (assuming local thermal equilibrium such that mixture temperature $\theta = \theta^s = \theta^f$):

generalized Darcy's law:

$$
n^f \tilde{\boldsymbol{v}}_f \overset{\text{def}}{=} -\hat{k}(n^f) \left[\frac{\partial p_f}{\partial \boldsymbol{x}} + \rho^{fR}(\boldsymbol{a}_f - \boldsymbol{b}^f) \right] \tag{41}
$$

$$
\hat{k}(n^f) = \frac{\varkappa \, \delta(n^f)}{\eta_f \, \delta(n_0^f)} \;,\; \delta(n^f) = \frac{(n^f)^3}{1 - (n^f)^2}
$$

where $\varkappa$ is the intrinsic permeability, η_f is the fluid viscosity, and $\delta(n^f)$ is the Cozeny-Karman relation for porosity dependence of $\hat{k}$ (as a function of solid skeleton volume change J_s as $n^f = 1 - n^s$, $n^s = n_0^s/J_s$), with n_0^f the initial porosity (Coussy, 2004).

Fourier's law:

$$\boldsymbol{q} = \boldsymbol{q}^{\mathrm{s}} + \boldsymbol{q}^{\mathrm{f}} \stackrel{\mathrm{def}}{=} -k^{\theta^{\mathrm{mix}}}\frac{\partial \theta}{\partial \boldsymbol{x}} \ , \ k^{\theta^{\mathrm{mix}}} = n^{\mathrm{s}}k^{\theta^{\mathrm{s}}} + n^{\mathrm{f}}k^{\theta^{\mathrm{f}}} \tag{42}$$

We now consider specific equations for the Helmholtz free energy functions:
Fluid: we assume the following form for the Helmholtz free energy function for the fluid:

$$\rho^{\mathrm{f}}\psi^{\mathrm{f}}(\rho^{\mathrm{f}R}, \theta^{\mathrm{f}}) = \frac{1}{2}B(n^{\mathrm{f}}K_{\mathrm{f}})(\ln\rho^{\mathrm{f}R})^2 + g^{\mathrm{f}}(\theta^{\mathrm{f}}) \tag{43}$$

where $g^{\mathrm{f}}(\theta^{\mathrm{f}})$ is a temperature-dependent term, if needed. We assume homogeneous temperature, isothermal conditions for now. Using Eq.(38)$_2$, we can derive the constitutive equation for the real mass density of the fluid $\rho^{\mathrm{f}R}$ in terms of the Cauchy pore fluid pressure p_{f} as,

$$\rho^{\mathrm{f}R} = \rho_0^{\mathrm{f}R}\exp\left[\frac{p_{\mathrm{f}} - p_{\mathrm{f0}}}{K_{\mathrm{f}}}\right] \tag{44}$$

Solid skeleton: we assume the following form for the Helmholtz free energy function for the solid skeleton (neo-Hookean compressible isotropic elasticity (Ogden, 1984)):

$$\rho_0^{\mathrm{s}}\psi^{\mathrm{s}}(\boldsymbol{C}_{\mathrm{s}}, \theta^{\mathrm{s}}) = U(J_{\mathrm{s}}) + \frac{1}{2}\mu(tr\boldsymbol{C}_{\mathrm{s}} - 3) + g_0^{\mathrm{s}}(\theta^{\mathrm{s}}) \ , \ U(J_{\mathrm{s}}) = \frac{1}{2}\lambda\left(\ln J_{\mathrm{s}}\right)^2 - \mu\left(\ln J_{\mathrm{s}}\right) \tag{45}$$

where $g_0^{\mathrm{s}}(\theta^{\mathrm{s}})$ is a temperature-dependent term. Using Eq.(38)$_1$, we then derive the constitutive equation for the effective Second Piola-Kirchhoff stress as,

$$\boldsymbol{S}_{\mathrm{s}}' = \left[\lambda\left(\ln J_{\mathrm{s}}\right) - \mu\right]\boldsymbol{C}_{\mathrm{s}}^{-1} + \mu\boldsymbol{1} \tag{46}$$

By assuming functional form $\rho_0^{\mathrm{s}}\psi^{\mathrm{s}}(\boldsymbol{C}_{\mathrm{s}}, \theta^{\mathrm{s}})$ for the solid skeleton, we can later generalize for anisotropy (fiber directions) of soft tissues (Holzapfel and Gasser, 2000).

3   Stabilized Finite Element Implementation

The nonlinear finite element formulation and implementation (Newton-Raphson nonlinear solution, Newmark time integration) is discussed in Li, Borja, and Regueiro (2004); Ebrahimi (2007); Regueiro and Ebrahimi (2010), and thus details are not presented. We will focus on the stabilized term to be added to the variational equation for the balance of mass of the solid-fluid biphasic mixture as discussed in the references.

3.1 Stabilized term

For stabilizing the tri-linear hexahedral Q8P8 element near the undrained condition (upon transient loading, with low permeability, and assuming nearly incompressible fluid phase $K_{\text{f}} \to \infty$), we follow the approach of Truty and Zimmermann (2006), which is based on the method of Brezzi and Pitkaranta (1984). We attempted to apply the stabilization procedure of White and Borja (2008) for projecting pore fluid pressure p_{f} by integral-averaging over an element e, along with its weighting function value η, but based on our implementation, it was ineffective for our particular applications of soft tissues at finite strain. Sun, Ostien, and Salinger (2013) apparently were successful in extending the approach of White and Borja (2008) to finite strain, and they combined it with an assumed enhanced strain approach for the solid skeleton deformation gradient (for near incompressibility of the solid skeleton), which is an additional step we did not take in the paper. For our purposes, the Brezzi and Pitkaranta (1984) approach appears effective, and we will use it in the numerical examples.

After applying the method of weighted residuals to Eq.(14) (Hughes, 1987), substituting Darcy's law from Eq.(41), dropping the $(\bullet)_{\text{s}}$ or $(\bullet)^{\text{s}}$ designation, we obtain the variational equation of the mixture balance of mass in the reference configuration (of the solid skeleton) $\mathscr{B}_0$ as,

$$\mathscr{H} = \mathscr{H}_1^{INT} + \mathscr{H}_2^{INT} + \mathscr{H}_3^{INT} + \mathscr{H}_4^{INT} + \mathscr{H}^{\text{stab}} - \mathscr{H}_1^{EXT} = 0 \qquad (47)$$

$$\mathscr{H}_1^{INT} = \int_{\mathscr{B}_0} \eta \left(\frac{Jn^{\text{f}}}{K_{\text{f}}} \dot{p}_{\text{f}} + \dot{J} \right) dV$$

$$\mathscr{H}_2^{INT} = \int_{\mathscr{B}_0} \eta \frac{J}{K_{\text{f}}} \frac{\partial p_{\text{f}}}{\partial X_I} F_{Ii}^{-1} (n^{\text{f}} \tilde{v}_{i(\text{f})}) dV$$

$$\mathscr{H}_3^{INT} = \int_{\mathscr{B}_0} \hat{k} \frac{\partial \eta}{\partial X_I} F_{Ii}^{-1} \frac{\partial p_{\text{f}}}{\partial X_K} F_{Ki}^{-1} J dV$$

$$\mathscr{H}_4^{INT} = \int_{\mathscr{B}_0} \frac{\partial \eta}{\partial X_I} F_{Ii}^{-1} \hat{k} \rho^{\text{f}R} (a_i - g_i) J dV$$

$$\mathscr{H}^{\text{stab}} = \int_{\mathscr{B}_0} \alpha \frac{\partial \eta}{\partial X_I} F_{Ii}^{-1} \frac{\partial \dot{p}_{\text{f}}}{\partial X_K} F_{Ki}^{-1} J dV$$

$$\mathscr{H}_1^{EXT} = \int_{\Gamma_0^q} \eta Q_{\text{f}} dA$$

where α is the stabilization parameter, and Q_{f} is the normal component of the pore fluid flux (positive inward) across the boundary Γ_0^q. In Truty and Zimmermann (2006), an analysis was conducted to determine estimates of α for 3D problems, based on permeability, solid skeleton stiffness, pore fluid unit weight, time step, and

finite element size, but since various assumptions were made on other factors, we ended up estimating α by a trial-and-error approach. Further investigation may be needed to more efficiently estimate α in the context of dynamic loading of biphasic soft tissues at finite strain. We note that although we have implemented the $\mathscr{H}_2^{INT}$ term, it makes little difference in the results, and then may be left out of future simulations.

3.2 Element

For the mixed formulation, we use a Q27P8 hexahedral element as shown in Fig.4 (Regueiro and Ebrahimi, 2010). The stabilized Q8P8 hexahedral element just uses the vertex nodes 1-8.
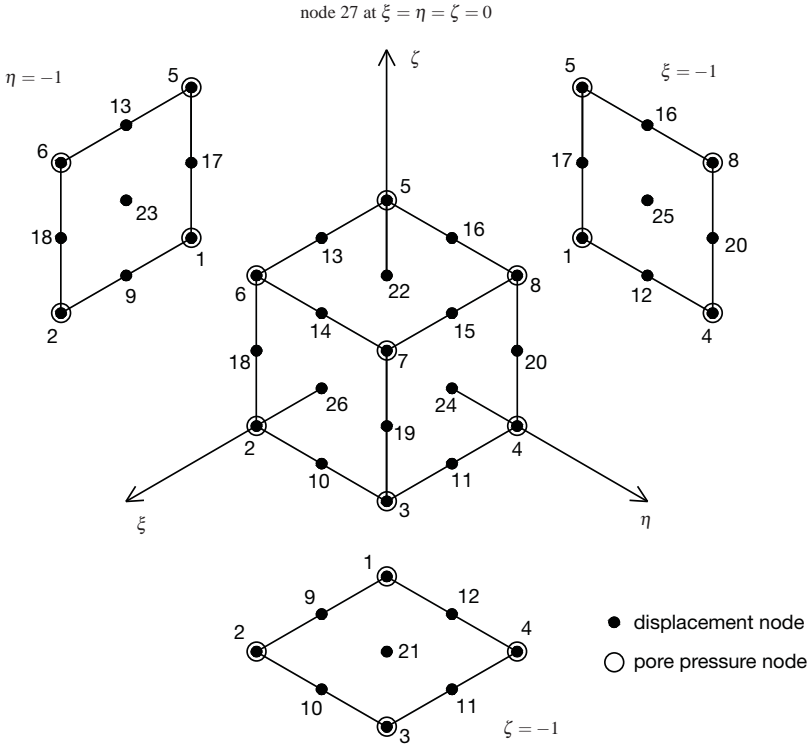
Figure 4: Q27P8: 27 nodes for tri-quadratic interpolation of solid skeleton displacement $\boldsymbol{u}^{h^e}$, and 8 nodes for tri-linear interpolation of pore fluid pressure $p_{\mathrm{f}}^{h^e}$. Q8P8: 8 nodes for tri-linear interpolation of solid skeleton displacement $\boldsymbol{u}^{h^e}$, and 8 nodes for tri-linear interpolation of pore fluid pressure $p_{\mathrm{f}}^{h^e}$.

4 Numerical examples

Three numerical examples are presented to demonstrate the Q27P8 and Q8P8 elements (no stabilization, and stabilized). The stable Q27P8 formulation is implemented in the `FSSolidFluidMixT` class in Tahoe, and the stabilized Q8P8 element is implemented in the `FSSolidFluidMixQ8P8T` class in Tahoe (stabilization is turned off by setting $\alpha = 0$).

4.1 Uniaxial strain compression using 3D FE

We start with a uniaxial strain in compression example, with undrained boundaries at all sides except the top boundary (see Fig.5). The meshes are composed of ten Q27P8 and ten Q8P8 elements. The parameters used are shown in Table 1.

Table 1: Parameters for lung parenchyma examples.

source	parameter	units	value
Lande and Mitzner (2006) (air through parenchyma)	$\hat{k}_a$	m^3.s/kg	1×10^{-5}
Lande and Mitzner (2006)	n_0^{f}	.	0.99
Lande and Mitzner (2006) (alveolar)	ρ^{sR}	kg/m^3	1000
Lande and Mitzner (2006)	ν	.	0.3
Levental, Georges, and Janmey (2006) (guinea pig)	E	Pa	5000
this paper	t^{σ}	Pa	80, 1000, 10,000

To calculate the hydraulic conductivity $\hat{k}_w$ for water, we consider the intrinsic permeability calculated from the hydraulic conductivity for air (Lande and Mitzner, 2006) $\varkappa = \hat{k}_a \eta_a = (1 \times 10^{-5} \text{ m}^2/\text{Pa.s})(1.83 \times 10^{-5} \text{ Pa.s}) = 1.83 \times 10^{-10} \text{ m}^2$. Then, we use the viscosity of water to calculate $\hat{k}_w = \varkappa/\eta_w = 1.83 \times 10^{-10} \text{ m}^2/1 \times 10^{-3}$ Pa.s $= 1.83 \times 10^{-7} \text{ m}^2/\text{Pa.s}$. The bulk moduli of air and water are $K_a = 1 \times 10^5$ Pa and $K_w = 2.2 \times 10^9$ Pa, respectively, at $20°C$.

Referring to Fig.5, we will consider three types of loadings and solutions: (1) drained (quasi-static, pore fluid pressure $p_{\mathrm{f}} = 0$, $t^{\sigma} = 1,000$Pa), (2) consolidating (coupled pore fluid flow and solid skeleton deformation, $t^{\sigma} = 1,000$Pa), and (3) dynamic impulse loading (coupled pore fluid flow and solid skeleton deformation with inertia terms, $t^{\sigma} = 10,000$Pa). For each loading case, we keep the solid skeleton parameters the same for the lung tissue, and then assume the saturating fluid is either (a) air, or (b) water, with parameters given in Table 1.

For pore air, the solid skeleton vertical displacement upon traction loading is shown in Fig.6(a). It can be seen that given the low viscosity of the pore air, the drained and consolidating solutions are nearly the same, meaning the pore air pressure dissipates as the column is loaded over 0.1s, as illustrated in Fig.6(b). Nodes 8 and 91
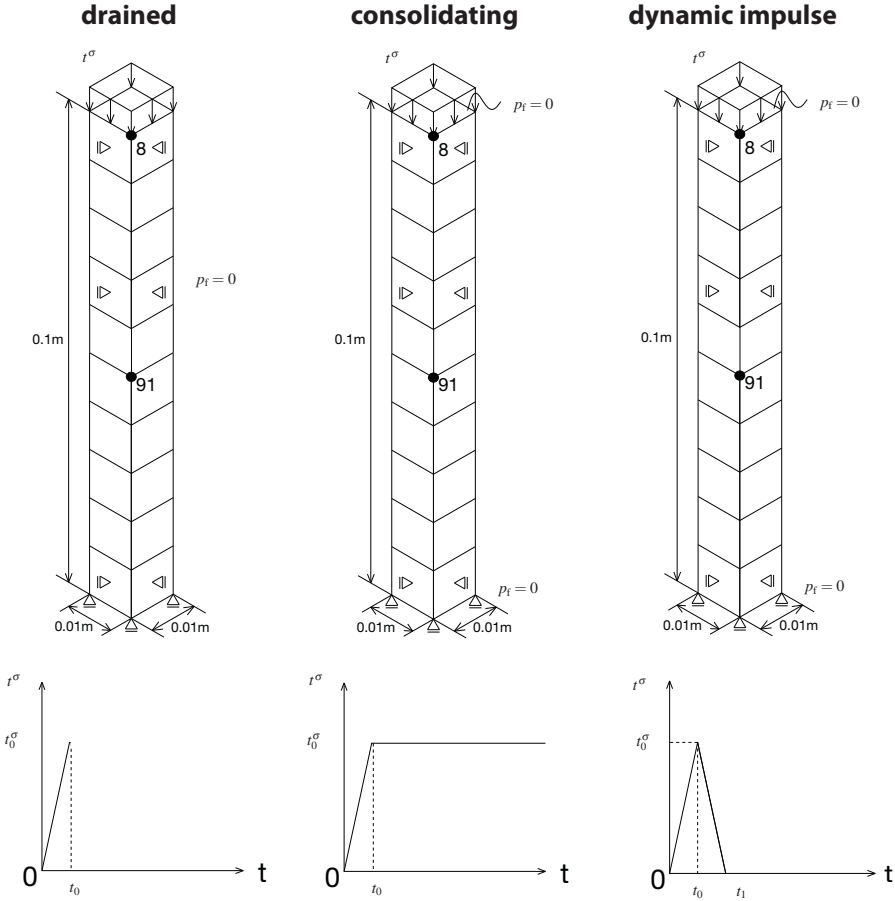
Figure 5: Ten hexahedral element column mesh for the three analysis cases: (a) drained, (b) consolidating, (c) dynamic impulse.

are the locations where the solutions are plotted in Fig.5. In Fig.6(b), in addition to the pore fluid pressure p_f being plotted with time, the mean effective Cauchy stress p', and effective vertical stress σ'_{zz} are plotted. Recall that σ'_{zz} and p' are positive in tension, and p_f is positive in compression. Gravity is ignored, and the problem is uniaxial strain, so σ'_{xx} and σ'_{yy} are not zero, and thus $p' \neq \sigma'_{zz}$.

Next, we conduct the same simulations, but switch out the pore fluid from air to water properties (viscosity, compressibility). The solid skeleton vertical displacement

(a) (b)
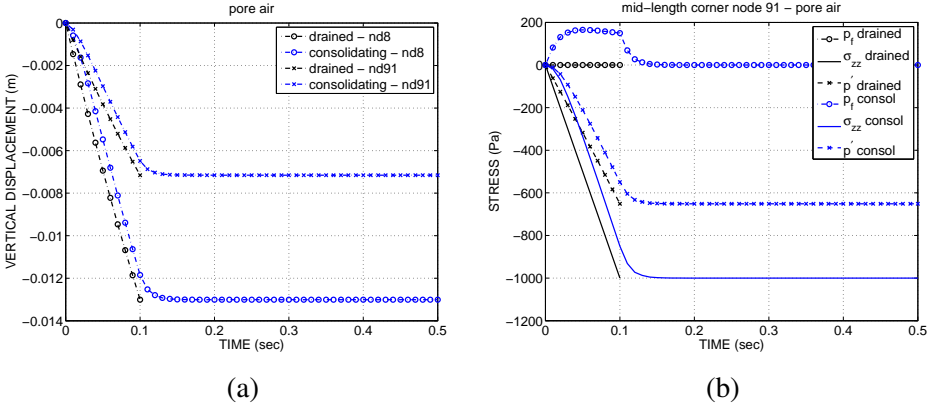
Figure 6: (a) Vertical displacement, and (b) Stress for drained and consolidating solutions with pore air flow.

(a) (b)
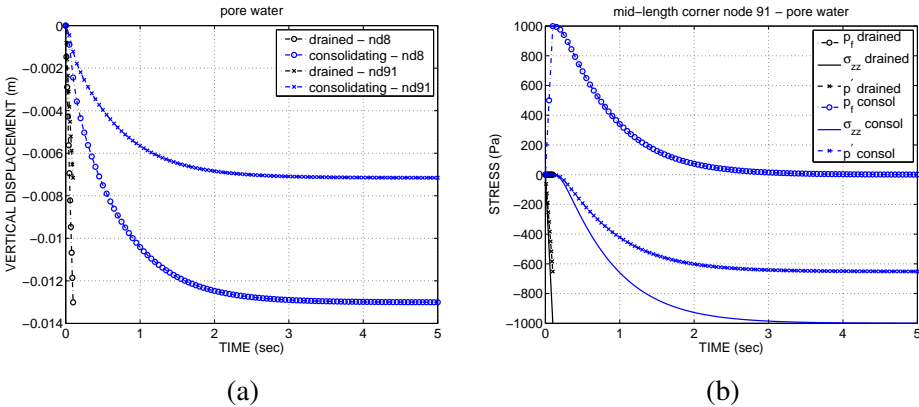
Figure 7: (a) Vertical displacement, and (b) Stress for drained and consolidating solutions with pore water flow.

upon traction loading is shown in Fig.7(a). It can be seen that given the higher viscosity of the pore water, the drained and consolidating solutions are now different, as it takes longer for the pore water pressure to dissipate with time, as illustrated in Fig.7(b).

Now, to investigate the significance of inertia effects, a traction load of $t^\sigma = 10,000$ Pa is applied over 0.1s and then released over the next 0.1s for the pore air case (Fig.5), and loaded over 0.01s and unloaded over 0.01s for the pore water case. The effect of pore fluid (air and water) is investigated. We also study the effect of globally undrained BC as compared to the ends of the column being drained. In Fig.8(a),

we plot the vertical displacement versus time for nodes 8 and 91 for drained and undrained BCs for the coupled dynamic simulations with pore air. Recall that the bulk modulus of air at ambient temperature is relatively low ($K_a = 1 \times 10^5$Pa), thus in Fig.8(a) there is compressive vertical displacement even for the undrained BC case (as opposed to when there is pore water, which is nearly incompressible, and thus the displacement will be zero for the undrained BC case in Fig.9(a)). Also, in Fig.8(a), note that for the case with drained BC, there is compressibility of pore air and also relative flow of pore air, reaching a displacement near 0.06m, which for an initial column length of 0.1m, is nominally $= 0.06/0.1 = 60\%$ axial strain, which is clearly a large strain (see Fig.8(c) for actual deformed mesh and p_f contour). In Fig.8(b), we see that for the undrained BC case, the pore fluid pressure p_f spikes up to nearly 10,000Pa as expected (the applied traction load), while because of the compressibility of air and relative fluid flow even during globally undrained BCs, there is a small buildup of effective stress.
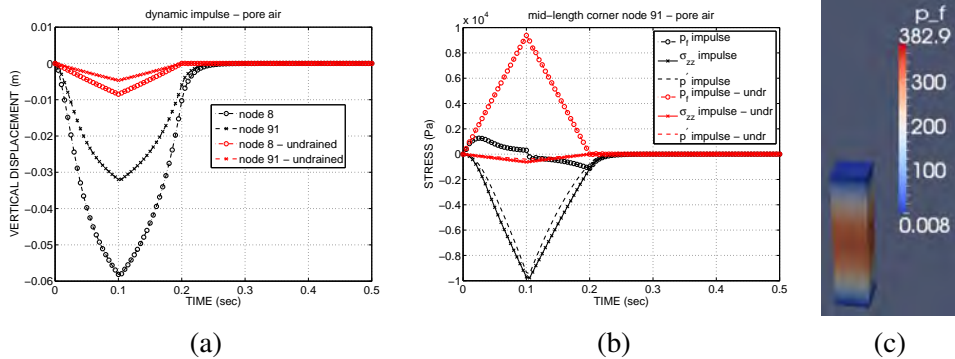
Figure 8: (a) Vertical displacement, and (b) Stress for impulse loading solution with pore air flow. (c) Actual deformed mesh for impulse loading with pore air flow, with drained BCs. Displacement magnification 1×. Note the large deformation. Note the original aspect ratio in Fig.5 for comparison.

Next, we run the simulation for pore water with 10,000Pa traction over 0.01s, with displacement results for drained and undrained BCs shown in Fig.9(a). We note now what we expect for undrained BC, that the displacement of the solid skeleton is zero because the pore water is nearly incompressible and the boundaries are impermeable. For the drained BC, we observe oscillation of the solid skeleton vertical displacement at nodes 8 and 91, which eventually damps out due to the relative fluid flow effect. Likewise, in Fig.9(b), we observe similar expected behavior, where for the undrained BC, the traction is completely taken up by the pore fluid pressure p_f ($t^\sigma = 10,000$Pa), while the effective stress is zero. For the drained BC, pore
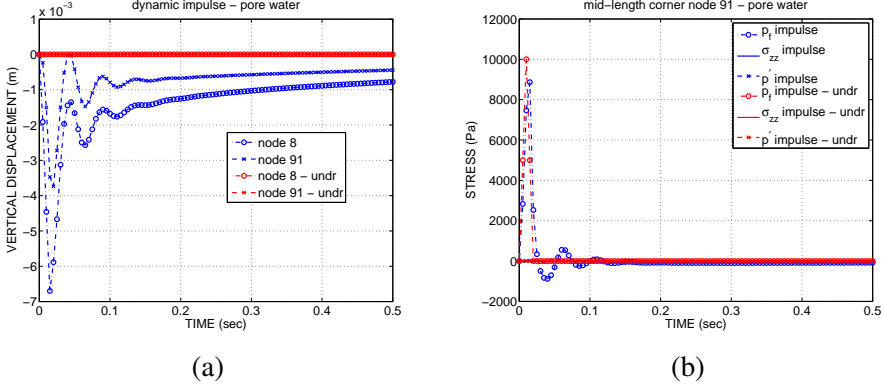
Figure 9: (a) Vertical displacement, and (b) Stress for impulse loading solution with pore water flow.

fluid pressure p_f builds up and oscillates, until it damps out to near zero at about 0.2sec.

Lastly, we compare the impulse solution as if the material were completely solid (no relative fluid flow; locally drained), with results shown in Fig.10. Since the real mass densities of solid and fluid (water) are the same for the lung alveolar tissue ($\rho^{sR} = \rho^{fR} = 1000$kg/m^3), the initial total mass density is also $\rho_0 = 1000$kg/m^3. We can compare the axial wave speed estimated from the curve in Fig.10(a) to the small strain theoretical solution as follows:

$$(\text{curve}) \; v_{\text{axial}} \quad \approx \quad \frac{2(0.1m)}{0.085sec} = 2.4m/sec \tag{48}$$

$$(\text{theory}) \; v_{\text{axial}} \quad = \quad \sqrt{\frac{\lambda + 2\mu}{\rho}} = \sqrt{\frac{(2885Pa) + 2(1923Pa)}{1000kg/m^3}} = 2.6m/sec \tag{49}$$

Figure 10(b) demonstrates the stress solution versus time, showing that for the solid dynamic solution (no pore fluid coupling), we get the expected oscillatory response, with little algorithmic damping for the Newmark time integration method used, with integration parameters $\beta = 0.3025$, $\gamma = 0.6$, unconditionally stable, with high frequency dissipation (pg534 of Hughes (1987)). Note that there is a clear difference between solid deformation analysis (locally drained material points, black curves) and coupled pore fluid flow with solid skeleton deformation analysis, for both undrained BC (red curves) and drained BC (blue curves). The drained BC (blue curve) would be closest to the actual experimental condition in the lab, whereas the undrained BC (red curves) could be replicated if the lung parenchyma tissue were completely sealed along its boundaries with an impermeable membrane.

Clearly, the solid analysis (black curves) is not a reasonable assumption for the transient behavior of a soft biological tissue treated as a biphasic (solid-fluid) mixture at finite strain.
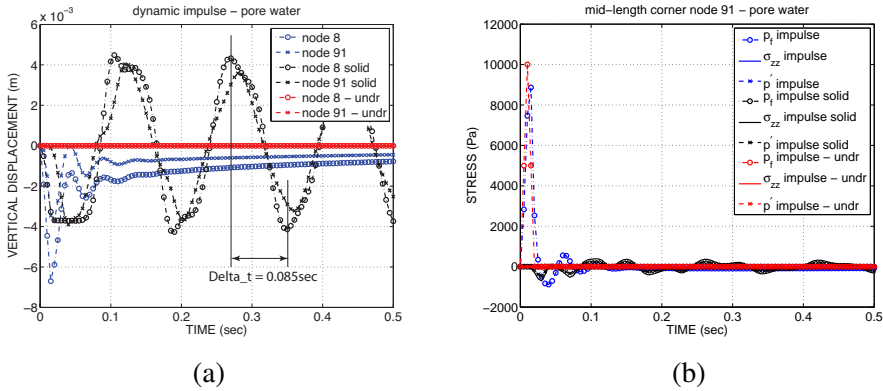
Figure 10: (a) Vertical displacement, and (b) Stress for impulse loading solution with pore water flow, compared to solid (locally drained) case.

4.2 *Uniaxial strain compression, with stabilization*

We now re-run the simulations for pore water consolidation and impulse loading, but decrease the permeability to $\hat{k} = 1 \times 10^{-10}$ m²/Pa.s to test the stabilization term in Eq.(47) for $\alpha = 1 \times 10^{-6} m^3 s^2 / kg$. Results are presented in Fig.11 for pore fluid pressure contours, and Fig.12 for pore fluid pressure and vertical displacement versus time. We see in the contour plots the stable solution for Q27P8 element, with near uniform pore fluid pressure of 1000Pa in the middle of the mesh in Fig.11(a), and the unstable solution with the Q8P8 element, showing oscillatory pore fluid pressure along the depth of the mesh in Fig.11(b). In Fig.11(c), the solution is stabilized. The instability is evident in Fig.12 too, showing apparent consolidation, when the near undrained condition caused by low permeability should show slow decrease in pore fluid pressure p_f and displacement d_z, as is the case for the Q27P8 element and the stabilized Q8P8 element.

4.3 *Pressure impulse loading of slab of lung parenchyma*

The second numerical example considers a Neo-Hookean isotropic poroelastic slab loaded with a pressure pulse to observe transient response of effective stress and pore fluid pressure (Fig.13). The slab is initially assumed to be saturated with water. The top face of the slab is assumed drained, and the other faces are impermeable.
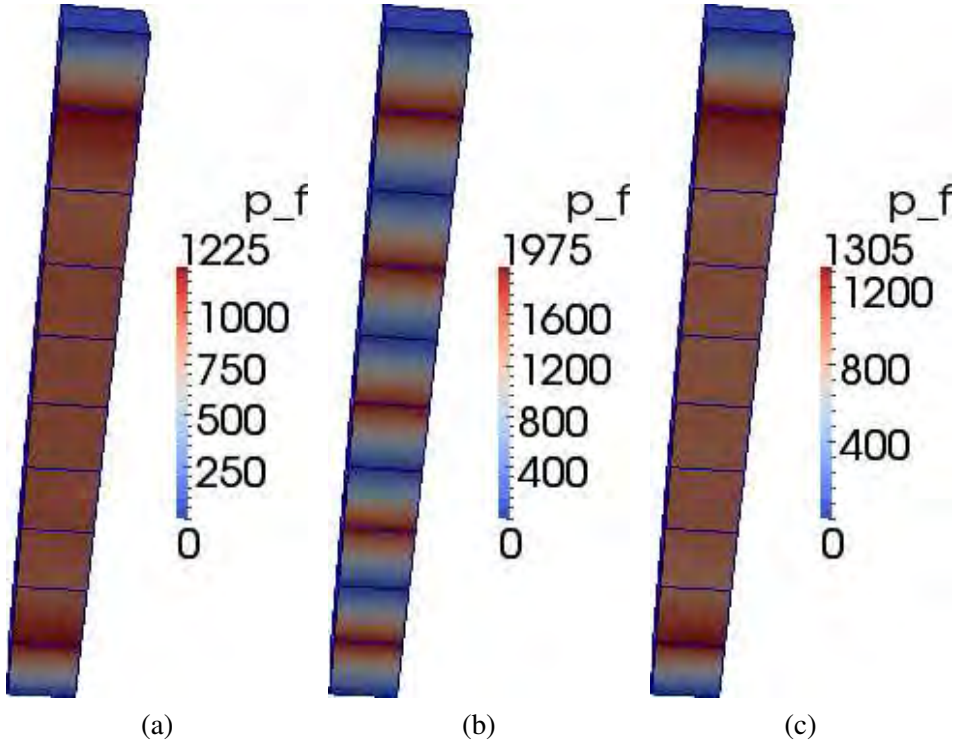
Figure 11: Contours of pore fluid pressure p_f for the 3 cases, at second time step $t =$ 0.1sec: (a) Q27P8 element showing stable, smooth p_f contour; (b) Q8P8 element solution showing unstable, oscillatory p_f contour, for non-stabilized solution; (c) Q8P8 element solution with stabilization term.

The dynamic loading of the slab as biphasic soft tissue is shown in Fig.13. The load-time schedule functions for drained, consolidating (same as load and hold for dynamic simulation), and dynamic load and release (impulse) are also illustrated in Fig.13. For constitutive parameters, we use the same as in Table 1. For the Q27P8 element, 50 and 200 element meshes are considered. For the Q8P8 element, a 1350 element mesh is considered.

First, consider the drained and consolidating deformed meshes in Fig.14. This gives a general deformation pattern for the deformed meshes. Note nearly the same deformation is obtained with the 3 meshes. Next, consider the deformed meshes for dynamic simulation for hold and impulse loadings in Fig.15 for pore water, for the 50 Q27P8 element mesh. The hold loading generates more deformation and also higher peak pore fluid pressure than the impulse loading, as shown in Fig.16.

(a)   (b)
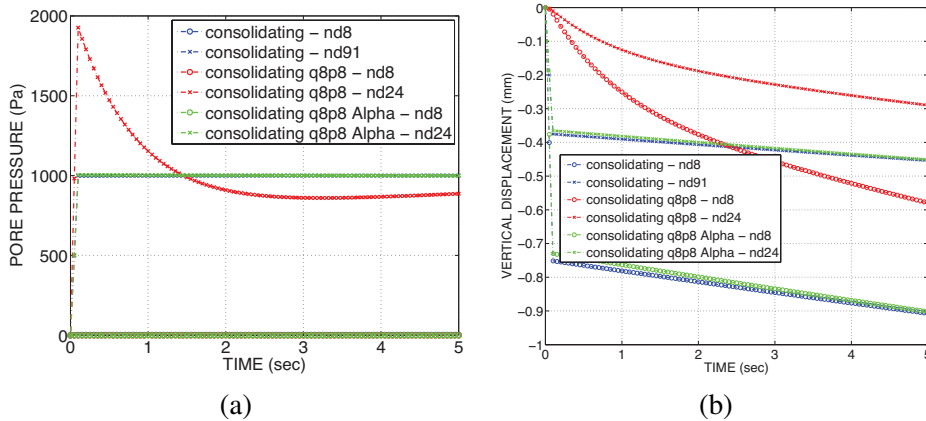
Figure 12: (a) Pore water pressure p_f versus time at middle section of the mesh, comparing result of Q27P8 mesh (stable, blue lines) and Q8P8 meshes (non-stabilized (red) and stabilized (green)). (b) Displacement in z direction d_z versus time at top and middle sections of the mesh, comparing result of Q27P8 mesh (stable) and Q8P8 meshes (non-stabilized and stabilized).

In Fig.16, we compare the pore fluid pressure p_f at the corner node for the various analysis types. We see that for the dynamic hold loading, p_f is much larger than for dynamic impulse loading. For all drained solutions, $p_f = 0$, and for the consolidating solution, there is a small negative p_f before immediate consolidation (the solid skeleton at the bottom impermeable face is in tension). The 200 Q27P8 element mesh gives almost the exact same result as in Fig.16(a) (and is thus not shown), and the non-stabilized 1350 Q8P8 element mesh gives nearly the same result as in Fig.16(a), with result shown in Fig.16(b). Thus, for some soft biological tissues with higher permeability (such as the lung parenchyma, not the case for the low permeability vertebral disc), stable results can be achieved with the non-stabilized Q8P8 element implementation. In Fig.17, we compare displacement d_y at the corner node for the various analyses, plotting over 0.1sec and 1sec. We see that the excited displacement frequencies are different for the dynamic hold and impulse simulations, the hold one having a higher frequency partly due to stiffening by enabling geometric nonlinearity. We see in Fig.17(c), the 1350 Q8P8 element mesh result is nearly the same as the 50 Q27P8 element mesh result in Fig.17(a). Given the small pore pressure p_f generated during impulse loading (red curves in Fig.16), there is no noticeable difference between "dynamic impulse" and "dynamic impulse drained" displacement time histories in Fig.17, whereas for "dynamic hold" and "dynamic hold drained," there is a small difference in displacement amplitude.
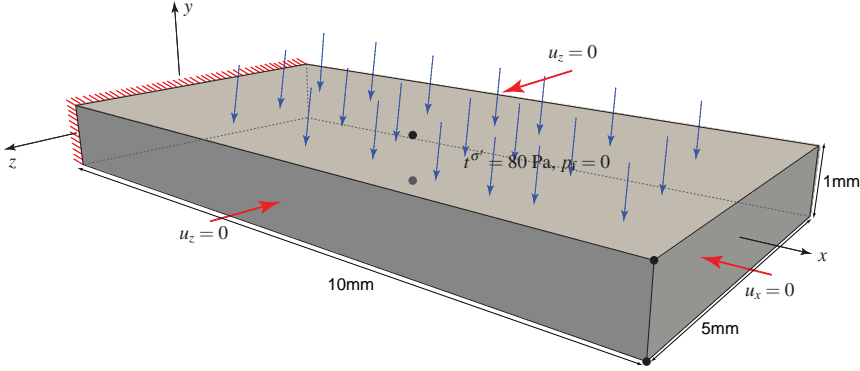
$10 \times 5 \times 1$mm slab, $1 \times 1 \times 1$mm cube 50 element mesh

drained   consolidating   dynamic impulse

$t_0 = 1$ms, $t_1 = 2$ms
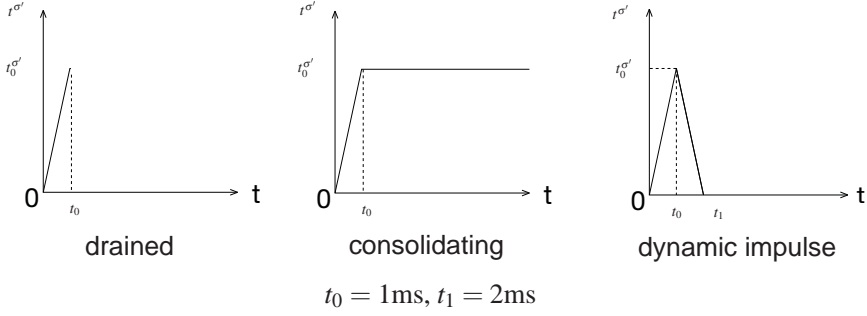
Figure 13: (top) Schematic of pressure loading of cantilevered poroelastic slab. (bottom) Various load schedule functions applied.

(a)   (b)   (c)
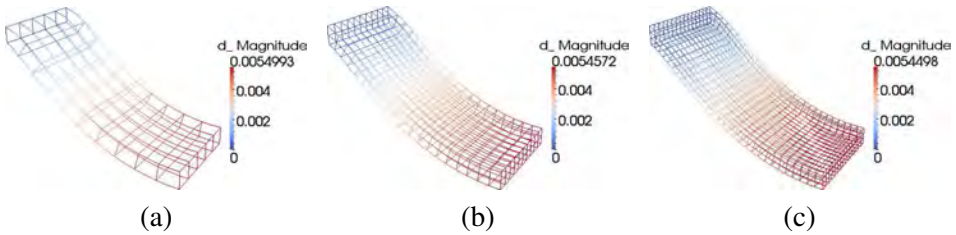
Figure 14: The deformed mesh for drained loading, and end of consolidation (no inertia terms) for pore water. Displacement units in meters, with displacement magnification 1×. (a) 50 Q27P8 elements, (b) 200 Q27P8 elements, (c) 1350 Q8P8 elements.

Figure 15: The deformed meshes for dynamic simulation with pore water for hold (a) and impulse (b) loadings (with inertia terms). p_f units in Pa.
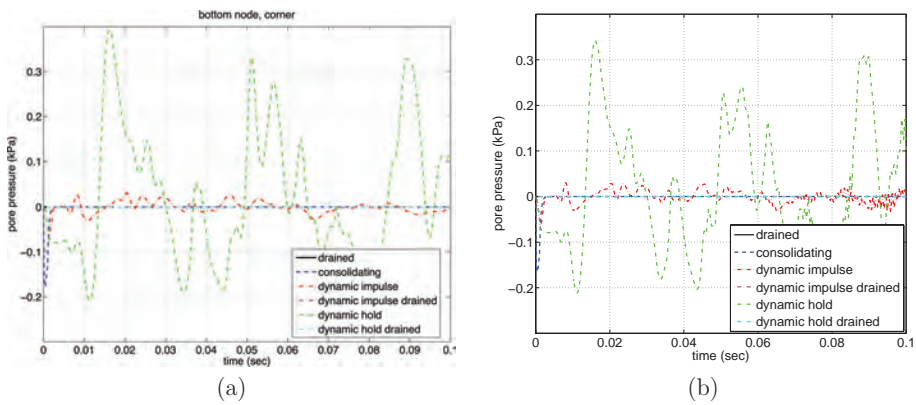
Figure 16: Plot of pore water pressure p_f versus time for the various analyses. (a) 50 Q27P8 element mesh results, (b) 1350 Q8P8 element mesh results without stabilization.
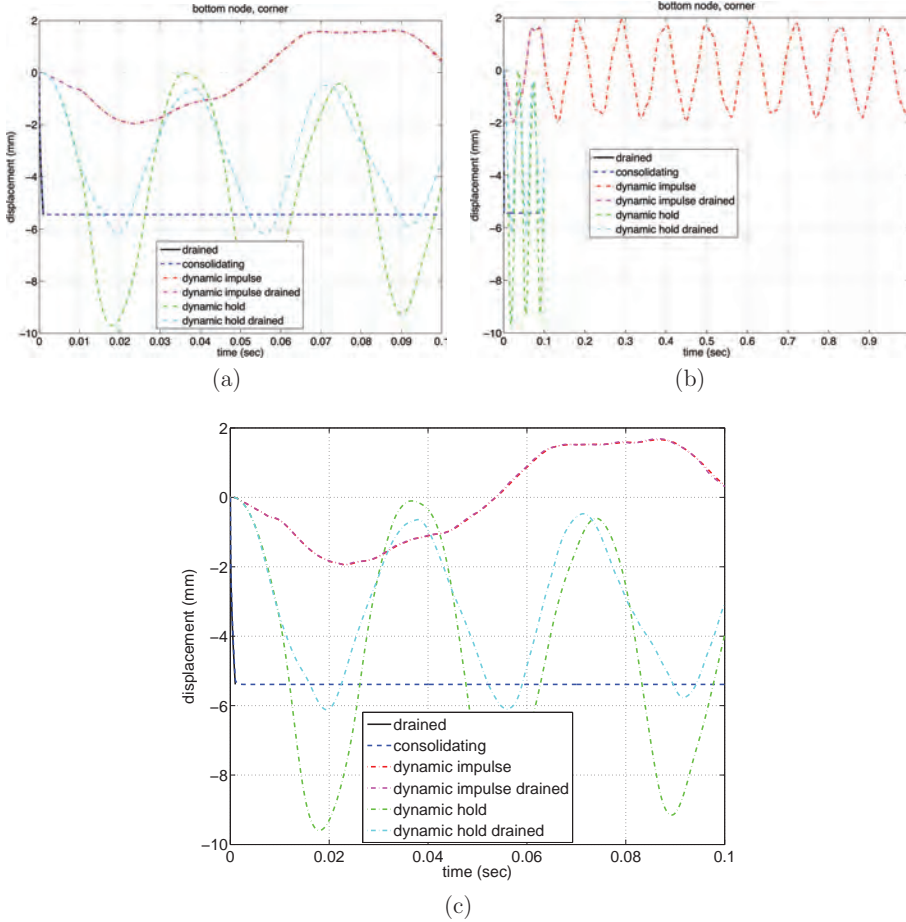
Figure 17: Plot of displacement d_y versus time for the various analyses ((a) up to 0.1sec, (b) up to 1sec for 50 Q27P8 element mesh) for pore water. (c) 1350 Q8P8 element mesh results without stabilization.

Next, we consider the deformed meshes for dynamic simulation for impulse and hold loadings in Fig.18 for pore air. In this case for pore air, the peak pore air pressures are not noticeably different between dynamic hold and impulse loadings, as also shown in Fig.19(a) for p_f versus time. In Fig.19(b), we compare displacement d_y at the corner node, plotting over 0.1sec for pore air. We see that the dynamic hold and impulse simulations have nearly the same frequency, while there is a small poromechanical effect noticeable for the dynamic impulse simulation (difference in curves after 0.05sec). For the Q8P8 element mesh, the results are similar as shown in Fig.20.
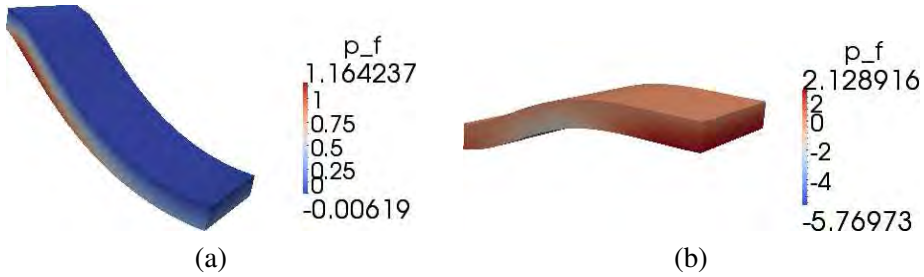
Figure 18: The deformed meshes for dynamic simulation with pore air for hold (a) and impulse (b) loadings (with inertia terms). p_f units in Pa.

(a)   (b)
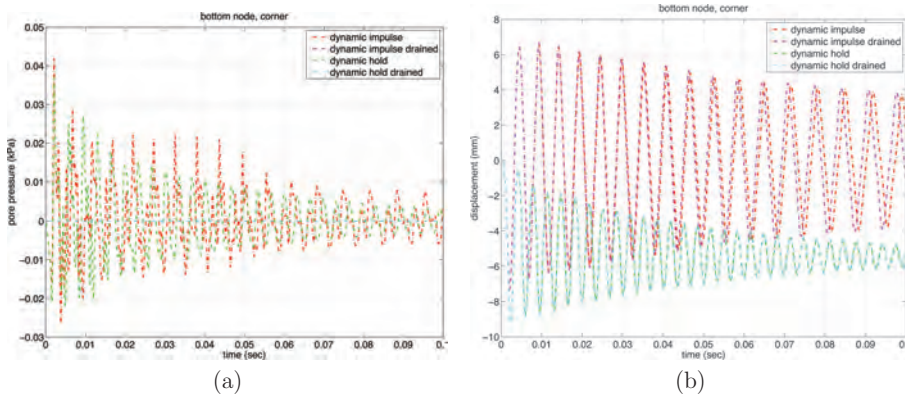
Figure 19: 50 Q27P8 element mesh results: (a) Plot of pore air pressure p_f versus time for the various analyses. (b) Plot of displacement d_y versus time for the various analyses.

(a)   (b)
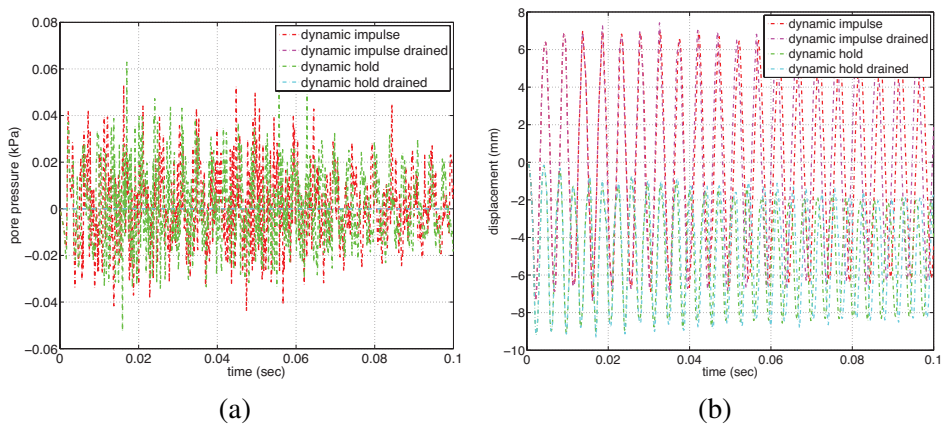
Figure 20: Non-stabilized 1350 Q8P8 element mesh results: (a) Plot of pore air pressure p_f versus time for the various analyses. (b) Plot of displacement d_y versus time for the various analyses.

In summary, for longer duration loadings (in this case, up to 0.1 sec), the pore water pressure can build up and thus affect the solid skeleton deformation, and in turn the effective stresses. When the pore water is substituted with pore air, differences in results are observed between the two pore fluids. For pore water (higher mixture mass density), different loadings (dynamic impulse, dynamic hold) trigger different modes of vibration at different frequencies. On the other hand, for pore air (lower mixture mass density), different loadings (dynamic impulse, dynamic hold) trigger the same mode of vibration (with slightly different frequencies due to geometric nonlinearities). For pore air, the overall mixture is less dense, thus the frequency of free or forced vibration is higher than when saturated with pore water; the permeability is $55\times$ higher than for pore water, thus there is little build up of pore air pressure during dynamic loading of the thin slab.

Also, it was noted that there is no distinguishable difference between a 50 element and 200 element mesh for Q27P8 implementation, and likewise for a 1350 element Q8P8 mesh without stabilization. Because of the higher permeability of the lung parenchyma, the stabilizing term $\mathscr{H}^{\text{stab}}$ is not needed. We will see in the next example for the vertebral disc that has a much smaller permeability, the stabilizing term is needed to obtain meaningful, stable results.

4.4 *Vertebral disc compression loading*

Vertebral disc compression using the Q27P8 element, and Q8P8 element with and without stabilization, is simulated with parameters in Table 2 (taken from Tables 1 and 2 of Williams, Natarajan, and Andersson (2007)) and coarsest mesh in Fig.21; two finer Q8P8 meshes are shown in Fig.22. The geometry of the lumbar spine disc was simplified for the simulations. The annulus fibrosus was modeled as an ellipse with a major axis of 0.02646 m and a minor axis of 0.02016m with a height of 0.00945 m (minus the nucleus volume). The nucleus pulposus was modeled as an ellipse with a major axis of 0.02016 m and a minor axis of 0.01386 m with a height of 0.00945 m. The permeabilities $\hat{k}$ are averaged from the values reported in different directions in Williams, Natarajan, and Andersson (2007), assuming anisotropy in that paper; we assume isotropic permeability in this paper, which can be generalized for anisotropy in the future. A downward traction load of 0.5 MPa (Ferguson, Ito, and Nolte, 2004) is applied, with similar time histories as shown in Fig.5 for drained, consolidating, and dynamic impulse. We do not verify that the material properties in Williams, Natarajan, and Andersson (2007) for annulus and nucleus of the disc, nor the compressive loading of 0.5MPa by Ferguson, Ito, and Nolte (2004) are physiologically correct or not. The purpose of the paper is to investigate the difference in results in assuming a drained versus consolidating versus dynamic (with inertia terms) coupled poromechanical analysis. All analyses

use stabilization parameter $\alpha = 1 \times 10^{-6}\, m^3 s^2/kg$.

Table 2: Parameters for vertebral disc compression (Williams, Natarajan, and Andersson, 2007).

tissue	parameter	units	value
nucleus	$\hat{k}$	m³.s/kg	1.8×10^{-15}
nucleus	n_0^f	.	0.83
nucleus	ρ^{sR}	kg/m³	1000
nucleus	λ	Pa	3.1×10^6
nucleus	μ	Pa	0.345×10^6
annulus	$\hat{k}$	m³.s/kg	1.7×10^{-15}
annulus	n_0^f	.	0.78
annulus	ρ^{sR}	kg/m³	1060
annulus	λ	Pa	3.6×10^6
annulus	μ	Pa	0.893×10^6
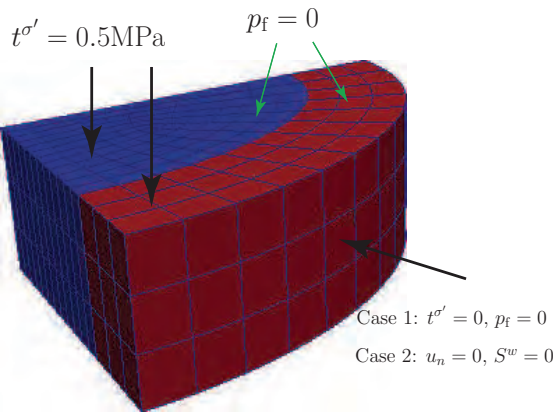
Figure 21: Coarsest mesh (432 elements) used in analyzing vertebral disc compression, showing applied effective traction $t^{\sigma'}$ and drained $p_f = 0$ boundary at top, and Cases 1 and 2 BCs on the curved surface of the annulus. The nucleus (blue) and annulus (red) sections are modeled as distinct materials. The symmetry planes are impermeable with fixed normal displacements.

4.4.1 *Vertebral disc compression loading with lateral expansion and drainage - Case 1*

For the Case 1 BCs ($t^{\sigma'} = 0$, $p_f = 0$ on curved annulus surface) shown in Fig.21, we present the time histories of displacement d_z (vertical, in direction of traction loading) and d_x (lateral, along long axis), and pore fluid pressure p_f, in Fig.25 for the three nodes shown in Fig.23. The time histories in Fig.25 provide a comparison between drained, consolidating, and dynamic impulse results, as well as various meshes (Q27P8 and Q8P8 element types). Unless otherwise indicated, it is assumed the result is that of the coarsest mesh (432 elements) with Q27P8 element type. In Fig.24, we see contour plots of p_f with deformed meshes for the consolidating analysis. Note from Fig.25, that upon end of traction loading at 0.1s, the displacements d_z and d_x and pore fluid pressure p_f remain nearly constant, where in fact there is a slow consolidation process ongoing (note the small permeability values in Table 2 for nucleus and annulus). Another observation is that the Q27P8 mesh provides a higher p_f, yet with nearly the same displacement as the stabilized Q8P8 meshes (see Fig.25). It is likely that in the stabilized Q8P8 mesh results, there is added diffusion of pore fluid leading to lower p_f values as observed in Fig.24. Mesh refinement on the Q27P8 mesh is required for further study, but given the expense of this element type, and the lack of parallel execution for the Q27P8 currently, we do not present finer mesh results for the Q27P8 element. The Q8P8 element can be executed in parallel computation. For the dynamic impulse analysis, given the three-dimensional nature of loading and pore fluid flow, the disc essentially damps out the impulse wave completely, with small oscillation after release of the impulse at 0.02s, as shown in Fig.25(a),(b) displacements. The drained
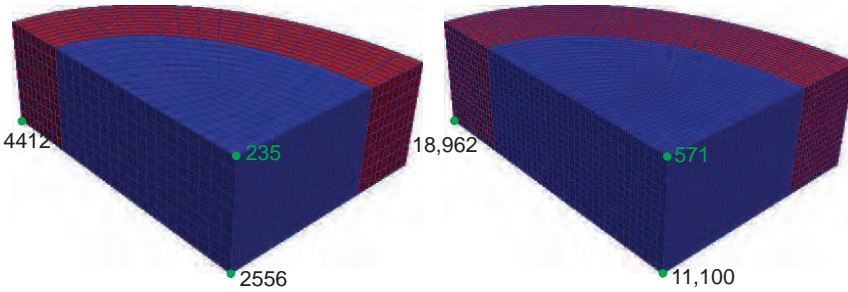
Figure 22: Two finer Q8P8 meshes used in the disc compression analysis, showing nodes where analysis results are compared. Left mesh has 3,465 elements, and the right mesh has 16,875 elements.

results (no consolidation, and no inertia terms) are provided as a benchmark for deformation comparison.
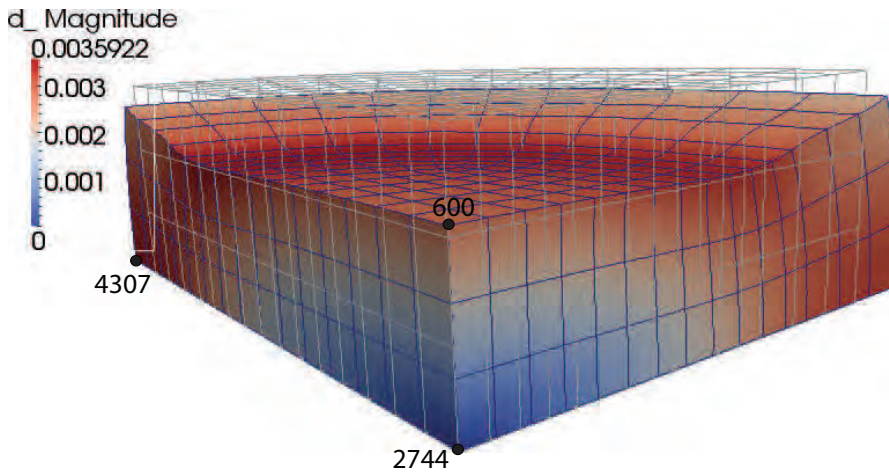
Figure 23: Q27P8 deformed mesh for drained analysis of Case 1 BC ($t^{\sigma'} = 0$, $p_f = 0$). Observe the undeformed mesh for comparison. Displacement magnification $1\times$.
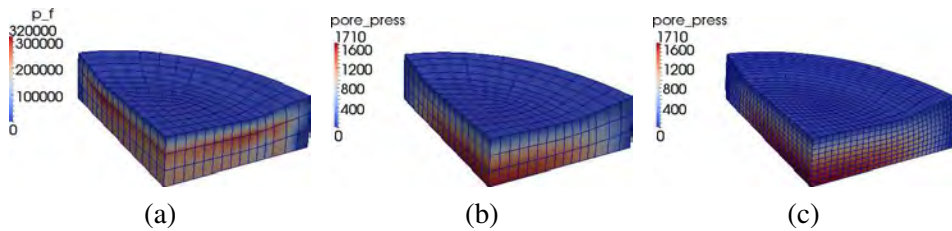
Figure 24: Deformed meshes (displacement magnification $1\times$), with contour of pore fluid pressure p_f, for the following meshes: (a) coarse Q27P8 mesh (432 elements), (b) stabilized coarse Q8P8 mesh (432 elements), (c) stabilized fine Q8P8 mesh (3465 elements).
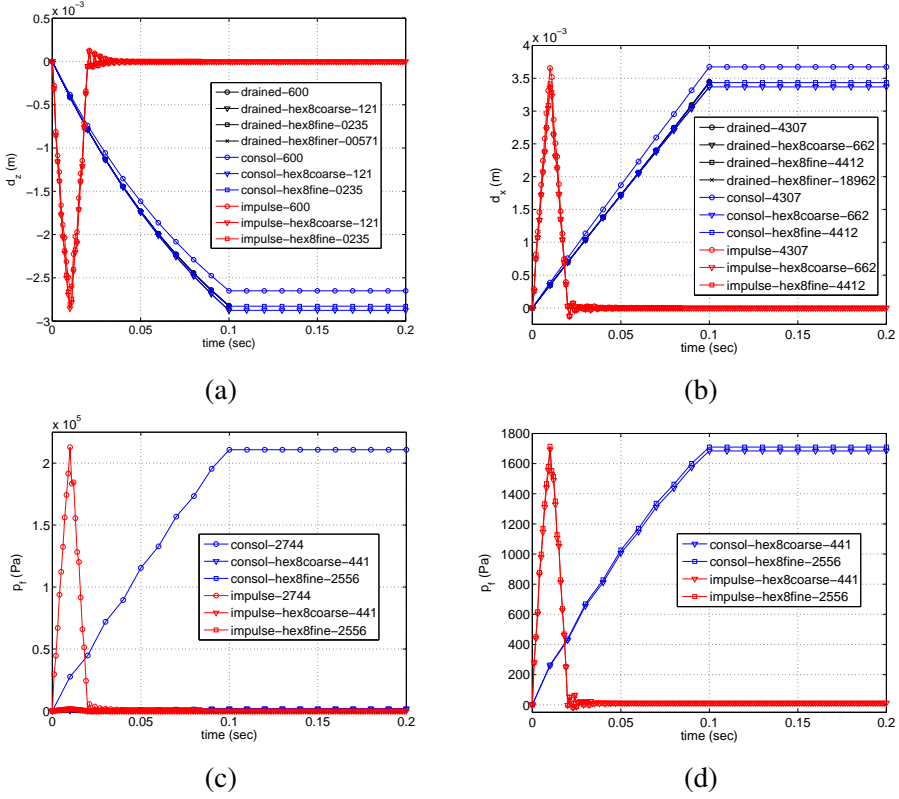
Figure 25: (a) Vertical displacement d_z. (b) Lateral displacement d_x along long axis. (c) Pore fluid pressure p_f. (d) Pore fluid pressure p_f without Q27P8 result.
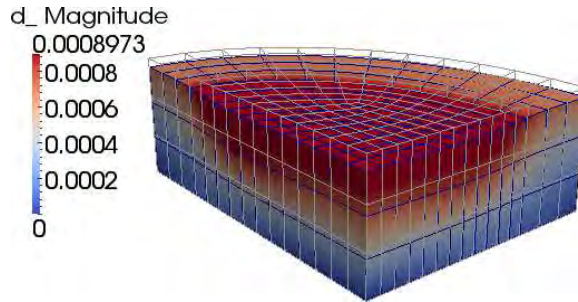
Figure 26: Q27P8 deformed mesh for drained analysis of Case 2 BC ($u_n = 0$, $S^w = 0$). Observe the undeformed mesh for comparison. Displacement magnification $1\times$.
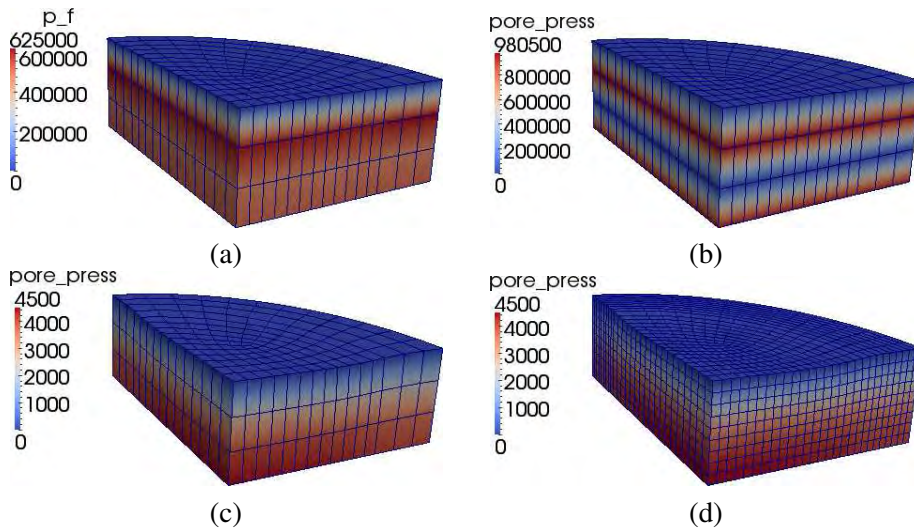
Figure 27: Deformed meshes (displacement magnification $1\times$), with contour of pore fluid pressure p_f, for the following meshes: (a) coarse Q27P8 mesh (432 elements), (b) non-stabilized coarse Q8P8 mesh (432 elements), (c) stabilized coarse Q8P8 mesh (432 elements), (d) stabilized fine Q8P8 mesh (3465 elements).
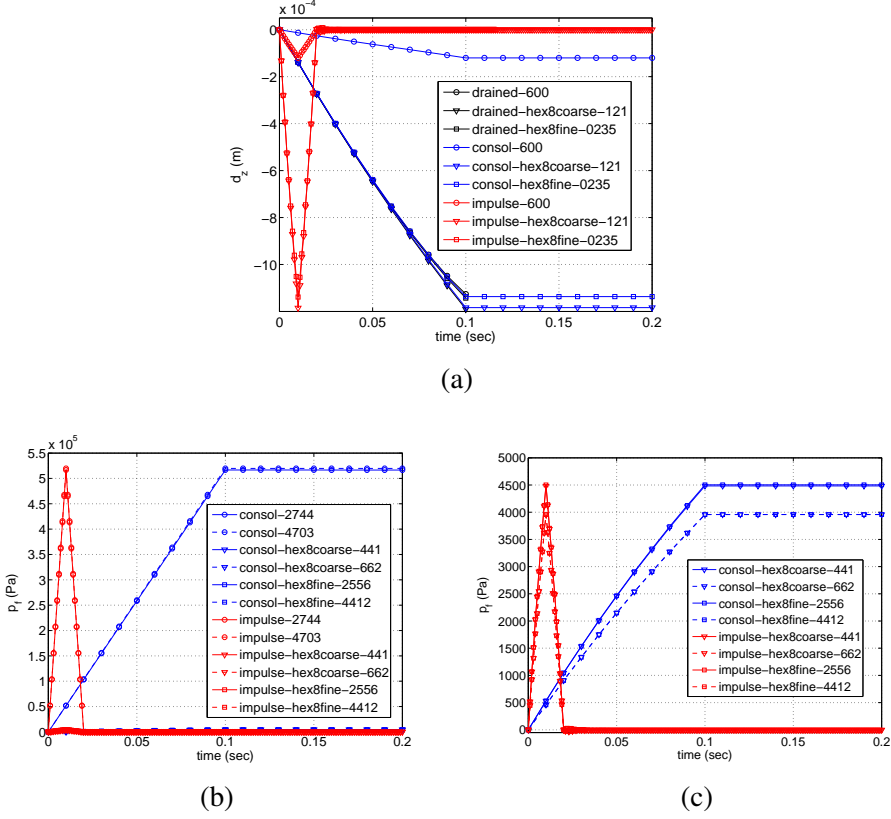
Figure 28: (a) Vertical displacement d_z. (b) Pore fluid pressure p_f. (c) Pore fluid pressure p_f without Q27P8 result.

4.4.2 *Vertebral disc compression loading in uniaxial strain - Case 2*

For the Case 2 BCs ($u_n = 0$, $S^w = 0$ on curved annulus surface) shown in Fig.21, we present the time histories of displacement d_z and d_x, and pore fluid pressure p_f, in Fig.28 for the same three nodes shown in Fig.23, with drained deformed mesh solution shown in Fig.26. Here, the higher pore fluid pressure p_f generated in the Q27P8 element mesh indicates a near locking behavior because of the low permeability, that stiffens the overall compressibility of the disc such that d_z is less for the Q27P8 mesh versus the Q8P8 meshes with stabilization (see Fig.28(a)). The two stabilized Q8P8 meshes compare well with each other as seen in Fig.28(a),(c). Also note for non-stabilized Q8P8 coarse mesh, the classical oscillating pore fluid pressure is observed in Fig.27(b), which the stabilized term alleviates in Fig.27(c). Similar to Case 1, there is only a small oscillation in solid skeleton displacement

upon release of the impulse traction, implying that the forced solid skeleton compression and driven pore fluid flow almost completely damps out the impulse load.

5   Conclusions

The paper presented finite strain three-dimensional finite element analysis (FEA) of coupled pore fluid flow and solid skeleton deformation of soft biological tissues at finite strain, including wave propagation (i.e., inertia terms). Compressibility of the pore fluid is considered, as well as porosity dependent permeability. The FEA results of a full mixed formulation Q27P8 (triquadratic in displacement, trilinear in pore fluid pressure) hexahedral element is compared to an equal order interpolation mixed formulation Q8P8 (trilinear in displacement, trilinear in pore fluid pressure) hexahedral element with stabilization. It was shown that the stabilization method of Brezzi and Pitkaranta (1984) is effective for finite strain coupled FEA of biphasic mixtures of soft tissues with small permeability (such as the vertebral disc), and is not needed for higher permeability tissues (such as the lung parenchyma). It is useful to have the Q27P8 element implementation (even though computationally expensive), as a benchmark for comparison to the Q8P8 element implementation (non-stabilized, and stabilized).

Two soft biological tissues are considered: (1) lung parenchyma, and (2) vertebral disc. For (1), it was observed that switching out the pore fluid between water and air leads to different dynamical results, where the less viscous and lighter (but more compressible) pore air can nearly damp out any applied impulse wave, but also lead to different excited mode shapes as a result of the lower mass density. For the pore water case, some waves can be observed after application of an impulse traction load, but they are damped quickly due to the dissipation associated with relative pore fluid flow and solid skeleton deformation. For (2), given the low permeability of the disc, and assuming saturation by pore water, application of traction dynamic impulse load leading to large compressive solid skeleton deformation (and corresponding relative pore fluid flow) does not allow any significant waves to propagate in time, providing a near fully damped response, but with observable change in pore fluid pressure.

It is clear that there is an interplay of solid skeleton deformation (and, in turn, solid skeleton effective stress) and build-up of pore fluid pressure over time, that would not be properly accounted for by a more simple finite strain viscoelastic constitutive model, without treating the soft tissue as a biphasic mixture. The effective stress governs the constitutive response of the solid skeleton, which is influenced by the changing pore fluid pressure with time. Thus, if appropriate anisotropic, damage constitutive models are to be considered for soft biological tissues loaded dynamically (such as during impact or blast loading), the biphasic nature of the soft tissue

should be taken into account. With that said, the paper provides a glimpse into how such biphasic dynamic (with inertia terms) analyses may be conducted, benchmarking against drained and consolidating FEA results, with further research needed: (i) consider physiological BCs and tissue geometries for in-vivo conditions; (ii) more study of the stabilization parameter α and how to select it for various tissue elastic moduli, geometries, etc.; (iii) anisotropic permeability and solid skeleton constitutive models appropriate for fibrous soft biological tissues; (iv) inclusion of pore fluid acceleration vector different than solid skeleton acceleration (i.e., $\boldsymbol{a}_\mathrm{f} \neq \boldsymbol{a}_\mathrm{s}$) and modification of the coupled governing equation solution algorithm (see Remark 1 in Sect.2.4); and (v) extension to dynamic explicit analysis capability for high rate dynamic loading.

Acknowledgements

References

Almeida, E.; Spilker, R. (1998): Finite element formulations for hyperelastic transversely isotropic biphasic soft tissues. *Comput. Methods Appl. Mech. Engrg.*, vol. 151, pp. 513–538.

Balzani, D.; Brinkhues, S.; Holzapfel, G. (2012): Constitutive framework for the modeling of damage in collagenous soft tissues with application to arterial walls. *Computer Methods in Applied Mechanics and Engineering*, vol. 213-216, pp. 139 – 151.

Bowen, R. (1980): Incompressible porous media models by use of the theory of mixture. *Int. J. Engrg. Sci.*, vol. 18, pp. 1129–1148.

Bowen, R. (1982): Compressible porous media models by use of the theory of mixtures. *Int. J. Engrg. Sci.*, vol. 20, pp. 697–735.

Brezzi, F.; Pitkaranta, J. (1984): On the stabilization of finite element approximations of the Stokes problem. In Hackbusch, W.(Ed): *Efficient Solutions of*

Elliptic Problems, Notes on Numerical Fluid Mechanics, volume 10, pp. 11–19. Vieweg, Wiesbaden.

Coleman, B. D.; Noll, W. (1963):   The thermodynamics of elastic materials with heat conduction and viscosity. *Arch. Ration. Mech. Anal.*, vol. 13, pp. 167–178.

Coussy, O. (2004):   *Poromechanics*. John Wiley & Sons.

de Boer, R. (2005):   *Trends in Continuum Mechanics of Porous Media: Theory and Applications of Transport in Porous Media*. Springer.

Ebrahimi, D. (2007):   *Three-dimensional finite element implementation for a dynamic solid-fluid mixture at finite strain*. MS Thesis, University of Colorado at Boulder, 2007.

Eringen, A. (1962):   *Nonlinear Theory of Continuous Media*. McGraw-Hill, 1 edition.

Ferguson, S.; Ito, K.; Nolte, L.-P. (2004):   Fluid flow and convective transport of solutes within the intervertebral disc. *Journal of Biomechanics*, vol. 37, pp. 213–221.

Holmes, M. (1986):   Finite deformation of soft tissue: Analysis of a mixture model in uni-axial compression. *Journal of Biomechanical Engineering*, vol. 108, no. 4, pp. 372 – 381.

Holzapfel, G. A. (2000):   *Nonlinear Solid Mechanics: A Continuum Approach for Engineering*. John Wiley & Sons.

Holzapfel, G. A.; Gasser, T. C. (2000):   A new constitutive framework for arterial wall mechanics and a comparative study of material models. *J. Elast.*, vol. 61, pp. 1–48.

Hughes, T. J. R. (1987):   *The Finite Element Method*. Prentice-Hall: New Jersey.

Jeremic, B.; Cheng, Z.; Taiebat, M.; Dafalias, Y. (2008):   Numerical simulation of fully saturated porous materials. *Int. J. Numer. Anal. Methods Geomech.*, vol. 32, pp. 1635–1660.

Lande, B.; Mitzner, W. (2006):   Analysis of lung parenchyma as a parametric porous medium. *J. Appl. Physiol.*, vol. 101, pp. 926–933.

Levenston, M.; Frank, E.; Grodzinsky, A. (1998):   Variationally derived 3-field finite element formulations for quasistatic poroelastic analysis of hydrated biological tissues. *Comput. Methods Appl. Mech. Eng.*, vol. 156, no. 1-4, pp. 231 – 46.

Levental, I.; Georges, P.; Janmey, P. (2006):   Soft biological materials and their impact on cell function. *Soft Matter*, vol. 2, pp. 1–9.

Li, C.; Borja, R.; Regueiro, R. (2004): Dynamics of porous media at finite strain. *Comp. Meth. App. Mech. Engr.*, vol. 193, no. 36-38, pp. 3837 – 70.

Ogden, R. W. (1984): *Nonlinear Elastic Deformations*. Chicheste, Ellis Horwood.

Pena, E. (2011): Prediction of the softening and damage effects with permanent set in fibrous biological materials. *Journal of the Mechanics and Physics of Solids*, vol. 59, no. 9, pp. 1808 – 1822.

Regueiro, R.; Ebrahimi, D. (2010): Implicit dynamic three-dimensional finite element analysis of an inelastic biphasic mixture at finite strain. Part 1: application to a simple geomaterial. *Comp. Meth. App. Mech. Engr.*, vol. 199, pp. 2024–2049.

Suh, J.-K.; Spilker, R.; Holmes, M. (1991): A penalty finite element analysis for non-linear mechanics of biphasic hydrated soft tissue under large deformation. *Int. J. Numer. Methods Engrg.*, vol. 32, pp. 1411–1439.

Sun, W.-C.; Ostien, J.; Salinger, A. (2013): A stabilized assumed deformation gradient finite element formulation for strongly coupled poromechanical simulations at finite strain. *Int. J. Numer. Anal. Meth. Geomech.*, DOI: 10.1002/nag.2161, 2013.

Terzaghi, K. (1943): *Theoretical Soil Mechanics*. John Wiley and Sons.

Truesdell, C.; Toupin, R. (1960): *The classical field theories*. Handbuch der Physik, Springer, Berlin.

Truty, A.; Zimmermann, T. (2006): Stabilized mixed finite element formulations for materially nonlinear partially saturated two-phase media. *Comput. Methods Appl. Mech. Engrg.*, vol. 195, pp. 1517–1546.

White, J.; Borja, R. (2008): Stabilized low-order finite elements for coupled solid-deformation/fluid-diffusion and their application to fault zone transients. *Comp. Meth. App. Mech. Engr.*, vol. 197, no. 49-50, pp. 4353 – 4366.

Williams, J.; Natarajan, R.; Andersson, G. (2007): Inclusion of regional poroelastic material properties better predicts biomechanical behavior of lumbar discs subjected to dynamic loading. *Journal of Biomechanics*, vol. 40, pp. 1981–1987.

Zhu, Q.; Suh, J.-K. F. (2000): Dynamic finite element analysis of biphasic poroviscoelastic model for hydrated soft tissue. *Annals of Biomedical Engineering*, vol. 28, no. SUPPL. 1, pp. S – 50.

Zhu, Q.; Suh, J.-K. F. (2001): Dynamic biphasic poroviscoelastic model simulation of hydrated soft tissues and its potential applications for brain impact study. In *American Society of Mechanical Engineers, Bioengineering Division (Publication) BED*, pp. 835–836. Snowbird, UT, United states.

D Journal Paper

The appendix includes a journal paper, to which is referred in early sections of this Final Report: Burd, H.J., Regueiro, R.A. (2015) "Finite element implementation of a multiscale model of the human lens capsule," Biomech. Model. Mechanobiology 14(6):1363-1378.

CrossMark

Finite element implementation of a multiscale model of the human lens capsule

H. J. Burd[1] · R. A. Regueiro[2]

Abstract An axisymmetric finite element implementation of a previously described structural constitutive model for the human lens capsule (Burd in Biomech Model Mechanobiol 8(3):217–231, 2009) is presented. This constitutive model is based on a hyperelastic approach in which the network of collagen IV within the capsule is represented by an irregular hexagonal planar network of hyperelastic bars, embedded in a hyperelastic matrix. The paper gives a detailed specification of the model and the periodic boundary conditions adopted for the network component. Momentum balance equations for the network are derived in variational form. These balance equations are used to develop a nonlinear solution scheme to enable the equilibrium configuration of the network to be computed. The constitutive model is implemented within a macroscopic finite element framework to give a multiscale model of the lens capsule. The possibility of capsule wrinkling is included in the formulation. To achieve this implementation, values of the first and second derivatives of the strain energy density with respect to the in-plane stretch ratios need to be computed at the local, constitutive model, level. Procedures to determine these strain energy derivatives at equilibrium configurations of the network are described. The multiscale model is calibrated against previously published experimental data on isolated inflation and uniaxial stretching of ex vivo human capsule samples. Two

independent example lens capsule inflation analyses are presented.

Keywords Multiscale · Human lens capsule · Accommodation · Collagen

1 Introduction

The ocular lens is one of the components of the optical system that exists within the human eye, to focus light entering the pupil onto the retina. The lens is connected to the ciliary body by a set of radial fibres, known as zonules. When the ciliary muscle is relaxed, radial forces are imposed on the lens, via the zonules. In this state, the normal eye is able to focus on distant objects. To view a close object (according to the widely accepted mechanism proposed by Helmholtz), the ciliary muscle contracts, thereby reducing the radial forces applied to the lens by the zonules. As a consequence, the lens assumes a thicker, more rounded shape, with increased optical power. This process, known as accommodation, is highly effective in the normal young eye. The effectiveness of the accommodation process declines with age, however, with the consequence that, from late middle-age onwards, the ability of the eye to vary its optical power becomes minimal. This limiting condition is known as 'presbyopia'. The detailed causes of presbyopia remain a matter of debate, although it is generally understood that age-related changes in the mechanical characteristics of the lens are major contributing factors.

The lens is composed of a soft cellular matrix (the lens substance) surrounded by a thin, relatively stiff, membrane known as the capsule (e.g. Oyster 1999; Bron et al. 1997). The lens capsule is a basement membrane, consisting principally of a network of collagen IV filaments stabilized by a surrounding matrix comprising proteoglycans and glycopro-

✉ H. J. Burd
harvey.burd@eng.ox.ac.uk

R. A. Regueiro
richard.regueiro@colorado.edu

[1] Department of Engineering Science, Oxford University, Oxford, UK

[2] Department of Civil, Environmental, and Architectural Engineering, University of Colorado Boulder, Boulder, CO, USA

🖄 Springer

teins (e.g. Danysh and Duncan 2009; Krag and Andreassen 2003).

The performance of the natural lens during the accommodation process has been previously investigated using numerical modelling procedures based on finite element analysis (e.g. Burd et al. 2002; Hermans et al. 2006; Stachs et al. 2006; Belaidi and Pierscionek 2007). In these models, the lens capsule is typically represented as a linearly elastic material with stiffness data determined either from the uniaxial tests of Krag et al. (1997) or from the biaxial tests of Fisher (1969). It is shown in Burd (2009) that data on Young's modulus inferred by Fisher (1969) on the basis of (biaxial) capsule inflation tests are inconsistent with data on capsule Young's modulus determined from the uniaxial tests conducted by Krag et al. (1997). This finding supports the view that linear elasticity is an unsuitable basis for a constitutive model of the human lens capsule. An alternative Fung-type constitutive model for the lens capsule is proposed by Pedrigi et al. (2007). It is shown in Burd (2009) that this Fung-type model, which is calibrated using data from a set of biaxial tests, provides a poor representation of the uniaxial test data given by Krag et al. (1997).

In Burd (2009), an alternative form of constitutive model for the human lens capsule is proposed. This model is based on a structural approach that is inspired by the geometry of the collagen IV filaments that exists within the capsule (e.g. Barnard et al. 1992). The mechanical behaviour of the collagen filaments is represented in the model by an irregular periodic 2D hexagonal network of pin-jointed bars; this network is embedded in a neo-Hookean matrix. It is shown in Burd (2009) that this structural model is capable of being calibrated to provide a good fit with both biaxial and uniaxial test data. A detailed discussion is given in Burd (2009) on the sensitivity of the model to changes in the joint positions of the hexagonal network and also on the performance of the network model for biaxial and uniaxial loading. For uniaxial loading, the network tends to become aligned in the direction of the imposed load; the resulting geometric effects are consistent with the large strain nonlinear behaviour that is apparent in the uniaxial data of Krag et al. (1997).

The purpose of the current paper is to describe a numerical implementation of the structural constitutive model described in Burd (2009); this constitutive model is referred to in the current paper as "micronet". The implementation has been carried out in the *Oxfem_hyperelastic* finite element program that has been developed at Oxford University for ophthalmic modelling. The micronet model represents the behaviour of the lens capsule at the microscopic scale (corresponding to typical length scales inherent in the collagen network which are of the order of tens of nanometres); the macroscopic finite element model represents the capsule at the scale of the overall lens dimensions (of the order of millimetres). The performance of the resulting multiscale model

is demonstrated via several example analyses involving inflation of the lens capsule.

The proposed formulation can be compared with previously published structural constitutive models as follows. Fan and Sacks (2014) describe a multiscale approach, intended for soft biological tissues in which a fibrous network is embedded in an amorphous matrix. This approach is similar to the one presented in the current paper in the sense that two separate components are considered (fibrous network and matrix), both components are modelled using a hyperelastic framework, and the resulting constitutive model is embedded in a macroscopic finite element model. In the Fan and Sacks model, the fibrous network deforms in an affine manner (i.e. given an applied stretch ratio λ, all joint coordinates of the network are mapped linearly); this contrasts with the current approach in which the network deformations are non-affine (i.e. given an applied stretch ratio λ, only external joint coordinates of the network are mapped linearly). The non-affine approach adopted in the current paper is computationally expensive in the sense that repeated nonlinear analyses are needed at the level of the constitutive model to compute the equilibrium configurations of the network. However, this non-affine approach provides a procedure in which the structural influence of the underlying network is incorporated, directly, within the model and allows for extension to failure mechanics as part of future work. D'Amore et al. (2014) describe an alternative approach, based on non-affine mechanics and a random network. This model was implemented in a commercial finite element program for the purpose of conducting analyses at the scale of a single representative volume element (RVE).

Agoram and Barocas (2001) and Stylianopoulos and Barocas (2007a, b) present a multiscale modelling approach for collagen fibre networks in which a 3D random network is formulated within a RVE. This structural model is embedded at the Gauss points of continuum finite elements for mechanical modelling of tissues. Similar to the current paper, displacements are applied to the constitutive model only at the RVE boundaries, thus allowing non-affine deformation of the network. The local stresses are determined from the constitutive model via a volume averaging procedure (Stylianopoulos and Barocas 2007a). This contrasts with the approach adopted in the current paper in which data are transferred from the microscopic model to the macroscopic model by means of strain energy derivatives (within the framework of hyperelasticity). Full details on the linearization procedures that were adopted in these previous models or the convergence performance that was achieved are not provided [although some discussion is given in the appendix of Agoram and Barocas (2001)]. In the current paper, it is demonstrated how a consistent link between a non-affine structural constitutive model and a macroscopic finite element model can be derived.

The multiscale formulation developed in the current paper is intended for use in axisymmetric finite element analyses (e.g. Burd et al. 2002; Hermans et al. 2006; Stachs et al. 2006) in which the capsule is represented—at the macroscopic scale—by zero-thickness membrane elements. This restriction to the axisymmetric case has the important consequence that the directions of the principal stretches imposed on the micronet model remain coincident with the meridional and circumferential directions in the macroscopic model. Material rotation in the plane of the capsule does not need to be considered.

The modelling procedures described in the current paper are intended to contribute to the development of detailed multiscale models of the mechanical behaviour of the lens during the natural accommodation process. Numerical models of the accommodation process also require the use of appropriate modelling procedures for the lens substance and the zonules although these aspects are outside the scope of the current paper. Numerical models of the natural lens form an obvious starting point for the development of computational procedures to investigate the performance of proposed treatments for presbyopia such as femto-second laser treatment of the lens (e.g. Schumacher et al. 2009) and accommodating intraocular lens implants (e.g. Charman 2014).

2 Detailed specification of the micronet model

Essential background to the micronet model is given in Burd (2009). It should be noted that, in this earlier paper, the model is formulated in terms of strain energy density with respect to initial *area*, whereas in the current paper the formulation is in terms of strain energy density with respect to initial *volume*. For an incompressible hyperelastic membrane, the two methods are essentially equivalent. However, the current approach facilitates the application of the model to membranes (such as the lens capsule) in which the thickness varies spatially at the macroscopic level. It should also be noted that, in places, the current nomenclature departs from that adopted in Burd (2009).

The micronet model consists of a certain number of stacked layers of an irregular hexagonal mesh of nonlinear bars (to represent the mechanical behaviour of the collagen IV network) embedded in an incompressible hyperelastic matrix. The reference periodic dimensions of the mesh are A_X, A_Y with out-of-plane capsule thickness T (Fig. 1). Because of the incompressibility assumption, the reference and current volumes are equal, such that $A_X A_Y T = a_x a_y t$, where a_x, a_y are the current periodic dimensions and t is the current out-of-plane capsule thickness. The total strain energy E of the micronet model at a material point in the continuum, with reference volume ($A_X A_Y T$), is,
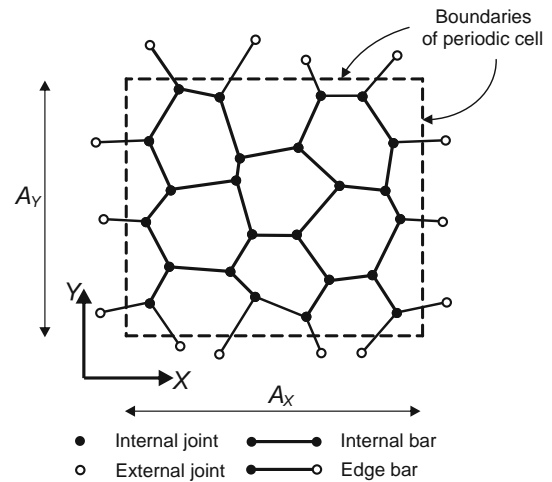
Fig. 1 Network in the periodic cell [modified from Burd (2009)]

$$E = (A_X A_Y T) W \tag{1}$$

where the strain energy density W (energy per unit initial volume) is the sum of the two components of the model,

$$W(\lambda_x, \lambda_y, \lambda_z) = W_{\text{net}}(\lambda_x, \lambda_y) + W_{\text{mat}}(\lambda_x, \lambda_y, \lambda_z) \tag{2}$$

In this equation, W_{net} is the strain energy density associated with the structural network, and W_{mat} is the strain energy density associated with the matrix. The choice of W_{mat} is arbitrary, although it is intended that a relatively simple phenomenological model is adopted. [In the current paper, and also in Burd (2009), an incompressible neo-Hookean model is selected.] The in-plane stretches are λ_x, λ_y. It is noted that incompressibility of the matrix requires that the out-of-plane stretch, λ_z, is related to the in-plane stretches by $\lambda_x \lambda_y \lambda_z = 1$. As a consequence, the strain energy density for the matrix can be regarded as a function of the in-plane stretches alone, $W_{\text{mat}}(\lambda_x, \lambda_y)$. This functional form of strain energy density for the matrix is adopted in the following formulation. The in-plane principal stretches prescribed to the micronet model by the macroscopic model are denoted by Λ_1, Λ_2. As described later in the paper, the macroscopic principal stretches Λ_1, Λ_2 are not necessarily aligned with the network in-plane coordinates x, y, giving flexibility in prescribing in-plane stretches to the network model (i.e. $(\lambda_x, \lambda_y) = (\Lambda_1, \Lambda_2)$ or $(\lambda_x, \lambda_y) = (\Lambda_2, \Lambda_1)$).

2.1 Geometric model for the collagen network

A regular hexagonal network, consisting of bars of length L_0, is generated within a two-dimensional periodic cell of dimensions A_X, A_Y. This network is then distorted by imposing random perturbations on a normal distribution (mean zero, standard deviation γL_0, where γ is a scalar). An infinite peri-

Table 1 Values of the mapping constant for the mapped joints

Edge bar external joint location		θ_X	θ_Y
$X^{(\text{ext})} \geq A_X$	$Y^{(\text{ext})} \leq 0$	1	−1
	$0 < Y^{(\text{ext})} < A_Y$	1	0
	$Y^{(\text{ext})} \geq 0$	1	1
$0 < X^{(\text{ext})} < A_X$	$Y^{(\text{ext})} \leq 0$	0	−1
	$Y^{(\text{ext})} \geq 0$	0	1
$X^{(\text{ext})} \leq A_X$	$Y^{(\text{ext})} \leq 0$	−1	−1
	$0 < Y^{(\text{ext})} < A_Y$	−1	0
	$Y^{(\text{ext})} \geq 0$	−1	1

odic lattice is generated from this periodic cell. This approach allows the behaviour of an infinite network to be represented by a relatively small number of internal variables (i.e. the joint positions).

The calculations described in this paper were all conducted using the network shown in Fig. 1 ($\gamma = 0.1$). This network is identical to the one plotted in Fig. 9b of Burd (2009). Joint coordinates and dimensions of the periodic cell are given in "Appendix 1".

In general, the periodic cell contains a set of independent internal joints. The coordinates of internal joint q in the periodic cell in the reference (i.e. the stress-free) configuration are $(X^{(q)}, Y^{(q)})$. Each joint q in the periodic cell maps onto a joint $q_{(\alpha,\beta)}$ in an infinite lattice where

$$X^{(q_{\alpha,\beta})} = X^{(q)} + \alpha A_X, \quad Y^{(q_{\alpha,\beta})} = Y^{(q)} + \beta A_Y, \quad \forall \alpha, \beta \in \mathbb{Z} \tag{3}$$

where $\mathbb{Z}$ is the set of integers. The joints in the periodic cell are connected by $n_{\text{int-bars}}$ internal bars (i.e. bars connected between two internal joints) and $n_{\text{edge-bars}}$ edge bars (i.e. bars connected between one internal joint and one joint in an adjacent cell).

Each joint in an adjacent cell connected to an edge bar is termed as an "external joint". Each external joint has associated with it an internal joint (termed "mapped joint") with coordinates:

$$X^{(\text{ext})} = X^{(q)} + \theta_X A_X, \quad Y^{(\text{ext})} = Y^{(q)} + \theta_Y A_Y \tag{4}$$

where $(X^{(\text{ext})}, Y^{(\text{ext})})$ are the coordinates of the external joint ext, $(X^{(q)}, Y^{(q)})$ are the coordinates of the mapped joint and the mapping constants θ_X, θ_Y are given in Table 1.

2.2 Imposed deformation field

The stretch ratios at a material point in the macroscopic model are (Λ_1, Λ_2). These deformations are imposed on

the network by prescribing the periodic lengths in the current configuration to be $a_x = \lambda_x A_X$ and $a_y = \lambda_y A_Y$ where $(\lambda_x, \lambda_y) = (\Lambda_1, \Lambda_2)$ or $(\lambda_x, \lambda_y) = (\Lambda_2, \Lambda_1)$. The current coordinates of joint $q_{(\alpha,\beta)}$ in the infinite lattice are:

$$x^{(q_{\alpha,\beta})} = x^{(q)} + \alpha a_x + k_x \tag{5}$$
$$y^{(q_{\alpha,\beta})} = y^{(q)} + \beta a_y + k_y, \quad \forall \alpha, \beta \in \mathbb{Z}$$

where k_x and k_y represent an arbitrary rigid body motion. Each external joint has the current coordinates:

$$x^{(\text{ext})} = x^{(q)} + \theta_X a_x, \quad y^{(\text{ext})} = y^{(q)} + \theta_Y a_y \tag{6}$$

The coordinates $(x^{(q)}, y^{(q)})$ are required to satisfy equilibrium at each joint in the lattice. Equation (5) ensures that the network conforms to the required deformation field at the scale of the periodic lengths a_x, a_y. Within the periodic cell, however, the bars deform in a non-affine manner subject to the requirements of equilibrium at the joints.

2.3 Variational form of the balance of linear momentum for the network

The strain energy per unit reference length for each bar in the network is denoted W_{bar}. An appropriate selection needs to be made for the functional form of W_{bar}. The strain energy density (energy per unit initial volume) for the network is obtained from the sum, over the periodic cell, of the contribution of the individual bars (noting that a factor of 1/2 appears as a consequence of the fact that each edge bar appears twice in the summation). This gives,

$$W_{\text{net}} = \frac{\rho_{\text{net}}}{A_X A_Y} \left[\sum_{b=1}^{n_{\text{int-bars}}} L_b W_{\text{bar}}(\lambda_b) + \frac{1}{2} \sum_{c=1}^{n_{\text{edge-bars}}} L_c W_{\text{bar}}(\lambda_c) \right] \tag{7}$$

where ρ_{net} is a parameter termed the "packing density". The packing density is a notional measure of the number of layers of network per unit initial thickness of capsule. It is assumed in the current implementation that the packing density does not vary spatially within the macroscopic model.

The kinematics of the bars is specified as follows. Internal bar b has reference length L_b. The stretch ratio λ_b is,

$$\lambda_b = \frac{\ell_b}{L_b}, \quad \ell_b^2 = (x_2 - x_1)^2 + (y_2 - y_1)^2 \tag{8}$$

where the bar connects internal joints with coordinates in the current configuration (x_1, y_1) and (x_2, y_2); ℓ_b is the current length of the bar. Edge bar c has reference length L_c. Each
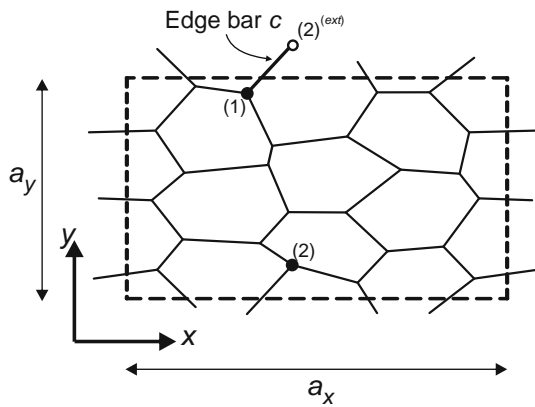
Fig. 2 Joint connections for a typical edge bar c shown in the current configuration. Joint (1) is, by convention, an internal joint, and joint (2) is the mapped joint corresponding to the external joint $(2)^{(ext)}$ that is attached to bar c. The coordinates of joint (1) are (x_1, y_1), and the coordinates of joint $(2)^{(ext)}$ are $(x_2 + a_x \theta_X, \ y_2 + a_y \theta_Y)$ where (x_2, y_2) are the coordinates of joint (2)

edge bar connects an internal joint to an external joint as illustrated in Fig. 2. The stretch ratio λ_c for the edge bars is,

$$\lambda_c = \frac{\ell_c}{L_c}, \quad \ell_c^2 = (x_2 + \theta_X a_x - x_1)^2 + (y_2 + \theta_Y a_y - y_1)^2 \tag{9}$$

where ℓ_c is the current length of edge bar c.

Note that only the edge bar current lengths ℓ_c are explicit functions of the in-plane stretches (λ_x, λ_y) through a_x and a_y. The positions of the internal bar joints, and in turn current lengths ℓ_b and ℓ_c, are determined by satisfying the balance of linear momentum, in this paper via the variational form. Furthermore, it is convenient to introduce the following vectors:

$$\boldsymbol{x}_b = \begin{bmatrix} x_1 \\ y_1 \\ x_2 \\ y_2 \end{bmatrix}_b, \quad \boldsymbol{x}_c = \begin{bmatrix} x_1 \\ y_1 \\ x_2 \\ y_2 \end{bmatrix}_c, \quad \boldsymbol{d}_c = \begin{bmatrix} x_2 + \theta_X a_x - x_1 \\ y_2 + \theta_Y a_y - y_1 \end{bmatrix}_c \tag{10}$$

To reach a desired minimum energy state in terms of internal joint coordinates $\boldsymbol{x}$, with prescribed in-plane stretches $\boldsymbol{\lambda} = [\lambda_x \ \lambda_y]^T$, the stationarity condition is applied, such that,

$$\delta E(\delta \boldsymbol{x}, \boldsymbol{x}) = (A_X A_Y T) [\delta W_{\text{net}}(\delta \boldsymbol{x}, \boldsymbol{x}) + \delta W_{\text{mat}}]$$
$$= (A_X A_Y T) \delta W_{\text{net}}(\delta \boldsymbol{x}, \boldsymbol{x}) \tag{11}$$

where $\delta W_{\text{mat}} = 0$ with respect to variations on internal joint coordinates $\delta \boldsymbol{x}$. It is noted that,

$$\delta W_{\text{net}} = \frac{\rho_{\text{net}}}{A_X A_Y} \left[\sum_{b=1}^{n_{\text{int-bars}}} L_b \, \delta W_{\text{bar}}(\lambda_b) \right.$$
$$\left. + \frac{1}{2} \sum_{c=1}^{n_{\text{edge-bars}}} L_c \, \delta W_{\text{bar}}(\lambda_c) \right] \tag{12}$$

where

$$\delta W_{\text{bar}}(\lambda_b) = \frac{dW_{\text{bar}}}{d\lambda_b} \delta \lambda_b, \quad \delta \lambda_b = \frac{\delta \ell_b}{L_b}$$
$$\delta \ell_b = \boldsymbol{B}_{x(b)} \cdot \delta \boldsymbol{x}_b$$
$$\boldsymbol{B}_{x(b)} = \frac{1}{\ell_b} \left[-(x_2 - x_1) \ \ -(y_2 - y_1) \ \ (x_2 - x_1) \ \ (y_2 - y_1) \right]_b$$
$$\delta \boldsymbol{x}_b = \left[\delta x_1 \ \ \delta y_1 \ \ \delta x_2 \ \ \delta y_2 \right]_b^T \tag{13}$$
$$\delta W_{\text{bar}}(\lambda_c) = \frac{dW_{\text{bar}}}{d\lambda_c} \delta \lambda_c, \quad \delta \lambda_c = \frac{\delta \ell_c}{L_c}$$
$$\delta \ell_c = (\boldsymbol{B}_{x(c)} + \boldsymbol{\Theta}_c) \cdot \delta \boldsymbol{x}_c$$
$$\boldsymbol{\Theta}_c = \frac{1}{\ell_c} \left[-\theta_X a_x \ \ -\theta_Y a_y \ \ \theta_X a_x \ \ \theta_Y a_y \right]_c$$
$$\delta \boldsymbol{x}_c = \left[\delta x_1 \ \ \delta y_1 \ \ \delta x_2 \ \ \delta y_2 \right]_c^T \tag{14}$$

In summary, the variational form of the balance of linear momentum of the network with respect to variations on the internal joint coordinates $\boldsymbol{x}$ is:

$$\delta E(\delta \boldsymbol{x}, \boldsymbol{x}) = \rho_{\text{net}} T \left[\sum_{b=1}^{n_{\text{int-bars}}} \delta \boldsymbol{x}_b^T \cdot \boldsymbol{f}_b^{\text{int-bar}} \right.$$
$$\left. + \frac{1}{2} \sum_{c=1}^{n_{\text{edge-bars}}} \delta \boldsymbol{x}_c^T \cdot \boldsymbol{f}_c^{\text{edge-bar}} \right] = 0 \tag{15}$$
$$\boldsymbol{f}_b^{\text{int-bar}} = \frac{dW_{\text{bar}}}{d\lambda_b} \boldsymbol{B}_{x(b)}^T$$
$$\boldsymbol{f}_c^{\text{edge-bar}} = \frac{dW_{\text{bar}}}{d\lambda_c} (\boldsymbol{B}_{x(c)}^T + \boldsymbol{\Theta}_c^T)$$

where $\boldsymbol{f}_b^{\text{int-bar}}$ is the force vector of internal bar b, and $\boldsymbol{f}_c^{\text{edge-bar}}$ is the force vector of edge bar c.

2.4 Linearized form of the balance of linear momentum for the network

The variational equation for the network balance of linear momentum is in general nonlinear in terms of the internal joint coordinates $\boldsymbol{x}$, such that a nonlinear solution procedure is required. Resorting to Newton–Raphson, the linearization of $\delta E(\delta \boldsymbol{x}, \boldsymbol{x})$ gives,

$$\mathscr{L}[\delta E(\delta \boldsymbol{x}, \boldsymbol{x})] = \delta E(\delta \boldsymbol{x}, \boldsymbol{x}) + \Delta[\delta E(\delta \boldsymbol{x}, \boldsymbol{x}, \Delta \boldsymbol{x})] = 0 \tag{16}$$

where $\Delta x = x^{k+1} - x^k$ is the increment in internal joint coordinates, and recall the directional derivative, in this case in the direction of internal joint coordinate increments Δx, such that,

$$\Delta[\delta E(\delta x, x, \Delta x)] = D_{\Delta x}[\delta E(\delta x, x)]$$
$$= \frac{\partial[\delta E(\delta x, x)]}{\partial x} \cdot \Delta x \quad (17)$$

It is straightforward to show that:

$$\frac{\partial(\delta E)}{\partial x} = \rho_{\text{net}} T \left[\sum_{b=1}^{n_{\text{int-bars}}} \delta x_b^T \cdot k_b^{\text{int-bar}} \right.$$
$$\left. + \frac{1}{2} \sum_{c=1}^{n_{\text{edge-bars}}} \delta x_c^T \cdot k_c^{\text{edge-bar}} \right] = 0 \quad (18)$$

where

$$k_b^{\text{int-bar}} = \frac{\partial f_b^{\text{int-bar}}}{\partial x_b}$$

$$\frac{\partial f_b^{\text{int-bar}}}{\partial x_b} = \frac{1}{\ell_b} \frac{dW_{\text{bar}}}{d\lambda_b} \left(C - B_{x(b)}^T \cdot B_{x(b)} \right)$$
$$+ \frac{1}{L_b} \frac{d^2 W_{\text{bar}}}{d\lambda_b^2} B_{x(b)}^T \cdot B_{x(b)}$$

$$C = \begin{bmatrix} 1 & 0 & -1 & 0 \\ 0 & 1 & 0 & -1 \\ -1 & 0 & 1 & 0 \\ 0 & -1 & 0 & 1 \end{bmatrix}$$

and

$$k_c^{\text{edge-bar}} = \frac{\partial f_c^{\text{edge-bar}}}{\partial x_c}$$

$$\frac{\partial f_c^{\text{edge-bar}}}{\partial x_c} = \frac{1}{\ell_c} \frac{dW_{\text{bar}}}{d\lambda_c} \left(C - (B_{x(c)} \right.$$
$$\left. + \Theta_c)^T \cdot (B_{x(c)} + \Theta_c) \right)$$
$$+ \frac{1}{L_c} \frac{d^2 W_{\text{bar}}}{d\lambda_c^2} (B_{x(c)} + \Theta_c)^T \cdot (B_{x(c)} + \Theta_c)$$

After applying essential boundary conditions by constraining one of the internal joints and prescribing the stretches (λ_x, λ_y), the force vectors and stiffness matrices of all internal and edge bars are assembled to give the global force vector F^{bar} and the global stiffness matrix K^{bar}. The linearized form of the variational equation for balance of linear momentum of the network is then,

$$\mathcal{L}[\delta E] = (\rho_{\text{net}} T)\delta x^T \cdot (F^{\text{bar}} + K^{\text{bar}} \cdot \Delta x) = 0 \quad (19)$$

Recall that the variations of the internal joint coordinates δx are arbitrary, thus, to satisfy Eq. (19) at each iteration k, for

$(\rho_{\text{net}} T) \neq 0$, Δx is solved and the internal joint coordinates are updated,

$$F^{\text{bar}} + K^{\text{bar}} \cdot \Delta x = 0 , \quad x^{k+1} = x^k + \Delta x \quad (20)$$

Convergence is then checked given a user-defined tolerance tol_{net},

$$\| F^{\text{bar}, k+1} \|_\infty < tol_{\text{net}} \quad (21)$$

If Eq. (21) is satisfied, the internal joint coordinates are converged $x = x^{k+1}$, and the solution continues to the next time step, repeating the nonlinear solution process, else it iterates.

2.5 Strain energy density derivatives

As mentioned earlier in the paper, the macroscopic model calculates principal values of in-plane stretch $\Lambda = [\Lambda_1 \ \Lambda_2]^T$. Values of Λ_1 or Λ_2 are prescribed to the in-plane stretches of the network, such that $(\lambda_x, \lambda_y) = (\Lambda_1, \Lambda_2)$ or $(\lambda_x, \lambda_y) = (\Lambda_2, \Lambda_1)$. Either way, the macroscopic model requires values of the derivatives, $\partial W/\partial \Lambda$ and $\partial^2 W/\partial \Lambda^2$, which in turn requires values of the derivatives, $\partial W/\partial \lambda$ and $\partial^2 W/\partial \lambda^2$ for equilibrium configurations of the network. The contribution of W_{mat} to these derivatives is determined straightforwardly. The components due to W_{net} are evaluated as follows.

The strain energy density for the network, W_{net}, is available as an explicit function of the equilibrium joint coordinates x and the local stretches λ. The required derivatives of W_{net} are implicit derivatives (i.e. the dependence $x = x(\lambda)$ is included, implicitly). These derivatives are determined at the equilibrium configuration at which $\delta E = (\rho_{\text{net}} T)\delta x^T \cdot F^{\text{bar}} = 0$, which for arbitrary δx and $(\rho_{\text{net}} T) \neq 0$ gives $F^{\text{bar}} = 0$ (to within the specified tolerance tol_{net}).

The first strain energy derivatives are determined as follows,

$$\frac{\partial W_{\text{net}}}{\partial \lambda} = \left(\frac{\partial W_{\text{net}}}{\partial \lambda} \right)_x + \left(\frac{\partial x}{\partial \lambda} \right) \cdot \left(\frac{\partial W_{\text{net}}}{\partial x} \right)_\lambda \quad (22)$$

The first term on the right-hand side of Eq. (22) is determined explicitly,

$$\left(\frac{\partial W_{\text{net}}}{\partial \lambda} \right)_x = \frac{\rho_{\text{net}}}{2 A_X A_Y} \sum_{c=1}^{n_{\text{edge-bars}}} \frac{1}{\ell_c} \left(\frac{dW_{\text{bar}}}{d\lambda_c} \right) \Pi_c \cdot d_c \quad (23)$$

where

$$\Pi_c = \begin{bmatrix} \theta_X A_X & 0 \\ 0 & \theta_Y A_Y \end{bmatrix} \quad (24)$$

It is noted that, in the equilibrium configuration,

$$\left(\frac{\partial W_{\text{net}}}{\partial \boldsymbol{x}}\right)_{\lambda} = \frac{\rho_{\text{net}}}{A_X A_Y} \boldsymbol{F}^{\text{bar}} = \boldsymbol{0} \tag{25}$$

The second term on the right-hand side of Eq. (22) therefore vanishes.

To determine the second derivatives,

$$\frac{\partial}{\partial \lambda} \left(\frac{\partial W_{\text{net}}}{\partial \lambda}\right) = \frac{\partial}{\partial \lambda} \left[\left(\frac{\partial W_{\text{net}}}{\partial \lambda}\right)_{x} + \frac{\rho_{\text{net}}}{A_X A_Y} \left(\frac{\partial \boldsymbol{x}}{\partial \lambda}\right) \cdot \boldsymbol{F}^{\text{bar}} \right] \tag{26}$$

Since $\boldsymbol{F}^{\text{bar}} = \boldsymbol{0}$ and $\partial \boldsymbol{F}^{\text{bar}}/\partial \lambda = \boldsymbol{0}$ in the equilibrium configuration, Eq. (26) may be written as

$$\frac{\partial}{\partial \lambda} \left(\frac{\partial W_{\text{net}}}{\partial \lambda}\right) = \left(\frac{\partial^2 W_{\text{net}}}{\partial \lambda^2}\right)_{x} + \frac{\partial}{\partial \boldsymbol{x}} \left[\left(\frac{\partial W_{\text{net}}}{\partial \lambda}\right)_{x} \right]_{\lambda} \cdot \left(\frac{\partial \boldsymbol{x}}{\partial \lambda}\right) \tag{27}$$

The derivatives on the right-hand side of Eq. (27) can be determined explicitly, with the exception of $\partial \boldsymbol{x}/\partial \lambda$. This derivative is determined as follows. Note that,

$$\frac{\partial \boldsymbol{F}^{\text{bar}}}{\partial \lambda} = \boldsymbol{0} = \left(\frac{\partial \boldsymbol{F}^{\text{bar}}}{\partial \lambda}\right)_{x} + \left(\frac{\partial \boldsymbol{F}^{\text{bar}}}{\partial \boldsymbol{x}}\right)_{\lambda} \cdot \left(\frac{\partial \boldsymbol{x}}{\partial \lambda}\right) \tag{28}$$

Equation (28) is solved (noting that $(\partial \boldsymbol{F}^{\text{bar}}/\partial \boldsymbol{x})_{\lambda} = \boldsymbol{K}^{\text{bar}}$) to determine $\partial \boldsymbol{x}/\partial \lambda$. The derivative $(\partial \boldsymbol{F}^{\text{bar}}/\partial \lambda)_{x}$ is determined as follows. Note that the only contribution to $\boldsymbol{F}^{\text{bar}}$ with explicit functional dependence on the in-plane stretches λ is that of the edge bars. This matrix is therefore assembled from the edge bar contributions to give,

$$\left(\frac{\partial \boldsymbol{F}^{\text{bar}}}{\partial \lambda}\right)_{x} = \frac{1}{2} \overset{n_{\text{edge-bars}}}{\underset{c=1}{\mathbf{A}}} \left(\frac{\partial \boldsymbol{f}_c^{\text{edge-bar}}}{\partial \lambda}\right)_{x} \tag{29}$$

where $\boldsymbol{f}_c^{\text{edge-bar}}$ is given in Eq. (15), and $\mathbf{A}$ is the assembly operator. It may be shown that:

$$\left(\frac{\partial \boldsymbol{f}_c^{\text{edge-bar}}}{\partial \lambda}\right)_{x} = \frac{1}{\ell_c} \left(\frac{\mathrm{d} W_{\text{bar}}}{\mathrm{d}\lambda_c^2}\right) \boldsymbol{C}_{(4\times2)} \cdot \boldsymbol{\Pi}_c$$
$$+ \frac{1}{\ell_c^3} \left[\lambda_c \left(\frac{\mathrm{d}^2 W_{\text{bar}}}{\mathrm{d}\lambda_c^2}\right) \right.$$
$$\left. - \frac{\mathrm{d} W_{\text{bar}}}{\mathrm{d}\lambda_c} \right] \boldsymbol{C}_{(4\times2)} \cdot (\boldsymbol{d}_c \otimes \boldsymbol{d}_c) \cdot \boldsymbol{\Pi}_c \tag{30}$$

where

$$\boldsymbol{C}_{(4\times2)} = \begin{bmatrix} -1 & 0 \\ 0 & -1 \\ 1 & 0 \\ 0 & 1 \end{bmatrix} \tag{31}$$

Similarly, the remaining derivatives in (27) are obtained as follows,

$$\left(\frac{\partial^2 W_{\text{net}}}{\partial \lambda^2}\right)_{x} = \frac{\rho_{\text{net}}}{2 A_X A_Y} \sum_{c=1}^{n_{\text{edge-bars}}} \left\{ \frac{1}{\ell_c} \left(\frac{\mathrm{d} W_{\text{bar}}}{\mathrm{d}\lambda_c^2}\right) \boldsymbol{\Pi}_c \cdot \boldsymbol{\Pi}_c \right.$$
$$+ \frac{1}{\ell_c^3} \left[\lambda_c \left(\frac{\mathrm{d}^2 W_{\text{bar}}}{\mathrm{d}\lambda_c^2}\right) - \frac{\mathrm{d} W_{\text{bar}}}{\mathrm{d}\lambda_c} \right]$$
$$\left. \times \boldsymbol{\Pi}_c \cdot (\boldsymbol{d}_c \otimes \boldsymbol{d}_c) \cdot \boldsymbol{\Pi}_c \right\} \tag{32}$$

With $\partial \boldsymbol{x}/\partial \lambda$ determined from (28), the second term in (27) is derived as follows:

$$\frac{\partial}{\partial \boldsymbol{x}} \left[\left(\frac{\partial W_{\text{net}}}{\partial \lambda}\right)_{x} \right]_{\lambda} \cdot \left(\frac{\partial \boldsymbol{x}}{\partial \lambda}\right)$$
$$= \frac{\rho_{\text{net}}}{2 A_X A_Y} \sum_{c=1}^{n_{\text{edge-bars}}} \left\{ \frac{1}{\ell_c} \left(\frac{\mathrm{d} W_{\text{bar}}}{\mathrm{d}\lambda_c}\right) \frac{\partial}{\partial \boldsymbol{x}} [\boldsymbol{\Pi}_c \cdot \boldsymbol{d}_c]_{\lambda} \right.$$
$$\left. + \frac{\partial}{\partial \boldsymbol{x}} \left[\frac{1}{\ell_c} \left(\frac{\mathrm{d} W_{\text{bar}}}{\mathrm{d}\lambda_c}\right) \right]_{\lambda} (\boldsymbol{\Pi}_c \cdot \boldsymbol{d}_c) \right\} \cdot \left(\frac{\partial \boldsymbol{x}_c}{\partial \lambda}\right) \tag{33}$$

which is further evaluated to give,

$$\frac{\partial}{\partial \boldsymbol{x}} \left[\left(\frac{\partial W_{\text{net}}}{\partial \lambda}\right)_{x} \right]_{\lambda} \cdot \left(\frac{\partial \boldsymbol{x}}{\partial \lambda}\right) \tag{34}$$
$$= \frac{\rho_{\text{net}}}{2 A_X A_Y} \sum_{c=1}^{n_{\text{edge-bars}}} \left\{ \frac{1}{\ell_c} \left(\frac{\mathrm{d} W_{\text{bar}}}{\mathrm{d}\lambda_c}\right) \left[\boldsymbol{C}_{(4\times2)} \cdot \boldsymbol{\Pi}_c \right]^T \right.$$
$$+ \left[\lambda_c \left(\frac{\mathrm{d}^2 W_{\text{bar}}}{\mathrm{d}\lambda_c^2}\right) \right.$$
$$\left. - \frac{\mathrm{d} W_{\text{bar}}}{\mathrm{d}\lambda_c} \right] \boldsymbol{\Pi}_c \cdot (\boldsymbol{d}_c \otimes \boldsymbol{d}_c) \cdot \boldsymbol{C}_{(4\times2)}^T \left. \right\} \cdot \left(\frac{\partial \boldsymbol{x}_c}{\partial \lambda}\right)$$

The geometry of the network adopted in this implementation is irregular. To avoid an arbitrary departure from isotropy, the strain energy density of the network, W_{net}, and its derivatives are computed twice and averaged. In one computation, the X-axis in the microstructural network is oriented in the Λ_1 direction, and in the second computation, the X-axis in the microstructural network is oriented in the Λ_2 direction.

2.6 Wrinkling

The lens capsule is thin compared to the dimensions of the lens. This has the consequence that it will become unstable

in compression and susceptible to wrinkling (e.g. Ligarò and Barsotti 2008; Barsotti and Ligarò 2014).

Wrinkles can develop in the lens capsule in a variety of ways. In the in vivo lens, for example, wrinkles are typically observed around the circumference of the lens in frontal views (e.g. Fig. 2 of Rosen et al. 2006). These wrinkles are a consequence of the combined effect of the shape of the lens capsule and any intralenticular pressures that may exist. The capsule may also become wrinkled if the natural physiological condition is perturbed (e.g. by surgery) or during in vitro mechanical testing. The possibility of wrinkling is therefore included in the current model.

Wrinkling is a geometric nonlinear phenomenon. Following Barsotti and Ligarò (2014), however, it is treated by incorporating an equivalent material nonlinearity within the constitutive model. This approach is described below.

The in-plane wrinkle stretch ratio $\boldsymbol{\Lambda}^{(w)}$ ($\Lambda_i^{(w)} \leq 0$, $i = 1, 2$) is defined such that,

$$\boldsymbol{\Lambda} = \boldsymbol{\Lambda}^{(con)} + \boldsymbol{\Lambda}^{(w)} \tag{35}$$

where $\boldsymbol{\Lambda}$ is the total in-plane stretch ratio and $\boldsymbol{\Lambda}^{(con)}$ is the in-plane macroscopic stretch ratio applied to the constitutive model. The following three separate states exist.

1. Taut. $\partial W / \partial \Lambda_i^{(con)} > 0$ ($i = 1, 2$). In this case, $\boldsymbol{\Lambda}^{(con)} = \boldsymbol{\Lambda}$ and $\boldsymbol{\Lambda}^{(w)} = \boldsymbol{0}$.
2. Wrinkled. $\partial W / \partial \Lambda_i^{(con)}$ is positive for one of the coordinate directions m. In the other direction, n, this derivative is zero. Wrinkles exist parallel to the m direction and $\Lambda_n^{(w)} \leq 0$.
3. Inactive. $\partial W / \partial \boldsymbol{\Lambda}^{(con)} = \boldsymbol{0}$ and $\Lambda_i^{(w)} \leq 0$ ($i = 1, 2$).

To implement this behaviour, at the start of any call to the micronet constitutive model, $\partial W / \partial \boldsymbol{\Lambda}^{(con)}$ and $\partial^2 W / \partial (\boldsymbol{\Lambda}^{(con)})^2$ are first computed for $\boldsymbol{\Lambda}^{(con)} = \boldsymbol{\Lambda}$.

If $\partial W / \partial \Lambda_i^{(con)} > 0$ ($i = 1, 2$), then the material is locally taut. In other cases, the state is classified as either wrinkled or inactive. In the inactive state $\partial W / \partial \boldsymbol{\Lambda}^{(con)} = \partial^2 W / \partial (\boldsymbol{\Lambda}^{(con)})^2 = \boldsymbol{0}$. In each of the two possible wrinkled states, the capsule behaves in a uniaxial stress manner. For wrinkles parallel to the m direction, the boundary condition imposed on the constitutive model is $\Lambda_m^{(con)} = \Lambda_m$, $\partial W / \partial \Lambda_n^{(con)} = 0$, and $\Lambda_n^{(con)}$ is determined by iteration. $\partial W / \partial \Lambda_m^{(con)}$ is computed directly from the constitutive model, $\partial^2 W / \partial (\Lambda_m^{(con)})^2$ is computed by numerical differentiation, and $\partial W / \partial \Lambda_n^{(con)} = \partial^2 W / \partial (\Lambda_n^{(con)})^2 = 0$.

3 Implementation of the model

3.1 Macroscopic finite element model

The macroscopic finite element program is based on a conventional hyperelastic formulation (e.g. Bonet and Wood 1997; Holzapfel 2000). The lens capsule is modelled using an axisymmetric finite element formulation that is consistent with the equations for membrane kinematics and virtual work given in Wriggers and Taylor (1990), Verron and Marckmann (2003). The membrane is discretized using isoparametric finite elements. Solution of the nonlinear finite element equations is by Newton–Raphson.

The macroscopic finite element model makes repeated calls to the micronet routines to compute the strain energy derivatives. To minimize computation time, the current joint positions of the network, at each of the macroscopic stress points, are stored as internal variables. These joint positions are continuously updated as the macroscopic analysis proceeds.

3.2 Capsule thickness

The reference capsule thickness T is known to vary with position on the lens meridian. This spatial variation of capsule thickness is specified in the macroscopic finite element model.

Fisher and Pettet (1972) used an optical technique to determine capsule thickness variations for lenses of a range of ages. More recently, Barraquer et al. (2006) measured capsule thickness using a histological technique. The Barraquer et al. (2006) data show broadly the same patterns as those seen in the Fisher and Pettet (1972) data, although the values of capsule thickness (particularly for the anterior portion of the lens) tend to be lower than the values reported by Fisher. A discussion on the differences in capsule thickness determined using histology and optical methods is given by Ziebarth et al. (2005). In the current paper, the Barraquer et al. (2006) data have been adopted to define the spatial variation of capsule thickness.

Figure 7 of Barraquer et al. (2006) gives data on capsule thickness in three groups: Group A (average age 36 years), Group B (average age 65 years) and Group C (average age 65 years). Numerical values of these data have been supplied to the current authors by R.I. Barraquer; these data are plotted in Fig. 12 and tabulated in Table 5 (see "Appendix 2"). An automatic routine was developed within *Oxfem_hyperelastic* in which the normalized position (see Fig. 12) of each stress point in each element representing the capsule is determined. The value of thickness T to be assigned at this stress point is then computed from the appropriate group in the Barraquer et al. (2006) data by linear interpolation.

Table 2 Optimized constitutive parameters for micronet model

Free parameters			Fixed parameter
μ_{mat}	$(\rho_{\text{net}} c_1 / L_0)$	c_2	λ^L
452.2 kPa	113.8 kPa	37.3	1.1

Note that $(\rho_{\text{net}} c_1 / L_0)$ is treated as a single parameter

3.3 Strain energy functions

The following incompressible form of the neo-Hookean model is used to represent the matrix,

$$W_{\text{mat}} = \frac{\mu_{\text{mat}}}{2} \left[\lambda_x^2 + \lambda_y^2 + \frac{1}{\lambda_x^2 \lambda_y^2} - 3 \right] \tag{36}$$

where μ_{mat} is a constitutive parameter.

The strain energy density (per unit initial bar length) adopted for the bars in the network for $1 \leq \lambda_{\text{bar}} \leq \lambda^L$ where λ_{bar} is the bar stretch ratio and λ^L is a constitutive parameter is,

$$W_{\text{bar}}(\lambda_{\text{bar}}) = c_1 \exp(c_2 E_{\text{bar}}^2) \tag{37}$$

where $E_{\text{bar}} = \frac{1}{2}(\lambda_{\text{bar}}^2 - 1)$. This function is based on previous models (e.g. Holzapfel et al. 2002). Since exponential strain energy functions of this form can become unrealistically stiff at large values of stretch ratio, a separate strain energy density has been adopted for $\lambda_{\text{bar}} > \lambda^L$,

$$W_{\text{bar}}(\lambda_{\text{bar}}) = k_1 \left(\lambda_{\text{bar}} - \lambda^L \right)^2 + k_2 (\lambda_{\text{bar}} - \lambda^L) + k_3 \tag{38}$$

where the constants k_1, k_2 and k_3 are chosen to ensure continuity of W_{bar} and its first and second derivatives at $\lambda_{\text{bar}} = \lambda^L$. For $\lambda_{\text{bar}} < 1$ (corresponding to compression), the strain energy density is,

$$W_{\text{bar}}(\lambda_{\text{bar}}) = c_1 c_2 \left[(\lambda_{\text{bar}} - 1)^2 \right] \tag{39}$$

A normalized bar force $\bar{f}_{\text{bar}}$ is defined,

$$\bar{f}_{\text{bar}} = \left(\frac{\rho_{\text{net}}}{L_0} \right) \frac{dW_{\text{bar}}}{d\lambda_{\text{bar}}} \tag{40}$$

The relationship between $\bar{f}_{\text{bar}}$ and λ_{bar}, for the particular case of the data in Table 2, is plotted in Fig. 3.

4 Example calculations

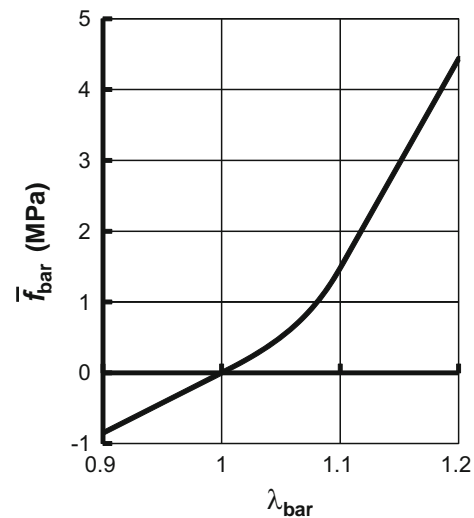A calibration exercise and two example calculations are described below.

Fig. 3 Relationship between normalized bar force $\bar{f}_{\text{bar}}$ and the bar stretch ratio, λ_{bar} for the data in Table 2

4.1 Calibration

In the analyses in Burd (2009), the micronet model was calibrated using the Krag data [i.e. the uniaxial stress data of Krag et al. (1997)] and equi-biaxial data determined from the Fung model developed by Pedrigi et al. (2007). The use of these extremes of equi-biaxial and uniaxial calibration data provides a well-conditioned approach. The Krag data are adopted for calibration purposes in the current paper (making use of the raw data provided to the authors by S. Krag). However, for the reasons set out below, the Fung model has not been used. Instead, biaxial calibration data have been obtained from capsule inflation test results given in Fisher (1969).

The Fung model proposed by Pedrigi et al. (2007) is based on in situ capsule inflation tests in which the constitutive parameters were determined from the experimental data using the Seshaiyer and Humphrey (2003) subdomain inverse finite element approach. In this procedure, a finite element subdomain, consisting of four constant strain triangular membrane elements, defined by the positions of five markers on the surface of the capsule, is used to determine the constitutive parameters by inverse analysis. The use of five markers to define the subdomain is insufficient for a complete representation of the local surface curvatures. This lack of complete surface curvature information means that, in general, the virtual work terms associated with the internal pressure will be evaluated incorrectly during the inverse analysis.

In the Fisher (1969) test, a portion of anterior capsule was clamped between two plates that contained a circular hole of radius 2 mm. The centre of the hole was aligned with the anterior pole of the capsule. The capsule was inflated by fluid pressure, and measurements were made of the volume

of fluid used to inflate the capsule and the corresponding pressure. Fisher conducted tests on numerous samples, but, unfortunately, detailed volume/pressure data are only presented for two cases (ages 30 and 45 years). The 45-year data are regarded as being unsatisfactory for calibration purposes (see Burd 2009), and so, the calibration exercise is conducted solely on the 30-year sample.

Uniaxial calibration data have been selected from the Krag et al. (1997) tests conducted on samples that are close to 30 years of age (for consistency with the inflation test data). Five of the Krag et al. (1997) uniaxial tests have been selected (samples between the ages of 24 and 32 years, average age 28 years) for values of stretch ratio from 1.0 to 1.16 in increments of 0.01. Experimental data on membrane traction (force per unit initial sample width) were averaged to form the calibration data. The value of capsule thickness, T, assigned to these data is $12.6\,\mu$m. This value is based on the Barraquer et al. (2006) Group A data (mean age 36 years), at a normalized position $R_d = 32$, which is estimated to correspond to the location of the capsular rings tested by Krag et al. (1997) on the basis of arc lengths along the lens meridian computed using the 29-year outline in Hermans et al. (2008).

The constitutive parameters μ_{mat}, $(\rho_{\mathrm{net}}c_1/L_0)$ and c_2 were adjusted to provide an optimum fit with the calibration data. The parameter λ^L is set, arbitrarily, at $\lambda^L = 1.1$. The uniaxial response of the model [for comparison with the Krag et al. (1997) data] is determined directly. To calibrate against the Fisher inflation data, an axisymmetric finite element analysis of the inflation test is used to compute a volume/pressure response. Data are not provided in Fisher (1969) on the initial shape of the lens capsules that were tested. In the absence of this information, the initial (stress-free) geometry of the capsule in the finite element model is represented by the 29-year lens outline at maximal accommodation (8D) developed in a separate study given in Hermans et al. (2008). The Barraquer et al. (2006) Group A data are adopted to define the spatial variation of capsule thickness in the finite element model. The optimization is conducted by minimizing the objective function $\Phi(\mu_{\mathrm{mat}}, (\rho_{\mathrm{net}}c_1/L_0), c_2)$ given by,

$$\Phi = \left(\frac{1}{N_{\mathrm{biax}}} \sum_{m=1}^{N_{\mathrm{biax}}} \left[\frac{\bar{v}(p_m) - v_m}{(v_m)_{\mathrm{mean}} - V} \right]^2 \right)^{1/2}$$
$$+ \left(\frac{1}{N_{\mathrm{uni}}} \sum_{n=1}^{N_{\mathrm{uni}}} \left[\frac{\bar{P}(\lambda_n) - P_n}{(P_n)_{\mathrm{mean}}} \right]^2 \right)^{1/2} \tag{41}$$

The first summation relates to the capsule inflation data where (v_m, p_m), $m = 1, N_{\mathrm{biax}}$ are the experimental volume/pressure from the Fisher (1969) data and $\bar{v}$ is the computed volume enclosed by the capsule ($N_{\mathrm{biax}} = 8$). The initial enclosed volume (computed from the initial lens
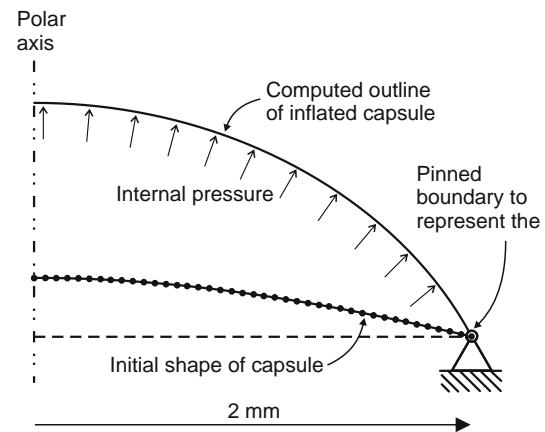
Fig. 4 Finite element model for the Fisher (1969) inflation test on a 30-year capsule. The mesh consists of 20, three-noded, axisymmetric isoparametric elements. Micronet parameters are given in Table 2. The computed outline is shown at an internal pressure of 16 kPa

geometry) is V. The second summation relates to the uniaxial data where (λ_n, P_n) $n = 1, N_{\mathrm{uni}}$ are the calibration stretch/traction data from the Krag et al. (1997) uniaxial tests and $\bar{P}(\lambda_n)$ are the values of traction computed using the micronet model ($N_{\mathrm{uni}} = 16$) with $T = 12.6\,\mu$m. The parameters $(v_m)_{\mathrm{mean}}$ and $(P_n)_{\mathrm{mean}}$ are the mean values of the enclosed volume (from the Fisher data) and the membrane traction (from the Krag data), respectively.

The optimized parameters (determined using the optimization routines in MATLAB) are listed in Table 2.

The final computed outline for the inflation test analysis is plotted in Fig. 4. In this final configuration, the stretch ratio developed in the capsule is in the region of 1.18. Comparisons between the calibration data and the micronet model are shown in Fig. 5.

4.2 Convergence performance

Care has been taken in this multiscale model to develop a correct formulation for the strain energy derivatives that are needed to form the tangent stiffness matrix in the macroscopic finite element program. To illustrate the convergence performance that is achieved in the macroscopic model (dependent upon the linearization with respect to the micronet model), data have been gathered (Table 3) on the convergence of the out-of-balance forces for the final calculation step (corresponding to an increment in pressure from 13.6 to 16 kPa) in the Fisher (1969) inflation test analysis. The solution converges in a way that is consistent with the quadratic convergence performance expected of the global Newton–Raphson algorithm. The observed macroscopic convergence performance is dependent on the accuracy of the computed strain energy derivatives. To achieve the convergence performance shown in Table 3, a
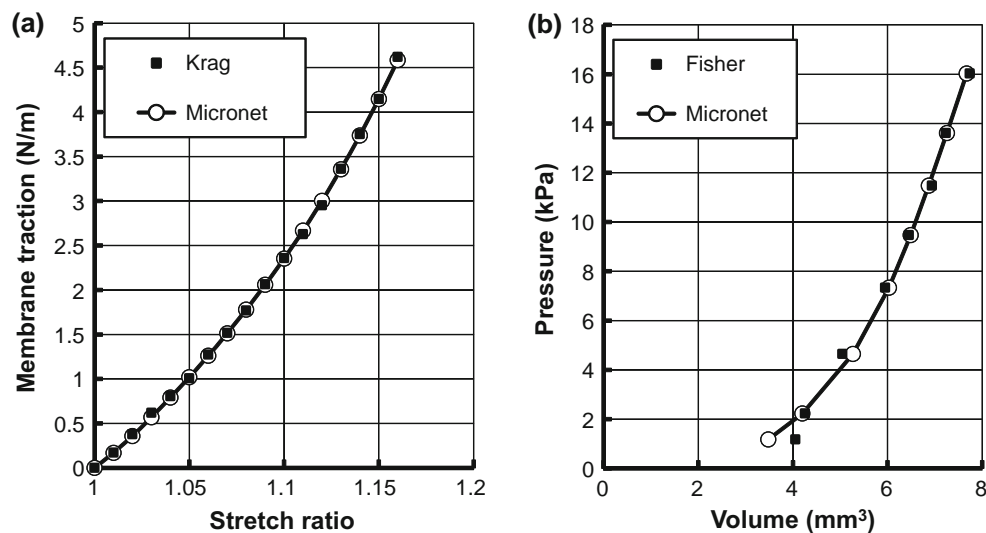
Fig. 5 a Uniaxial calibration data from Krag et al. (1997) and the uniaxial micronet response. **b** Experimental capsule inflation data from Fisher (1969) for a 30-year capsule. Also shown is the volume/pressure response computed using the finite element model shown in Fig. 3. Micronet parameters are given in Table 2

Table 3 Illustrative convergence performance of the multiscale model

Iteration 1	Iteration 2	Iteration 3	Iteration 4
5.2×10^{-1}	5.4×10^{-3}	5.9×10^{-7}	1.2×10^{-11}

The data shown in the table relate to the infinity norm of the out-of-balance force vector (units mN) computed by the macroscopic finite element model, for the final loading step in the analysis illustrated in Fig. 4

tight tolerance ($tol_{net} = 10^{-9}$ mN in the current example) is required in the computations conducted at the constitutive model level.

4.3 Analysis of the isolated capsule inflation tests described by Martin et al. (2003)

Martin et al. (2003) describe an isolated capsule inflation test that is broadly similar to the Fisher (1969) test. A key development, however, is that Martin et al. (2003) quantify the deformations induced in the capsule during the inflation process by measuring the displacement of the pole of the capsule sample (using an ultrasonic transducer). This removes the need for a volume measurement. The Martin et al. (2003) data were all obtained using a circular inflation aperture of radius 1.25 mm [in contrast to the 2-mm-radius aperture employed by Fisher (1969)].

H. Martin has given the authors access to the numerical values of the data that were obtained during this test program. The inflation pressures adopted in the Martin et al. (2003) tests typically deformed the capsule samples to stretch ratios of the order of 1.04. This level of deformation is regarded as

being insufficient for calibration purposes. The data do, however, provide a useful independent check on the calibrated model.

The capsule samples tested by Martin et al. (2003) were in the age range 48–93 years. Consequently, there are no data that correspond to the age of the samples (in the region of 30 years) that form the current calibration data. The youngest four samples, for which complete sets of raw data are available, were selected for this comparison exercise.

To conduct this comparison, a multiscale finite element model was built for the Martin et al. (2003) test configuration. The initial capsule shape is represented by the 45-year fully accommodated (8D) anterior profile given in Hermans et al. (2008). The Group B data of Barraquer et al. (2006) (mean age 65 years) are used to define the thickness variation. Comparisons between the computed vertical displacement at the anterior pole and the Martin data are shown in Fig. 6. The computed data fall within the range of the experimental results. This provides a degree of confidence in the veracity of the model. The computed final shape of the capsule is shown in Fig. 7.

4.4 Analysis of the in situ capsule inflation test of Pedrigi et al. (2007)

Pedrigi et al. (2007) describe an alternative inflation test in which the capsule of an intact in vitro lens is inflated by the injection of fluid (balanced salt solution) at the capsule/lens interface. This causes an anterior portion of the capsule to become detached from the lens and inflated by the fluid pressure. The tests were conducted on enucleated
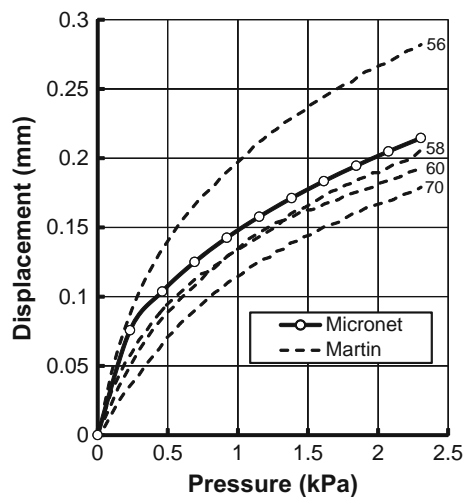
Fig. 6 Comparison between the anterior pole displacement computed using the multiscale micronet model and data from the Martin et al. (2003) capsule inflation tests. The age in years of the capsule samples are indicated on the graph. Micronet parameters are given in Table 2
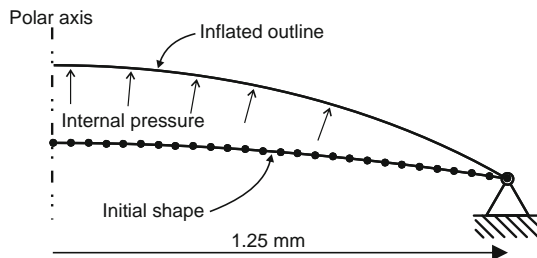

Fig. 7 Finite element model of the Martin et al. (2003) capsule inflation test for the 56-year sample. The mesh consists of 13, three-noded, axisymmetric isoparametric elements. Micronet parameters are given in Table 2

human donor eyes; the cornea and iris were removed prior to testing. The procedure adopted in these tests [based on the descriptions given in Pedrigi et al. (2007)] is illustrated, diagrammatically, in Fig. 8. For the purposes of the current analyses, it is assumed that, during the test, the lens is supported on the vitreous (i.e. support provided via the zonules is negligible). During the tests, the motion of the capsule was recorded by tracking sets of markers attached to the capsule surface. Using the kinematic data from these markers, the local strains in the capsule, in both the circumferential and meridional directions, were determined. Data on the inferred Green strains in the inflated capsule (for normal, non-diabetic eyes) are given in Pedrigi et al. (2007) as average values, with mean age 65 years. Noting that residual stresses exist in the lens capsule, the strains were referred to a stress-free state determined, at the end of each test.

A finite element model of the test has been developed in which geometric data on the fully accommodated 45-year (4D) lens in Hermans et al. (2008) are adopted to define the initial lens outline. [This is the oldest lens profile reported
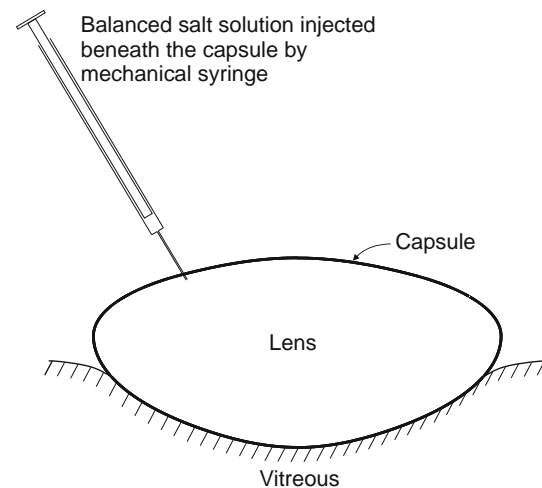

Fig. 8 Diagrammatic representation of the in situ capsule inflation test [based on the description in Pedrigi et al. (2007)]. The lens is shown with the anterior side uppermost

by Hermans et al. (2008)]. The mesh used in the study is shown in Fig. 9. This consists of 484 fifteen-noded axisymmetric triangular elements to represent the lens substance and 53 five-noded membrane elements generated around the lens meridian to model the capsule. The lens capsule is modelled using the micronet model with the spatial thickness variation based on Barraquer et al. (2006), Group B. Constitutive parameters for the capsule are given in Table 2. The lens is modelled as a homogeneous material (i.e. without a nucleus); this approach is adopted for simplicity and on the basis that the lens is only included in the analysis to provide an appropriate boundary condition for the capsule.

The lens substance is represented by a neo-Hookean model with strain energy density (per unit reference volume), $\Psi(\boldsymbol{C})$, given by,

$$\Psi(\boldsymbol{C}) = \frac{\mu_L}{2}\left(tr\left[J^{-2/3}\boldsymbol{C}\right] - 3\right) + \frac{\kappa_L}{2}(J-1)^2 \qquad (42)$$

where $\boldsymbol{C}$ is the right Cauchy–Green tensor, $J^2 = \det \boldsymbol{C}$ and μ_L and κ_L are constitutive parameters. In the current analysis, the shear modulus is $\mu_L = 10$ kPa and the bulk modulus is $\kappa_L = 500$ kPa. [This value of shear modulus is adopted on the basis that it is broadly consistent with the shear modulus data reported in Weeber et al. (2007) for lenses of age in the region of 65 years. It is also consistent with the trends in the Model H data given in Wilde et al. (2012).] The bulk modulus is an order of magnitude greater than the shear modulus, thereby representing a nearly incompressible material.

During the test, an anterior portion of the capsule becomes separated from the lens; the capsule remains attached in the equatorial region. At some radial location between the anterior pole and the equator, a separation point exists. To conduct the analysis, an a priori assumption is made on the location
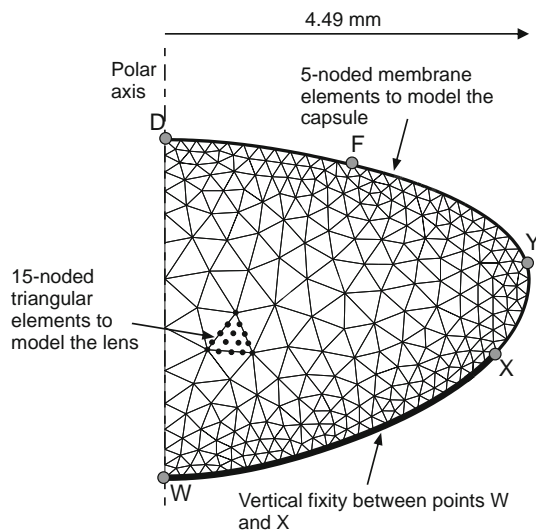
Fig. 9 Axisymmetric finite element mesh based on the 45-year fully accommodated (4D) outline in Hermans et al. (2008). Vertical fixity (to represent the support provided by the vitreous) is imposed on the mesh between points W and X. The membrane elements are fully coupled to the continuum mesh between point W and the separation point, point Y. Between points Y and D (anterior pole), the membrane elements are uncoupled from the continuum mesh. The inflation test is modelled by prescribing an internal pressure along the interface YD. Micronet parameters are given in Table 2

Fig. 10 Deformed mesh for an internal pressure 4.666 kPa

of the separation point on the anterior surface of the lens. The choice of separation point is limited to the end nodes on the membrane elements representing the capsule. All of the membrane elements between the assumed separation point and the anterior pole are defined in terms of nodes which do not share any connectivity with those on the lens surface (although the initial node coordinates are coincident). The portion of capsule between the separation point and the capsule anterior pole is inflated by applying an internal hydrostatic pressure.

The appropriate location of the separation point is selected by trial and error. For the current analysis, point Y on Fig. 9 was selected. For values of inflation pressure less than about 1.39 kPa, this separation point is invalid (since it would imply that the capsule penetrates the lens). For greater values of pressure, however, the use of point Y as a separation point appears to provide a reasonable approach. Wrinkles were found to develop in the equatorial region in the initial stages of the analysis. These wrinkles disappeared as the calculation progressed. The deformed mesh at the end of the analysis is shown in Fig. 10.

Pedrigi et al. (2007), in their Fig. 2, present data at two five-point marker locations in the capsule (identified as D and F). Location D corresponds to the anterior pole. The precise location of F is not specified. However, Pedrigi et al. (2007) do say that "The total arc length spanned by these 23 video tracking markers along either axis was about 4 mm from the pole". This suggests that the centre of the marker set
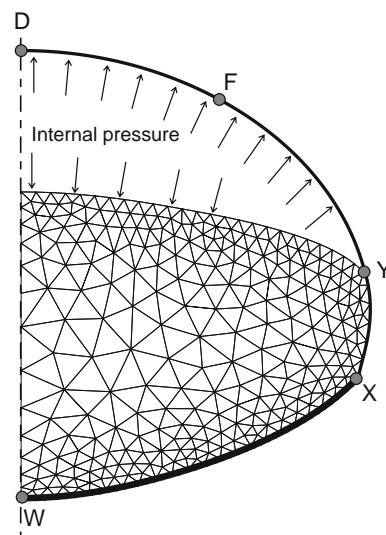
representing location F lies at an arc length of about 2.29 mm from the anterior pole. These locations are indicated by the points D and F in Figs. 9 and 10.

Computed data on Green strain versus internal pressure are plotted in Fig. 11 for the stress point closest to the anterior pole (corresponding to point D) and a stress point at the initial arc length of 2.3 mm, assumed to correspond to point F. The computed Green strain/pressure response shows reasonable agreement with the Pedrigi data. This suggests that an anisotropic model with regional variations (of the sort proposed by Pedrigi et al. (2007)) is not needed for a plausible model of this capsule inflation test.

There are differences in the two data sets. These may be associated with shortcomings in the constitutive models, incorrect assumed values of capsule thickness variation, neglect of the presence of residual stresses in the capsule, sensitivity of the results to the particular choice of initial lens shape and errors associated with the assumed locations of points F and Y. An exploration of these potential causes is beyond the scope of the current paper.

5 Conclusion

The micronet model has been implemented in a hyperelastic axisymmetric finite element program with consistent linearization, demonstrating quadratic convergence of the global Newton–Raphson solver. There is limited availability of experimental data to calibrate the model. As a consequence, a single calibration was conducted on lens capsule samples with ages in the region of 30 years.

The calibrated model was found to correspond well to lens inflation data given by Martin et al. (2003) and Pedrigi et al. (2007). The comparison with the Pedrigi et al. (2007) data is
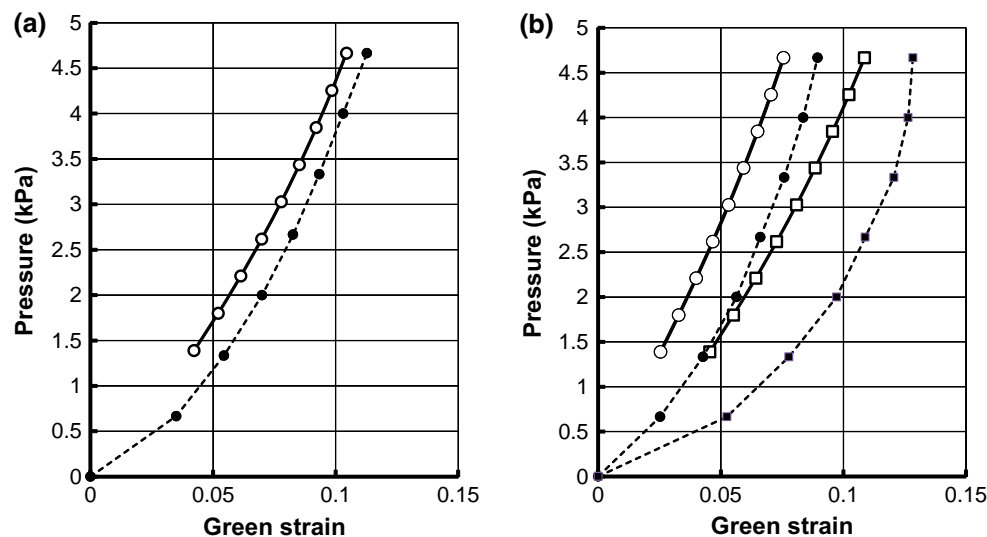
Fig. 11 Computed Green strain/pressure response compared with the experimental data of Pedrigi et al. (2007). *Open symbols* indicate the micronet results, and the *filled symbols* represent the experimental data.

Circles indicate circumferential strains, and *squares* indicate meridional strains. **a** The strains at point D; **b** the strains at point F

particularly interesting in the sense that the observed performance of the capsule appears to be well represented by the current model (in which spatial variations of capsule constitutive parameters are not included and which is isotropic). A spatially varying anisotropic model of the sort proposed by Pedrigi et al. (2007) is not needed in order to achieve this comparison.

The results presented in the current paper demonstrate the feasibility of embedding a non-affine structural model for the lens capsule within a macroscopic axisymmetric finite element analysis. This structural modelling approach provides a systematic way of linking the mechanical behaviour of the capsule to the geometric arrangement of the underlying collagen structure. This provides considerable potential for future research, based on detailed imaging of the collagen network, in which the topology of the network adopted in the model is made to be representative of the observed collagen topology in the lens capsule. This procedure provides opportunities, for example, in developing enhanced forms of the model in which any observed age-related changes in the topology of the collagen network can be used to suggest appropriate age-related configurations of the network component of the micronet model. In the current model, the topology of the collagen network is assumed to be isotropic. Anisotropy could be included within the model by imposing an appropriate form of geometric anisotropy on the collagen network (e.g. Stylianopoulos and Barocas 2007a).

It should be noted that the detailed performance of the micronet model depends on the particular values of the joint coordinates that are adopted. The constitutive parameters adopted in the current paper are based on the joint coordinates

given in "Appendix 1". If a different set of joint coordinates are adopted, or if modifications are made to the topology of the network, then recalibration of the model parameters will be necessary.

Appendix 1: Table of joint coordinates

See Table 4.

Table 4 Initial joint coordinates for the network shown in Fig. 1 $A_X/L_0 = 6$, $A_Y/L_0 = 3\sqrt{3}$

X/L_0	Y/L_0	X/L_0	Y/L_0	X/L_0	Y/L_0
0.48006	0.67919	4.11156	1.11437	0.90756	2.96186
3.47784	3.81507	2.61282	0.79226	4.99452	1.22390
2.23416	3.14762	5.40222	3.91520	3.64176	0.37599
0.39396	2.31494	4.3221	3.03606	1.08606	4.99755
5.48052	0.47275	2.55048	2.03715	5.2497	2.94081
1.89438	4.83211	0.88218	1.39428	3.45534	2.02821
0.4539	3.95583	3.9486	4.85502	2.10216	1.30356
5.55792	2.36050	2.29278	3.59667	4.77402	4.85710

Appendix 2: Capsule thickness data from Barraquer et al. (2006)

See Table 5 and Fig. 12.

Table 5 Numerical values of capsule thickness data (units μm) from Fig. 7 of Barraquer et al. (2006)

R_d	Group A	Group B	Group C
0	11.0	14.5	15.1
5	10.6	14.6	14.8
10	10.9	14.7	14.5
15	11.0	14.3	14.2
20	11.2	14.1	14.2
25	11.7	14.2	14.6
30	12.3	14.6	15.0
35	13.0	15.2	15.4
40	13.4	15.7	15.4
45	13.5	16.0	15.0
50	13.2	15.8	13.9
55	12.5	15.2	12.4
60	11.4	14.0	10.6
65	10.2	12.5	8.6
70	9.0	10.8	6.9
75	8.0	9.1	5.8
80	7.5	7.7	5.4
85	7.4	6.8	5.8
90	7.6	6.5	6.8
95	7.8	6.8	7.6
100	7.8	7.0	6.8
105	8.0	6.8	6.3
110	7.9	6.0	5.3
115	7.9	5.4	4.7
120	7.8	5.1	4.3
125	7.6	5.1	3.9
130	7.4	5.3	3.6
135	7.0	5.6	3.3
140	6.6	5.7	3.1
145	6.1	5.6	2.9
150	5.5	5.4	2.8
155	5.0	5.0	2.7
160	4.4	4.6	2.7
165	4.0	4.6	2.7
170	3.7	4.6	2.6
175	3.9	4.7	2.6
180	4.1	5.3	2.5
185	4.4	6.4	2.5
190	4.1	4.9	2.4
195	3.5	5	2.4
200	3.5	4.3	2.6

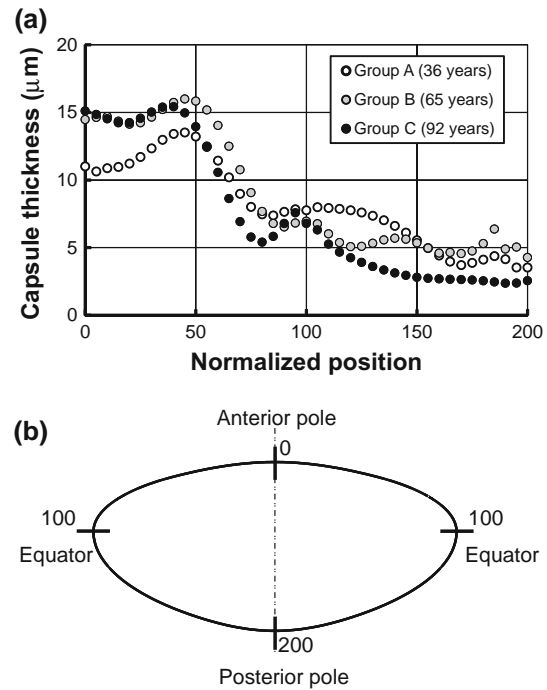**Fig. 12** **a** Data on lens capsule thickness re-plotted from Fig. 7 of Barraquer et al. (2006). Group A, mean age = 36 years; Group B, mean age = 65 years; Group C, mean age = 92 years. R_d is normalized position, measured along the lens meridian from the anterior pole. Normalized position is determined such that at the anterior pole $R_d = 0$, at the equator $R_d = 100$ and at the posterior pole $R_d = 200$ (see **b**)

References

Agoram B, Barocas VH (2001) Coupled macroscopic and microscopic scale modeling of fibrillar tissues and tissue equivalents. J Biomech Eng 123:362–369

Burgess SA, Carter DA, Woolley DM (1992) Three-dimensional structure of type IV collagen in the mammalian lens capsule. J Struct Biol 108(1):6–13

Barraquer RI, Michael R, Abreu R, Lamarca J, Tresserra F (2006) Human lens capsule thickness as a function of age and location along the sagittal lens perimeter. Invest Ophthalmol Vis Sci 47(5):2053–2060

Barsotti R, Ligarò SS (2014) Static response of elastic inflated wrinkled membranes. Comput Mech 53(5):1001–1013

Belaidi A, Pierscionek BK (2007) Modeling internal stress distributions in the human lens: can opponent theories coexist? J Vis 7(11):1–12

Bonet J, Wood RD (1997) Nonlinear continuum mechanics for finite element analysis. Cambridge University Press, Cambridge

Bron AJ, Tripathi RC, Tripathi BJ (1997) Wolff's anatomy of the eye and orbit. Chapman Hall, London

Burd HJ, Judge SJ, Cross JA (2002) Numerical modelling of the accommodating lens. Vis Res 42(18):2235–2251

Burd HJ (2009) A structural constitutive model for the human lens capsule. Biomech Model Mechanobiol 8(3):217–231

Charman WN (2014) Developments in the correction of presbyopia II: surgical approaches. Ophthalmic Physiol Opt 34(4):397–426

D'Amore A, Amoroso N, Gottardi R, Hobson C, Carruthers C, Watkins S, Wagner WR and Sacks MS (2014) From single fiber to macro-level mechanics: a structural finite-element model for elastomeric fibrous biomaterials. J Mech Behav Biomed Mater 39:146–161

Danysh BP, Duncan MK (2009) The lens capsule. Exp Eye Res 88(2):151–164

Fan R, Sacks MS (2014) Simulation of planar soft tissues using a structural constitutive model: finite element implementation and validation. J Biomech 47(9):2043–2054

Fisher RF (1969) Elastic constants of the human lens capsule. J Physiol 201(1):1–19

Fisher RF, Pettet BE (1972) The postnatal growth of the capsule of the human crystalline lens. J Anat 112(2):207–214

Hermans EA, Dubbelman M, Van der Heijde GL, Heethaar RM (2006) Estimating the external force acting on the human eye lens during accommodation by finite element modelling. Vis Res 46(21):3642–3650

Hermans EA, Dubbelman M, Van der Heijde GL, Heethaar RM (2008) Change in the accommodative force on the lens of the human eye with age. Vis Res 48(1):119–126

Holzapfel GA (2000) Nonlinear solid mechanics: a continuum approach for engineering. Wiley, London

Holzapfel GA, Gasser TC, Stadler M (2002) A structural model for the viscoelastic behavior of arterial walls: continuum formulation and finite element analysis. Eur J Mech A Solids 21(3):441–463

Krag S, Andreassen TT (2003) Mechanical properties of the human lens capsule. Prog Retin Eye Res 22(6):749–767

Krag S, Olsen T, Andreassen TT (1997) Biomechanical characteristics of the human anterior lens capsule in relation to age. Invest Ophthalmol Vis Sci 38(2):357–363

Ligarò SS, Barsotti R (2008) Equilibrium shapes of inflated inextensible membranes. Int J Solids Struct 45(21):5584–5598

Martin H, Schmidt W, Schmitz KP, Schneider H, Guthoff R, Terwee T (2003) Material properties of the isolated human capsular bag. Curr Asp Hum Accommod II:127–133

Oyster CW (1999) The human eye: structure and function. Sinauer, Sunderland, MA

Pedrigi RM, David G, Dziezyc J, Humphrey JD (2007) Regional mechanical properties and stress analysis of the human anterior lens capsule. Vis Res 47(13):1781–1789

Rosen AM, Denham DB, Fernandez V, Borja D, Ho A, Manns F, Parel JM, Augusteyn RC (2006) In vitro dimensions and curvatures of human lenses. Vis Res 46(6–7):1002–1009

Schumacher S, Oberheide U, Fromm M, Ripken T, Ertmer W, Gerten G, Wegener A, Lubatschowski H (2009) Femtosecond laser induced flexibility change of human donor lenses. Vis Res 49(14):1853–1859

Seshaiyer P, Humphrey JD (2003) A sub-domain inverse finite element characterization of hyperelastic membranes including soft tissues. J Biomech Eng 125(3):363–371

Stachs O, Martin H, Behrend D, Schmitz KP, Guthoff R (2006) Three-dimensional ultrasound biomicroscopy, environmental and conventional scanning electron microscopy investigations of the human zonula ciliaris for numerical modelling of accommodation. Graefe's Arch Clin Exp Ophthalmol 244(7):836–844

Stylianopoulos T, Barocas VH (2007a) Multiscale, structure-based modeling for the elastic mechanical behavior of arterial walls. J Biomech Eng 129(4):611–618

Stylianopoulos T, Barocas VH (2007b) Volume-averaging theory for the study of the mechanics of collagen networks. Comput Methods Appl Mech Eng 196(31–32):2981–2990

Verron E, Marckmann G (2003) Inflation of elastomeric circular membranes using network constitutive equations. Int J Non Linear Mech 38(8):1221–1235

Weeber HA, Eckert G, Pechhold W, Van der Heijde GL (2007) Stiffness gradient in the crystalline lens. Graefes Arch Clin Exp Ophthalmol 245(9):1357–1366

Wilde GS, Burd HJ, Judge SJ (2012) Shear modulus data for the human lens determined from a spinning lens test. Exp Eye Res 97(1):36–48

Wriggers P, Taylor RL (1990) A fully non-linear axisymmetrical membrane element for rubber-like materials. Eng Comput 7:303–310

Ziebarth NM, Manns F, Uhlhorn SR, Venkatraman AS, Parel JM (2005) Noncontact optical measurement of lens capsule thickness in human, monkey, and rabbit postmortem eyes. Invest Ophthalmol Vis Sci 46(5):1690–1697

FEDERAL FINANCIAL REPORT

(Follow form instructions)

1. Federal Agency and Organizational Element to Which Report is Submitted	2. Federal Grant or Other Identifying Number Assigned by Federal Agency (To report multiple grants, use FFR Attachment)	Page of 1	
			pages

3. Recipient Organization (Name and complete address including Zip code)

4a. DUNS Number	4b. EIN	5. Recipient Account Number or Identifying Number (To report multiple grants, use FFR Attachment)	6. Report Type ☐ Quarterly ☐ Semi-Annual ☐ Annual ☐ Final	7. Basis of Accounting ☐ Cash ☐ Accrual

8. Project/Grant Period (Month, Day, Year)		9. Reporting Period End Date (Month, Day, Year)
From:	To:	

10. **Transactions**	Cumulative

(Use lines a-c for single or combined multiple grant reporting)

Federal Cash (To report multiple grants separately, also use FFR Attachment):

a. Cash Receipts	
b. Cash Disbursements	
c. Cash on Hand (line a minus b)	

(Use lines d-o for single grant reporting)

Federal Expenditures and Unobligated Balance:

d. Total Federal funds authorized	
e. Federal share of expenditures	
f. Federal share of unliquidated obligations	
g. Total Federal share (sum of lines e and f)	
h. Unobligated balance of Federal funds (line d minus g)	

Recipient Share:

i. Total recipient share required	
j. Recipient share of expenditures	
k. Remaining recipient share to be provided (line i minus j)	

Program Income:

l. Total Federal share of program income earned	
m. Program income expended in accordance with the deduction alternative	
n. Program income expended in accordance with the addition alternative	
o. Unexpended program income (line l minus line m or line n)	

11. Indirect Expense	a. Type	b. Rate	c. Period From	Period To	d. Base	e. Amount Charged	f. Federal Share
				g. Totals:			

12. Remarks: Attach any explanations deemed necessary or information required by Federal sponsoring agency in compliance with governing legislation:

13. Certification: By signing this report, I certify to the best of my knowledge and belief that the report is true, complete, and accurate, and the expenditures, disbursements and cash receipts are for the purposes and intent set forth in the award documents. I am aware that any false, fictitious, or fraudulent information may subject me to criminal, civil, or administrative penalties. (U.S. Code, Title 18, Section 1001)

a. Typed or Printed Name and Title of Authorized Certifying Official	c. Telephone (Area code, number, and extension)
	d. Email Address
b. Signature of Authorized Certifying Official	e. Date Report Submitted (Month, Day, Year)

14. Agency use only:

Standard Form 425 - Revised 10/11/2011
OMB Approval Number: 0348-0061
Expiration Date: 2/28/2015